University of Strathclyde, Glasgow

Department of Naval Architecture, Ocean and Marine

Engineering

Drag Coefficient and Damping of Moorings and Their Effect on FPSO's Response

By

Zhengqiang Xu

A thesis presented in fulfilment of the requirements for the

degree of Doctor of Philosophy

2014

Declaration

This thesis is the result of the author's original research. It has been composed by the author and has not been previously submitted for examination which has led to the award of a degree.

The copyright of this thesis belongs to the author under the terms of the United Kingdom Copyright Acts as qualified by University of Strathclyde Regulation 3.51. Due acknowledgement must always be made of the use of any material contained in, or derived from, this thesis.

<div align="right">Zhengqiang Xu</div>

Signature: Date:

Acknowledgement

First, I would like to thank Professor Nigel Barltrop for his supervision and advice. I am full of respect, for his expertise, friendliness, patience and modesty, to him, a notable professor with vast knowledge, excellent character and personality.

I would like to show my gratitude to Professor Shan Huang, who had been my supervisor for three years before he moved to work in BP. He is one of the most important people that change my life. I would not have a chance to pursue my PhD study abroad, without his help. Throughout my studies, he gave me constant support and invaluable advice in project research, technical report and this thesis writing. He is not only a supervisor that inspired me to be a researcher but also a friend that guided me to enjoy the life abroad.

I am grateful to the faculty and staff in the department, especially Thelma Will, who is always eager to offer help with smile, for their support and help. Also, I would like to thank Dr Qinxin Gao and other PhD students, who gave me help and made my life full of fun.

I acknowledge with gratitude to the three-years stipend support from GL Noble Denton based in London. I must also thank Dr Alexandros Argyros, Dr Xiaoming Cheng, Dr Yahui Zhang from GL Noble Denton for their help, especially the valuable advice about my annual report from Dr Argyros.

I would thank my lovely Thai girlfriend, Noon, who has made my life more colourful during most of my PhD study. Being in love is easy, being married may be not. It is to be cherished.

Finally, I would like to thank my parents and family for the support they have provided throughout my life: I always love you and my heart will always stay with you no matter where I am.

Contents

List of Figures

List of Figures

List of Figures

List of Tables

List of Tables

Nomenclature

General symbols

A	Amplitude of oscillation
A_s	Section area
B	Breadth of ship
c	Equivalent linear damping
C_a	Added mass coefficient
C_B	Block coefficient of ship
c_c	Critical damping
C_D	Drag coefficient
C_F	Tangential component of viscous resistance coefficient
C_L	Lift coefficient
C_M	Inertia coefficient
C_N	Normal component of viscous resistance coefficient
C_v	Viscous resistance coefficient
C_{Xc}	Longitudinal current force coefficient
D	Diameter
E	Energy dissipation
F_D	Drag force
$\vec{F}_C$	Conservative force
F_{Xc}	Surge current force
F_H	Horizontal force
F_L	Lift force
H	Water depth

H_s	Significant wave height
K	Stiffness
L	Length
L_{BP}	Length between perpendiculars of ship
M_T	Total mass of vessel
N_L	Normalized fundamental lift frequency
P	Pressure
$\vec{r}$	Vector of turret origin
S	Surge motion
S_W	Wetted surface of hull
S_{rr}	Response spectrum
T	Period of oscillation motion
T_D	Draft of ship
T_{zr}	Zero-crossing period
T_p	Peak wave period
$T_H\,(T_{Ho})$	Horizontal (pre-tension) tension force
u	Velocity
U	Velocity of flow
U_M	Velocity amplitude of oscillation motion
V	Structure response velocity
V_c	Velocity of current
w	Weight per unit length of submerged line
X_{max}	Maximum horizontal co-ordinate of the fairlead
x_0	Original horizontal co-ordinate of the fairlead
$x\,,y\,,z$	Cartesian coordinates

Greek Characters

η	Transverse motion of line segment
η_0	Displacement of transverse motion
ζ	Damping ratio
ρ	Density
ρ_w	Water density
ρ_a	Air density
φ	Angle between the mooring line and the horizontal
k	Turbulent kinetic energy
ω	Angular frequency (or rate of energy dissipation)
ε	Turbulent dissipation
$\vec{\xi}$	Vector of translational motions
$\vec{\Omega}$	Vector of angular motions
σ	Standard deviation
μ	Fluid viscosity
υ	Fluid kinematic viscosity
τ_ω	Wall shear stress
δ	First cell height
δ_F	Goodness-of-fit parameter
β	Frequency number
η	Transverse motion of line segment
Δz	Total vertical displacement of the element

Abbreviations

2D	Two-dimensional

3D	Three-dimensional
API	American Petroleum Institute
CFD	Computational fluid dynamics
DNV	Det Norske Veritas
FPSO	Floating production storage and offloading
HF	High-frequency
LES	Large eddy simulation
LF	Low-frequency
KC	Keulegan-Carpenter number
OG	Origin of global coordinate
OT	Turret origin
PSD	Power spectral density
QTFs	Quadratic transfer functions
RAO	Response amplitude operator
Re	Reynolds number
RMS	Root mean square
SCR	Steel catenary riser
TLP	Tension leg platform
TDZ	Touch-down zone
UDF	User defined function
URANS	Unsteady Reynolds-averaged Navier–Stokes
WF	Wave-frequency
VIV	Vortex induced vibration
VLCCs	Very large crude carriers

Abstract

The exploitation of oil and gas is gradually moving to deep-water areas, where FPSOs are particularly effective and economical. Damping effect of moorings and risers is especially important to surge excitation of the FPSO vessel due to its low-damped characteristic and hence coupled analysis is normally preferred to accurately predict the floater motions as well as the mooring and riser system response.

The aims of this thesis are to investigate mooring line damping, drag coefficient of mooring chain and their effect on the motions of FPSOs. In particular the aim is to determine the C_D values of a stud-less chain under different flows by numerical methods due to limited C_D data for chains.

A turret moored FPSO with 20 moorings operating in 400m water-depth is selected. Effects of environmental loads, including floater motions, current and waves, on the mooring line damping are investigated. Effect of random WF motions on mooring line damping, according to the study, can be represented by an equivalent harmonic WF motion if the variation of C_D is negligible. So the estimated mooring line damping has more practical applications and can be used as a reference in uncoupled analysis.

Mooring line damping is mainly caused by hydrodynamic drag force, so variations of C_D would definitely affect the mooring line damping and line dynamic tension. Through the sensitivity study, it is found that at the top and town-down zone of a mooring line, where chain segment is normally used for a chain-wire-chain line, mooring line damping and dynamic tension are more sensitivity to the C_D variations. This indicates the importance of C_D selection for chains.

Therefore, drag coefficients of a smooth stud-less chain under different flows are determined by CFD methods due to their recent advancement and the limitations of experiments. Validations of numerical models are completed by simulating steady and unsteady flows past a smooth circular cylinder. Performance of two different turbulence models, namely LES and $k - \omega\,SST$ models, is assessed by comparison of results obtained by these two models.

Finally, by coupled analysis, damping effect of moorings on the motions of the moored FPSO system is investigated with C_D variation taken into consideration. It is observed that a change of C_D by a factor of 2.0 for mooring lines will decrease the vessel's LF surge motion and noticeably increase the dynamic WF tension of lines due to the increase of mooring line damping.

Overall, this study has widened the knowledge about the hydrodynamic coefficients of chains under different flows. It also deepens the understanding of mooring line damping and its effect on the motions of the FPSO system. Through the study, it is known that mooring designers need to pay special attention to the touch-down zone for catenary moorings, not only due to the structure reliability but also because of the hydrodynamic implications.

1. Introduction

1.1 Background

FPSOs (Floating Production, Storage and Offloading vessels) are popular for oil/gas exploitations in deepwater. For the moored floating FPSO system, the integrity of mooring lines is of high importance to keep the system on station and to protect the risers connected to it. About the design of mooring systems, one of the key points is to accurately predict the dynamic response of moorings, which is closely related to motions of the top FPSO system. In deepwater, the coupling effect between the slender structures and the floater becomes more important, and hence a coupled analysis is required to accurately obtain the individual responses of the floater, moorings and risers. This is especially true for the low-damped FPSO system, whose natural frequency is close to the frequency of slow drift loads. The damping of moorings, which might account for high proportion of system damping, could dominate the LF motions of the FPSO system.

Deepwater oil/gas exploitation

Due to the large consumption of energy, the oil and gas contained in the land and shallow water areas are becoming less and less. The exploitation of oil and gas has gradually moved to more deep water. Deepwater production started in 1979 when Shell's Cognac Field entered service, which was followed by Lena Field of ExxonMobil five years later. With tremendous advances in technology, deepwater exploration and development grew fast over the following years.

Deepwater is traditionally defined as those water depths greater than or equal to 1,000 feet (305m) and ultra-deepwater as those water depths greater than or equal to 5,000 feet (1,524m). In the past several decades, an overall expansion has been taken place in all phases of deepwater activity. 54 percent of the 8,000 active leases in the

1

GOM are classified in deepwater. Productions of deepwater oil and gas grew around 840 percent and 1,600 percent respectively (MMS, 2005). In 2007, approximately 70 percent of the GOM's oil production and 36 percent of its natural gas were from wells in 1,000 ft (305 m) of water or greater. At the end of 2008, 57 percent of all GOM leases were located in deepwater (MMS, 2009).

Figure 1-1 and Figure 1-2 illustrate historic trends in shallow- and deepwater oil/gas production in GOM. It can be seen that deepwater oil production experienced a dramatic increase in the last two decades. Actually from 2000, more oil from the deepwater areas of the GOM is produced than from shallow waters. The gas production shows similar trends as oil production- a significant reduce in shallow water and a noticeable increase in deepwater during the last 20 years.
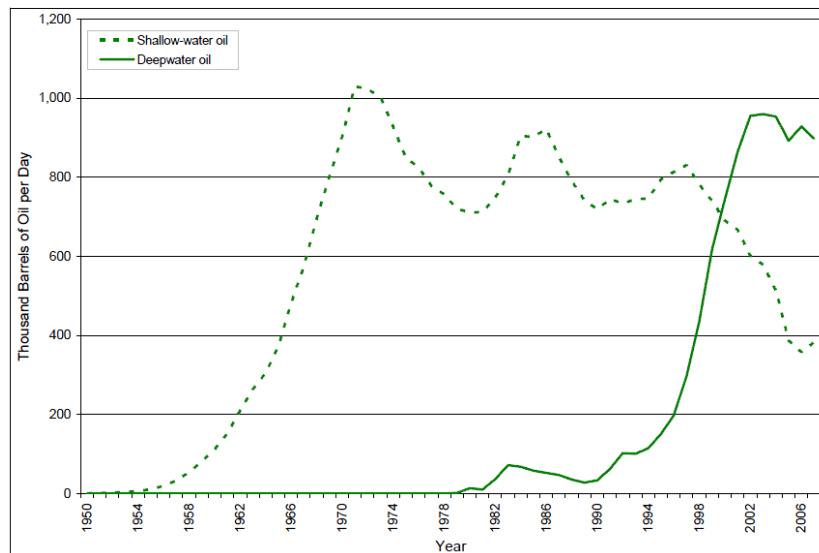
Figure 1-1 Comparison of average annual shallow- and deepwater oil production (MMS, 2009)

2
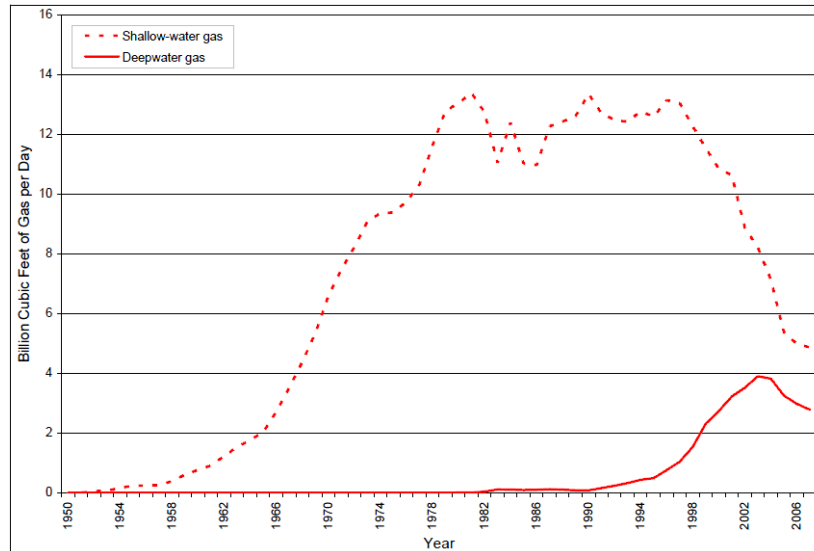
Figure 1-2 Comparison of average annual shallow- and deepwater gas production (MMS, 2009)

With the increase of water depth, fixed offshore platforms, such as gravity platform, jacket platform, are becoming not economical. In these deepwater open areas, dominant floating platforms are TLP, Spar, Semi-submersible and FPSOs, as shown in Figure 1-3.
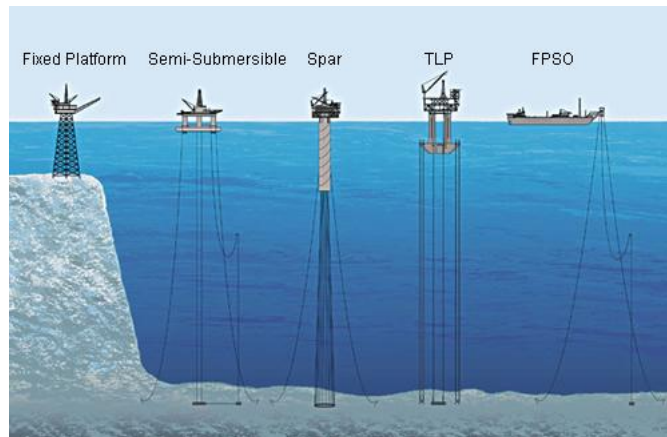
Figure 1-3 Different types of offshore oil platforms

Whereas semisubmersible, TLP, and spar designs all have the attributes to be a production host facility, FPSOs are particularly effective in remote or deepwater locations where seabed pipelines are not cost effective. In these circumstances

storing oil on the facility for offloading and shipping is an obvious solution, while Semisubmersible, TLP, or spar platforms show little advantage.

Besides, FPSOs are also economical option for smaller oil fields. These small oil fields can be exhausted in a few years and do not justify the cost of installing a fixed oil platform. For this kind of oil field, the expense can be reduced by reusing the FPSO in a new location after the oil field depleted.

Due to the advantages of FPSOs, the desire for FPSOs increased dramatically during the last decade. The number of FPSOs in service jumped by 83%, from 83 units in 2003 to 153 units in 2013(IMA/EMA, 2013). According to the study of International Maritime Associates (IMA) and Energy Maritime Associates (EMA), FPSOs account for 61% of the existing floating production systems. Meanwhile, the backlog of FPSOs orders is at high proportion of current order backlog of production floaters, which accounts for 56% of total 72 production-floater orders (IMA/EMA, 2013).

There are two main types of FPSOs, the converted oil tanker option or the purpose built option, the selection of which option will partly depend on the area of operation. In benign waters the FPSO may be a converted tanker with an external turret, which could avoid massive transformation of the hull structure. For more harsh environments, such as the North Sea, the more likely option is that the vessel has a refined shape with an internal turret. All ship-shaped FPSOs in the North Sea are purpose-built and most are permanently moored. The turret (Figure 1-4) could keep the vessel weathervane in order to position itself towards the wind/wave and hence to reduce environmental forces on the moorings.
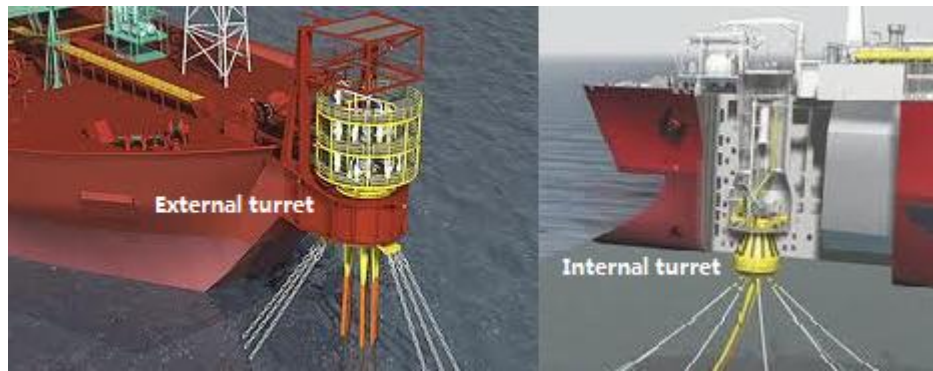
Figure 1-4 External- and internal turrets of FPSOs

The industry has gained much experience through years of deepwater exploitation, however, the exploitation of deepwater energy still faces more challenges and uncertain dangerous factors when compared to conventional offshore exploitation. These challenges arise in reservoir identification, well construction, oil/gas processing, risers and so on—almost every related aspects of the industry. Some of the challenges relate to the high cost of current technology, while others are associated with hostile environment, technical and mechanical limitations.

Integrity of a mooring system

FPSOs need to be kept on station through mooring systems in these deepwater open areas, where the floating structures are totally unshielded from the harsh environment. The adverse motion of platforms due to fierce wave, current and wind loads should be suppressed by moorings, which aims to protect the risers connected to the FPSO by limiting the maximum excursion of the FPSO in the range of the allowable offset of risers.

Thus, a challenge to the deepwater exploitation is the integrity of moorings of the floating platforms, as the failure possibility of deepwater mooring lines increases due to combinations of environmental loads, motions of platforms, impact with the seabed, abrasion, and salt water corrosion. Meanwhile, with the increase of water depth, the length of mooring lines grows up rapidly, consequently, the weight of the

mooring lines also increases. Significant problems arise during mooring deployment and recovery due to the weight of the mooring system.

Between 2000 and 2011, there were more than 20 mooring failures—an average of more than two per year (Ma et al., 2013). Special attention is needed for the Floating Production Systems (FPS's), such as FPSOs, semi-submersible and Spars, which will stay at fixed positions year after year without regular dry docking for inspection and repair. According to the HSE's report (HSE, 2003), during year 1996-2002, 9% of specific FPSO incidents arise from mooring and DP incidents. From the mooring line failure statistics in the 'FPS Mooring Integrity JIP Report' (NobleDenton, 2005), it can be seen that the number of operating years per failure is 8.8 for FPSOs in North Sea, which means the probability of line failure per operating year is relatively high.

A recent accident of mooring system failure occurred in February 2011 whilst the Gryphon Alpha FPSO was in production operations. The FPSO lost heading and position during stormy conditions (about 111.1 km/h maximum wind speed with a significant wave height of between 10m to 15m). Multiple mooring lines failed due to the high environmental forces they were subjected to, which were thought to exceed the design criteria. As a consequence of position loss, there was significant damage to the sub-sea infrastructures, such as risers and flow-lines. The Gryphon FPSO went back online in 2013 to restart oil production after a two-year break.

Regarding the failure modes of mooring system, most of the situations are the failure of a single mooring line. Although the single line failure condition is within the normal design criteria for the mooring system and should not threaten the integrity of the system directly. However, if failure of a single line is undetected, this may expose the remaining lines to higher loads for an extended period, which may cause failure of multiple mooring lines. Multiple failures in the mooring system are classified as the highest category—safety critical risk category 1. Once failure of multiple lines occurs, the chance of the complete system failure will increase dramatically (especially for station keeping dependent systems, such as marine

risers). So, the integrity of the mooring lines is of vital importance to the moored system.

Given moorings as category 1 safety critical systems, multiple lines divided into several groups with 3~4 lines in a group are usually desirable for a floating platform. However, great attention is still needed because deterioration of the lines over time can increase the likelihood of single or multiple line failures.

Many of the line breakages are due to the extreme sea-states (such as hurricane Lili, 2002; hurricane Ivan, 2004). Hence many codes, such as API RP2SK (2005), DNV-OS-E301(2010), have specified/recommended the maximum design condition (usually 100-year design environment), and mooring systems should be designed to withstand the extreme load caused by the combination of wind, wave and current in the design environment. For the designer of mooring system, one of the key problems is to predict the peak load of the mooring line under such environment and select proper diameter and grade of mooring line. However, experience shows that failures have occurred in moderate conditions as well. This is not only because the sources of line failure can be overloading, corrosion, wear, fatigue and so on, but also because in many cases line failure is caused by the interaction of several of the sources.

Special attention should also be paid to large ship-shaped FPSOs, which are dominated by low frequency (LF) motions. The frequency of LF motion is usually near to the natural frequency of moored FPSO systems, which means resonant motion could be triggered. Once it occurs, large LF motion can yield quite high mooring load, which could be more severe than that due to the extreme sea-state (such as100-year waves) (API-RP2SK, 2005).

Coupled analysis of a moored FPSO system in deepwater

Due to the actions of wind, waves and current, motions of a floating moored structure contain three different time scales, namely wave frequency, low frequency

and high frequency. Wave frequency (WF) motions of the structure are caused by the largest wave loads on offshore structures, so they take place at the same frequencies as the waves. Higher-order wave loads yield high frequency (HF) resonant vertical motions, springing and ringing, of tensioned buoyant platforms like TLPs, while for FPSO systems the effect normally can be ignored. The low-frequency (LF) resonant horizontal motions, also named slow-drift motions, are due to slowly varying wave and wind loads. The time-invariant components of wave and wind, together with current, give rise to the mean offset of a moored system.

The LF motion and mean offset of floating structures increase considerably as water depth increases, which is mainly due to the increase of current forces and the decrease of mooring stiffness. It is noticed that offset related to LF motion and mean offset accounts for 50% in 70m water depth, while this value jumps to approximately 95% of total offset in 2000m water depth (Ormberg and Larsen, 1998), as shown in Figure 1-5. Hence, in deepwater zone, the peak load of the mooring line which is related to the peak offset of the mooring line, to some extent, could be mainly determined by the LF motion and mean offset. In fact, this is also one main incentive for the coupled analysis in recent years when predicting the motions of moored floating structures. The main reason for performing coupled analysis, as mentioned by Ormberg and Larsen (1998), 'is therefore to obtain a more accurate estimate of the mean offset and low frequency (LF) motion, and, consequently, improved estimates of dynamic loads in the moorings'.
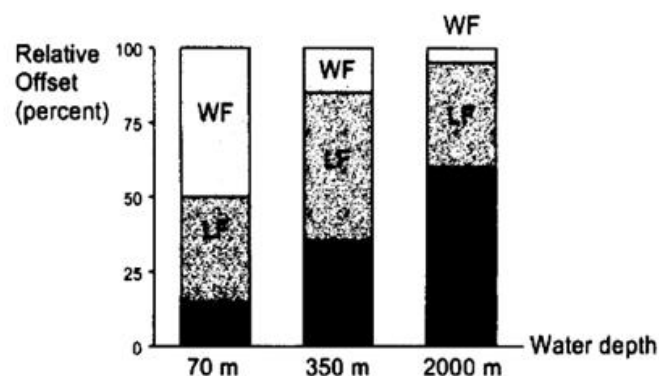
Figure 1-5 Proportion of different motions at different depths (Ormberg and Larsen, 1998)

8

Traditionally, the motions of moored floating structures and the load effects in the moorings and risers are calculated by separated two-step approach (uncoupled method), as shown in Figure 1-6 (left). In Step1, first calculate the motions of the floater, including wave frequency and low frequency motions, by simplifying the modelling of moorings and risers. The effects of the mooring and riser system are included quasi-statically using nonlinear springs, i.e. quasi-static restoring force characteristics. The current forces and velocity-dependent forces (low frequency damping contribution) from moorings and risers are either neglected or simplified. Followed by Step2, dynamic responses of moorings and risers are analysed by using the motion response calculated from the Step1.
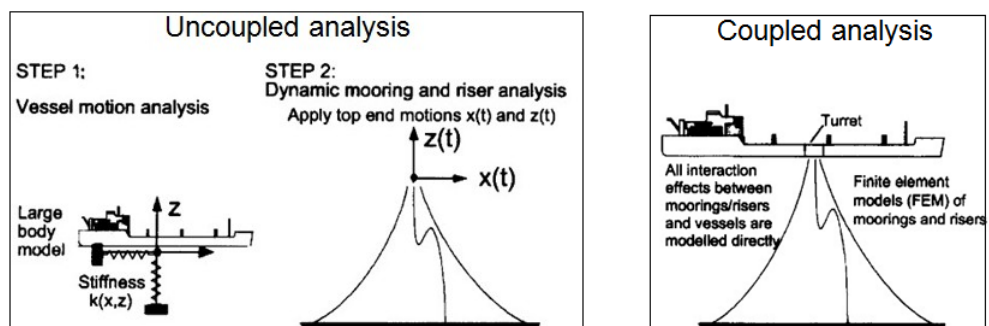
Figure 1-6 Global analysis by uncoupled- and coupled methods (Ormberg and Larsen, 1998)

In shallow water, the floater motions are to a large extent excited and damped by fluid forces on the floater itself. So, even by uncoupled analysis, motions of the floater can be predicted with desirable accuracy in Step1, and consequently the accurate results of dynamic response of moorings and risers in Step2. As the water depth increases, however, the interaction/coupling between the slender structures and the large volume floater becomes more important. A coupled analysis will be required to capture the interaction between the two, in order to accurately predict the individual responses of the floater, risers and moorings.

In coupled analysis (Figure 1-6, right), the vessel and slender structures (such as moorings and risers) are integrated in a single model and dynamically analysed to fully capture their interaction. All the effects of slender bodies, such as damping,

wave and current loads, stiffness and inertia can be included. The LF motions and mean offset, which account for high proportion of total offset of the deepwater floater, can be predicted more accurately by considering the effects of damping and environmental loads from the slender bodies.

Especially when calculating the motions of low-damped FPSOs, which are dominated by LF motions, this approach can get more accurate results by considering the damping of moorings/risers in the analysis. As is known, the amplitude of dynamic response is dramatically dependent on the system damping, especially at the resonant situation, as illustrated in Figure 1-7. Similarly, for a moored FPSO system, whose natural frequency is close to the frequency of slow drift loads, the magnitude of LF motions will mainly depend on the system damping. Traditional uncoupled method could be severely inaccurate, especially for deepwater floating FPSOs, partly due to the neglecting/simplification of LF damping from moorings and risers (Ormberg and Larsen, 1998).
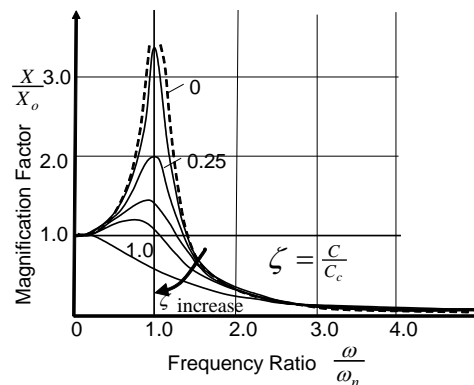
Figure 1-7 Damping effect on magnification factor of a amplitude-frequency curve at resonance

Damping of moorings/risers

The damping of moorings/risers is mainly due to the fluid viscous drag force acting on the mooring lines and risers. For such slender structures, the hydrodynamic loads are usually calculated using Morison equation, which is formulated below for viscous oscillatory flows on stationary slender vertical cylinders (Eq. 1-1):

$$F(t) = \frac{1}{4}\rho\pi D^2 C_M \dot{U} + \frac{1}{2}\rho C_D D U |U| \qquad\qquad \textbf{Eq. 1-1}$$

where, C_M is inertia coefficient; C_D is drag coefficient; ρ is fluid density; U is flow velocity; $\dot{U}$ is flow acceleration; D is effective diameter of slender cylinder structure ; $F(t)$ is the hydrodynamic force on the unit length of slender structure.

In the formula, the first item is inertia force related to the acceleration and the second item is drag force related to fluid relative velocity. It can be seen that drag force is directly related to the drag coefficient C_D, which varies with the various flow parameters, such as Reynolds number Re, Keulegan-Carpenter number KC, and the roughness of surface.

Previously when predicting the motions of moored systems, people were prone to ignore the damping of moorings/risers, because the drag areas represented by moorings/risers are quite small when compared to that of the vessel. However, according to relevant studies, damping of moorings/risers is quite considerable. For instance, the main contribution (as much as 80%) to the surge damping of the moored system can be the mooring line damping, which is mainly caused by the drag force acting on the mooring line (Huse and Matsumoto, 1989, Huse, 1991). In the study of Ormberg and Larsen (1998), it was found that the damping of risers accounts for 30% of the total damping.

The damping of moorings/risers has more or less influence on the LF motions of floaters. The importance of the influence depends on the number, size and type of moorings and risers, type of vessel, water depth and met-ocean environment. According to Marintek's experiment (Huse, 1986), surge amplitude reductions of 20 to 25 percent have been measured when damping of mooring lines are included. The amplitude of slow drift motion is overestimated if the mooring line damping is ignored (Nakamura et al., 1991). So, in order to obtain good prediction of LF motion through coupled dynamic analysis, one key point is to precisely define the damping of moorings/risers.

1.2 Existing problems and study scope

1.2.1 Existing problems

As mentioned above, the continued integrity of mooring system is of prime importance for the operation of these floating platforms, especially for those permanently moored vessels (such as FSO's, FPSOs). During the design period of mooring system, extreme loads of moorings are evaluated in order to avoid overloading.

Traditionally, quasi-static or uncoupled dynamic analysis methods are used to predict the extreme loads of mooring system, which tends to be overly conservative. Conservative design would be good for the integrity of mooring systems, however, cost-effectiveness is becoming more and more important due to the high completion costs of deepwater exploitation, which emphasizes the necessity of optimum design by accurate prediction of extreme load.

The accuracy of predicting the mooring extreme response can be dramatically improved, especially for a deepwater situation, by coupled analysis. Many global analyses, including numerical calculations and model tests, have shown this advantage of coupled analysis. This is mainly achieved by considering the coupling effect of slender bodies, such as risers and moorings.

However, there are still several important unresolved problems. Here, a summary of these problems is made as follows:

1) The numerical prediction of mooring line damping under superimposed WF motions;

A lot of researches have been done to predict the magnitude of the mooring line damping under different motions of top floaters. The theoretical calculation results have good agreements with the experiment results when only LF motion are taken

into account, while a big discrepancy still exists between the theoretical calculation and the experiment in the case of considering superimposed WF motions. For instance, in the study of Huse and Matsumoto (1989), it was found that with the superimposed WF motion, compared with the experimental results, the numerical calculations over-predict the mooring line damping by a factor in the range of 1.2 to 2. It is to be mentioned that it was also found in the study that superimposed WF motions of the system as tested increase the LF damping by a factor in the range of 2 to 4 for typical sea states.

Another problem about the prediction of mooring line damping is that, when considering the effect of superimposed WF motions on mooring line damping, only single- or bi-harmonic WF motions are considered in all the available former researches. Due to the fact that in reality the moored system is under the random WF motions, the effect of random WF motions on mooring line damping needs to be studied.

The prediction of magnitude of mooring line damping is mainly for the uncoupled analysis, where the damping is directly treated as an input in the calculation of the floater motions. In coupled analysis, mooring line damping is presented explicitly by the drag force, which is related to the drag coefficient. The selection of drag coefficient could be the potential reason causing the discrepancy between the theoretical calculation and the experiment when considering the superimposed WF motions (Huse and Matsumoto, 1989). So it is crucial to select proper drag coefficient when calculating damping contributions as well as current/wave loading of mooring lines.

2) The uncertainty of drag coefficients of mooring line chain;

Almost all the numerical calculations in the coupled analysis took the drag coefficients of moorings as constant values, which is partly due to limited knowledge about the values of drag coefficients. Very coarse values (ranges) of drag coefficients for chains are recommended/specified in related rules (practices), such as DNV-RP-

F205 (2010), DNV-RP-C205 (2010), DNV-OS-E301 (2010), API 2RD (1998). Most of these values are obtained through experiments in steady flow, which means the effect of KC is not included. For example, in DNV-OS-E301, the recommended value of normal drag coefficient is 2.6 for stud chain and is 2.4 for stud less chain. These typical values for Reynolds numbers in the range $10^4 - 10^7$ are normal to the longitudinal slender structure axis and without effects of marine growth or any influence from oscillation.

However, it can be seen from the work of Huse and Matsumoto (1989) that under superimposed WF motion, without considering drag coefficients variations due to Re and KC numbers, the damping of moorings estimated by numerical calculations has big discrepancy with experimental results. The drag coefficients could be also critical to the mooring line dynamic response and fatigue performance, so the establishment of consistent drag coefficients is likely very important, especially for deepwater applications.

3) The lack of way to implement drag-coefficient variations in coupled analysis;

The uncertainty of drag coefficients is the main reason why implementation of drag-coefficient variations is unavailable in the coupled analysis. Once the relationships between drag coefficients, Re, KC and roughness number have been decided, no matter by tests or by numerical simulations, the next step is to implement drag coefficients variations during the analysis. However, a proper way to achieve this is still not available mainly due to the dependence of drag coefficients on KC number, which is related to the periodic oscillatory motion.

It is easy to consider in the dynamic analysis the effect of roughness and Re number upon drag coefficients. The roughness can be taken as constant in a short period and then its effect on drag coefficients can be decided before the analysis. The Re number can be updated by relative instant velocities of fluid during the analysis, and then the corresponding drag coefficients can be updated, according to their

14

relationships. However, KC numbers are related to the oscillation periods, which means the drag coefficients affected by different KC numbers are obtained from lengths of time rather than from time points. So, during the analysis the update of drag coefficients according to the KC number becomes a problem at current time step because it is hard to know the present value of that KC number (including Re in oscillating flows), especially for moorings under superimposed WF motions of floaters in a random sea state.

4) The importance of the damping effect of moorings upon the motions of floaters;

Several people have studied the importance of damping effect on motions of floaters by changing the drag coefficients of moorings. Some of them (Luo and Baudic, 2003) found that the variations of C_D had little effect on the motions of floaters, while some others (Wichers and Devlin, 2001) concluded that effect of C_D variations on motions of floaters is significant. The damping of moorings could be very important in reducing amplitudes of LF motions. However, the mean drag of the moorings due to current/wave force could also increase the mean offset of floaters. Depending on the contributions of these two components, the final impact of the C_D variations could be case-dependent (Luo and Baudic, 2003). In fact, even the effect of mooring line damping on LF motions of the floater is hard to determine, because it will depend on its proportion in the system damping and magnitude of the system damping.

5) The unclear relationship between line tension and damping of mooring line;

The total tensile load of a mooring line consists of two parts, namely static tension and dynamic tension. The static tension is determined from the displacements of the upper floater by quasi-static analysis, while dynamic tension is more related to the WF motions of the upper floaters. For a catenary mooring line, the main sources of dynamic tension could be hydrodynamic forces, especially the drag force, which also causes the mooring line damping. The increase of mooring line damping can

decrease the static tension by reducing the LF motion amplitude and hence the displacement of the floater, but also could increase the dynamic tension in the mooring line. The question is that if the total tension will increase or decrease when the mooring line damping increases.

Obviously, there are still other problems unmentioned. The results of some problems discussed above will depend on many factors. For instance, the importance of damping of moorings will depend on water depth, type of floaters, and numbers of moorings and so on; the relationship between total tension of mooring line and its damping will depend on ocean environments, type of mooring line and other factors.

1.2.2 Study scope

Because there are many problems, it is necessary to define the study scope. Among different kinds of floating platforms, FPSOs are popular due to their advantages in remote or deepwater locations (Shimamura, 2002), so an FPSO located in North Sea operating in about 400m water-depth is selected as study object. The studies will include:

1) Assessment of the damping of moorings under different top motions and other environmental loads;

The effect of superimposed WF motions, including harmonic and random WF motions, on the damping of moorings is studied. Also, effects of environmental loads, such as steady current and waves are considered. Constant values of C_D are assumed, however, when evaluating the damping of moorings under different influential factors.

2) Sensitivity studies of damping and line tension of moorings to the C_D variations;

A chain-wire-chain combination is very common for a catenary mooring line in deepwater. The chain is normally selected at the two most challenging locations, namely the seabed touch down area and the vessel interface. From the sensitivity study, it can be seen that these two parts are more sensitive to C_D variations with respect to mooring line damping, so the proper selection of drag coefficients of the chain is quite important.

3) Determining drag coefficients of the chain by CFD simulations;

Owing the limitations mentioned later in the review of the experimental methods, the CFD method is used to determine drag coefficients of the chain under different flows. Validations of the CFD models are achieved by simulating flows past a circular smooth cylinder, which are classical problems with good benchmarks for numerical models.

There are two types of chains, namely stud-less chain and stud chain. Considering the fact that stud-less chain is more popular for deepwater FPSO moorings, drag coefficients of a stud-less chain will be predicted by the CFD method.

4) Evaluating the damping effect of moorings/risers upon the motions of the moored FPSO system and discussing the relationship between line tension and mooring line damping;

The system damping in surge direction of the moored FPSO system will be first assessed. Then by coupled analysis, the damping effect of moorings on the motions of the moored FPSO will be studied for a typical 100-year hurricane by considering drag coefficient variations of the chain. The effect of C_D variations on line tensions is also investigated.

1.3 Approach to research

As mentioned before, a turret moored FPSO system operating in about 400m water depth is selected. The studies of mooring line damping and C_D values of chain are completed by considering the vessel WF motions under given environmental conditions. The damping of moorings and C_D values of chain can be used in analysing vessel motions by uncoupled analysis and coupled analysis respectively. A flow chart of the research strategy can be seen from Figure 1-8.
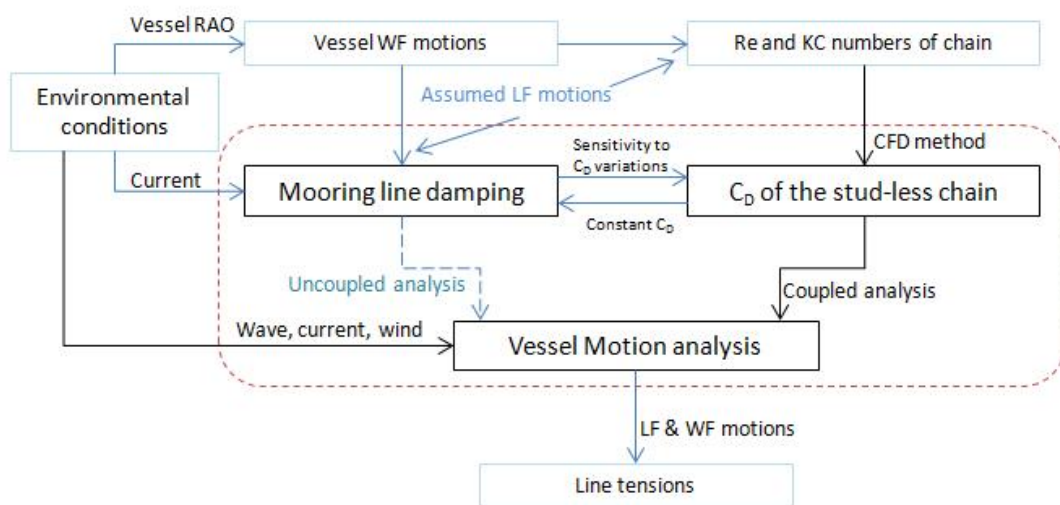
Figure 1-8 Research strategy and approach of the thesis

First, the damping of moorings under different influential factors is assessed by assuming constant C_D values for the wire and chain. The prediction of damping of moorings is determined from the 'Energy dissipation' using the 'Indicator diagram' method. The effect of superimposed random WF motions on mooring line damping is investigated by comparing the results with those under equivalent harmonic WF motion.

Then, the sensitivity of mooring line damping to the C_D variations is studied, which determines the importance of chain C_D selection in the calculation of mooring line damping and line tension.

The CFD method is used to determine C_D values of the stud-less chain under different Re and KC numbers owing to the limitations of experimental methods. The validations of numerical models are conducted by simulating the flows around a circular smooth cylinder and verifying the numerical results with experimental values.

The damping effect of moorings on the motions of the moored FPSO system is studied by considering the C_D variations of the moorings. Through the comparisons of results from different C_D of the moorings, the relative importance of mooring line damping to the motions of the moored FPSO is investigated.

1.4 Objectives

Based on the introductory remarks, the main specific objectives are as follows:

1) Clarifying effects of different parameters (such as top motions, environmental loads) on damping of moorings and quantifying the equivalent linear damping of moorings for the given mooring system, which can be used as reference in the uncoupled analysis;

2) Emphasizing the importance of C_D selection of chain by sensitivity study of mooring line damping to the C_D variations under different motions;

3) Determining the selection of C_D of chain under the effect of Re and KC number by CFD methods while the performance of different turbulence models is also assessed;

4) Evaluating the proportion of damping of compliant structures among the system damping in surge;

5) Investigating the damping effect of moorings upon the motions of the moored FPSO by coupled analysis and analysing the surge response of the moored FPSO and corresponding tensions of mooring lines.

1.5 Structure of the thesis

The thesis is basically organised in 5 parts. In the first part, an introduction and critical review are presented. In the second part, the effects of different parameters upon mooring line damping are investigated and the sensitivity of mooring line damping to the C_D variations is also included. The main effort is to determine the C_D selection of a stud-less chain under different flows by the CFD method in the third part. Validations of numerical models are first completed in this part and then the C_D values of the stud-less chain are determined under different Re and KC numbers as required by the numerical models. Followed in the fourth part, by coupled analysis, the damping effect of moorings on the motions of the moored FPSO is studied by considering the C_D variations of chain. Finally, conclusions are summarized and future work is recommended in the last part.

2. Critical review

2.1 Overview

In Appendix A, classic problems of flows past a smooth circular cylinder are reviewed, which includes steady and unsteady flows around a circular cylinder. The purpose of the review is to have a good understanding of the hydrodynamic forces, especially the drag force. These experimental results are also used as benchmarks for validation of CFD models in Chapter 5. Then the review is moved to drag coefficients, which are used to calculate the drag force. Available values of drag coefficients of chain and related experiments are discussed. Subsequently, a brief review is made of related literature about mooring line damping mainly caused by the drag force. In the review of global analysis of a moored FPSO system, the coupling effect of moorings and existing work will be described. Finally, in order to carry out the CFD calculation of drag coefficients of chain, the challenge of turbulence simulation and performance of different turbulence models are reviewed.

2.2 Drag coefficient determination of chains

In this review, first, various influential factors of drag coefficients of bluff bodies are discussed, from which it can be seen the determination of drag coefficients is really tough work. Then related experiments to determine the hydrodynamic coefficients of chain are reviewed.

2.2.1 Influential factors of drag coefficient

The drag force of a bluff body under high Reynolds-number flow mainly originates from the form drag due to separation while skin friction due to fluid viscosity is normally very small. The drag force of a bluff body is very difficult to calculate due to the flow separation, and hence is usually calculated by semi-empirical formula.

One needs to decide the empirical C_D to use in the drag equation $F_D = \frac{1}{2}\rho U^2 C_D A_s$, which is attributed to Lord Rayleigh (Rayleigh, 1876). In Appendix A, only two influential factors of drag coefficient C_D, namely Re number and KC number are mentioned. Actually, C_D is affected by many other factors, such as surface roughness, transverse oscillations and flow regimes (patterns).

1) Surface roughness

In reality there is a wide variety of surface roughness, from small protrusions existing in the texture of the surface itself to large roughness in the form of marine growth. The roughness will not only increase the projected area, but also affect various aspects of the flow, such as the separation angle, the turbulence level and vortex shedding. Therefore, the effect of the surface roughness upon the drag coefficients normally can not be neglected.

2) Transverse oscillations

Once the resonant vortex-induced oscillation occurs, the transverse oscillation can have an effect of increasing the drag force, which can be explained by two 'popular and pragmatic' approaches (Journée and Massie, 2001):

a) The wake of the cylinder becomes wider as the cylinder is oscillating. This has an effect similar to that of increasing D, which is usually expressed by increasing the value of drag coefficient C_D, instead;

b) The instantaneous incident flow velocity relative to the cylinder increases because the cylinder now also moves with speed, which also increased drag force.

3) Flow regimes

In fact, all kinds of dimensionless numbers (Re and KC), to some extent, depict different flow regimes. Here, it mainly refers to different physical circumstances, such as harmonic flow only, wave-current combination flow field or random oscillatory flow.

a) The effect of random oscillatory flow

Research work done by Longoria et al. (1991) indicated that there are differences between in-line and transverse forces caused on cylinders by sinusoidal and random oscillatory flows. A significant difference in the inline drag and inertia coefficients was particularly evident in the inertia/drag regime. As mentioned in the publication, the cycle-by-cycle shedding and pairing of vortices in sinusoidal flow that lead to the characteristic drag and inertia coefficients curves reported in the literature are not so dominant under random flow.

b) The effect of current on the harmonic flow

According to the investigation (Sarpkaya and Storm, 1985), the current has profound effects on both the drag and inertia coefficient, which usually will decrease the drag coefficient. The work also substantiates the fact that the drag coefficients obtained from tests at sea will always be smaller than those obtained under lab conditions, especially in the drag-inertia dominated regime (normally defined by $8 < KC < 25$). This is because for tests at sea there are always some currents while lab conditions with zero current will often be considered.

The presence of currents also gives rise to some problems associated with the use of Eq. 1-1 (Laya, 1980). A different form of the drag force term was proposed by Moe and Verley (1978, 1980) using an independent flow fields model, as formulated below:

$$F_D = \frac{1}{2}\rho C_{DU} DU|U| - \frac{1}{2}\rho C_{DV} DV|V|$$ **Eq. 2-1**

in which C_{DU} is the oscillatory drag force coefficient on a stationary cylinder and C_{DV} is the oscillatory drag force coefficient for a cylinder vibrating in still water.

The total hydrodynamic force, after incorporating the independent flow fields assumption into the inertia force term, can be expressed as

$$F(t) = \frac{1}{2}\rho D[C_{DU}U|U| - C_{DV}V|V|] + \frac{\rho\pi D^2}{4}[C_{MU}\dot{U} - (C_{MV} - 1)\dot{V}]$$ **Eq. 2-2**

in which C_{MU} is the inertia coefficient for fluid oscillation and C_{MV} is the inertia coefficient for structural oscillation.

The independent flow fields interative form of Morison's equation was proposed in view of the uncertainties associated with the application of the relative velocity interative form of Morsion formular, which is the extension of Morison' s equation to allow for the structural motion and is expressed as

$$F(t) = \frac{1}{2}\rho C_D D(U - V)|U - V| + \frac{\rho\pi D^2}{4}[C_M\dot{U} - (C_M - 1)\dot{V}]$$ **Eq. 2-3**

It is important to recognize that the relative velocity form of the drag term is based on the existence of a well defined wake and a quasi-steady flow (Laya, 1980). So the applicability of the instantaneous relative velocity model can be deteremined by two parameters, the reduced velocity, V_r, and the KC number. For a harmonic flow $U = U_o \sin(2\pi t / T)$ past an oscillating cylinder $V = V_o \sin(2\pi t / T_o)$, the reduced velocity is defined as $V_r = U_o T_o / D$, and the KC number is defined as $KC = U_o T / D$. The region of validity of the relative

velocity form was summarized by Laya (1980) based on the experimental work of Moe and Verleys' (1978, 1980), as illustrated in Figure 2-1.
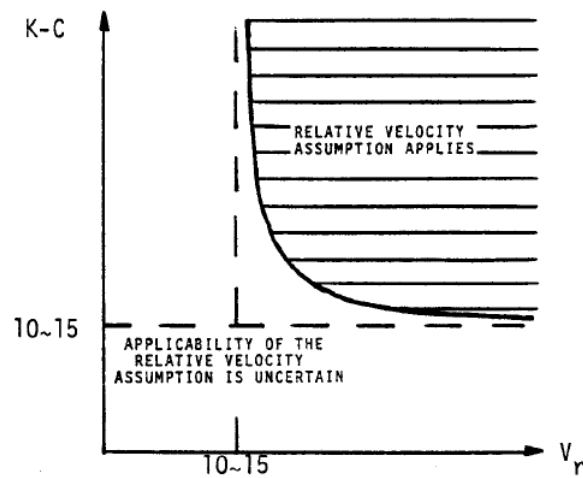
Figure 2-1 Range of the applicability of the relative velocity assumption (Laya, 1980)

It can be seen that the relative velocity form of Morison equation does apply for the case with high KC and V_r, which is possible to argue that the drag force will result from the superposition of two 'dependent', quasi-steady flow fields; one due to an almost 'steady' flow past the cylinder at rest and the other due to the slow motion of the cylinder through relatively 'calm' water (Laya et al., 1984). A more detailed discussion can be seen from the work of Laya (1980).

Considering the KC values of moorings under the WF and LF motions investigated later, the relative velocity form of Morison equation is used in this thesis when computing the mooring line damping.

Overall, the hydrodynamic coefficient will be affected by many different factors. That is also the reason why it is a complicated problem to decide the hydrodynamic coefficients under different flows.

2.2.2　Experimental determination of drag coefficients of chains

Due to limitations of the force model for slender bodies (the empirical Morison equation), the force transfer coefficients are mainly determined from laboratory experiments or field tests. However, field measurement of Morison force coefficients is complicated by the uncertainty of the ocean environment and the high cost of the experimental set-up. Many experiments have been conducted in the laboratory to find the correct values of these coefficients for several types of bodies (spheres, plates, and especially circular cylinders) under diverse flow conditions. For instance, the determination of drag coefficients for cylinders under oscillating flows is mainly dependent on experiment measurements in various ways, which include U-tube, oscillating cylinders in still water and fixed cylinders in regular waves. Once the necessary data time series have been measured through experiment, the next problem is to choose a data processing method to determine the appropriate hydrodynamic coefficients. Several methods of data processing are available, such as Morison's method, Fourier Series Approach, Least Squares Method (See Appendix C). One frustrating thing is that each method yields a different pair of C_D and C_M coefficient values for a same time record.

Empirical data on Morison force coefficients for chain-shaped bodies in oscillatory flow is scarce. Most of the available data of chain drag coefficient is from simple towing tests, which are occasionally conducted by the chain manufacturers. These drag coefficients of chains are normally defined with respect to their nominal diameters. In Figure 2-2, the drag coefficients of chain mainly under towing tests conducted by Marintek are illustrated. These results can be seen from FPS2000 reports 'Mooring and Positioning' (FPS2000, 1992).

```
── Cd for circular cyl. ref. Schlichting
□  Cd, model chain d=1.05mm , towing tests
×  Cd, model chain d=1.05mm, w/lead beads,towing tests
◁  Cd, stud-link chain d=30mm, oscillation tests KC=163-306
✶  Cd, stud-link chain d=30mm, towing tests
◇  Cd, stud-link chain d=65mm (0/90-45/45), towing tests
+  Cd, stud-link chain d=65mm (45/45-5/85), towing tests
```
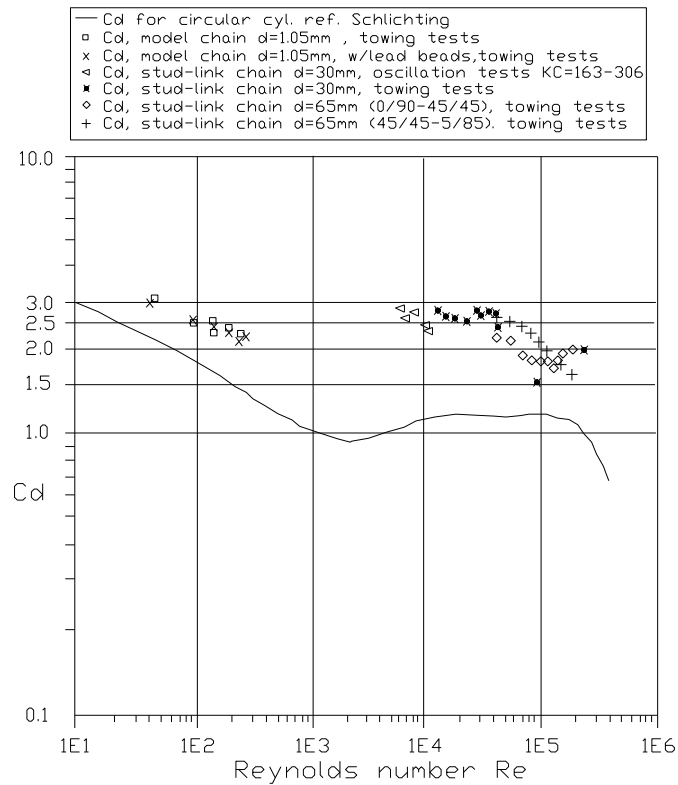
Figure 2-2 Drag coefficient of chain (referring to nominal diameter) (FPS2000 reports, 1992)

Complexity of shape is one of the major factors that complicate experiments with chain. Direct force measurement on the chain using a force gauge is also difficult due to the interconnected links. Due to these reasons, predicting the hydrodynamic loading on moving chain is quite challenging, which could explain why public publications about the experimental results of chains are less than the conducted experiments.

Lyons et al. (1997) conducted some model tests by using chain samples with a large geometric scale and considering different oscillatory motions. In their model tests, the mooring segments were mounted on oscillators which provided synchronised in-line and transverse movements by using two different motion carriages. In order to ensure the chain did not significantly deform laterally or rotationally due to fluid loading, a square section steel rod was passed through the chain to form a stiff stick of chain elements. The tri-axial forces were measured by the load cells fixed at both ends of the mooring segment. The velocities of the carriage and oscillator were taken

from their velocity controllers for analysis purposes, and subsequently accelerations could be derived. Then, using a Fourier series approach, drag coefficients were calculated from measurement of fluid forces on vertically orientated sections of chain. For single frequency oscillations, a series of fixed amplitude oscillations are tested respectively with different frequencies. Experimental results of drag coefficient with KC values ranged from 70 to 580 are plotted against angular frequency in the publication, as shown in Figure 2-3. Herein, the chain is stud-link type with nominal diameter $D = 25mm$.
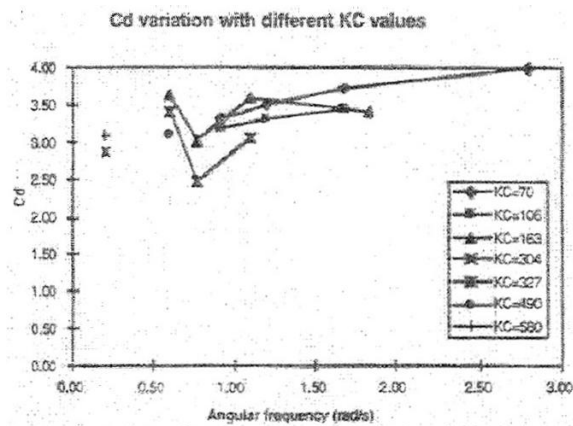
Fig 9. Drag coefficients for single frequency and amplitude motions

Figure 2-3 Drag coefficients of chain under single frequency oscillations (Lyons et al. , 1997)

It can be seen that for the lower KC values of 70 and 106, drag coefficient increases with the increase of frequency. However, for KC values of 163 and 327, an obvious drop of drag coefficient at frequency around 0.78 rad/s has occurred, which seems to be anomalous. The potential cause according to the author's opinion could be due to the Reynolds number effects. It should be noted that Reynolds numbers of all the tests mentioned above are ranging from 10^3 to 10^4, which are much smaller than Sarpkaya's tests of an oscillating cylinder at same KC number. It can be seen from Sarpkaya's tests (Sarpkaya, 1976) that at KC number 70, Reynolds numbers varies from 3×10^4 to 3×10^5. More importantly, in Sarpkaya's tests the drag coefficient of single oscillatory cylinder decreases with the increase of Reynolds numbers, i.e. the oscillating frequency.

For bi-harmonic oscillations tests with a superimposed high frequency component, the experimental results are open to discussion as well. Compared to the drag coefficients under low frequency oscillations only, an increase in drag coefficients would occur when superimposed high-frequency motion was applied. However, this anticipation did not always hold according to the results. For the two cases with lower HF amplitude this is seen to be so, but some reduction in drag coefficient occurs for other two cases with higher HF amplitude, as shown in Figure 2-4.
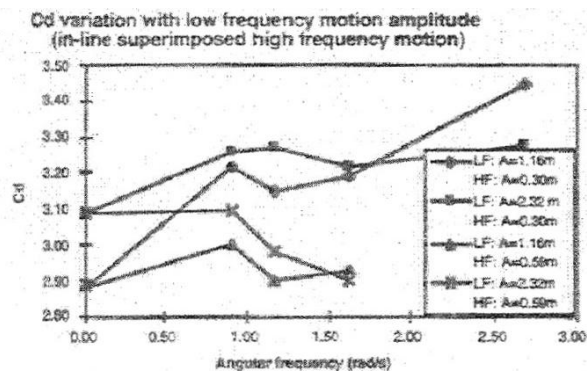
Fig 10.   Drag coefficients for combined in-line HF and LF motions

Figure 2-4 Drag coefficients of chain under bi-harmonic oscillations (Lyons et al. , 1997)

By employing an optical tracking system, an investigation of hydrodynamic force acting on chains was implemented by Yang (2007) in the laboratory. The tests involve free and forced oscillations of long chain segments under conditions representative of mooring systems in still water. The fluid force is obtained from the solution of the slender body dynamic equations of motion using the measured line displacement and end-force, since there is no available technique for directly measuring the hydrodynamic force on an oscillating slender body such as chain. For the free oscillation tests, instantaneous values of drag coefficients were derived, which still exhibited a considerable range of scatter even after criteria were introduced to filter out unreasonable data due to measurement errors. The instantaneous values of drag coefficients of a big stud-less chain are shown in Figure 2-5 (Here, C_D related to equivalent diameter which is equal to 1.8 times nominal diameter of chain).
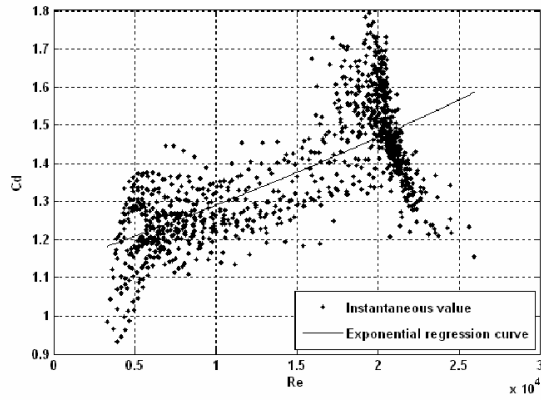
Figure 2-5 Drag coefficients for big stud-less chain in free oscillation tests

(Equivalent diameter 1.954cm) (Yang, 2007)

For the forced oscillation tests, the derived added mass coefficients in general showed more scatter than the drag coefficients (see Figure 2-6) and they did not have a consistent KC-dependence, as Yang (2007) stated "The variation of the added mass coefficient at low KC is mainly affected by experimental error and the variation at high KC is driven by both experimental error and the fact that the Morison equation is reliable only in the drag-inertia regime" (Yang, 2007).
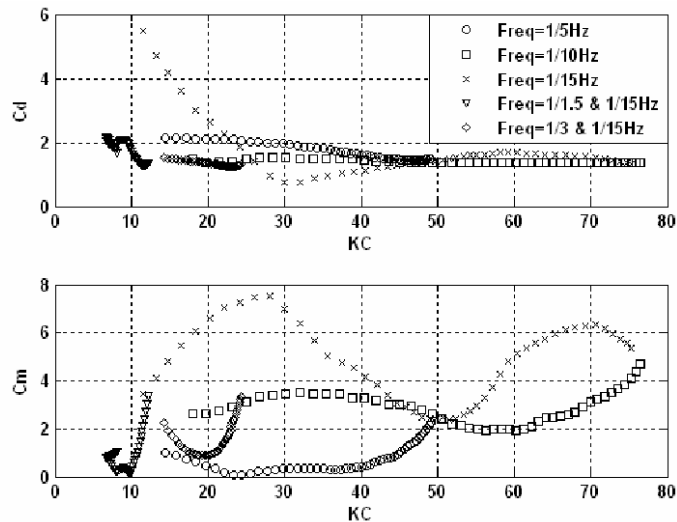
Figure 4.23   Time-averaged drag and added mass coefficient of chain (diameter:

1.954 cm) with semi-taut catenary configuration

Figure 2-6 Time-averaged drag and added mass coefficients of chain in forced oscillation tests

(Equivalent diameter 1.954cm) (Yang, 2007)

From the review of previous experiments on chain, it can be seen that for chain under oscillation tests there are big discrepancies in the drag coefficients. For smooth chain under steady flows /towing tests, the experimental values of drag coefficients only related to the Reynolds number are in fair agreement between different tests. These values are basically in the DNV recommended range, as shown in Table 2-1.

Table 2-1 Recommended range of drag coefficient for chains by DNV-RP-C205 (2010)

Normal drag coefficient C_D ($\mathrm{Re} = 10^4 - 10^7$)	
Chain Type	C_D
Stud Chain	2.2 – 2.6
Stud less Chain	2.0 – 2.4

In summary, the measurement of hydrodynamic coefficients of chain by experiments is more difficult than that of other slender bodies such as cylinder. A reliable database of measured hydrodynamic coefficients of chain has very important engineering significance but the behaviour is not yet fully understood and this makes further model work on the hydrodynamic coefficients of chain necessary.

2.3 Mooring Line Damping

The mooring line damping for a catenary mooring will result from the line friction on the seabed, internal friction within the chain and the hydrodynamic drag force along the line as it moves through the fluid. Among those, the hydrodynamic drag is the most important one. The friction between the seabed and touch down area of a catenary mooring line also has some contribution to the mooring line damping but normally is quite small when compared to the contribution of drag forces. This damping will also depend on the nature of the bottom soil and thus this damping effect could be different for different situations. The Rayleigh damping (structural damping) of mooring line due to internal friction is usually very small and sometimes can be ignored. However, in the study of Webster (1995), a structural damping of approximately 0.8% of critical damping was considered, which is actually negligible.

When predicting the motion of a moored system, it was very common practice to neglect the effect of mooring line damping until Huse (1986) proposed his opposite opinion. Since then, more and more attention has been attracted to the subject of mooring line damping and lots of research work (Huse and Matsumoto, 1988, Huse and Matsumoto, 1989, Huse, 1991, Webster, 1995, Liu and Bergdahl, 1998, Brown and Mavrakos, 1999, Bauduin and Naciri, 2000, Johanning et al., 2007) has been done. Most of these publications use one of 3 ways of determining the mooring line damping, namely, experiment, simple quasi-static analytical model or dynamic model.

Experiments include model tests and full scale tests, which are performed in the ocean laboratory and outdoors respectively. Huse et al. (1986, 1988, 1989, 1991) did some model tests to compare with the numerical results. In their model tests, a new test set-up was carried out to directly measure the energy dissipation of a mooring line. A pendulum was used to excite the horizontal motion of mooring line at the top end. The energy dissipated by the mooring line per cycle can be obtained accurately from the amplitude decay of pendulum motion. It is to be noted that the effect of superimposed WF motions on LF damping was also investigated by model tests, through which it was found that superimposed WF motions of the system dramatically increased the LF damping (by a factor in the range of 2 to 4 for typical sea states) (Huse and Matsumoto, 1989).

Large-scale experiments were conducted by Johanning et al. (2007) at Orkney in calm sea condition. Only extinction tests were performed for the large-scale experiments. However, in their study, small-scale investigations were also considered, where the differences between extinction tests and driven tests were discussed.

Experiment methods can be more reliable and usually provide good bases for bench marking different analysis models, while the disadvantages of experiments are that they are time- and money- consuming. For deepwater applications, however, some problems arise in the experiments. Full (large) scale tests become totally unrealistic,

while lots of uncertainties exist in model tests due to the scale effect. Although a reasonable scaled model (1:50-1:100) can be tested in a model basin for relatively shallow water, the truncation or ultra-small scale method has to be adopted for deepwater moorings and risers due to the limited depth of model basins. Problems due to the truncation and ultra-small scale still need to be solved. In those cases where the model basin is large enough to include the whole model, the ultra-small scale makes the mooring lines have a very small diameter. It is tedious but possible to match the physical properties of the mooring lines, while it is more difficult to ensure that the hydrodynamic forces are correctly modelled because the Reynolds numbers corresponding to the flow across the scaled mooring lines are very low so the flow may be quite different from full scale.

As an alternative to the experimental method, numerical methods, including quasi-static and dynamic methods, are widely adopted. The quasi-static method proposed by Huse (1986) is mainly based on the following assumptions:

1) Drift motion is slow and the mooring line will always keep the catenary shape;
2) Drag forces are normal to the line and motion components are in the plane of line;
3) Stiffness of the mooring line is dominated by the changes in the catenary shape.

Based on the assumptions above, the energy dissipation of the mooring line during one period of oscillation with angular frequency ω can be estimated as follows. First, calculate the energy dissipation of a line element with length Δs by the formula:

$$\Delta E = 2 \int_{-\eta_0}^{\eta_0} \Delta F_D \cdot d\eta \qquad \text{Eq. 2-4}$$

where, η is the transverse motion of the small line element, $\eta = \eta_0 \cdot \sin \omega t$, the drag force ΔF_D on the small line element can be written as

$$\Delta F_D = \tfrac{1}{2} \rho D \cdot C_D \cdot \dot{\eta} |\dot{\eta}| \cdot \Delta s \qquad \text{Eq. 2-5}$$

and hence the energy dissipation of line element is $\Delta E = \frac{4}{3}\rho \cdot D \cdot C_D \cdot \omega^2 \cdot \eta_0^3 \cdot \Delta s$.

In order to integrate along the line to get the energy dissipation of the whole line, the transverse displacement η_0 is approximated by the form $\eta_0 = \frac{1}{2}\Delta z \cdot \cos(\varphi)$, in which the Δz is the total vertical displacement of the element during one cycle and φ is the angle between the mooring line and the horizontal. Finally, the energy dissipation per cycle along the mooring line can be expressed by

$$E = \frac{1}{6} \cdot \rho D C_D \omega^2 \int_0^{X_{\max}} \frac{|\Delta z|^3}{1 + \sinh^2\left[(w/T_{H0})(x - x_0)\right]} dx \qquad \textbf{Eq. 2-6}$$

Here $X_{\max}$ is the maximum horizontal co-ordinate of the fairlead, x and x_0 are the horizontal co-ordinate and reference position, respectively, w is weight per unit length of submerged line, and T_{H0} is the horizontal pre-tension.

Realising that the normal displacement η_0 is not symmetric about the mid position, owing to geometric nonlinearities inherent in the catenary equations, Liu and Bergdahl (1998) provides two normal displacement amplitudes, one for each half-cycle. This modification will provide a higher accuracy when using the quasi-static equations.

However, when the dynamic response of the mooring line is dominant, the quasi-static method can result in large errors, which has been verified by experimental investigation. The top-end tension for dynamic responses may have values well above the values for quasi-static tension, and the response typically becomes non-sinusoidal and is marked by a steep increase in tension (Papazoglou et al., 1990).

Quasi-static approaches are not as rigorous as dynamic methods, therefore, dynamic methods are more widely used in calculating the mooring line damping. Based on non-linear time-domain dynamic simulation, Webster (1995) studied the damping of

mooring lines in a parametric investigation. The energy dissipated by the mooring line in surge direction is calculated by the formula

$$E = \int_{t}^{t+T} F_H \cdot \frac{dS}{dt} dt \qquad \textbf{Eq. 2-7}$$

The surge motion S at the attachment point is plotted on the horizontal axis while the horizontal force F_H is plotted on the vertical axis. The energy dissipated by the mooring line during one drift motion period T is the area contained within the trace on the plot, which gives a quick visual interpretation of the energy dissipation of the mooring line. This presentation of the results is the same as the 'indicator diagrams' used to evaluate the performance of reciprocating engines. Therefore, the plot will be referred to as such (see Figure 2-7)(Webster, 1995). The indicator diagram plots only the displacement-force curves that result after a reasonable steady state has been achieved.
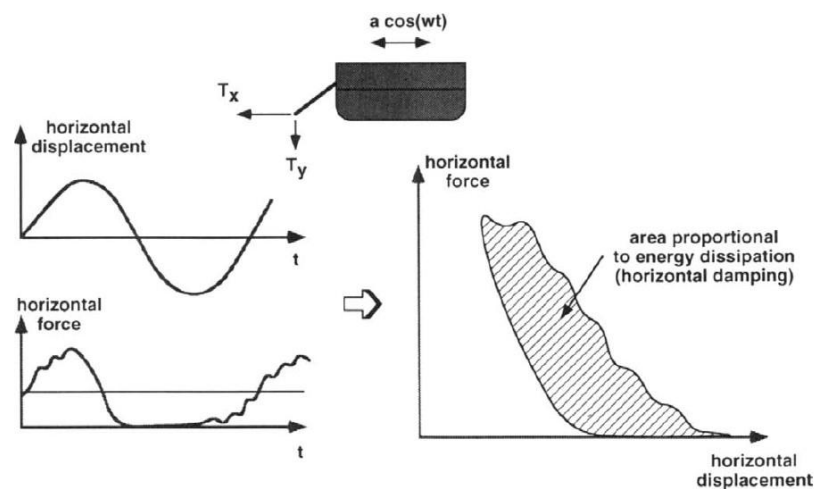
Figure 2-7 Indicator diagram for mooring line damping (Webster, 1995)

In Webster's study (1995), to characterise the behaviour of the baseline mooring line, simulations were carried out for six pretensions ranging from a moderately slack line to an almost taut line. In Figure 2-8, variation of mooring line damping with pretension and amplitude is illustrated. The dimensionless damping is defined as

D/awH, where D is energy dissipation of the line per cycle; w is wet weight per unit length of the line; a is the amplitude of the sinusoidal motion; H is the water depth. For the slack line the non-dimensional damping increases as the motion amplitude increases, while for the line with higher pretension, the non-dimensional damping becomes less dependent on the motion amplitude.
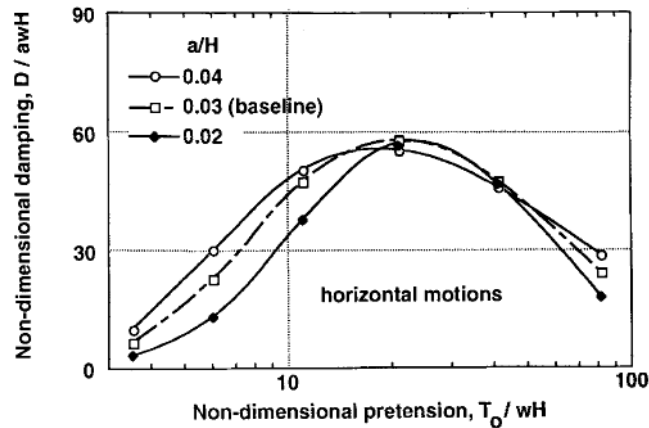
Figure 2-8 Variation of mooring line damping with pretension and amplitude (Webster, 1995)

A series of parametric variations of the mooring line characteristics were performed to study the effects of motion frequency, scope, drag coefficient, current. It was found the effect of these parameters on mooring line damping can vary significantly with the line pretension. For example, as shown in Figure 2-9, at low non-dimensional pretension the damping of a slack line is bigger under the high frequency (small oscillation period) motion than that under the low frequency motion.

As the non-dimensional pretension increases, the horizontal motions with lower frequencies cause higher mooring line damping. The strong variation of damping with the parameters may indicate why there is no uniform agreement concerning the importance of mooring line damping within the community (Webster, 1995). It also emphasises the need to specify the mooring line configurations and characteristics before discussing the effect of mooring line damping.
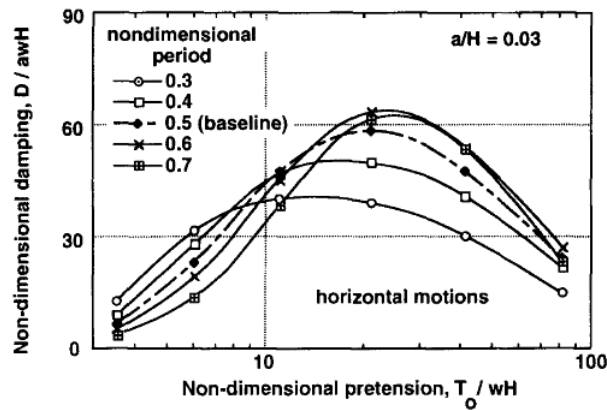
Figure 2-9 Variation of mooring line damping with excitation period

A comprehensive study comparing the result from time and frequency domain methodologies was performed by Brown and Mavrakos (1999). It was found that results based on time-domain methods are in broad agreement with each other while wider discrepancies exist between results obtained from frequency-domain methods. The influence of drag coefficients was also included in the study and the need to establish consistent values of hydrodynamic coefficients for the design community was emphasised.

2.4 Global Analysis of a Moored FPSO system by coupled method

In shallow water, the motions of the floater are mainly excited and damped by fluid forces acting on the floater itself, and hence the traditional uncoupled method is quite desirable in predicting the floater motions due to its high efficiency and sufficient accuracy. As the water depth increases, the coupling/interaction effect between the large floater and the slender structures becomes more important, while the validity of uncoupled approach becomes questionable.

The need for coupled analysis was recognised early by Paulling and Webster (1986) when they realised that in deepwater applications, due to the appreciable mass of the moorings and risers in comparison with that of the platform, considerable dynamic interaction between the two systems could probably exist. The necessity of a coupled

approach in global analysis was further emphasized as the importance of mooring line damping gradually became accepted by the industry. Consequently, a number of coupled analysis tools (Chakrabarti et al., 1996, Ormberg and Larsen, 1998, Ma et al., 2000, Heurtier et al., 2001, Garrett et al., 2002, Low and Langley, 2006, Low and Langley, 2008) have been introduced.

The coupled analysis can be conducted in frequency or time domain. Due to the geometric and hydrodynamic nonlinearities and dynamic coupling between the platform, moorings and risers, a fully coupled time-domain analysis is preferred for an accurate prediction. The disadvantage of a fully coupled time domain analysis is the expensive computational effort for routine design purposes notwithstanding the advances in computer hardware. Owing to practical needs, different efficient methods have been proposed. For instance, Low and Langley (2006) developed an efficient frequency domain coupled analysis which can provide high accuracy for the analysis of ultra-deepwater floating systems that are not governed by geometric nonlinearity. For a floating system moored in shallow water, where the geometric nonlinearity is significant, the frequency domain analysis suffers considerable loss of accuracy. Therefore, a hybrid frequency/time domain approach was proposed by Low and Langley (2008), whose results show quite good agreement with a fully coupled analysis for a floating system moored in 200m water depth.

Related practices are also provided by different organisations. The first version of recommended practice DNV-RP-F205, issued in 2004, is especially about the global performance analysis of floating structures in deepwater. In the appendix of recommended practice API 2SK (3rd edition, 2005), global analysis guidelines resulting from project DeepStar for deepwater floating systems are included and important findings are also incorporated. As a JIP project, one of DeepStar's focuses is on the global performance of deepwater production systems, where different kinds of platforms (FPSO, Spar, TLP and Semi-Submersible) are selected for the studies. All these practices try to provide general design and analysis principles about global performance analysis of deep-water floating structures.

The global dynamic characteristics of FPSOs under the combination of wind, wave, and current conditions have been studied by several researchers. For example, taking a turret-moored FPSO in irregular waves as object, Wichers (1988) initiated a comprehensive study using the uncoupled method, which solved the dynamics of the rigid body and mooring line separately. Ormberg and Larsen (1998) argued that, due to the typical shortcomings in the traditional uncoupled method, the separated approach could lack sufficient accuracy especially for deepwater floaters. In their study, the dynamic responses of a turret-moored FPSO system operating in 150m, 330m and 2000m water depths were analysed by experiments, the traditional uncoupled method and a coupled approach. The results between the experiments and coupled analysis were generally in good agreement, while over-estimated LF motions and under-predicted mean offset were obtained by the use of uncoupled analysis. This argument was later verified by the work of Wichers and Devlin (2001), which also showed that a large error in the dynamics of an FPSO system may be obtained from the uncoupled analysis.

In the study conducted by Wichers and Devlin (2001), the values of drag coefficients of risers and moorings were systematically varied to show the effect on the fully coupled responses. Two different weather conditions, namely Hurricane and Loop-current conditions were considered. The dynamic riser tensions increase significantly at increasing drag coefficients for both weather conditions. However, for Hurricane condition, the effect of C_D variations (=1 or 2) on the mooring forces and the FPSO motions is relatively small, while for Loop-current condition the sensitivity of C_D on the displacements of the FPSO and mooring forces is significant. According to the study, this is caused by the fact that in Loop-current condition the current loads on the moorings and risers dominate the displacement of the FPSO system.

Kim and Kim (2002) emphasized damping effect of risers upon surge/sway modes in their study of the global performance of the FPSO system. It was also concluded that the use of Newman's approximation slightly under-estimates the actual horizontal-plane motions but seems to be adequate in practical applications. The importance of

reliable estimation of the second-order mean and slowly varying wave forces and the magnitude of total system damping was emphasized as well in predicting the dominant slowly varying components of the horizontal-plane motions. A sensitivity study of a tanker-based FPSO was performed by coupled dynamic analysis (Tahar and Kim, 2003), and the role of various hydrodynamic contributions was analysed and assessed. By comparing the results of two different cases (without or with C_D on moorings/risers), they found that without C_D a significant increase occurred in surge and sway RMS values that was mainly due to the absence of riser/mooring viscous damping. As a result, the corresponding riser/mooring tension was greatly over-predicted. For instance, the maximum tension of mooring line 2 was over-estimated by a factor of 2, although the mean tension of the line decreased a little because the neglect of current force ($C_D = 0$) caused a decreased mean offset.

In the study of Luo and Baudic (2003), the effect of C_D variation of moorings and risers were also considered. In their case, they found that the effects of C_D variation on maximum tension and offset were insignificant. Their explanation was that with an increase of drag coefficients of mooring and riser the mean offset increases while RMS values of the slow drift motion decreases (See Figure 2-10), and the final impact depends on the contributions of these two components.
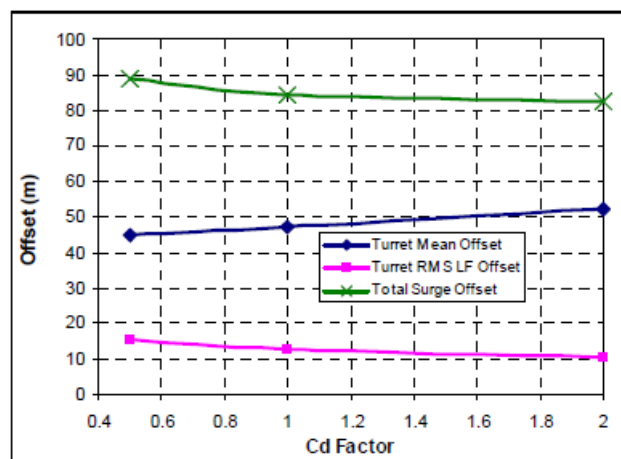
Figure 2-10 Impact of drag coefficient variation on FPSO offsets (Luo and Baudic, 2003)

They also concluded the coupled analysis is the preferred approach for analysing deepwater FPSOs. In their opinion, the model test approach has its limitations due to the anchoring leg truncation and current turbulence and hence should be combined with the numerical method to best predict the system responses. Also, on the limitations of model test, Kim et al. (2005) found that with a truncated mooring system, dynamic mooring tension can be under-predicted when mooring dynamic effects are significant. Meanwhile, damping of moorings/risers can also be severely under-estimated depending on the level of mooring line/riser truncation.

It should be noted that almost all these numerical studies only considered FPSOs in hurricane environments. Also most of model tests were conducted for FPSOs under severe hurricane conditions (Kim et al., 2001, Kim et al., 2005). The exception is the study made by Wichers and Devlin (2001), where loop-current conditions were also included. However, as mentioned in API RP 2SK (2005), for large ship-shaped vessels, lower waves with shorter periods could trigger larger LF motions and hence higher mooring loads than 100-year design environments. Global analysis of FPSO under hurricane conditions may be insufficient in order to obtain the extreme mooring loads.

2.5 Turbulence and numerical modelling

2.5.1 Turbulence and Turbulence modelling

Most kinds of the fluid flows in reality are turbulent. Turbulence is a phenomenon of fluid flow that occurs when inertial effects dominate viscous effects, while in laminar flow viscous effects dominate inertial effects. Turbulence is characterised by random fluctuating motion of the fluid masses in three dimensions and by randomly fluctuating velocity fields over a wide range of length and time scales.

Turbulent flow is irregular and random. That is the reason why turbulence problems are normally treated statistically rather than deterministically. Turbulent flow is

dissipative, which means that kinetic energy in the small (dissipative) eddies is transformed into internal (heat) energy. The small eddies receive kinetic energy from larger eddies while the largest eddies extract their energy from the mean flow. This process of transferred energy from the largest turbulent scales (eddies) to the smallest is called a cascade process. This phenomenon of turbulence makes it quite difficult to simulate the turbulence directly.

Turbulent flow could be thought of as instability of laminar flow that occurs at high Reynolds numbers (Re). Such instabilities result from interactions between viscous terms and non-linear inertial terms in the Navier-Stokes equation (N-S equation). These interactions are rotational, fully time-dependent and fully three-dimensional. Rotational and three-dimensional interactions are mutually connected via vortex stretching which is not possible in two-dimensional space. That is also why normally no satisfactory two-dimensional approximations for turbulent phenomena are available.

Turbulence modelling

Characterized by rapidly fluctuating velocity fields both in space and time, turbulent flows are quite computationally expensive to model in numerical simulations. A grid is required which can directly simulate the high frequency, small scale, and larger scale fluctuations which, for problems of practical engineering significance, occur with sizes over several orders of magnitude. Although, with the improvement of high computing capacity recently some direct numerical simulations (DNS) have been conducted to resolve the smallest scales of the flow directly in N-S equation, those simulations are still limited to very simple geometry and low Re number.

Usually, two methods namely time averaging and space filtering can be used to eliminate the need to resolve the high frequencies and small scales and to allow a larger grid. Most of the turbulence models, in the CFD program FLUENT, can be classified into two groups based on either time averaging or space filtering method, as illustrated in Figure 2-11.
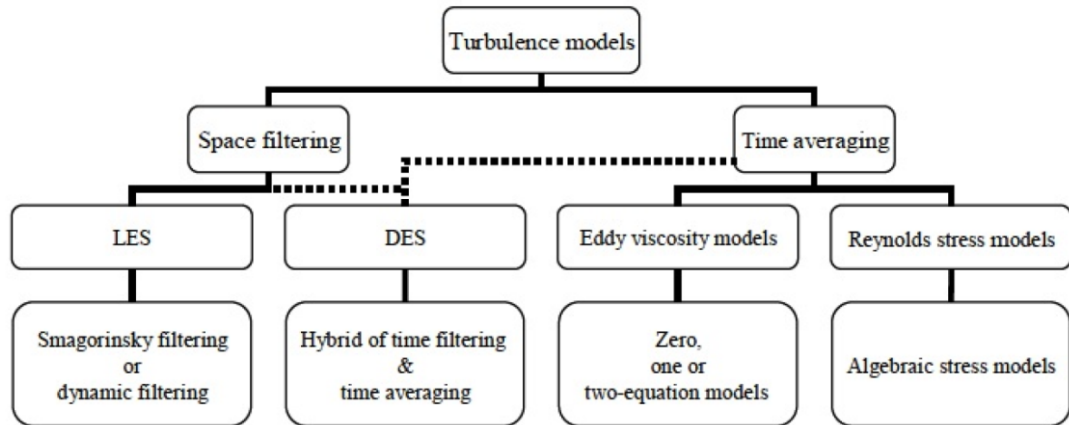
Figure 2-11 Classification of turbulence models (Patel, 2010)

Time averaging and RANS (Reynolds-Averaged Navier-Stokes) models

The concept of time averaging (Reynolds averaging) was introduced by Reynolds in 1895 (Reynolds, 1895). The main idea of Reynolds averaging is to decompose all the flow variables to averaged and fluctuating components. The time averaging introduces new terms in the N-S equation known as the Reynolds Stresses, which causes the closure problem. Different concepts and attempts have been made to solve the turbulence closure problem caused by Reynolds stresses. However, different from viscous stress which is a property of a fluid, Reynolds stress is a property of the flow and is dependent on the flow variables themselves. That is the reason why it changes from flow to flow and no general constitutive relations are available. There are mainly two approaches to model/solve Reynolds stresses and hence the closure problem. According to the approach adopted, RANS models can be classified into Reynolds stress models and eddy viscosity models as shown in Figure 2-11.

Reynolds stress models (RSM) result from an attempt to model the Reynolds stress tensor directly. A major problem with this approach is that it introduces even more new unknown variables for which constitutive relations are also unknown. By using a partial differential equation (PDE), Rotta (1951) managed to model the Reynolds stress tensor successfully. This model is more realistic than Boussinesq's turbulent viscosity model, which is described below. Since the RSM model accounts for the

effects of streamline curvature, swirl, rotation, and rapid changes in strain rate in a more rigorous manner than eddy viscosity models, it has greater potential to give accurate predictions for complex flows. However, computational cost is also high because it introduces six additional equations describing Reynolds stress and one additional equation describing turbulence length scale.

Eddy viscosity models are based on the idea of eddy viscosity in addition to molecular viscosity, as introduced by Boussinesq (1877). His hypothesis that 'turbulent stresses are linearly proportional to mean strain rates' is still the cornerstone of eddy viscosity turbulence models. However, the major problem of eddy viscosity models is how to obtain this property without carrying out an actual experiment involving that particular flow. A major breakthrough was first achieved by Prandtl (1925), who introduced the mixing length concept that is analogous to the mean free path of the molecules in gas. Models based on this concept are called zero-equation models as no additional transport equations besides energy, mass and momentum equations are needed. By introducing a concept of turbulent viscosity as a function of turbulent kinetic energy, Prandtl (1945) made another important breakthrough. Models using one additional transport equation to model turbulent kinetic energy are usually called one-equation models. Both zero- and one-equation models are incomplete because one still needs to have certain knowledge about the studied flow in advance to specify a turbulence length scale, which is also a flow dependent property. The first complete model was introduced by Kolmogorov (1942), who managed to model turbulent kinetic energy (k) and the rate of energy dissipation (ω) and then relate the missing information of length and time scales to these quantities. Two-equation models are called since two additional equations are used to model k and ω. They are also referred to as $k-\omega$ models while variations of this concept are so-called $k-\varepsilon$ models ($\varepsilon = k^n \omega^m$).

Space filtering and LES (Large Eddy Simulation) model

Space filtering in the context of LES is a mathematical operation intended to remove a range of small scales from the solution to the N-S equations, because the principal difficulty in modelling turbulent flows results from the wide range of length and time scales. After the filtering of the transport equations the LES model only resolves the larger eddies while smaller eddies are modelled. The space filtering method also introduces an additional term in the governing equations that needs to be modelled in order to achieve a "closure" for the unknowns. The unknown sub-grid-scale stresses are modelled by the sub-grid-scale turbulence models in program FLUENT which employs the Boussinesq hypothesis as in the RANS models.

Larger eddies directly resolved are difficult to model since they are anisotropic, subject to history effects and dependent upon flow configuration and boundary conditions. Smaller eddies are typically isotropic, so they are more amendable to modelling. The rationale behind LES can be summarized as follows (Fluent12.1, 2010):

1) Momentum, mass, energy, and other passive scalars are transported mostly by large eddies;
2) Large eddies are more problem-dependent. They are dictated by the geometries and boundary conditions of the flow involved;
3) Small eddies are less dependent on the geometry, tend to be more isotropic, and are consequently more universal;
4) The chance of finding a universal turbulence model is much higher for small eddies.

For different turbulence models the modelling extend of turbulence is illustrated in Figure 2-12.
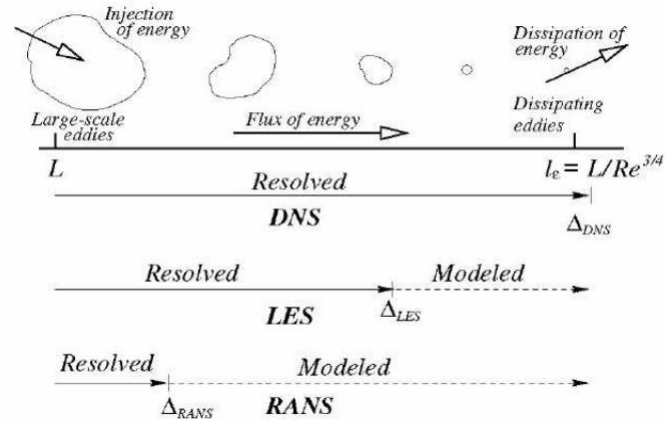
Figure 2-12 Modelling extend for certain types of turbulent models (Bell, 2003)

It is clearly seen that the LES resolve shorter length scales than RANS models. So for most flows the LES model should get better simulation results. However, the LES model usually requires much greater computer power.

2.5.2 Numerical modelling of turbulence flows past bluff bodies

Steady flow past a circular smooth cylinder

To model high Re number turbulent flows past circular cylinders or bluff bodies in general, three approaches have been mainly explored by CFD practitioners. One approach is based on the unsteady Reynolds-averaged N-S (URANS) model because the periodic shedding requires an unsteady time dependent solution. The URANS-based approach has fairly low computational cost, mainly due to less demanding mesh resolution requirement. However, the accuracy of numerical results could be case-dependent. For instance, Franke et al. (1989) and Tutar and Holdo (2001) evaluated numerically the detailed experiments of Cantwell and Coles (1983) at $\mathrm{Re} = 1.4 \times 10^5$, which is in the sub-critical flow regime at the start of the drag crisis. Franke et al. (1989) applied URANS with the standard high Reynolds number $k - \varepsilon$ model while Tutar and Holdo (2001) used both the standard high Reynolds number $k - \varepsilon$ model and non-linear $k - \varepsilon$ models. Both studies concluded that the $k - \varepsilon$ models give an inaccurate prediction of flows with strong anisotropic turbulence.

Catalano et al. (2003) and Ong et al. (2009) studied the flow around a 2D smooth circular cylinder for very high Reynolds numbers, covering the supercritical to upper-transition flow regime, using 2D URANS in conjunction with a standard high Reynolds number $k - \varepsilon$ model. Both of their numerical results give satisfactory qualitative agreements with the published experimental data for Reynolds number in the range of 1.0×10^6 to 3.6×10^6.

The LES method for bluff-body flows is fundamentally more viable than the URANS-based approach. The LES approach can capture large-scale turbulent structure presented in the flows which is ill simulated by the URANS approach, although the LES approach is comparatively more expensive in computation cost. The first attempt of a comprehensive LES study of the flow over a cylinder was conducted by Beaudan and Moin (1994). The Reynolds number considered is 3900, which is in a sub-critical regime. The same flow has been simulated later using LES by several different people (Mittal and Moin, 1997, Breuer, 1998a, Breuer, 1998b, Kravchenko and Moin, 2000, Young and Ooi, 2007). There are less LES studies published in the literature of flows around cylinders at high Reynolds number. Breuer (2000) did a challenging test case for LES at high Re number, $\mathrm{Re} = 1.4 \times 10^5$, at which the experiment of Cantwell and Coles (1983) was conducted. In general, the LES results were in fairly good agreement with the experimental data. Using wall modelling function to solve the boundary layer, Catalano et al. (2003) attemped LES for even higher Reynolds numbers in critical to super-critical Reynolds regimes ($\mathrm{Re} = 5 \times 10^5, 1.0 \times 10^6, 2.0 \times 10^6$). They captured correctly the delayed boundary layer separation and reduced drag coefficients consistent with experiments after the drag crisis, while the mean pressure distribution was reasonably predicted as well. However, the Reynolds number dependence of the mean drag coefficient was not captured and the solution became less accurate as Reynolds number increased. More recently, Kim and Mohan (2005) carried out LES for two Reynolds numbers ($\mathrm{Re} = 1.4 \times 10^5, 1.0 \times 10^6$) in the sub-critical and super-critical Reynolds regimes and the global flow parameters (mean drag coefficient, *RMS* value of force coefficient and Strouhal number) were predicted with a commendable accuracy, which all fell

within the scatter of the experimental data. The main difference of their work from the work of Catalano et al. (2003) is that they used quite fine mesh in the boundary layer to resolve the laminar sub-layer directly rather than using wall functions.

The third approach normally called 'Detached eddy simulation' (DES) is becoming popular in turbulence modelling of bluff-body flows. DES turbulence models essentially deteriorate to URANS models in the near-wall region or when the local mesh size is too coarse to explicitly resolve energy-containing eddies, so the computing cost is between URANS models and LES. However, one fundamental criticism about DES can be summarised as the lingering questions of how to reconcile two very different models (URANS and sub-grid-scale turbulence models) at the common interface (Kim and Mohan, 2005).

Unsteady flow past a circular smooth cylinder

The reviews mentioned above are mainly about numerical studies of steady flow past a circular cylinder. Many numerical simulations of unsteady flow around a cylinder have also been conducted during the past several decades. Most of them are about a forced cylinder oscillating transversely in a free stream or the oscillation of a cylinder in still water. Also, some people (Lu et al., 1997, Lu and Ling, 2003, Saghafian et al., 2003, An et al., 2011) performed computational studies about oscillatory flow past a fixed cylinder. Considering the problem of concern in this thesis, the main attention of this review will be paid to those about the case of a cylinder oscillating in-line in still water.

Initially, due to the computational cost, 2D simulations were mainly conducted for an oscillating cylinder in water at low KC and Re numbers. Baba and Miyata (1987) made the first attempt to solve the 2D N-S equations for an oscillating cylinder in still water. Using a finite difference solution method, two situations (one for KC =5, Re=1000; the other for KC =7, Re=700) were considered without any turbulence model. In both calculations, the wake was symmetric in contrast to experimental

observations. Dutsch et al. (1998) numerically solved the 2D N-S equations and performed experiments for the investigation of three different Re-KC combinations (Re=100, KC =5; Re=200, KC =10 and Re=210, KC =6). The predicted velocity fields and in-line force coefficients were in fairly good agreement with experimental results. Also found were that strong cycle-to-cycle variations of the in-line forces acting on the oscillating cylinder, which Morison equation neglects as the flow is assumed to be fully periodic. Other similar work completed by 2D numerical studies for low KC and Re numbers includes Guilmineau and Queutey (2002), who obtained almost the same in-line force cofficients for the case with Re=100 and KC =5, as Dutsch et al. (1998) did before.

While unsteady 2-D laminar computations are now routine, the number of published 3D numerical studies is quite limited. Nehari et al. (2004) used both 2D and 3D models to simulate an oscillating cylinder in quiescent water and compared the results with each other. It was found the three-dimensionality of the vorticity field would affect the dynamic loads induced on the cylinder. The longitudinal and axial components of the force acting on the cylinder seemed to be weakly affected by the three-dimensional effects, while conversely the transverse force appeared to be significantly influenced by the 3D flow field. This finding explains why the in-line hydrodynamic force coefficients predicted by 2D simulations often agree fairly well with the data from experiments.

Several papers discuss about the applicability of two-dimensional simulations to unsteady flow around a cylinder, regarding the fact that 2D simulations are employed not only for laminar flows but also for flows at sub-critical Reynolds numbers (Blackburn and Henderson, 1999, Pan et al., 2007). It is known the structural vibration enhances spanwise correlation, which is reported by Blevins (2006). Also as mentioned by Blackburn and Henderson (1999), on the evidence that spanwise correlations of forces, wake velocities, etc. all increase with increasing cylinder motion amplitude, one would reasonably suggest that the harmonic motion of a long circular cylinder would suppress three-dimensionality and make flows more two-

dimensional than their fixed-cylinder counterparts, at least in the near-wake region. However, if the wake is actually three-dimensional, then the proper resolution of the flow field and hence the flow forces will significantly depend on a 3D resolution of the wake.

3D simulations of an oscillating cylinder in still fluid at higher Re numbers were carried out using LES by Rashid et al. (2011). In their studies, calculations of the force cofficients for KC up to 4 and β =11240 ($\beta = D^2 / \upsilon T$ is called frequency parameter), with corresponding $Re = 4.5 \times 10^4$, are in agreement with experimental results by Otter (1990) while they are smaller than Sarpkaya's measurements (Sarpkaya, 1986). Supplementary computations with smaller $\beta = 1035$ and KC =4.86, 6.28 and 8 also show when flow separation occurs the predicted drag coefficients are about 40% smaller than those measured by Sarpkaya (1986), while the calculated added-mass coefficients agree quite well with Sarpkaya's measurements. Since their numerical simulations fit well to the experiments by Otter, they speculated the input oscillatory channel flows maybe get polluted by turbulence in U-tube experiments performed by Sarpkaya. The difference between results obtained from these two tests has also been noticed by Garrison (1990), who thinks the likely cause of the disagreement of Sarpkaya's results is a 'wake-blockage' problem of the U-tube.

From the brief review of related numerical work about unsteady flows around a cylinder, it can be seen that most of the work is for laminar flows or for turbulent flows with small KC numbers. Further work should focus on the simulations of an oscillating cylinder in water for high Reynolds numbers and a wide range of KC numbers.

However, numerical simulations of flows past chains are not available from any publications. The work to be done in the thesis could be the first attempt to determine the drag coefficient of chain by numerical methods.

3.   Mooring line damping of a moored FPSO system

3.1 Overview

The significance of mooring line damping has been emphasized through the related review in Chapter 2, from which it can be seen that the magnitude of mooring line damping will depend not only on line configurations and characteristics but also on environmental factors, such as ocean current and top motions of platforms.

In order to determine the mooring line damping and later to assess its effect on the motions of an FPSO system, a specific turret-moored FPSO system with 20 chain-wire-chain moorings operating in 400m water-depth is selected. The characteristics of the moored FPSO system and displacement RAOs of the FPSO are first analysed in this chapter. Then the mooring line damping is evaluated for lines under different motions by dynamic analysis, which is completed in software OrcaFlex. It is to be noted that OrcaFlex calculates hydrodynamic loads on sleneder structures using a relative velocity form of Morison's equation. Considering the fact that when studying the effect of WF motions on mooring line damping only harmonic or bi-harmonic WF motions have been superimposed on the LF motions in the former work, the impact of random superimposed WF motions on the mooring line damping is included here. Subsequently, effects of current and wave on the mooring line damping are considered. At the end, the relationship between line dynamic tension and damping of moorings is also discussed.

3.2 Characteristics of a moored FPSO system

The given FPSO's hydrodynamic responses, including displacement RAOs, added mass are first calculated by WAMIT, which is a second-order diffraction/radiation program. The displacement RAOs will be used to decide the main WF motions of the FPSO, and hence to know their real effect on the mooring line damping. The stiffness and natural frequency of the moored FPSO system are then calculated in

order to determine the undesirable frequency of LF surge motion, which is near to the natural frequency of the moored system. The frequency of LF surge motion is important as the mooring line damping will be most important when the loads cause a resonance at this frequency.

3.2.1 Particulars of the given FPSO and its hydrodynamic response

The vessel used in this study has a length of 270m, a beam of 52m, and a draft of 12m with displacement of $1.42 \times 10^5 \text{MT}$. The internal turret mooring system is located 54.5m aft of the forward perpendicular of the vessel and has a diameter of 16m. The main particulars of the given turret-moored FPSO are given in Table 3-1.

Table 3-1 Main particulars of the given turret-moored FPSO

Designation	Symbol	Unit	Quantity
Length between perpendiculars	L_{PP}	m	270
Breadth	B	m	52
Draft	T_D	m	12
Block coefficient	C_B	-	0.82
Displacement	Δ	MT	1.42×10^5
Roll radius of gyration	K_{xx}	m	17
Pitch radius of gyration	K_{yy}	m	70
Yaw radius of gyration	K_{zz}	m	70
Centre of gravity (CG) above base	z_g	m	14
CG from forward perpendicular	x_g	m	141.9

For the computation of hydrodynamic coefficients and RAOs of the FPSO, commercial software WAMIT is used. This program is based on the three-dimensional panel method (boundary integral equation method) and Green's theorem with a free surface Green function. The wetted surface of the vessel will be

discretized by higher-order panels and only half of the domain is discretized considering the symmetry of hull with respect to the x-axis.

Although detailed hull lines of a particular FPSO were not used, the hydrodynamic response will not be significantly affected by the precise hull shape, which can be analytically represented by an elliptical bow, a rectangular mid-body and a prismatic stern in WAMIT's GEOMXACT.F file. The file written in Fortran programming language provides the definition of some common ocean platforms and geometries, such as FPSO, SPAR, TLP, cylinder, box and sphere. This approximation is due to the fact that many FPSOs have a nearly box-shaped hull with large block coefficient. In order to validate the results, tests for accuracy and convergence are completed for a Schiehallion FPSO (Ha, 2011). The Schiehallion FPSO's displacement RAOs in the head wave condition and added mass coefficient in surge direction are calculated by WamitV7 with 2692 panels and compared with the results of Ha (2011), as seen from Figure 3-1 and Figure 3-2. It can be seen that the results of displacement RAOs calculated by WamitV7 are in reasonable agreement with Ha's results. The discrepancies mainly occur around the natural period of heave motion. However, for the added-mass coefficient in surge, there is a considerable discrepancy between the two results, which could be caused by the approximation of hull shape in WamitV7.
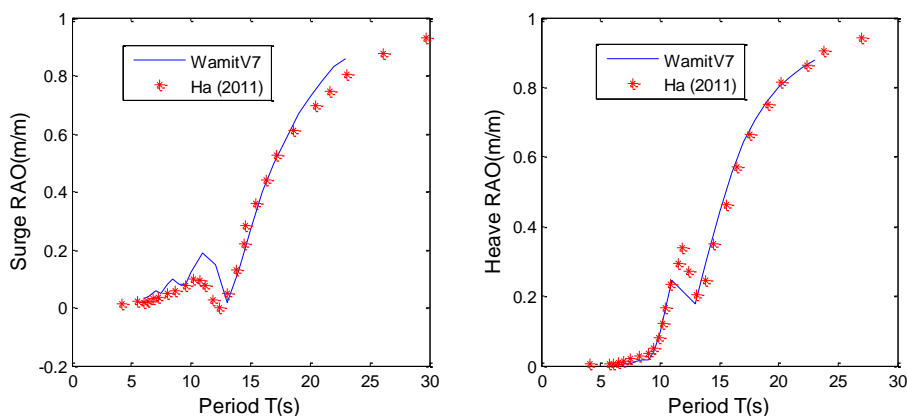
Figure 3-1 Surge and heave RAOs of Schiehallion FPSO under head wave condition
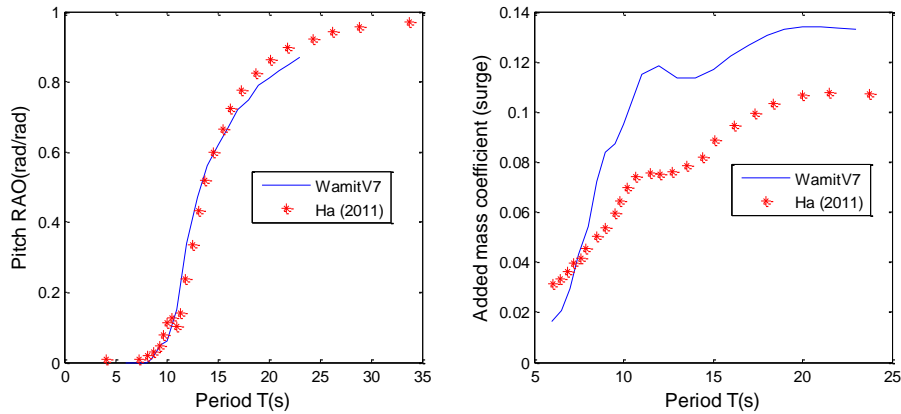
Figure 3-2 Pitch RAO of added-mass coefficient in surge under head wave condition

The numerical models, whilst not fully validated, are considered satisfactory for the purposes of this thesis. The wet surface of the specific FPSO hull is discretized by 2868 panels as shown in Figure 3-3. Given the weather-vaning characteristics of the FPSO and the problem of concern in this thesis, only two wave directions, namely 150 and 180 degree are considered with wave periods ranging from 5s to 23s.
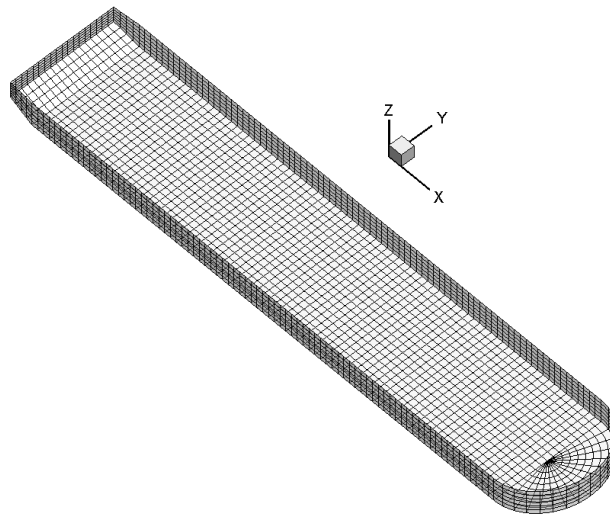
Figure 3-3 Grid modelling of wetted body surface of the FPSO

The calculated displacement RAOs of the given FPSO (relative to global origin, which is at the middle of ship for x- and y-axis and at free surface for z-axis) are given in Figure 3-4 and Figure 3-5. It can be seen that around the natural periods of heave and pitch, there are peak values in the curves. The heave natural period is

about 11 seconds, which is favourable to avoid heave resonance with both operational wind seas of two to seven seconds and persistent ocean swells of 12 to 18 seconds.
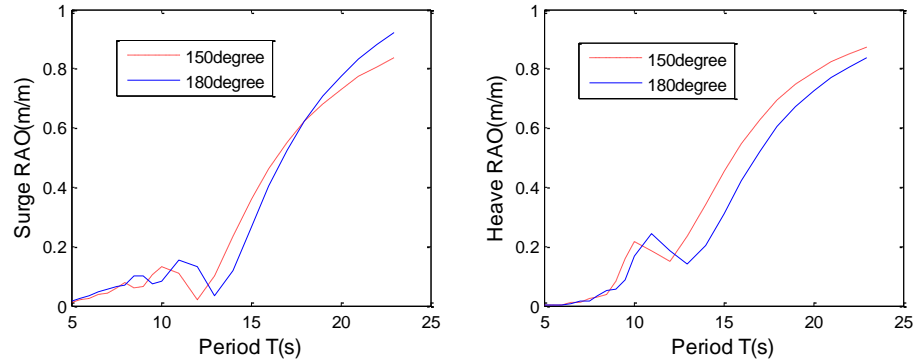
Figure 3-4 Surge and heave RAOs of the given FPSO
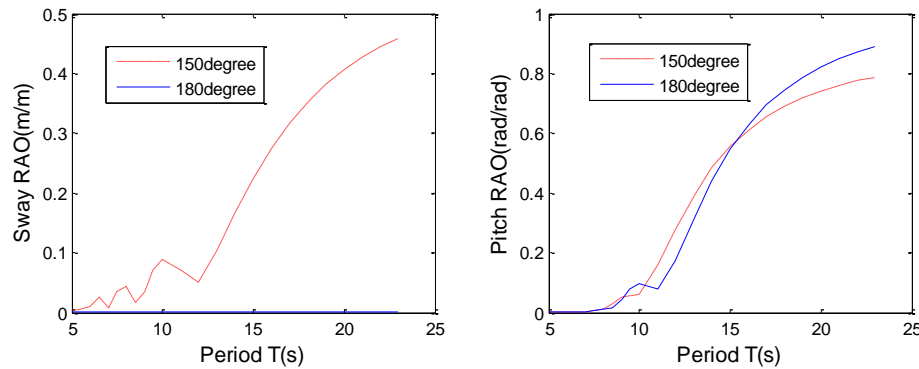
Figure 3-5 Sway and pitch RAOs of the given FPSO

The surge and heave RAOs will be used to determine the main WF motions under a given sea state. The FPSO's WF motions are especially important for the mooring line damping because it was found that superimposed WF motions dramatically increased the LF damping(Huse and Matsumoto, 1989). It should be noted that the LF motions could have a considerable interaction with mooring line damping: the amplitude of LF surge motion will depend on the mooring line damping, while the magnitude of mooring line damping is also affected by the LF motion amplitude.

The added-mass coefficient along the surge direction vs. wave period is shown in Figure 3-6. The value of 0.06 for added-mass coefficient in surge is selected to calculate the total mass M_T of the FPSO.
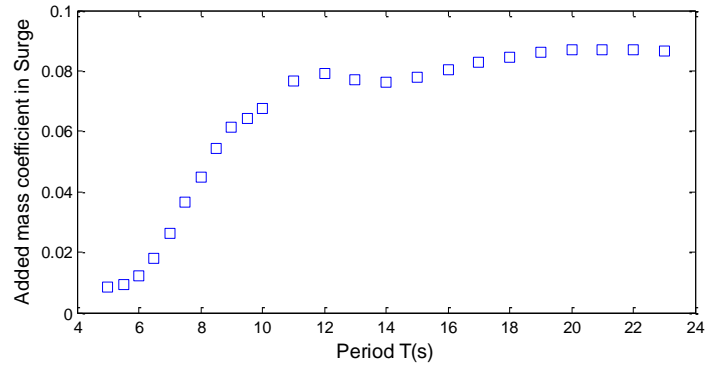
Figure 3-6 Added-mass coefficient in surge direction of the given FPSO

3.2.2 Moored FPSO system simplified as a spring oscillator model

The FPSO system contains 20 mooring lines and 24 steep wave risers, whose layout is shown in Figure 3-7. In Table 3-2 are the particulars for a single mooring line, which consists of R4 chain on the top, spiral strand wire in the middle and R3S chain on the bottom. The illustration of a single mooring line is shown in Figure 3-8. The detailed information of risers will be mentioned later when considering the damping effect and current force of risers in the coupled analysis.
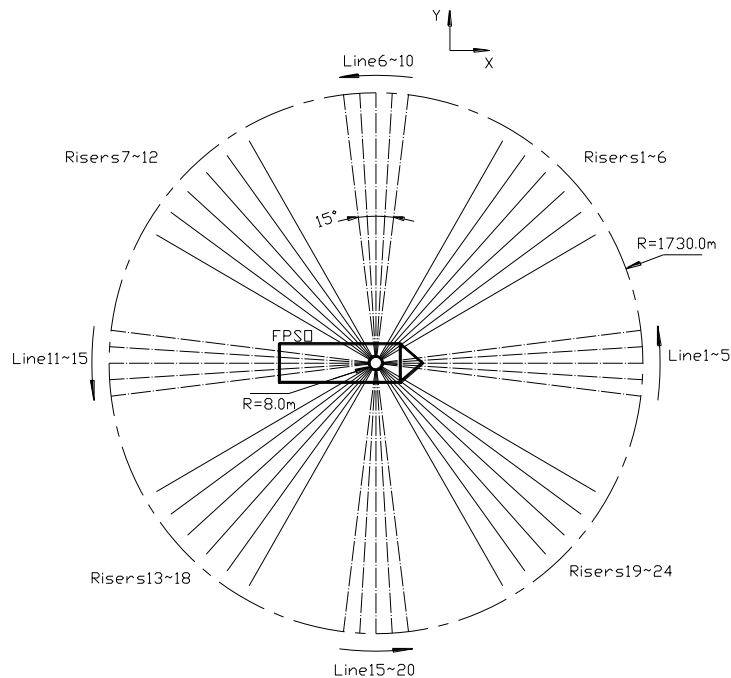
Figure 3-7 Layout of moorings and risers of the given FPSO

Table 3-2 Particulars of single mooring line

	R4 Chain	Spiral strand wire	R3S Chain
Length (m)	10	390	1480
Nominal Diameter (m)	0.157	0.144	0.152
Air weight (kg/m)	491	106	460
Wet weight (kg/m)	426	84	399
EA (mN)	3350	1893	2200
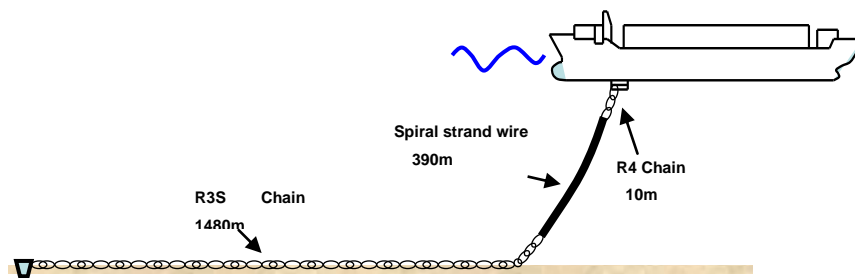
Figure 3-8 Illustration of a single mooring line

For a catenary type mooring system, the horizontal force component of the mooring lines is utilised to provide the restoring forces that maintain the moored FPSO on station. Any movement off station caused by environmental loads on the moored unit makes the catenary shape less steep, and hence increases the tension in the mooring. The effect of mooring lines is shown in Figure 3-9. For this moored FPSO system, the relationship between the offset and restoring force usually can be simplified as a spring oscillator model, which is illustrated in Figure 3-10.
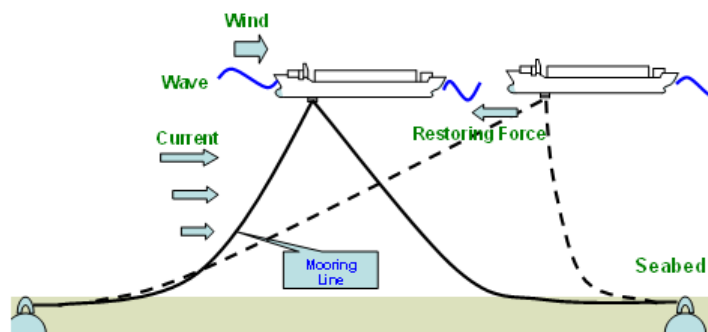
Figure 3-9 Illustration of loads of moored FPSO system
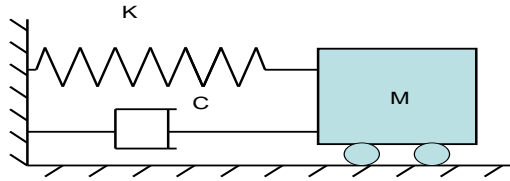
Figure 3-10 A spring-oscillator model for the moored FPSO system

The effect of the riser system on the total restoring force normally can not be neglected (Kim and Kim, 2002). But the contribution of risers to the stiffness of the whole moored system will be first ignored here. The stiffness K can be obtained by the relationship of horizontal displacement and horizontal restoring force, which can be obtained by quasi-static analysis. For a single mooring line, the stiffness K will increase as the line is becoming taut, which shows quite strong nonlinear characteristics, as illustrated in Figure 3-11. The dot-line is calculated according to the approximate formula proposed by Faltinsen (1990) for an inelastic catenary:

$$K = \frac{dT_H}{dX} = w\left[\frac{-2}{\left(1+2(T_H/wH)\right)^{1/2}} + \cosh^{-1}\left(1+\frac{wH}{T_H}\right)\right]^{-1} \quad \textbf{Eq. 3-1}$$
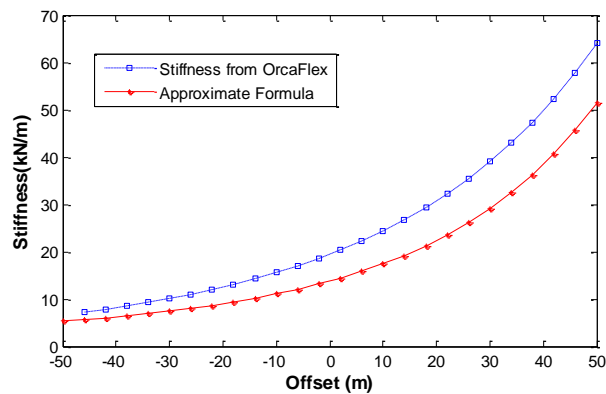
Figure 3-11 Nonlinear stiffness of a single mooring line

For the moored FPSO system, however, the stiffness K of all mooring lines approximately has a linear behaviour as illustrated in Figure 3-12. This is due to the balance of the slack and taut mooring lines. The original data in Figure 3-12 is obtained from quasi-static analysis.
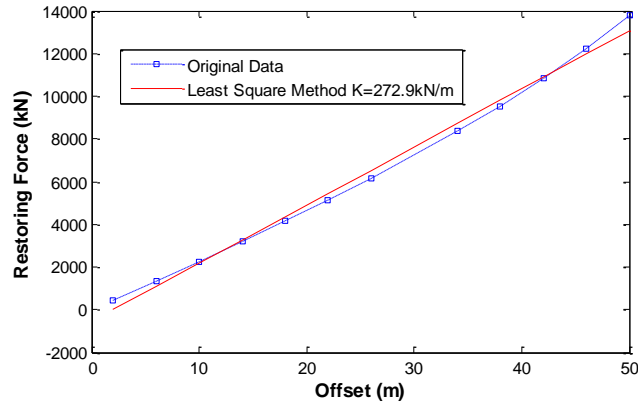
Figure 3-12 Relationship of horizontal offset and restoring force of 20 mooring lines

By the least square method, the mean stiffness K of the moored system can be calculated, which has a value of 272.9kN/m. The mean natural frequency of the whole moored FPSO system is obtained by the following equation (Eq. 3-2):

$$\omega = \sqrt{\frac{K}{M_T}}$$ **Eq. 3-2**

The critical damping of the moored FPSO system can be calculated by

$$c_c = 2\sqrt{M_T K}$$ **Eq. 3-3**

Given the added-mass coefficient of the vessel as 0.06, the total mass M_T of the vessel is $1.51 \times 10^5 MT$, and corresponding period and critical damping can be calculated. The characteristics of the whole moored system are listed in Table 3-3.

Table 3-3 Characteristics of the whole moored system in surge direction

Stiffness (KN/m)	Natural frequency (rad/s)	Natural period (s)	Critical damping ($N.s/m$)
272.9	0.042	149.6	6.42E+06

3.3 Effect of top motions of the FPSO on mooring line damping

As mentioned before, mooring line damping can be calculated by energy dissipation E of the lines, which is obtained by 'Indicator diagram' method. For sinusoidal motion $x = A \cdot \sin(2\pi / T \cdot t)$, an equivalent linear damping c is given by

$$c = \frac{ET}{2\pi^2 A^2}$$

Eq. 3-4

The corresponding damping ratio ζ is defined as

$$\zeta = c / c_c$$

Eq. 3-5

Here, the effect of current or waves on mooring line damping will be not included first. Only the effect of top motions of the FPSO, including LF motions and WF motions is considered. The drag coefficient C_D will be assumed constant. The value for wire is 1.2, for chain is 1.1 with respect to drag diameter ($2.10\,D$, D is nominal diameter of stud-less chain).

3.3.1 Effect of LF motion amplitudes on damping of moorings

Assuming the frequency of slow drift motion of the FPSO is the same as the mean natural frequency of the moored system, five different amplitudes are considered, namely 5m, 10m, 20m, 34m and 48m. The selection of mean natural period of the moored system as LF motion period is due to the fact that the damping effect is of most importance at resonance.

By the 'Indicator diagram' method and related formulae (Eq. 3-4 and Eq. 3-5), the calculated equivalent linear damping c and damping ratio ζ due to moorings under different amplitudes of LF motion are listed in Table 3-4. It can be seen that for the

given period, with the increase of LF motion amplitude, the damping of moorings also increases.

Table 3-4 Effect of LF motion amplitude on damping of moorings

Slow drift motion		c	Damping Ratio
Amplitude (m)	Period (s)	$(N \cdot s/m)$	ζ
5	149.6	8.59E+04	1.34%
10	149.6	1.73E+05	2.70%
15	149.6	2.63E+05	4.09%
20	149.6	3.56E+05	5.54%
34	149.6	6.46E+05	10.07%
48	149.6	1.02E+06	15.83%

From Figure 3-13 it can be seen that when the amplitude of LF motion is not big, the increase of damping ratio of moorings is linearly proportional to the increase of LF motion amplitude. However, the rate of increase of damping ratio of mooring line increases as the LF motion amplitude further increases.
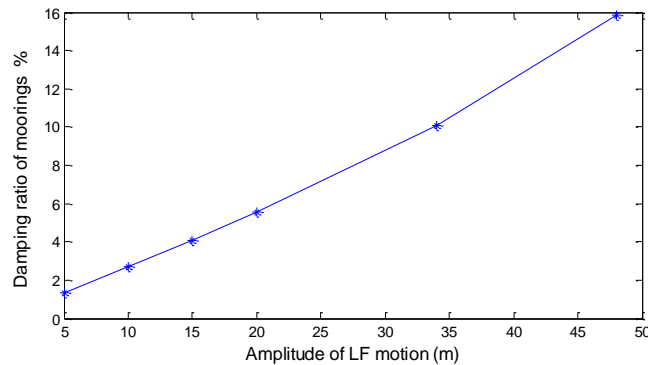
Figure 3-13 Effect of LF motion amplitude on mooring line damping

3.3.2　Effect of superimposed WF motions upon damping of moorings

The superimposed WF motions could dramatically increase the mooring line damping according to the study of Huse and Matsumoto (1989). The amplitude and frequency of WF motions are selected according to the displacement RAOs and the environment concerned.

A typical 100-year hurricane with significant wave height (H_s) of 12.2m and peak wave period (T_p) of 14s is selected as wave environment and JONSWAP spectrum with $\gamma = 2.5$ is used. From the spectra analysis, the response spectrum of certain motion at global origin (which is at the middle of the vessel for x- and y-axis and at free surface for z-axis) can be obtained by multiplying the wave spectrum with the square of the corresponding displacement RAO, as shown in Figure 3-14 and Figure 3-15. It can be seen that in the frequency range of 0.3 rad/s to 0.6 rad/s corresponding to the period range of 10s to 20s, there is the main energy in the surge and heave response spectra.

For the harmonic WF motions, therefore, the periods mainly from 10s to 20s are considered and the range of amplitudes is selected to be from 2m to 8m, which is approximately decided by the multiplication of H_s and heave/surge RAO at periods considered.
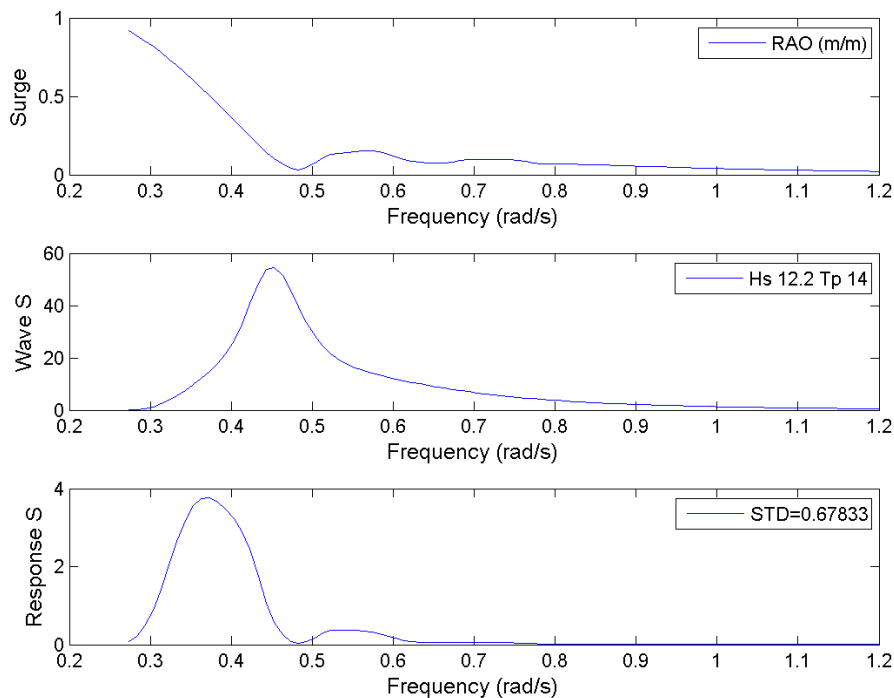
Figure 3-14 Response spectrum of surge motion of the given FPSO
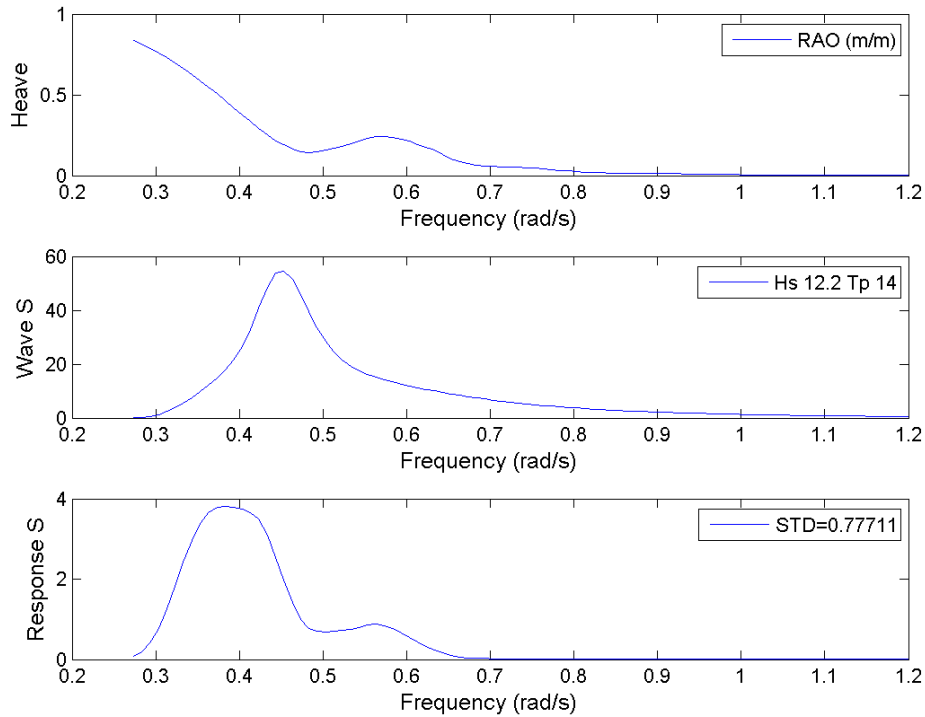
Figure 3-15 Response spectrum of heave motion of the given FPSO

Effect of harmonic WF motions on mooring line damping

When considering the superimposed WF motions, the drag coefficients of chain and wire will keep the same constant values as for the LF-motion simulation, namely 1.2 for wire, 1.1 for chain with respect to chain drag diameter ($2.10D$). The energy dissipation caused by moorings is also calculated according to the 'Indicator diagram', where the horizontal displacement is still corresponding to the LF motion while the horizontal force is due to the combination of the WF motion and LF motion (Brown and Mavrakos, 1999). Several periods of LF motion are considered and the energy dissipation is averaged over the cycles of periods. The calculated equivalent linear damping and damping ratio under different cases are listed in Table 3-5. A more visual comparison is depicted in Figure 3-16.

Table 3-5 Effect of surge WF motions on damping of moorings

Case	LF motion		WF motion		c	Damping	Increase
	$A_{LF}(m)$	$T_{LF}(s)$	$A_w(m)$	$T_w(s)$	$(N \cdot s/m)$	Ratio ζ	by
Case0 (NoWF)	15	149.6	0	0	2.63E+05	4.09%	-
Case1(A2T10)	15	149.6	2	10	8.30E+05	12.94%	216.4%
Case2(A4T10)	15	149.6	4	10	1.43E+06	22.30%	445.2%
Case3(A4T15)	15	149.6	4	15	9.97E+05	15.53%	279.7%
Case4(A4T20)	15	149.6	4	20	7.97E+05	12.42%	203.7%
Case5(A8T20)	15	149.6	8	20	1.47E+06	22.88%	459.4%
Case00 (NoWF)	34	149.6	0	0	6.46E+05	10.07%	-
Case01(A2T10)	34	149.6	2	10	1.01E+06	15.77%	56.6%
Case02(A4T10)	34	149.6	4	10	1.63E+06	25.34%	151.6%
Case03(A4T15)	34	149.6	4	15	1.21E+06	18.78%	86.5%
Case04(A4T20)	34	149.6	4	20	9.98E+05	15.54%	54.3%
Case05(A8T20)	34	149.6	8	20	1.68E+06	26.17%	159.9%
Case10(NoWF)	48	149.6	0	0	1.02E+06	15.83%	-
Case11(A2T10)	48	149.6	2	10	1.31E+06	20.38%	28.7%
Case12(A4T10)	48	149.6	4	10	1.89E+06	29.37%	85.5%
Case13(A4T15)	48	149.6	4	15	1.51E+06	23.47%	48.3%
Case14(A4T20)	48	149.6	4	20	1.31E+06	20.46%	29.2%
Case15(A8T20)	48	149.6	8	20	1.97E+06	30.64%	93.6%

It can be seen from Table 3-5 and Figure 3-16 that

1) With superimposed surge WF motions, the mooring line damping increases significantly when compared to the case with LF motion only;

2) With the increase of LF amplitude, the effect of superimposed surge WF motions on mooring line damping becomes comparatively less important;

3) As it is known, the mooring line damping is mainly due to the drag force, which is related to the square of fluid relative velocity. The ratio of A_w/T_w could be a reference of the velocity amplitudes of the WF motions. It can be seen that the ratio of A_w/T_w could reflect the importance of WF motions on the mooring line damping. For Case01 and Case04 with same ratio of A_w/T_w (also, Case02 and

Case05, Case11 and Case14, Case12 and Case15), their effects on the damping of moorings are quite similar.
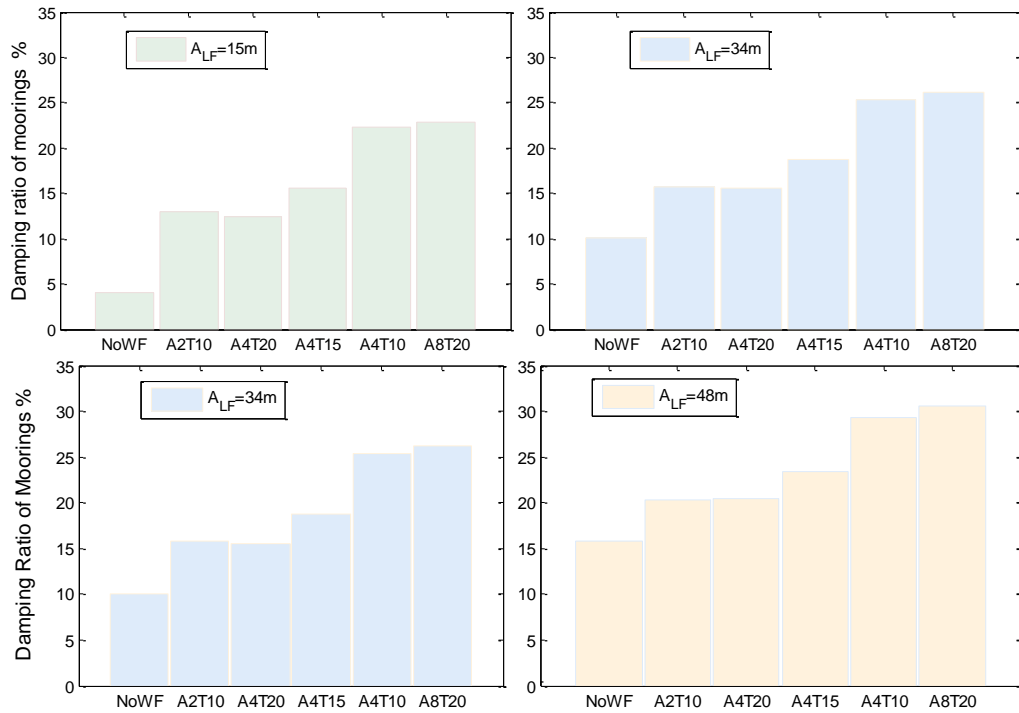
Figure 3-16 Effect of surge WF motions on damping of moorings

The effect of heave WF motion on mooring line damping is also considered, together with the combination of surge and heave WF motions. The base case for slow drift motion with amplitude of 34m is considered and the calculated results are shown in Table 3-6.

Table 3-6 Effect of heave and bi-harmonic WF motions on mooring line damping

Case	Surge WF Motion		Heave WF motion		c	Damping	Increase
	$A_w(m)$	$T_w(s)$	$A_w(m)$	$T_w(s)$	$(N \cdot s/m)$	Ratio ζ	by
CaseA	4	15	-	-	1.21E+06	18.78%	-
CaseB	-	-	4	15	1.27 E+06	19.81%	5.5%
CaseC	4	15	4	15	1.45 E+06	22.51%	19.9%
CaseC1[*]	4	15	4	15	1.63 E+06	25.44%	35.5%
CaseC2[*]	4	15	4	15	1.44 E+06	22.45%	19.5%

Note: * The difference between CaseC, CaseC1 and CaseC2 is the phase difference between surge and heave motion. In CaseC there is no phase difference, while in CaseC1 and Case2 the phase difference is around 90 degree and 180 degree respectively.

It can be seen from Table 3-6 that

1) The effect of superimposed heave WF motion on mooring line damping is similar as that of superimposed surge WF motion for the given mooring configurations;

2) Under the combination of superimposed surge and heave WF motions, the mooring line damping will increase when compared to that under single superimposed WF motion. The magnitude of increase will depend on the phase difference between the surge and heave WF motions.

The cause of superimposed WF motions giving rise to the increase of LF damping has been investigated by Huse and Matsumoto (1988). For an LF motion $V_{LF} = V_{LFo} \cos(\omega_{LF} t)$ and an WF motion $V_{WF} = V_{WFo} \cos(\omega_{WF} t + \varphi_W)$, the energy dissipation under cases with LF motion only and with the superimposed WF motion can be simply expressed by

$$E_o = \int_0^T F_{Do} \cdot V_{LF} \cdot dt \qquad \text{Eq. 3-6}$$

$$E_m = \int_0^T F_{Dm} \cdot V_{LF} \cdot dt \qquad \text{Eq. 3-7}$$

where $F_{Do} = \frac{1}{2} \rho D C_D V_{LF}(t) |V_{LF}(t)|$, $F_{Dm} = \frac{1}{2} \rho D C_D [V_{LF}(t) + V_{WF}(t)] |V_{LF}(t) + V_{WF}(t)|$.

Replacing the F_{Do} and F_{Dm} in Eq. 3-10 and Eq. 3-11, it yields:

$$E_o = \frac{1}{2} \rho D C_D V_{LFo}^3 \int_0^T \cos^2(\omega_{LF} t) |\cos(\omega_{LF} t)| \cdot dt \qquad \text{Eq. 3-8}$$

$$E_m = \frac{1}{2} \rho D C_D V_{LFo}^3 \int_0^T U_1 |U_1| \cos(\omega_{LF} t) \cdot dt \qquad \text{Eq. 3-9}$$

where, $U_1 = \cos(\omega_{LF} t) + \frac{V_{WFo}}{V_{LFo}} \cos(\omega_{WF} t + \varphi_W)$.

It can be shown by numerical integration that the ratio of E_m / E_o will be always larger than one. Although it was found that the relative velocity form of Morison's

equation could numerically overestimate the damping for certain seastates (Laya, 1980, Laya et al., 1984), the significant increase of LF damping due to superimposed WF motions, herein, which has been found by tests (Huse and Matsumoto, 1989), should be not due to the limitation of the relative velocity model.

Effect of superimposed random WF motions

When considering the effect of superimposed WF motions on the mooring line damping, only sinusoidal WF motions are considered in previous literature. However, the most common situation is that random WF motions exist in reality. The random effect could be different from the sinusoidal effect. For instance, Longoria et al. (1991) did some studies about the hydrodynamic coefficients of a cylinder under random oscillatory flows. It was found that the random flow values of C_D and C_M differ from the sinusoidal flow values by more than 30% to 40% in the inertia/drag regime of KC (normally $8 < KC < 25$). They concluded that the formation of shed vortex pairs is disrupted in random flow by the irregular fluid motion. The cycle-by-cycle shedding and pairing of vortices in sinusoidal flow that leads to the characteristic C_D and C_M curves reported in literature are not dominant under random flows.

Here, it is still assumed that the hydrodynamic drag coefficients are constant values (C_D, 1.2 for wire, 1.1 for chain with respect to drag diameter) when the effect of random WF motions on mooring line damping is investigated. The random WF motions are obtained under the wave environment of a typical 100-year hurricane mentioned above. The translational WF motions $\vec{\xi}^{OT}$ at the turret origin (x, y, z) can be determined by the translational motions $\vec{\xi}^{OG}$ at the origin of the global coordinate system and the angular motions $\vec{\Omega}$ as follows:

$$\vec{\xi}^{OT}(x, y, z) = \vec{\xi}^{OG}(0,0,0) + \vec{\Omega} \times \vec{r} \qquad \text{Eq. 3-10}$$

where, $\vec{\xi} = (\xi_1, \xi_2, \xi_3), \vec{\Omega} = (\xi_4, \xi_5, \xi_6), \vec{r} = (x, y, z)$;

The surge WF motion normally has only a small difference at the global origin and the turret, so the time history of random surge WF motion can be obtained by Fourier transform from the surge response spectrum as shown in Figure 3-14. Special attention should be paid to the random heave WF motions, because unlike the surge WF motions, the heave WF motions at global origin and the turret will be quite different mainly due to the pitch effect. The random heave WF motions at turret origin will be calculated according to the formula (Eq. 3-10) when considering the effect of random heave WF motions on mooring line damping.

For the random surge WF motions, a three-hour time history (see Figure 3-17) is first considered and the energy dissipation of moorings will be calculated for each period of the given LF motion.
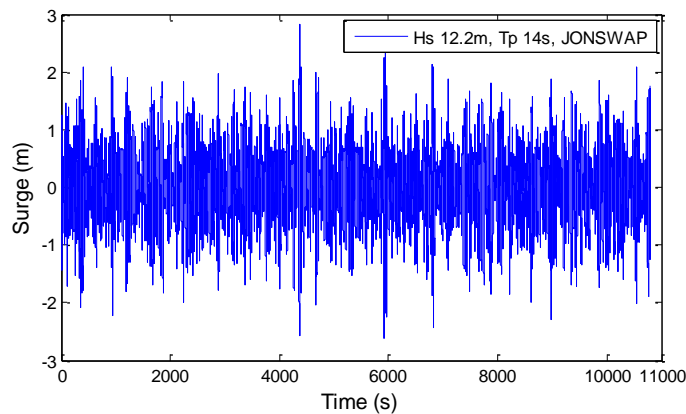
Figure 3-17 Time history of random surge WF motion of the FPSO

To compare with the effect of random surge WF motions, an equivalent harmonic WF motion is defined by the standard deviation σ and the zero-crossing period T_{zr} of the random WF motions. The amplitude of the equivalent harmonic WF motion is equal to $\sqrt{2}\sigma$, while the period is equal to the T_{zr}.

$$\sigma = \sqrt{\int_0^\infty S_{rr}(\omega)d\omega} \qquad \text{Eq. 3-11}$$

$$T_{zr} = \sqrt{\int_0^\infty S_{rr}(\omega)d\omega / \int_0^\infty \omega^2 \cdot S_{rr}(\omega)d\omega} \qquad \text{Eq. 3-12}$$

The standard deviation σ of the random surge WF motion is 0.68m, and the zero-crossing period T_{zr} is 15.5s. Hence, the equivalent harmonic motion is defined as $x_{hr} = 0.96 \cdot \sin(2\pi \cdot t / 15.5)$. The comparison of time histories of these two motions during 7000-7200s is shown in Figure 3-18.
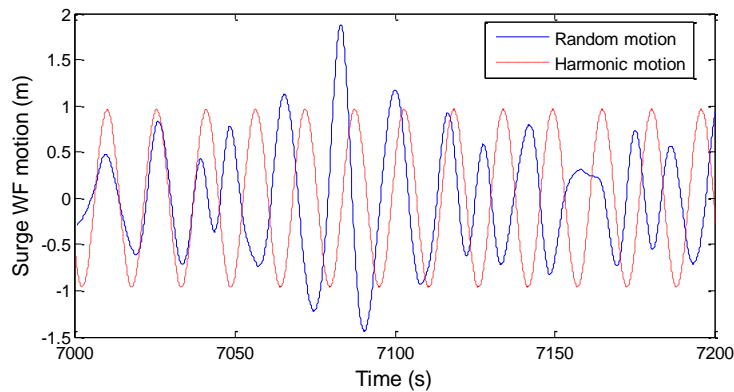
Figure 3-18 Comparison of time histories of random and equivalent harmonic WF motions

Two slow drift motions with amplitude of 15m and 34m respectively are assumed, while their periods are still selected as 149.6s. Considering the uncertainty of superimposed random WF motions, the energy dissipation of moorings during each period of LF motion will be different. In Figure 3-19, the scatter of damping ratio of moorings is illustrated for the LF motion with amplitude of 34m during the last 60 periods. To compare with the case under superimposed harmonic WF motion, the energy dissipation of moorings per LF period with the superimposed random WF motion is averaged over cycles of LF motion during the 3 hours simulation. The mean energy dissipation is then compared with that obtained under the superimposed equivalent harmonic WF motion.
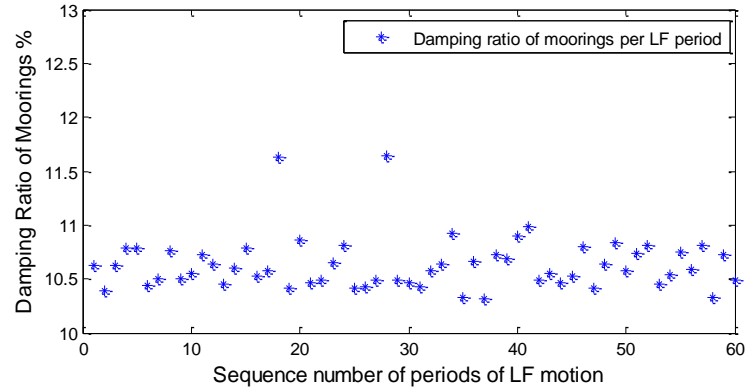
Figure 3-19 Scatter of damping ratio of moorings during last 60 LF periods

The calculated (mean) equivalent line damping and damping ratio under different cases are listed in Table 3-7.

Table 3-7 Effect of random surge WF motion on mooring line damping

Case		Random Surge WF Motion		Harmonic Surge WF motion		c $(N \cdot s/m)$	Damping Ratio ζ
		$\sigma(m)$	$T_{zr}(s)$	$A_w(m)$	$T_w(s)$		
$A_{LF} = 34m$	Random	0.68	15.5	-	-	6.83E+05	10.64%
	Harmonic	-	-	0.96	15.5	6.84E+05	10.65%
$A_{LF} = 15m$	Random	0.68	15.5	-	-	3.39E+05	5.29%
	Harmonic	-	-	0.96	15.5	3.38E+05	5.27%

It can be seen from Figure 3-19 and Table 3-7 that

1) Under the random surge WF motions, the damping of moorings during each cycle of LF motion will fluctuate, however, its mean value averaged by cycles is quite close to that obtained from the equivalent harmonic WF motion;

2) Considering response of the given FPSO under the hurricane environment, it seems the effect of random surge WF motions on mooring line damping becomes less important. For instance, under superimposed random surge WF motions, the damping ratio of moorings increases by 5.7% for case with $A_{LF} = 34m$ and by 29.3% for case with $A_{LF} = 15m$ when it is compared to the case under

corresponding LF motion only. This is mainly due to the small response (standard deviation) of surge motion under random waves, which can also be seen from the amplitude of the equivalent harmonic WF motion.

A three-hour time history of random heave WF motion at the turret location under a typical 100-year hurricane environment is considered as shown in Figure 3-20.
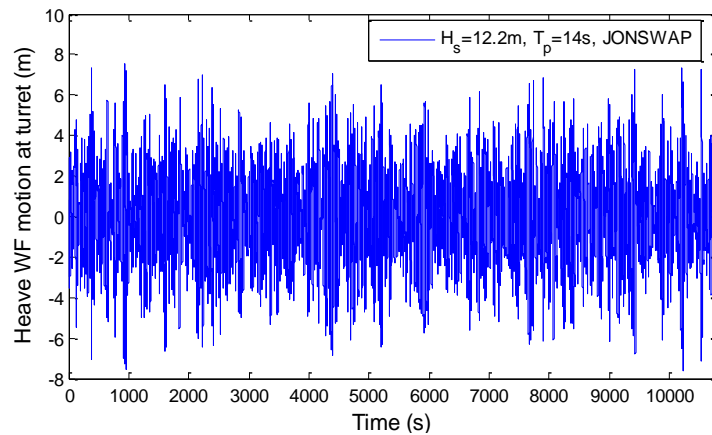
Figure 3-20 Time history of the FPSO's random heave WF motion at turret

The standard deviation σ of the random heave WF motion is 2.28m, and the zero-crossing period T_{zr} is 14.7s. Hence, the equivalent harmonic heave motion is defined as $z_{hr} = 3.22 \cdot \sin(2\pi \cdot t / 14.7)$. The comparison of time histories of these two motions during 9000-9200s is shown in Figure **3-21**.
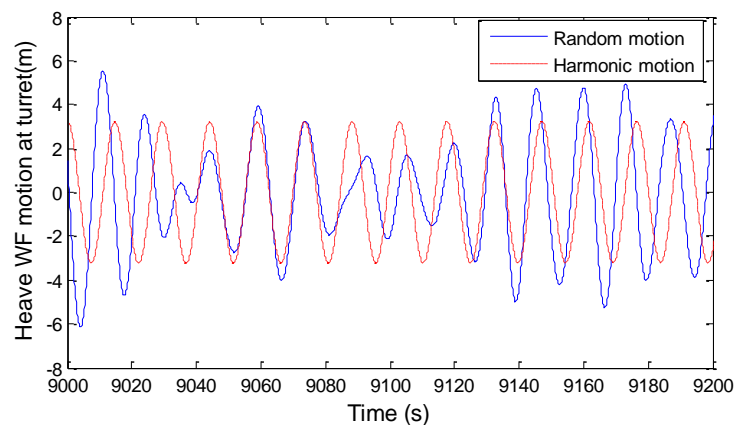
Figure 3-21 **Time histories of random and equivalent harmonic heave WF motions**

The effect of random heave WF motion on mooring line damping is considered for LF motion with amplitude of 15m. The calculated equivalent linear damping and damping ratio of moorings are listed in Table 3-8.

Table 3-8 Effect of random heave WF motion on mooring line damping

Case		Random heave WF Motion		Harmonic heave WF motion		c $(N \cdot s / m)$	Damping Ratio ζ
		$\sigma(m)$	$T_{zr}(s)$	$A_w(m)$	$T_w(s)$		
$A_{LF} = 15m$	Random	2.28	14.7	-	-	8.40E+05	13.09%
	Harmonic	-	-	3.22	14.7	8.82E+05	13.74%

It can be seen from Table 3-8 that the mean value of mooring line damping under the random heave WF motions is also quite close to that obtained from the equivalent harmonic WF motion.

So, from the statistical view, the effect of random WF motions on the mooring line damping can be represented by an equivalent harmonic WF motion. However, to be emphasized, the conclusion is made based on the assumption of same C_D values for moorings under both the random WF motions and the equivalent harmonic WF motion.

3.4 Effect of current/wave upon mooring line damping

The effect of current on mooring line damping has been considered by Webster (1995). In his study, a non-dimensional current parameter is defined as $\rho V_c^2 / 2wD_s$, which is proportional to the ratio of the hydrodynamic drag force per unit length on the reference mooring line due to the current to the weight of the mooring line in water per unit length (Webster, 1995). Three different non-dimensional current values were investigated and the results were shown in Figure 3-22. According to the results, the effect of horizontal current on the mooring line damping is negligible at low pretensions.
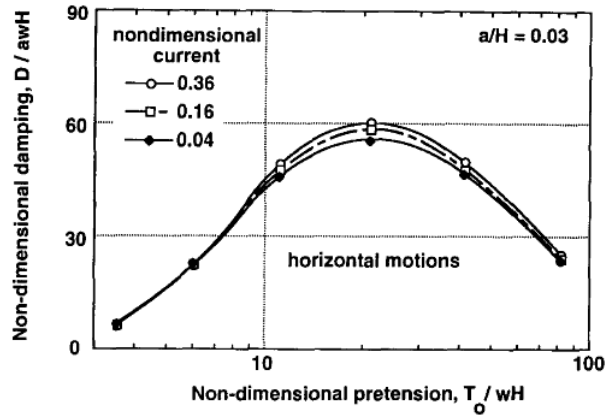
Figure 3-22 Variation of mooring line damping with current parameter (Webster, 1995)

It should be noted that in Webster's study the current velocities are quite low when compared to velocities of top motion, which could be the reason why the current has little effect on mooring line damping. Here, the effect of current upon damping of moorings is first considered for slow drift motion with amplitude of 34m. It is assumed that the slow drift motion is still symmetric around the equilibrium position and will not be affected by the current. Shear current is considered with several different surface current velocities and the profile of current along the water depth is shown in Figure 3-23.
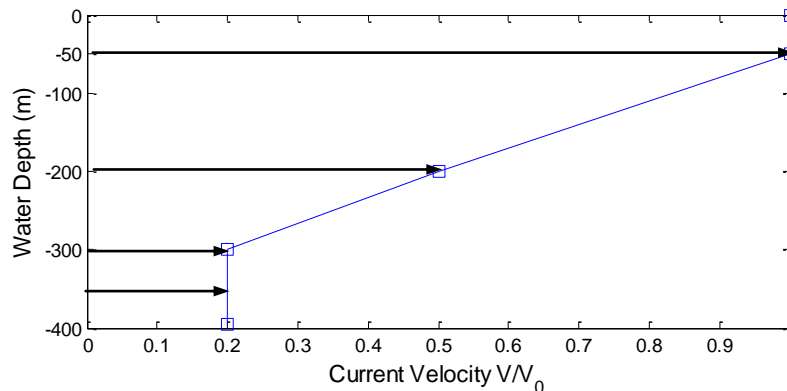
Figure 3-23 Velocity profile of shear current along the water depth

The 'Indicator diagrams' under different currents are plotted in Figure 3-24. When the system moves against the current direction, the total horizontal connection force at the turret will increase clearly. The increase of the horizontal force is mainly due to the change of departure angles of moorings due to the current drag effect.
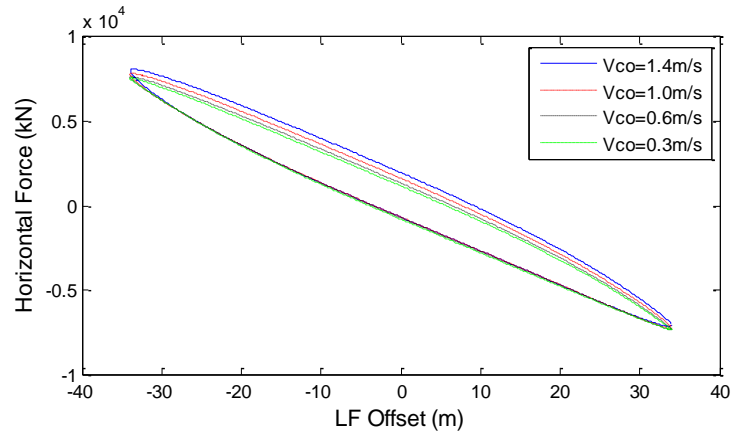
Figure 3-24 'Indicator diagrams' under different velocities of surface current

The calculation results of damping of moorings are listed in Table 3-9. It can be seen that due to the existence of current the mooring line damping increases. When the surface current velocity is small, the effect on the mooring line damping is insignificant. However, with the increase of surface current velocity, the effect of current on mooring line damping becomes important.

Table 3-9 Effect of current on damping of moorings under LF motion ($A_{LF} = 34m$)

V_{C0} (m/s)	c $(N \cdot s/m)$	Damping ratio	increased by
0	6.46E+05	10.07%	-
0.3	6.62E+05	10.31%	2.4%
0.6	7.05E+05	10.99%	9.1%
1.0	8.05E+05	12.53%	24.5%
1.4	9.38E+05	14.61%	45.1%

As mentioned before, the importance of current effect on mooring line damping could depend on the relationship between current velocity and line moving velocity. Several LF motions with different amplitudes but same period (149.6s) are further included to study the ocean current effect on damping of moorings. From Figure 3-25 it can be seen that for the LF motion with small amplitude, which means the velocity amplitude is also small, the effect of current on mooring line damping is more significant. The rate of increase of damping ratio of mooring line also increases as the current velocity increases.
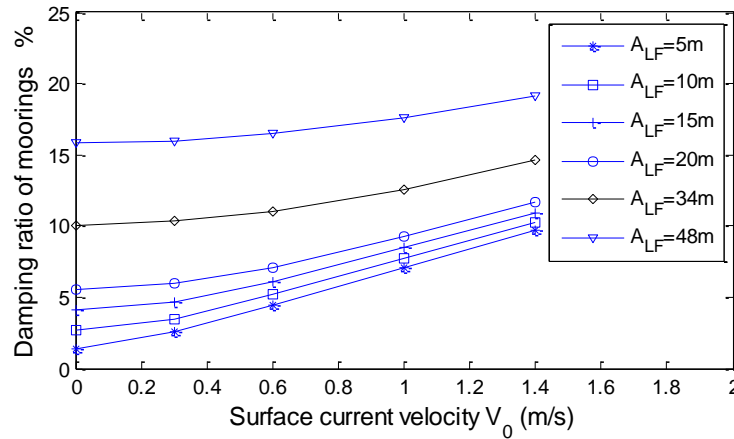
Figure 3-25 Effect of current on damping of moorings under LF motions

Taking surface current velocity as $1.0 m/s$, the current effect on mooring line damping is considered for the case with superimposed WF motion. The selected surge WF motion is with amplitude equal to $4m$ and a period of $15 s$ and the LF motion has the amplitude of $34m$. It is found that the effect of current on mooring line damping becomes less important for the case with superimposed WF motion when compared to that with LF motion only, as shown in Figure 3-26.
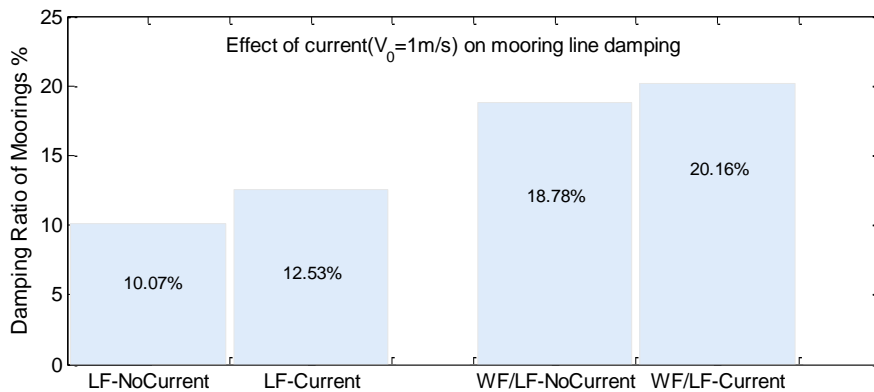
Figure 3-26 Effect of current on mooring line damping under different cases

The wave has an important effect upon the mooring line damping mainly by causing the WF motions of the floating structure and hence this effect is indirect. Here first ignoring this indirect effect, the direct influence of wave upon damping of moorings is studied. Assume the amplitude of LF motion of the FPSO system is 34m, two different wave situations are considered and the calculated mooring line damping

presented in Table 3-10 shows that the direct influence of wave on damping of moorings is negligible.

Table 3-10 Effect of different waves on damping of moorings under LF motion

Case	c $(N \cdot s / m)$	Damping Ratio	variation by
No Wave	6.46E+05	10.07%	-
Airy Wave $H = 7m, T = 8s$	6.64E+05	10.34%	3.09%
JONSWAP $H_s = 7m, T_z = 8s$	6.52E+05	10.16%	1.30%

3.5 Effect of mean offset on mooring line damping

As is known, under the effects of a mean current and wind force and mean wave drift force, the moored FPSO system will have a mean offset. The mean offset will make some of the mooring lines become a little tighter while some of the mooring lines become looser, which can be taken as the change of pretensions of the mooring lines. From the study of Webster (1995) it can be seen that for a single mooring line with the increase of pretension, the damping will increase under the same motion before the transition point appears (see Figure 2-8). For the whole mooring system, investigation needs to be made about the effect of mean offset, which will not only increase the pretensions of some lines but also will decrease the pretensions of some lines.

The assertion that the mean offset wouldn't affect the damping is studied by considering different mean offsets of the turret. Taking the slow drift motion ($A_{LF} = 34m$) with current surface velocity $V_{C0} = 1.0m / s$ for instance, the damping ratio of moorings is calculated for cases with 10m and 34m mean offsets respectively. For the case with 10m-mean-offset, it is found the damping ratio (12.99%) only increases by 3.7% when compared with the corresponding case without mean offset

(12.53%). However, for the case with 34m-mean-offset, the damping ratio is 19.03%, which increases by 51.9% compared to the case without mean offset.

The effect of superimposed WF motion on mooring line damping is re-checked with mean-offset taken into consideration. Case01 in Table 3-5 is selected as base case and 10m and 34m mean offsets are added respectively to the base case. It is found that for the case with 10m-mean-offset, the damping ratio (16.57%) only increases by 5.1% when compared to Case01. However, for case with 34m-mean-offset, an increase of 64.6% of damping ratio (25.95%) is achieved when compared to Case01.

3.6 Line tension and damping of mooring line

Damping of mooring line can reduce the LF surge motion of the moored FPSO system, consequently the related LF part of line tension. So, it seems desirable to increase the mooring line damping. However, the increase of damping of a mooring line normally means the increase of drag force, which could increase the dynamic tension. The variation of total line tension will depend on the proportion of static and dynamic tensions. An investigation of the relationship between line tension and damping of a single mooring line is attempted. The single mooring line13 is selected and its layout is shown in Figure 3-27.
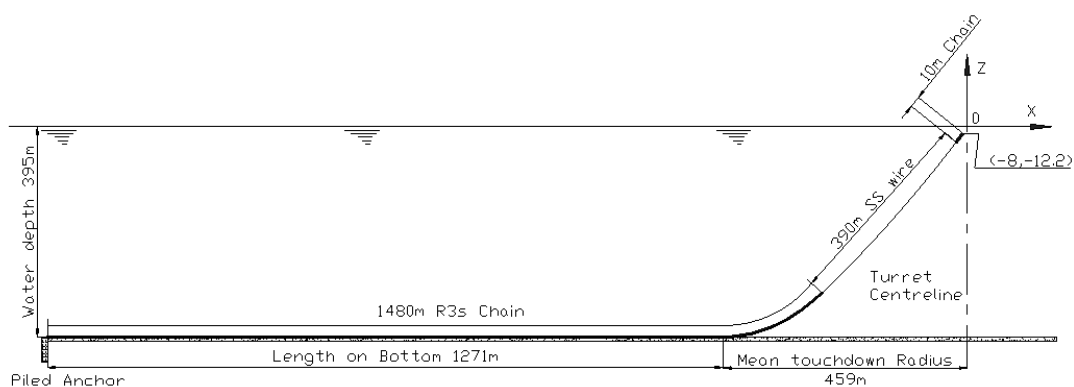
Figure 3-27 Configuration and layout of line13

3.6.1 Effect of superimposed WF motion on line tension

It is known the superimposed WF motions will increase the mooring line damping. The effect of superimposed WF motions on line tension is studied by comparison of top tensions of a single mooring line under LF motion only and under superimposed WF motion. The sinusoidal LF motion with 34m amplitude and period of 149.6s is selected, while the same-phase sinusoidal WF motion has an amplitude of 4m and period of 15s. The drag coefficients for chain and wire are 1.1 and 1.2 respectively with respect to the drag diameter. The added mass coefficients for chain and wire are both set as 1.0. Through time-domain dynamic analysis, the time histories of top tensions under these two different cases are shown in Figure 3-28. It can be seen that with the superimposed WF motion the maximum line tension will increase. The maximum dynamic component of line tension will occur around the period that line is most stretched.
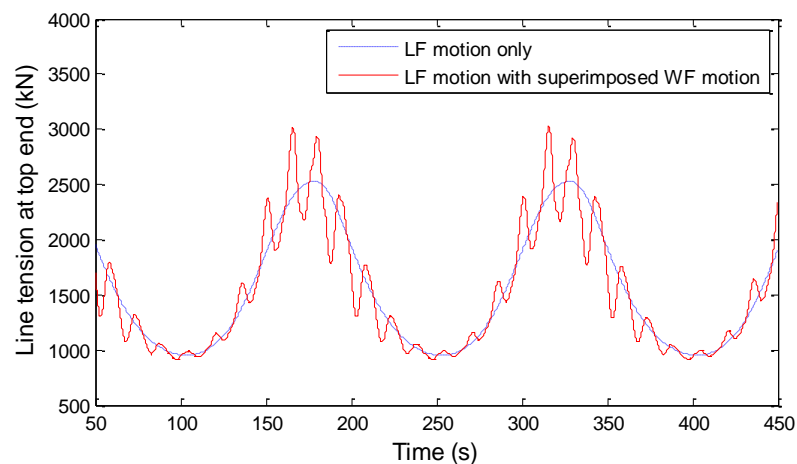
Figure 3-28 Time histories of top-end line tension under different motions

To study the dynamic component of line tension, the comparisons of tensions obtained from quasi-static analysis and dynamic analysis are completed by plotting the offset and corresponding maximum line tension, as shown in Figure 3-29. For the case with superimposed WF motion, the offset is the combination of LF and WF motions.
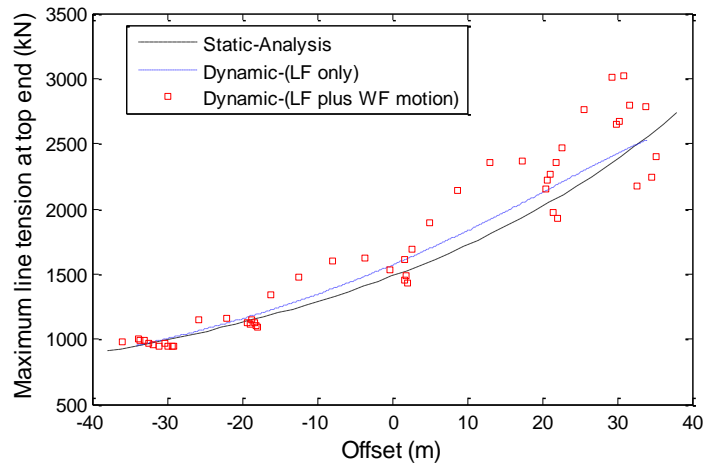
Figure 3-29 Maximum line tension of a single line (line13) at different offsets

It can be seen from Figure 3-29 that:

1) For the case with LF motion only, at the same peak offset the maximum line tensions are the same for static and dynamic methods, while at other offsets the maximum line tensions obtained by dynamic analysis are slightly bigger than those from quasi-static analysis. This is mainly due to the drag force which makes the departure angle larger when the line moves along the line lay-azimuth direction;

2) For the case with superimposed WF motion, at some offsets the maximum line tensions from dynamic analysis are much bigger than those from static method.

With superimposed WF motion, the peak line tension can occur before the top-end of the line reaches the peak offset. The dynamic component of line tension could be considerable when superimposed WF motions are exerted on the top-end of line and the quasi-static analysis would fail to predict the peak line tension.

3.6.2 Drag force vs. inertia force

The top line tension of mooring line mainly consists of two parts, namely static tension (catenary tension) and dynamic tension. The dynamic tension is usually

caused by the drag force and inertia force, which are due to both top motion and environmental loads such as current and waves. Drag force is related to the velocity while inertia force, which includes physical inertia due to its own mass and an inertia force in phase with the local flow acceleration, is related to the acceleration. Due to the relationship between velocity and acceleration, the maximum drag force and maximum inertial force can not occur simultaneously.

Papazoglou et al. (1990) argued that the main contributor to the dynamic response is the non-linear drag (damping) due to the velocity effects in the case of high frequency mooring line motion (However, line stretching (elastic stiffness) is the primary contributor for a fully lifted or taut mooring line.). However, according to the study of van den Boom (1985), the prime dynamic tension increase originated from the normal drag forces related to large global (first mode) line motions. Inertia became important at higher wave frequencies especially for steel wires and multi-component lines.

In order to figure out the contributions of drag and inertia forces to the dynamic tension, three different superimposed WF motions are considered here for the single mooring line while waves are not included. For each superimposed WF motion, two different cases are considered. The first case is that the mooring line will move in water and the second case is that the mooring line moves in air. This is achieved by setting the density of fluid as seawater density ($\rho_w = 1025 kg/m^3$) for first case and (approximately) the density of air ($\rho_a = 1.025 kg/m^3$) for second case. If the mooring line moves in air, then the dynamic tension is mainly due to the inertia force (although the added inertia force here is small, without the existence of drag force (resistance) to increase the 'impedance' of the motion, the inertial force of mooring line moving in air due to its own mass could be a little bigger than that in water), and Rayleigh damping (0.8% of critical damping) is added due to the lack of drag damping. When the mooring line moves in water both the drag force and inertia force may contribute to the dynamic tension. The static tension corresponds to the total offset at the moment when maximum tension occurs. Through the comparisons of

results (in air and in water) in Table 3-11, one could infer the main contribution to the dynamic tension when mooring line moves in water under different WF motions. At lower frequency of superimposed WF motion, the drag force is dominant in the dynamic tension, while with the increase of frequency of WF motion it seems the contribution of inertia force to dynamic tension becomes considerable.

Table 3-11 Components of line tensions under different superimposed WF motions

Line tension (kN)	LF motion (A=34m, T=149.6s)					
	WF (A=1m, T=6s)		WF (A=4m, T=10s)		WF (A=4m, T=15s)	
	Water	Air	Water	Air	Water	Air
Maximum tension	3058	3620	3529	3300	3026	2982
Static tension	2529	2892	2491	2750	2400	2828
Dynamic tension	529	728	1038	550	626	154

A more vivid study is plotted in Figure 3-30 for two different superimposed WF motions. One WF motion is with amplitude of 1m and period of 6s while the other has amplitude of 2m and period of 12s.
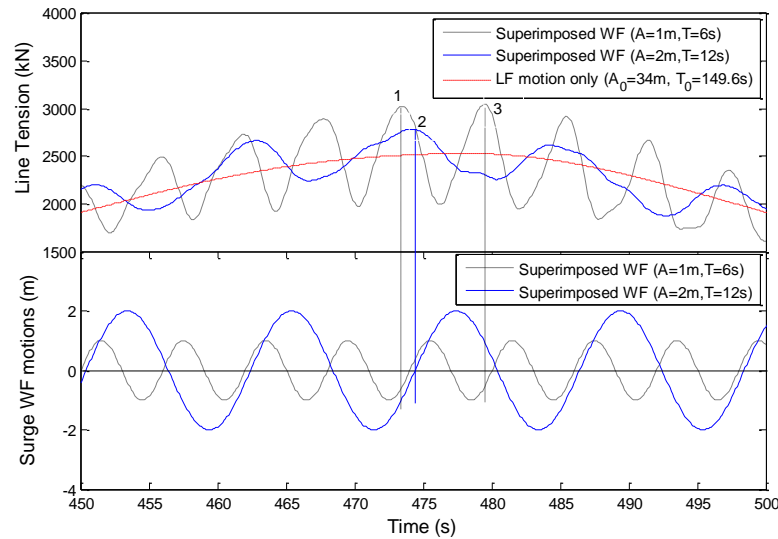
Figure 3-30 Line tensions under different superimposed WF motions

It can be seen from Figure 3-30 that when the maximum line tension occurs:

1) For the case with lower frequency WF motion, the drag force will dominate the dynamic tension (as Point2 indicated that the motion velocity reaches its peak value);

2) For the case with higher frequency WF motion, the contribution of inertia force to the dynamic tension is considerable (as Point1 and Point3 indicated that the motion has acceleration at those moments);

3) Although with same velocity amplitude, the case with higher frequency WF motion has bigger dynamic tension due to the contribution of inertia force. Occurrence of maximum line tension seems to be decided by the phase relationship of LF motion and WF motions.

3.6.3   Line tension and mooring line damping

The superimposed WF motion will increase the mooring line damping as well as the dynamic tension. Its effect on maximum line tension would depend on the contribution of mooring line damping. If the mooring line damping can significantly reduce the LF motion and hence the corresponding static tension, then the maximum line tension could be reduced. Under such case it is desirable to increase the mooring line damping by increasing the drag (coefficient) even with the increased dynamic tension. It can be seen from Table 3-12 for the case with superimposed WF motion ($A = 2m, T = 12s$) together with LF motion ($A_0 = 34m, T_0 = 149.6s$), the increase of drag coefficient would increase the mooring line damping and line tension as well when the drag force is dominant in the dynamic tension.

Table 3-12 C_D effect on line tension and damping for case with lower frequency WF motion

CASE	Drag coefficient C_D		Maximum tension (kN)	Damping ratio
	chain	wire		
1	0.8	0.85	2729.7	0.74%
2	1.1	1.2	2786.4	1.00%
3	1.5	1.7	2885.5	1.33%

There is another case that with the increase of drag coefficient the mooring line damping increases while the tension decreases. Taking the superimposed WF motion ($A = 1m, T = 6s$) together with LF motion ($A_0 = 34m, T_0 = 149.6s$) for instance, the effect of drag coefficient on mooring line damping and line tension is studied. It can be seen from Table 3-13 that with increase of drag coefficients the mooring line damping increases while the maximum line tension slightly decreases. This is because that under the higher frequency WF motions the increase of drag coefficients could add the resistance to reduce the inertia force which dominates in the dynamic tension.

Table 3-13 C_D effect on line tension and damping for case with higher frequency WF motion

CASE	Drag coefficient C_D		Maximum tension (kN)	Damping ratio
	chain	wire		
1	0.8	0.85	3070.7	0.75%
2	1.1	1.2	3058.2	0.98%
3	1.5	1.7	3053.3	1.30%

3.7 Concluding remarks

In this chapter, damping of moorings for a turret-moored FPSO system is systematically studied. Assuming constant C_D values of moorings, effects of environmental loads, such as vessel motions, current and wave on the mooring line damping are investigated. The relationship between line tension and mooring line damping is also discussed. Normally an increase of mooring line damping can reduce LF line tension but increase WF line tension if the drag force is dominant in the dynamic WF tension.

The superimposed WF motions, which are selected according to the given FPSO's displacement RAOs and environments, have significant influence on mooring line damping. However, this sinignificant influence could be slightly abated here because of the use of the relative velocity form of Morison's equation, which could

overestimate the damping according to the relavant study ((Laya, 1980, Laya et al., 1984)). For the case considered in this chapter of a constant C_D value, the effect of random superimposed WF motions on damping of moorings can be represented by an equivalent harmonic WF motion.

The magnitude of mooring line damping is affected not only by LF and especially WF motions but also by mean offset and current, and thus it is questionable to model mooring line damping as simple linear damping. However, if an equivalent linear damping of moorings could be determined with a desirable accuracy, then it could be used as input in an uncoupled analysis to get time-saving results.

4. Sensitivity of damping and tension of moorings to C_D variation

4.1 Overview

In Chapter 3, when calculating the mooring line damping under different motions, it is assumed that C_D values of wire and chain are not affected by Re and *KC* numbers. In fact, the drag coefficient will vary under different motions due to the different Re and *KC* numbers. The variation of drag coefficient, which directly changes the drag force, will consequently affect damping of moorings and dynamic tension.

In this chapter, the sensitivity of mooring line damping to drag coefficient variation ΔC_D is investigated first. This is then followed by a sensitivity study of dynamic tension to the drag coefficient variation. The purpose is to know which part of a single mooring line will be more sensitive to the variations of C_D in calculating the damping of moorings and dynamic tension. Then special attention will be paid to that part and the C_D of that part will be determined by numerical methods.

4.2 Sensitivity of mooring line damping to drag coefficient variations

According to the Taylor series

$$f(x+\Delta x) = f(x) + f'(x) \cdot \Delta x + \frac{f''(x)}{2!}(\Delta x)^2 + ... \qquad \textbf{Eq. 4-1}$$

if considering the small variation Δx, then second order and higher order of Δx can be neglected, then:

$$f(x + \Delta x) = f(x) + f'(x) \cdot \Delta x \qquad \textbf{Eq. 4-2}$$

Similarly, taking energy dissipation of moorings due to the small drag coefficient variation ΔC_D, then:

$$E(C_D + \Delta C_D) = E(C_D) + E'(C_D) \cdot \Delta C_D \qquad \textbf{Eq. 4-3}$$

where, $E(C_D)$ is base energy dissipation; $E(C_D + \Delta C_D)$ is the new energy dissipation due to the drag coefficient variation.

The sensitivity of energy dissipation to drag coefficient variation can be calculated by

$$E'(C_D) = \frac{E(C_D + \Delta C_D) - E(C_D)}{\Delta C_D} = \frac{\Delta E(C_D)}{\Delta C_D} \qquad \textbf{Eq. 4-4}$$

Line13 of the FPSO mooring system, as illustrated in Figure 3-27, is selected as a line of base case. For this base case, the drag coefficients of chain and wire are constant (C_D=1.1 for chain (drag diameter 2.10 D); C_D=1.2 for wire). As mentioned above, small variation of drag coefficient is preferred, so the drag coefficient variations are from 1.1 to 1.3 for chain and from 1.2 to 1.4 for wire.

In order to know the sensitivity of mooring line damping to the C_D variation along the whole catenary line, the chain-wire-chain line will be divided into many segments with same length (10m per segment here). In each new case the change of C_D for only one segment will be made when compared to the base case. The energy dissipation variation $\Delta E(C_D)$ of each new case compared to the base case is calculated. The sensitivity of energy dissipation of the corresponding segment can be obtained by division of the energy dissipation variation by the drag coefficient variation, as shown in Eq. 4-4.

The sensitivity of mooring line damping to drag coefficient variation can be easily obtained after the calculation of energy dissipation variation $\Delta E(C_D)$. For example, if the damping ratio ζ is taken as evaluation parameter, considering the Eq. 3-4 and Eq. 3-5 for a sinusoidal motion, then:

$$\zeta'(C_D) = \frac{E'(C_D)}{\omega \pi A_{LF}^2 \cdot C_c} \qquad \textbf{Eq. 4-5}$$

where, $\zeta'(C_D)$ is sensitivity of damping ratio of a small segment of mooring line due to C_D variation ; ω is circular frequency of slow drift motion; A_{LF} is amplitude of slow drift motion; C_c is critical damping of the moored FPSO system.

In order to have a direct understanding about the sensitivity of mooring line damping of a small segment due to C_D variation, a relative value r_E can be considered:

$$r_E = \frac{E'(C_D)}{E(C_D)} \times 100\% = \frac{\zeta'(C_D)}{\zeta(C_D)} \times 100\% \qquad \textbf{Eq. 4-6}$$

Different top motions of line are considered in order to consider the influence of FPSO motions, as illustrated in Table 4-1.

Table 4-1 Different base cases with respect to different top motions

| Base Case | Drag coefficient | | Surge motion | | | | Heave motion | |
| | Chain | Wire | LF | | WF | | WF | |
			A_{LF}/H	$T(s)$	$A_{WF}(m)$	$T(s)$	$A_{WF}(m)$	$T(s)$
1	1.1	1.2	5%	149.6	/	/	/	/
2	1.1	1.2	10%	149.6	/	/	/	/
3	1.1	1.2	10%	149.6	4	10	/	/
4	1.1	1.2	10%	149.6	4	15	/	/
5	1.1	1.2	10%	149.6	1	6	/	/
6	1.1	1.2	10%	149.6	/	/	4	10
7	1.1	1.2	10%	149.6	/	/	4	15
8	1.1	1.2	10%	149.6	/	/	1	6

Note: H means water depth ~400m;

For the base case1 (LF motion only), of which amplitude is equal to 5% of water depth, the relative values r_E of different segments are showed in Figure 4-1.
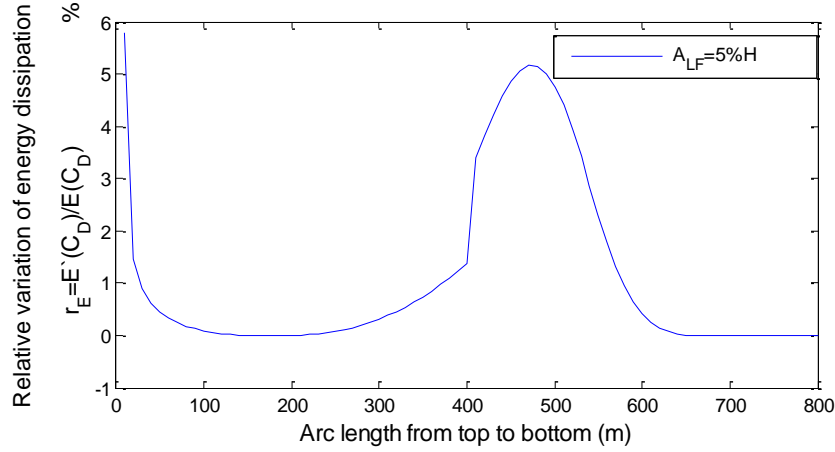
Figure 4-1 Relative values r_E of energy dissipation at different segments

From Figure 4-1, it can be seen that the top part and the part near touch down area are much more sensitive to the drag coefficient variation. At these positions for each segment with a length of 10m, unit drag coefficient variation will cause about 5% variation of the mooring line damping of base case.

Discussions

The energy dissipation of moorings moving in x-direction (surge) can be calculated by the following equation:

$$E_x = \int F_H \cdot dS = \int_t^{t+T} F_H \cdot \frac{dS}{dt} \cdot dt \qquad \textbf{Eq. 4-7}$$

where, F_H is restoring force at the turret connection in x-direction; S is slow drift motion at top end in x-direction;

F_H can be approximately taken as

$$F_H = \vec{F}_D + \vec{F}_C \qquad \textbf{Eq. 4-8}$$

where, $\vec{F}_D = \int_0^L \frac{1}{2}\rho \cdot D \cdot C_D \cdot \frac{d\tilde{S}}{dt} \cdot \left|\frac{d\tilde{S}}{dt}\right| \cdot dl$ is the drag force acting on the whole mooring

line in x-direction; $\tilde{S}$ is the motion of unit mooring line; $\vec{F}_C$ is conservative forces in

x-direction;

So, the energy dissipation of moorings is calculated as

$$
\begin{aligned}
E_x &= \int_t^{t+T}(\vec{F}_D + \vec{F}_C) \cdot \frac{dS}{dt} \cdot dt = \int_t^{t+T}\vec{F}_D \cdot \frac{dS}{dt} \cdot dt + \int_t^{t+T}\vec{F}_C \cdot \frac{dS}{dt} \cdot dt \\
&= \int_t^{t+T}\{\int_0^L \frac{1}{2}\rho \cdot D \cdot C_D \cdot \frac{d\tilde{S}}{dt} \cdot \left|\frac{d\tilde{S}}{dt}\right| \cdot dl\} \cdot \frac{dS}{dt} \cdot dt + (\sim 0) \qquad \textbf{Eq. 4-9} \\
&= \int_t^{t+T}\{\sum_{i=1}^n \frac{1}{2}\rho \cdot D \cdot C_D \cdot \frac{d\tilde{S}_i}{dt} \cdot \left|\frac{d\tilde{S}_i}{dt}\right| \cdot \Delta l_i\} \cdot \frac{dS}{dt} \cdot dt
\end{aligned}
$$

Compared with base case, each new case only has one small segment with different

C_D. So as a whole, the motion along the mooring line will be nearly the same

between base case and the new case. Then,

$$
\begin{aligned}
\Delta \hat{E}_x^j &= \hat{E}_x^j - E_{x|base} \\
&= (\hat{C}_{Dj} - C_{D|base}) \int_t^{t+T} \rho \cdot D \cdot \frac{d\tilde{S}_j}{dt} \cdot \left|\frac{d\tilde{S}_j}{dt}\right| \cdot \Delta l_j \cdot \frac{dS}{dt} \cdot dt \qquad \textbf{Eq. 4-10}
\end{aligned}
$$

Hence,

$$E'(C_{Dj}) = \frac{\Delta \hat{E}_x^j}{\hat{C}_{Dj} - C_{D|base}} = \int_t^{t+T} \rho \cdot D \cdot \frac{d\tilde{S}_j}{dt} \cdot \left|\frac{d\tilde{S}_j}{dt}\right| \cdot \Delta l_j \cdot \frac{dS}{dt} \cdot dt \qquad \textbf{Eq. 4-11}$$

where, script j means the j case (C_D variation on j segment); Δl_j means the

length of j segment.

From the equation above, it can be seen that $E'(C_{Dj})$, the sensitivity of energy dissipation to drag coefficient C_D variation of j segment, is related to the length of j segment Δl_j, the velocity of that segment $\left| d\tilde{S}_j / dt \right|$ and the diameter D of that segment. Different $E'(C_{Dj})$ of different segments, to some extent, will reflect the differences of those three parameters. For example, as illustrated in Figure 4-2, it can be seen that the range graph of normal relative velocity of the line has large values at top end and touch down areas, which is a similar conclusion to the relative values r_E along the mooring line.
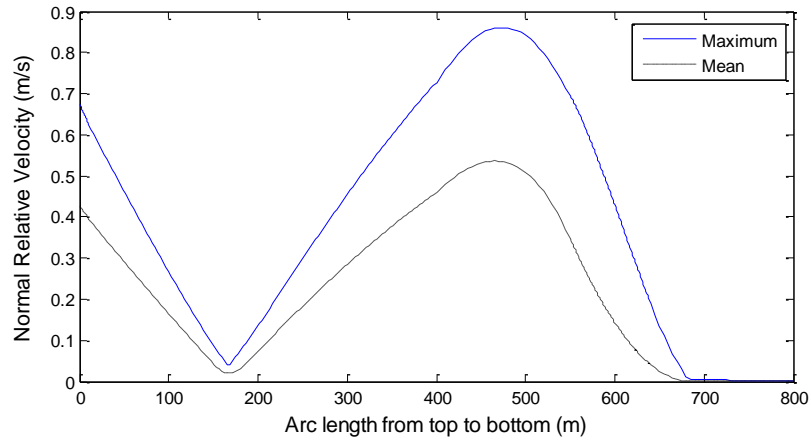
Figure 4-2 Range graph of normal relative velocity along the line

4.2.1 Effect of amplitude of LF motions

Here, another LF motion with amplitude equal to 10% of water depth is included in order to consider the effect of amplitudes of LF motion.
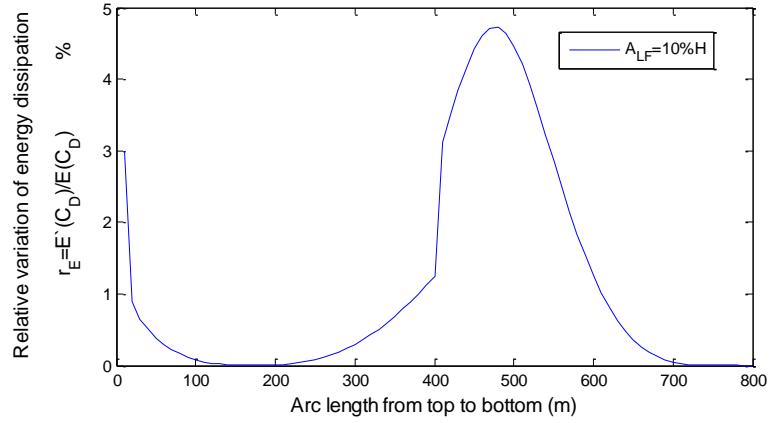
Figure 4-3 Relative values r_E of energy dissipation at different segments

From Figure 4-1 and Figure 4-3, it can be seen that:

1) Under this large amplitude ($A_{LF} = 10\% H$), the maximum relative values r_E along the arc length appears at the touch down area, while for the case with $A_{LF} = 5\% H$, the maximum r_E appears at the top end;

2) The relative values r_E become smaller under the case with $A_{LF} = 10\% H$ when compared to those under the case with $A_{LF} = 5\% H$. However, it should be noted that the energy dissipation variations under the case with $A_{LF} = 10\% H$ are bigger than those under the case with $A_{LF} = 5\% H$, as illustrated in Figure 4-4.
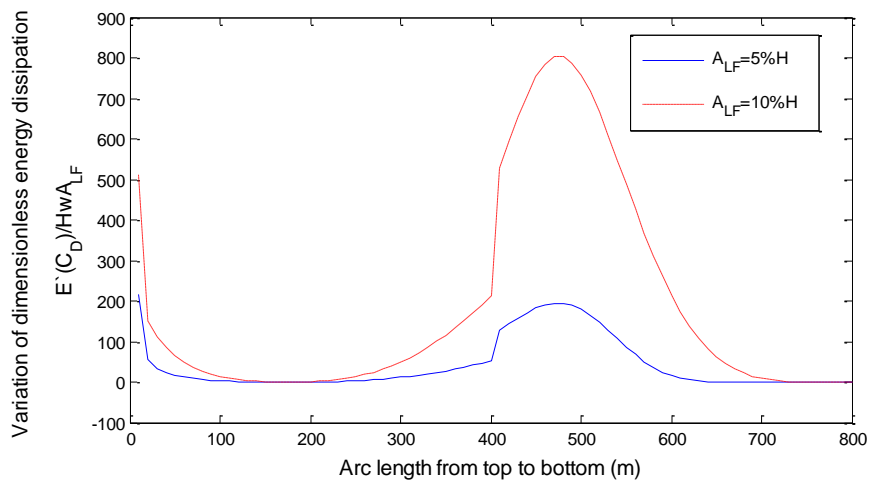
Figure 4-4 Comparisons of dimensionless energy dissipation variation along the line

Because the energy dissipations are different for the two base cases with different amplitudes of LF motion, the relative value r_E , which is equal to the energy dissipation variation dividing by energy dissipation of base case, can not be compared between the cases with different amplitudes.

4.2.2 Effect of surge WF motions with different amplitudes and frequencies

Here, three different superimposed surge WF motions are considered on the base of LF motion with amplitude $A_{LF} = 10\% H$. The related amplitude and frequency are listed in Table 4-1. The comparisons of energy dissipation variations under three different WF motions are shown in Figure 4-5.
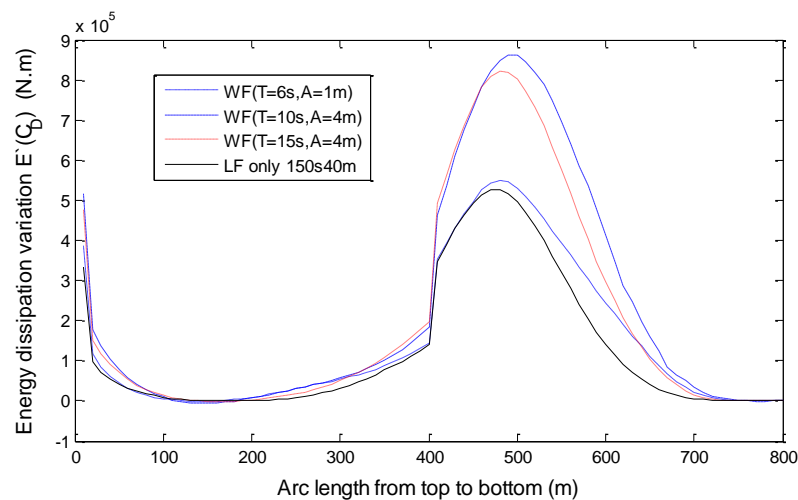
Figure 4-5 Comparison of energy dissipation variations under superimposed surge WF motions

From Figure 4-5, it can be seen that

1) Compared with the situation with LF motion only, for the cases with superposed WF motions, the energy dissipation becomes more sensitive to drag coefficient variation, especially at the touch down area;

2) Not only the amplitude but also the frequency of WF motion will affect the energy dissipation variations.

In Figure 4-6, the relative values r_E of energy dissipation under these three different WF motions are illustrated.
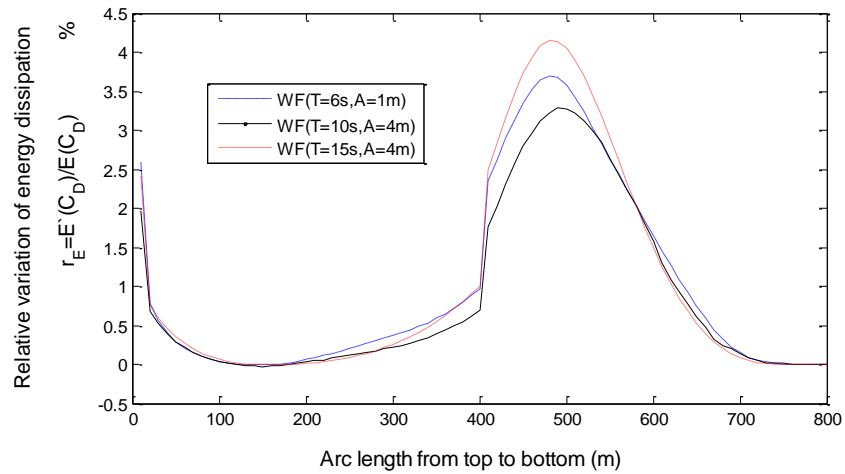
Figure 4-6 Relative values r_E of energy dissipation under three different WF motions

However, as mentioned before, relative value r_E is the ratio of energy dissipation variation to the energy dissipation of the base case. Because the energy dissipations of the base cases are different under the three WF motions, which are illustrated in Table 4-2, comparisons of r_E under those WF motions fail to reflect the relative importance of different WF motions' effects on the sensitivity of energy dissipation.

Table 4-2 Energy dissipation of different base cases (Line13)

Base cases	Energy dissipation ($N \cdot m$)	Damping ratio
LF motion only ($A = 40m, T = 149.6s$)	1.12E+07	0.85%
Superposed surge WF motion ($A = 4m, T = 10s$)	2.63E+07	1.99%
Superposed surge WF motion ($A = 4m, T = 15s$)	1.98E+07	1.50%
Superposed surge HF motion ($A = 1m, T = 6s$)	1.49E+07	1.13%

4.2.3 Surge WF motion vs. heave WF motion

Above, only the superimposed surge WF motions are considered. However, along with the slow drift motion, the heave motion of wave frequency is also very common for a moored FPSO system, so three different WF heave motions are considered here. The related amplitude and frequency are the same as those of WF surge motion. The energy dissipation variations under three superimposed WF heave motions are shown in Figure 4-7.
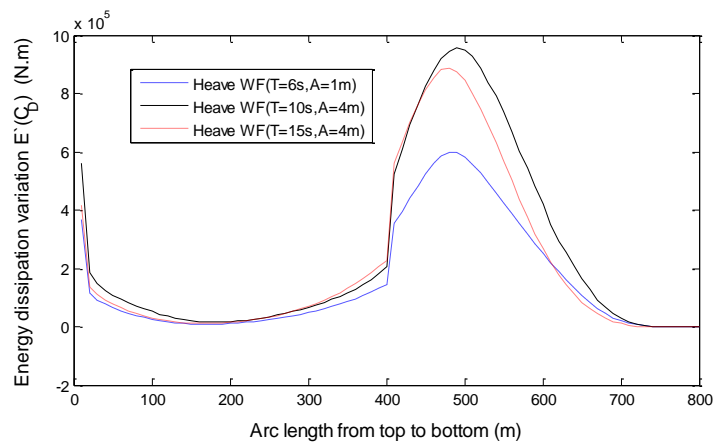
Figure 4-7 Energy dissipation variations under superposed heave WF motions

From Figure 4-7, it can be seen energy dissipation variations under superimposed heave WF motions have the similar tendency to those under superimposed surge WF motion. At top end and touch down areas of the mooring line, energy dissipation variations due to C_D variation are comparatively big.

One thing to be noted is that the energy dissipation (variation) under superposed heave WF motion here is bigger than that under corresponding superposed surge WF motion (see Figure 4-8 and Table 4-3). However, according to Webster (1995), if the pretension becomes bigger, then more energy will be dissipated by surge WF motion than by heave WF motion.
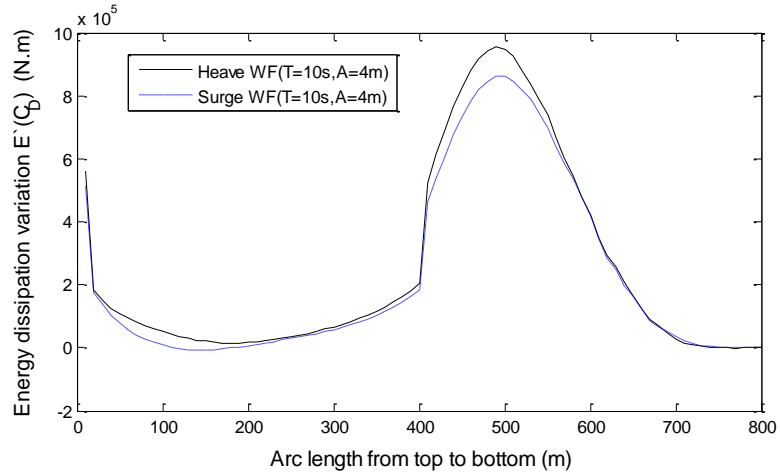
Figure 4-8 Energy dissipation variations under superimposed heave/surge WF motions

Table 4-3 Energy dissipation of different base cases (line13)

Base cases	Energy dissipation ($N \cdot m$)	Damping ratio
Superposed heave WF motion ($A = 4m, T = 10s$)	2.82 E+07	2.13%
Superposed surge WF motion ($A = 4m, T = 10s$)	2.63 E+07	1.99%

4.3 Sensitivity of line tension to drag coefficient variations

As mentioned before, increasing the mooring line damping is desirable while attention also needs to be paid to the increased dynamic tension. Here, the dynamic tension variation due to the drag coefficient variation is also investigated.

Through the calculations, it is seen that, for base case and the new cases with C_D variation, the maximum tension of each case appears at the same moment with same motion. At that moment, the static tension due to the offset is the same for all the cases. Then compared to the maximum tension of base case, the maximum tension variations are due to the drag force variations caused by the C_D variations. So the dynamic tension variation here can be measured according to the maximum tension variation:

$$T'(C_D) = \frac{T(C_D + \Delta C_D) - T(C_D)}{\Delta C_D} \qquad \textbf{Eq. 4-12}$$

Different heave/surge WF motions, including different amplitudes and frequencies, are considered. Their effects on the maximum tension variation due to drag coefficient variation are also compared, as illustrated in Figure 4-9 and Figure 4-10.
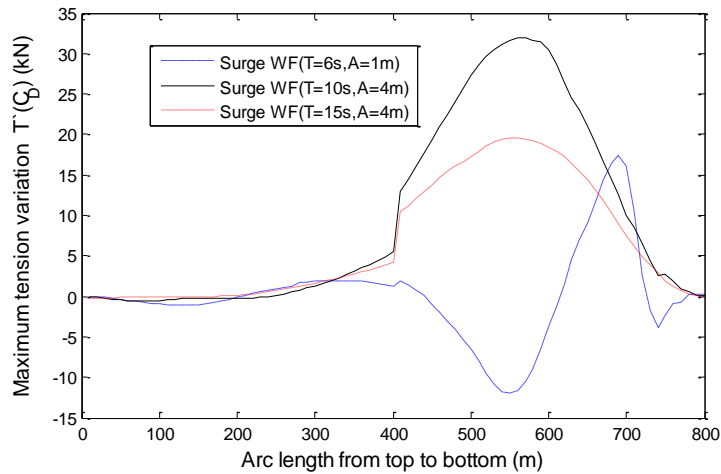
Figure 4-9 Maximum tension variations under different surge WF motions
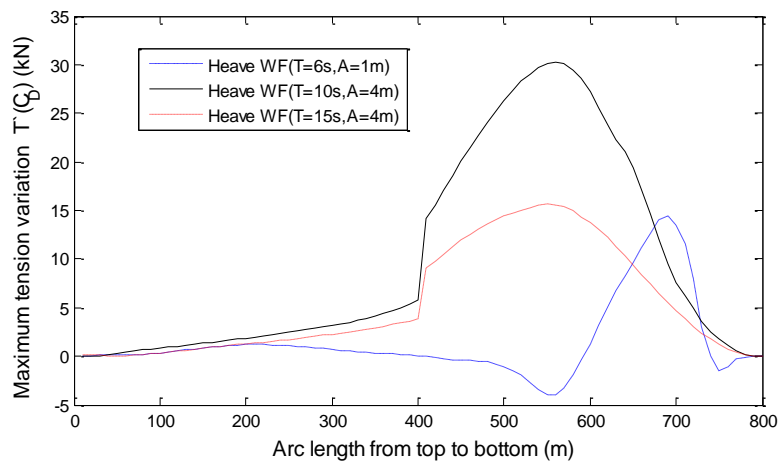
Figure 4-10 Maximum tension variations under different heave WF motions

From Figure 4-9 and Figure 4-10, it can be seen that:

1) Maximum tension variation due to C_D variation could be negative or positive, where the negative value means the maximum tension would decrease with the

increased C_D variation. Especially for the WF motion with higher frequency, such as the motion with period equal to 6s, the maximum tension variation would show more obvious fluctuation along the line;

2) Similar as the energy dissipation variation, maximum tension variation around the touch down area is most sensitive to the C_D variation.

One thing to be noted is that maximum tension variation to normal C_D variation is quite small at the top of the mooring line, which is different from the energy dissipation variation. This could be used to increase damping whilst avoiding an increase of line tension.

4.4 Concluding summary

In this chapter, the effect of drag coefficient variation upon damping of mooring line (energy dissipation) and dynamic tension is studied. Different WF motions, including different amplitudes and frequencies are considered. Through the study, it can be seen that:

1) For the energy dissipation variations due to normal C_D variations, the most sensitive parts along the line are at the top and touch down area; both parts are usually composed of chain for a chain-wire combination line. This also indicates the importance of determining the drag coefficients of chain;

2) The tendency of maximum tension variations due to C_D variations is somewhat similar to that of energy dissipation variations due to C_D variations. However, two differences need to be noted. One is that the sensitivity of maximum tension variations due to normal C_D variations at the mooring top is not high but low. The other is that under higher frequency WF motion, the maximum tension variations due to normal C_D variations in the touch down area show dramatic fluctuation.

5. CFD model validations- a circular cylinder under different flows

5.1 Overview

As can be seen from the critical review, experimental methods have many limitations in determining the drag coefficients of chain. As the development of high performance computers and CFD techniques, CFD methods have become more and more popular. Ongoing research yields software that improves the accuracy and speed of complex simulation scenarios such as transonic or turbulent flows. However, it is still a big challenge to numerically simulate chain under various flows and obtain the corresponding drag coefficients. Especially for the purpose of engineering practice, the turbulent flows around chain are characterised by strong separation, recirculation, and unsteady vortex shedding. So before attempting to determine the drag coefficients of chain by a CFD method, an appropriate CFD model needs to be selected and validated.

The selection and validation of CFD model for flows past chains are done by the CFD simulation of a smooth circular cylinder under different flows. The reasons why a cylinder is selected are twofold: first, flow characteristics around chain and cylinder could be similar due to the shape similarity; second, as a classical problem lots of experimental data about flows past a cylinder is available, which makes the CFD model validation much easier.

Commercial software FLUENT is used here. Two different turbulent models, namely $k-\omega\ SST$ and LES are mainly considered and compared. The 3D effect of turbulence is studied by comparing the 2D and 3D models for different turbulent models.

5.2 CFD model validation1-Steady flow past a smooth circular cylinder

5.2.1 Selection of turbulence models

The complex nature of the flow past a cylinder makes it a perfect case to assess the ability of certain CFD models. Lots of numerical simulation experiments have been done in the past several decades and especially with the increase in computer power more numerical studies of this flow at higher Reynolds numbers have been conducted recently.

As mentioned in Appendix A, the wake or boundary layer of the cylinder becomes turbulent at higher Reynolds numbers and this requires a turbulence model for its simulation. There are still many open questions on modelling turbulence and properties of turbulence itself, although lots of effort has been put since the beginning of turbulence study from fifteenth century. No universal turbulence model exists yet and unfortunately one has to select a most desirable turbulent model for specific turbulence flow. An ideal model should introduce the minimum amount of complexity into the modelling equations, while capturing the essence of the relevant physics.

The $k - \omega \ \ SST$ model of the URANS approach and LES are selected here to simulate the turbulent flow around the cylinder. Menter (1994) made an extensive comparison between (i) the classic model $k - \varepsilon$; (ii) the original model $k - \omega$; (iii) the $k - \omega$, BSL model; and (iv) the $k - \omega$, SST model for various well-documented flows. The main conclusion from this inter-comparison exercise was that the model $k - \omega \ \ SST$ gave the most accurate results while the model $k - \varepsilon$ did not yield results as accurate as the other three for the tested adverse-pressure-gradient flow cases. The selection of a $k - \omega \ \ SST$ model here is due to the fact that this model is mainly for separated flows under adverse pressure gradient, which is exactly experienced by circular cylinders under steady flows. Another reason is that the URANS approach is cheaper in computing cost. It would be quite desirable for

engineering practice if results with acceptable accuracy could be obtained by this turbulence model with low computing cost.

The selection of the LES model is because of its commendable performance which can be seen from other people's work, as described in the critical review. The Smagorinsky-Lilly sub-grid scale model with Smagorinsky constant of $C_s = 0.1$ is selected to model sub-grid scale (SGS) stresses. Although LES is comparatively more expensive in computing cost, with the recent advances in computing power the LES is nearly ready and feasible for practical applications. Several Reynolds numbers in the sub-critical regime will be considered for each of the turbulence models, in order to determine how well each turbulence model captures the Reynolds number dependency of drag coefficient.

5.2.2 Near-wall treatment for turbulent flows past cylinders

Turbulent flows could be significantly affected by the presence of walls where the viscosity-affected regions have large gradients in the solution variables. Hence, successful prediction of wall bounded turbulent flows is partly determined by the accurate presentation of the near-wall region. Similarly, for turbulent flows past circular cylinders, the simulation results would also depend on the proper modelling of the near-wall region. This is especially true as the accurate calculation of the separation point of boundary layer will generally define the width of the wake which is a major contribution to the drag experienced by the cylinder. The capture of the separation point would dramatically affect the prediction the flow parameters such as drag coefficient and Strouhal number (Young and Ooi, 2004).

The law of the wall

Central issues of wall bounded flows are the forms of the mean velocity profiles and the friction laws, describing the shear stress exerted by the fluid on the wall. Close to

the wall the flow is affected by viscous effects and the mean flow velocity depends on several parameters as formulized below:

$$U = f(y, \rho, \mu, \tau_\omega)$$ Eq. 5-1

where, y is the distance from the wall; ρ is fluid density; μ is fluid viscosity; τ_ω is the wall shear stress.

By dimensional analysis it is found that:

$$u^+ = \frac{U}{u_\tau} = f(\frac{y\rho u_\tau}{\mu}) = f(y^+)$$ Eq. 5-2

where, $u_\tau = \sqrt{\tau_\omega / \rho}$ is called the friction velocity .

Formula Eq. 5-2 contains the definitions of two important dimensionless parameters, u^+ and y^+. The relationship of u^+ and y^+ is called the 'Law of the Wall', which could represent the different layers of the near-wall region as shown in Figure 5-1.
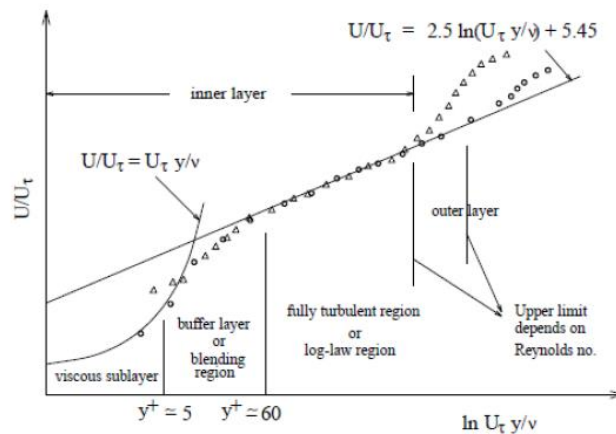
Figure 5-1 Subdivisions of the Near-Wall Region (Fluent12.1, 2010)

From Figure 5-1 it can be seen that the near-wall region consists of the inner layer and the outer layer. The inner layer (viscosity-affected region) is about 10-20% of

the total thickness of the wall layer and is composed of three zones corresponding to the wall y^+, namely the:

1) Viscous sub-layer ($y^+ < 5$): viscous stresses dominate the flow;

2) Buffer layer ($5 < y^+ < 30$): viscous and turbulent stresses are of similar magnitude;

3) Log-law layer ($y^+ > 30 \, to \, 60$): turbulent stresses dominate.

As a non-dimensional distance similar to local Reynolds number, the wall y^+ is often used in CFD to describe how fine or coarse a mesh is for a particular flow. The most desirable values of y^+ are close to the lower bound ($y^+ \approx 30$) for 'wall functions' models while less than 1 ($y^+ \leq 1$) for 'near-wall modelling' models.

Near Wall Treatment

Traditionally, in ANSYS FLUNET, there are two approaches to modelling the near-wall region, as depicted schematically in Figure 5-2. The first approach uses "wall functions", semi-empirical formulas to bridge the viscosity-affected region between the wall and the fully-turbulent region, which means the viscosity-affected inner region (viscous sub-layer and buffer layer) is not resolved. The use of wall functions obviates the need to modify the turbulence models to account for the presence of the wall, while in the second approach the turbulence models are modified to enable the viscosity-affected region to be directly resolved with a mesh all the way to the wall, including the viscous sub-layer. The second approach normally is termed as the "near-wall modelling" approach (FLUENT 12.1, 2010).
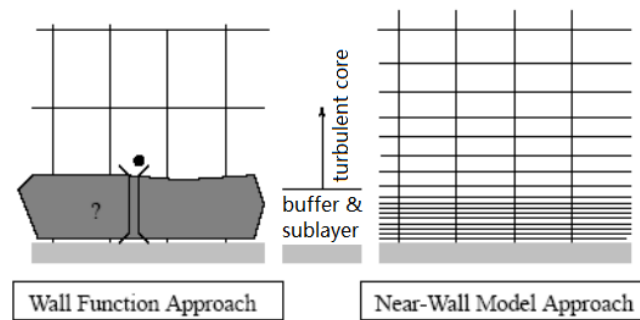
Figure 5-2 Near-Wall Treatments in FLUENT (Fluent12.1, 2010)

The wall function approach substantially saves computational resources in most high-Reynolds-number wall-bounded flows and is popular because it is economical, robust, and can be reasonably accurate. It can be a practical option for the near-wall treatments for industrial flow simulations. However, the wall function approach becomes less reliable when the flow conditions depart too much from the ideal conditions underlying the wall functions. One example of limitations of the wall function approach is for flows with severe pressure gradients leading to boundary layer separations.

One needs to carefully consider the ramification of using wall functions for the flow under separations, although wall functions together with near wall coarse mesh can be employed, often with some success, to reduce the cost of LES for wall-bounded flows (Catalano et al., 2003). Rodi (1997) questioned the validity of wall function approach for separated flows by comparing the effect of different near wall treatments on the simulation results of flows around bluff bodies. The wall function approach or a two-layer approach in which the viscous layer is resolved was adopted for the RANS models. It was found that, from results comparison, a considerable improvement can be obtained by the RANS models combined with the two-layer approach resolving the near-wall region. In his studies, the LES with wall models were also used to simulate the flow around bluff bodies and simulation results were compared with the results obtained from RANS models as well as experimental values. Overall significantly better predictions were obtained by LES methods, but

the discrepancies from the experiments still existed, which could originate from insufficient resolution near the side walls of the bluff body (Rodi, 1997).

The "near-wall modelling" approach is adopted here for the LES and $SST\ k-\omega$ models where the mesh in the boundary layer is fine enough to resolve the laminar sub-layer. To guarantee fine enough mesh in the near wall region, values of wall $y^+ \leq 1$ are much desirable.

5.2.3 Boundary conditions and computational domain

Boundary conditions

Different types of boundary conditions can be defined for different boundary locations. Taking the boundary condition at downstream for example, a 'pressure outlet' boundary condition ($P_{gauge} = 0$), defined below, can be replaced by an 'outflow' boundary condition ($\partial U / \partial \vec{n} = 0$) once the downstream boundary is far enough from the cylinder wall. The boundary conditions for the 2D and 3D simulations are shown in Figure 5-3.
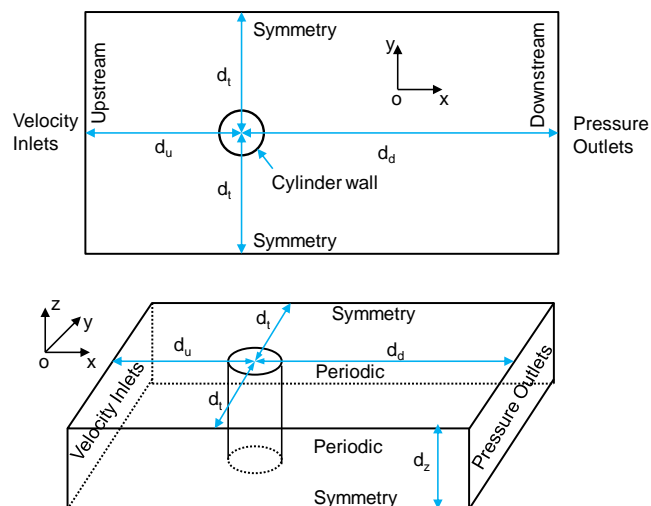
Figure 5-3 Schematic of boundary conditions and computation domain

Uniform flow with $U_x = constant$, $U_y = 0$, $U_z = 0$ (3D) at the upstream inlet is specified. Low turbulence intensity, $I = 1\%$, and a turbulent viscosity ratio $r_\mu = 1$ are assumed. The turbulence intensity is defined as $I = u'/U$, where u' is the root-mean-square of the turbulent velocity fluctuations and U is the mean velocity. The turbulent viscosity ratio, $r_\mu = \mu_t / \mu$, is the ratio between turbulent viscosity, μ_t, and the molecular dynamic viscosity, μ. The main advantage with using the turbulent viscosity ratio is that this directly says something about how strong the influence of the turbulent viscosity is compared to the molecular viscosity. A pressure outlet condition is imposed on the downstream outlet. The symmetry boundary condition is specified on lateral boundaries, which assumes that normal velocity at the boundary is zero and the scalar variable gradients normal to the boundary are also zero. For the 3D simulation, the periodic boundary condition is imposed on the top and bottom sides to model physical geometry of interest and expected flow pattern having a periodically repeating nature. The symmetry and periodic boundary conditions used here can reduce the computational effort in problem. About the wall boundary condition of the cylinder surface, a no slip condition is selected, which means the fluid velocity on the wall has a zero value. The boundary conditions for 2D/3D simulation of steady flow past a cylinder are summarised in Table 5-1.

Table 5-1 Boundary condition for steady flow past a circular cylinder

Boundary Locations	Boundary condition type
Upstream ($x = -d_u$)	Velocity Inlet
Downstream($x = d_d$)	Pressure Outlet
Left and right ($y = \pm d_t$)	Symmetry
Top and bottom ($z = 0 / d_z$) (3D)	Periodic
Cylinder surface	No Slip Wall

In fact, one needs to pay more attentions to the definition of turbulence quantities at the velocity inlet boundary, which could have non-negligible influence on the properties of flow around a cylinder. The effect of the free-stream turbulence on the

flow past a cylinder has been studied experimentally by many investigators (Surry, 1972, Kiya et al., 1982). Surry (1972) showed that severe large-scale turbulence could be considered to be qualitatively equivalent to an increase in the effective Reynolds number. However, according to the numerical study of Young and Ooi (2004), it seems that for low turbulence intensity (0.6% in his study) the turbulence length scales at the inlet has only limited implication on the overall time-averaged flow properties. In his study, he varied the length scales by a range of four orders of magnitude ($10^{-4}D \sim 10^{-1}D$) at the inlet while kept the turbulence intensity I as 0.6%, which referred to the experiment by Cantwell and Coles (1983). For flow past a cylinder at a high sub-critical Reynolds number of 1.4×10^5, the calculated values of mean drag coefficient obtained by $k - \omega$ SST turbulence model varied from -7% to +8.5% of the value averaged across all length scales, which indicated that incorrect estimation of length scale by an order of magnitude would not necessarily convey with it a result that is in error by a similar order (Young and Ooi, 2004). Given these factors, the low turbulence intensity $I = 1\%$ is selected here with the turbulent viscosity ratio $r_\mu = 1$, which has an equivalent length scale of about $10^{-3}D$.

Computational domain

The determination of computational domain is interrelated and interacted with the definition of boundary conditions as well as the physical properties. For instance, the boundary location of 'velocity inlet' boundary condition should be placed not too close to a solid obstruction, while the locations of 'periodic' boundary condition should guarantee the flow properties having a periodically repeating nature there.

The vortices are shed in cells in the span-wise direction for flows past a cylinder at $\text{Re} > 300$, which means shedding does not occur uniformly along the length of the cylinder. The average length of the cells may be termed the correlation length that changes with the Reynolds number. The span-wise correlation length is known to decrease as the Reynolds number increases. According to the study of Gerlach and Dodge (1970), the correlation length of a smooth cylinder is around $(15 \sim 20)D$ for

$40 < \text{Re} < 150$ and is about $(2 \sim 3)D$ for $150 < \text{Re} < 10^5$. What one should keep in mind is that the span-wise extent of the domain should be larger than the span-wise correlation length of turbulence (Kim and Mohan, 2005). So the span-wise length of the computation domain is selected as $d_z = \pi D$ here in order to consider all the Reynolds numbers at sub-critical regime. The computation domain size in X-Y plane is referred to Zhao (2010), namely $d_u = 15D$, $d_d = 25D$ and $d_t = 10D$, which in fact is big enough when compared to the domain size of the numerical simulation of Kim and Mohan (2005). The computational domain of the current simulation is summarised in Table 5-2.

Table 5-2 Computational domain of numerical simulations

Computational domain	Domain size	
	Current study (Re=$10^4 \sim 10^5$)	Kim and Mohan, 2005 (Re=$1.4 \times 10^5, 1.0 \times 10^6$)
d_u	15.0D	8.5D
d_d	25.0D	20.5D
d_t	10.0D	10.5D
d_z (3D Simulation)	πD	2.0D

5.2.4 Selection of numerical method

The simulations were conducted by using the 'Pressure-Based' unsteady solver in FLUENT. The setting of solution methods for $k - \omega \ SST$ URANS model and LES model are summarized in Table 5-3.

Upwind-biased schemes (such as 2nd order upwind scheme) for convective fluxes (momentum equations) have been widely used for URANS computations. However, discretisation of convective fluxes requires great caution in LES. In URANS computations for flows at high Reynolds number, the numerical diffusion caused by upwind schemes might be acceptable as the eddy-viscosity is larger than the

molecular viscosity by orders of magnitude. Because sub-grid-scale turbulent viscosity is much smaller than URANS-based eddy viscosity, the numerical diffusion introduced by upwind schemes can overwhelm physical diffusion that is typically much smaller in LES. Therefore, a bounded central differencing scheme is employed by default in FLUENT for the discretization of convection terms in LES model.

Table 5-3 Solution methods for URANS model and LES model

Solution parameters	Method choice	
	$k - \omega \ SST$ **model**	**LES model**
Pressure-velocity coupling	SIMPLE	Fractional Step (FSM, NITA)
Pressure	Standard	Standard
Momentum equations	2nd-order Upwind	Bounded Central Differencing
Gradient	Green-Gauss Cell Based	Green-Gauss Cell Based
Transient Formulation	2nd-order Implicit	2nd-order Implicit
SGS model	/	Smagorinsky-Lilly $C_s = 0.1$

To advance the solution in time for LES, an implicit fractional-step method (FSM) in combination with a 2nd-order accurate scheme is employed. For incompressible flows, the FSM does not have to perform costly outer iterations at each time step to couple velocity and pressure, and thus provides a highly efficient algorithm for CPU-intensive transient computations like LES.

5.2.5 Computational mesh and time stepping

Computational mesh and mesh independence

Firstly, the meshing strategy of the 2D simulation is discussed. The reason is because the mesh for a 3D simulation can be easily obtained by sweeping the 2D mesh along the span-wise direction.

Around the 2D circular cylinder with a diameter $D = 0.2m$, an O-type grid has been used as shown in Figure 5-4. Then the next step is to decide the mesh size along the

circumferential and radial directions. For the concerned problem of flow past a cylinder, the modelling of boundary layer is very important for the capture of separation point. Hence the near-wall quadrilateral mesh with the distance of $10^{-4}D$ from the cylinder surface at the wall-adjacent cells is created, which aims to resolve directly the near-wall region by keeping desirable values of y^+ less than 1 for all the Reynolds numbers at sub-critical regime. The successive ratio (growth ratio) along the radial direction of cylinder surface is approximately 1.08, which can guarantee more than 10 cells in the laminar region. The mesh along the circumferential direction has 160 wall-adjacent cells that can properly incorporate the cylinder curvature. For the 2D simulation of flow over a cylinder at the given computational domain, the total number of cells is around 26,300.
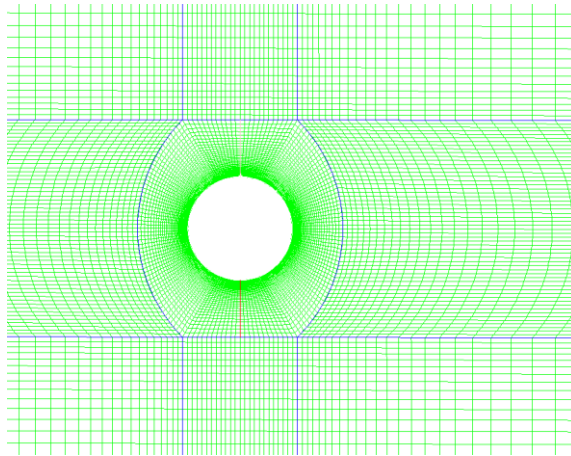
Figure 5-4 Computational mesh around the 2D circular cylinder

It is important to remember that the solution is the numerical solution to the problem that one posed by defining mesh and boundary conditions. The solution should be independent of the mesh resolution. As a part of CFD model validation, the effect of mesh size along the circumferential and radial directions of cylinder has been studied in order to select the optimal mesh which could save computation cost as well as guaranteeing mesh independence. While keeping the first cell height as $10^{-4}D$, a refinement factor of $\sqrt{2}$ is applied to all the edges which create higher density meshes in both the circumferential and radial directions. For the finer mesh, the growth ratio along the radial direction of cylinder is approximately 1.05 and total

number of cells is doubled. Turbulence model $k - \omega \ SST$ are used for each of the two meshes and the results of the global flow parameters for steady flow past a cylinder at $\mathrm{Re} = 6 \times 10^4$ are compared, as shown in Table 5-4.

Table 5-4 Mesh independence test for 2D simulation at $\mathrm{Re} = 6 \times 10^4$

Mesh	Number of cells	C_D	S_t
2D-C1	26,300	0.94	0.24
2D-C2	53,800	0.90	0.25
-	Experimental value	1.20	0.21

It can be seen from Table 5-4 that the calculated mean C_D and Strouhal number from the coarse mesh (2D-C1) are quite close to those obtained from the finer mesh (2D-C2), although the predicted C_D of both cases are smaller than the experimental values. Grid independence has been practically indicated because further mesh refinement only results in insignificant changes in the numerical solutions. The coarse 2D mesh (2D-C1) will be selected here for the calculations and the generation of 3D mesh. The discrepancies between predicted C_D from 2D simulations and experimental results will be discussed later.

The meshes of 3D simulations are based on the 2D simulations as mentioned before, and the effect of number of cells along the span-wise direction is investigated as well, which will be discussed later. Three different cell numbers along the span-wise direction are considered and the total number of cells of each case is listed in Table 5-5. A mesh around the 3D cylinder surface with $N_Z = 64$ cells along the span-wise direction is shown in Figure 5-5.

Table 5-5 Different meshes for steady flow around a 3D cylinder

Mesh case	First Cell Height	N_Z	Number of cells
3D-C0	$1 \times 10^{-4} D$	48	1.26Million
3D-C1	$1 \times 10^{-4} D$	64	1.68 Million
3D-C2	$1 \times 10^{-4} D$	80	2.10 Million
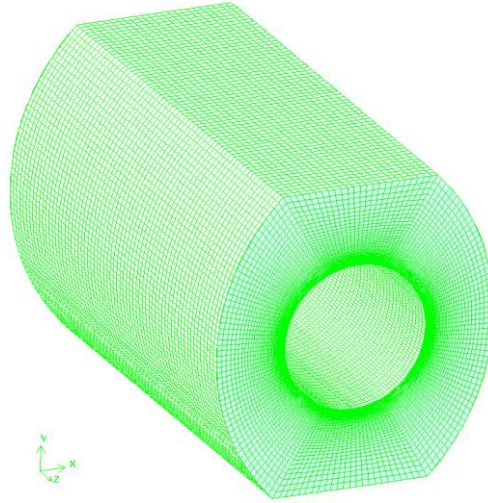
Figure 5-5 Computational mesh around the 3D circular cylinder

Time stepping

The selection of proper time stepping size is very important to get a reliable result with reasonable computation cost. For the URANS turbulence model ($k - \omega$ SST), the time-step size is referred to the work of Zhao (2010), which took the dimensionless time-step size ($\overline{\Delta t} = \Delta t U_o / D$) as 0.025, where U_o is the steady flow velocity and D is the diameter of cylinder. Considering the flow over a cylinder at sub-critical regime with $St \approx 0.20$, one period of the vortex-shedding is resolved with approximately 200 time steps, which actually indicates the $\overline{\Delta t}$ is small enough.

The LES turbulence model needs a smaller time-step size when compared to the URANS models in order to solve energy-containing eddies directly. In the literature the time-step size for LES model has been discussed by different CFD practitioners. For instance, in some publications (Breuer, 2000, Young and Ooi, 2007) the CFL condition which requires the Courant number ($\Delta t U_o / \Delta l$) less than one is applied to decide the time-step size, where Δl is the interval length. However, in the work of Kim and Mohan (2005), the time-step size was determined based on the estimate of the characteristic length and time scales of the smallest resolved eddies, $\tau = l / u'$, where l was taken as $0.05D$ and u' as $0.2U_o$. The dimensionless time-step size of

0.005 was decided from these rough estimates, which means that one turnover time of the smallest resolved eddies could be resolved with 50 time steps.

In fact, the CFL condition ($CFL \leq 1$) is a very strong requirement which is mainly used for explicit methods. For the LES model and implicit solver (default) the requirement of CFL condition would result in an unnecessary small time step size, and hence could significantly increase the computation cost. Taking the LES numerical simulation of flow past a cylinder at $Re = 1.4 \times 10^5$ for example, Breuer (2000) chose a dimensionless time-step size $\overline{\Delta t} = \Delta t U_o / D$ as 2×10^{-4} according to the CFL condition while the dimensionless time-step size adopted by Kim et al. (2005) was 5×10^{-3}. Both simulations, with comparable mesh resolution, obtained comparable results even with the different time-step sizes; so in the present study the values of time-step size for LES models are selected by refering to the work of Kim et al. (2005), while the effect of Reynolds number on the selection of dimensionless time-step size is also considered. When Reynolds number is lower, the value of $\overline{\Delta t}$ could be bigger, as Kim et al. (2005) showed in his publication, where $\overline{\Delta t} = 0.04$ was used for laminar flow around a cylinder at the Reynolds number of 100.

5.2.6   Results and discussions

As numerical model validations, various simulations of steady flow past a cylinder are conducted for several Reynolds numbers at sub-critical regime. The main aim is to see how well the Reynolds-number dependence of the drag coefficient of a cylinder can be captured respectively by the URANS ($k - \omega$ SST) and LES models. The global flow parameters predicted by different kinds of models (2D/3D URANS, LES) are investigated and compared with experimental data if available. The impact of grid resolution along the span-wise directions is studied for both the URANS and LES models, from which the effect of the three-dimensional feature of eddies is emphasized.

1. Numerically predicted Re-dependent global flow parameters

The global flow parameters, such as drag coefficient, *RMS* of the lift oscillations and Strouhal number as function of Re for a smooth circular cylinder under steady flow have been experimentally studied and plotted by different people (Hallam et al., 1977, Schewe, 1983). It is known that Strouhal number has almost a constant value of 0.2 while C_D has a practically constant value of 1.2 throughout the sub-critical Re range. The numerical predictions of global flow parameters are plotted as function of Re to compare with the experimental results, as illustrated in Figure 5-6 and Figure 5-7.
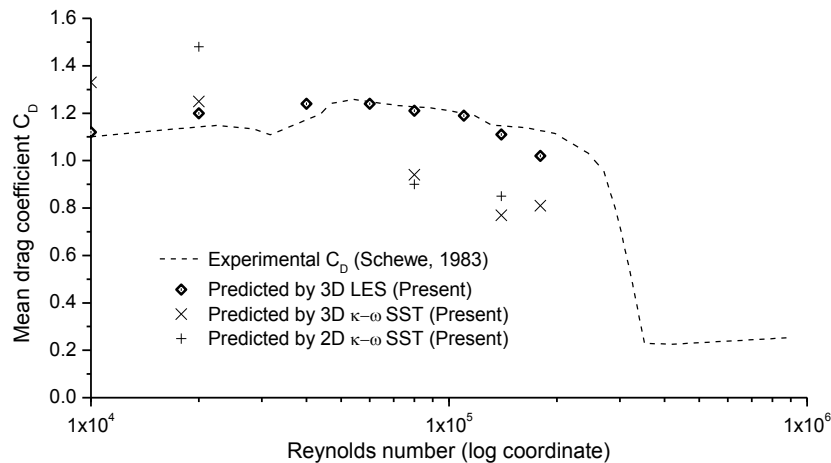
Figure 5-6 Calculated drag coefficient of a smooth cylinder as a function of Re
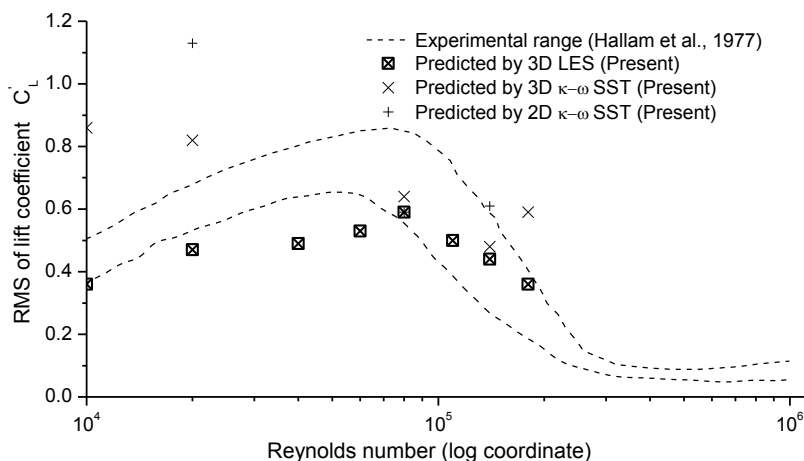
Figure 5-7 Predicted RMS of lift coefficient of a smooth cylinder as a function of Re

The detailed results calculated by 3D-LES models are summarized in Table 5-6. It can be seen from Figure 5-6, Figure 5-7 and Table 5-6 that numerical results of global flow parameters obtained by LES are in a fairly good agreement with the experimental values.

Table 5-6 Summarizations of calculated results of global parameters by LES model

Mesh Case	Re	C_D	C'_L	St
3D-C1	1×10^4	1.12	0.36	0.21
3D-C1	2×10^4	1.20	0.47	0.21
3D-C1	4×10^4	1.24	0.49	0.21
3D-C1	6×10^4	1.24	0.53	0.21
3D-C1	8×10^4	1.21	0.59	0.21
3D-C2	1.1×10^5	1.19	0.50	0.22
3D-C2	1.4×10^5	1.11	0.44	0.22
3D-C2	1.8×10^5	1.02	0.36	0.22

Table 5-7 Global flow parameters predicted by different turbulence models

Mesh Case	Re	Turbulence model	C_D	C'_L	St
3D-C1	1×10^4	LES	1.12	0.36	0.21
		$k-\omega$ SST	1.33	0.86	0.21
3D-C1	2×10^4	LES	1.20	0.47	0.21
		$k-\omega$ SST	1.25	0.82	0.22
3D-C1	8×10^4	LES	1.21	0.59	0.21
		$k-\omega$ SST	0.94	0.64	0.25
3D-C2	1.8×10^5	LES	1.02	0.36	0.22
		$k-\omega$ SST	0.81	0.59	0.26

However, from the comparison of results from 3D URANS model ($k-\omega$ SST) with those from LES model (see Figure 5-6 and Figure 5-7), it can be seen that

1) For the relative small Re numbers ($1\times10^4, 2\times10^4$), compared to the LES model, the $k-\omega$ SST turbulence model over-predicts the C_D and *RMS* of lift with an acceptable Strouhal number (see Table 5-7);

2) For high Re number (such as 8×10^{4}, 1.8×10^{5}) $k-\omega$ SST model will significantly under-estimate C_{D} and over-estimate Strouhal number (Table 5-7).

2. 3D URANS ($k-\omega$ SST) model vs. LES model

Comparative assessment of URANS and LES for flow past a cylinder at a high Reynolds number of 1.4×10^{5}

A detailed comparative assessment of URANS and LES has been conducted for flow over a cylinder at Re of 3900 (Young and Ooi, 2007), so a similar assessment of URANS and LES is completed at Re of 1.4×10^{5}. The selection of a high sub-critical Re of 1.4×10^{5} is based on two considerations: first, this high Reynolds-number flow is more close to real world applications; second, the experiment performed by Cantwell and Coles (1983) at this Reynolds number provides well-documented data as reference for the validation of numerical simulations.

The time histories of hydrodynamic coefficients (drag and lift) obtained from LES and URANS models are illustrated in Figure 5-8. The time traces of force coefficients calculated by the LES model reveal the quasi-periodic behaviour of drag and lift coefficients, with their amplitudes varying irregularly over time, while the time histories from URANS model partly failed to capture this characteristic.
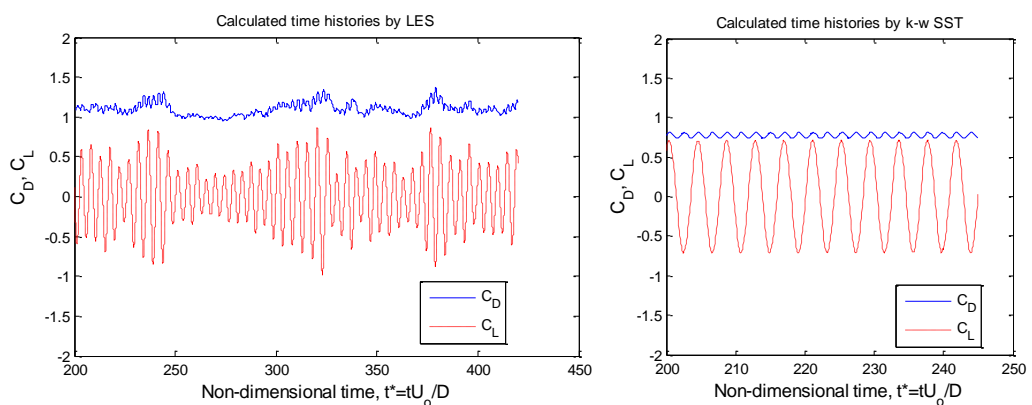
Figure 5-8 Time histories of force coefficients by different turbulence models ($\mathrm{Re}=1.4\times10^{5}$)

The global flow parameters of a cylinder at Re number of 1.4×10^5 calculated by LES and URANS models are summarized in Table 5-8, in which experimental values are also included. It can be seen that the LES model could produce good simulation results whilst the $k - \omega\ SST$ model noticeably under-predicted the mean drag coefficient.

Table 5-8 Results calculated by different turbulence model for $Re = 1.4 \times 10^5$ compared with other numerical results and experimental data (ZD: Zdravkovich (1997))

Turbulence model	Global flow parameters		
	C_D	C_L'	St
LES (Present)	1.11	0.44	0.22
LES (Breuer, 2000)	1.22	-	0.22
SST $k - \omega$ (Present)	0.77	0.48	0.24
Experimental Values(ZD)	1.15	0.5/0.6	0.18/0.21

An accurate prediction of pressure distribution around the cylinder surface is critical to realistically calculate forces on the cylinder, therefore, the time averaged pressure distribution on the cylinder surface calculated by LES and URANS models is shown in Figure 5-9, together with the experimental data obtained by Cantwell and Coles (1983).

The negative peak predicted by the numerical method is bigger than the measured one, especially for the $k - \omega\ SST$ model. However, good agreement exists between the measurement and the LES model for the separation angle deduced from the inflection point of the mean C_P curve, while the separation angle predicted by the $k - \omega\ SST$ model is comparatively larger. That could partly explain why the mean drag coefficient calculated by this URANS model is much smaller that the measured value.
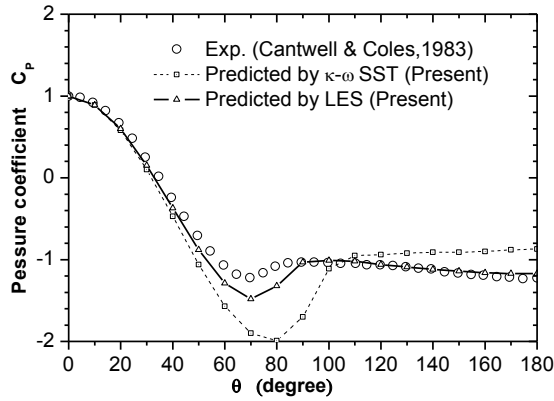
Figure 5-9 Mean pressure coefficient on the cylinder surface for $\mathrm{Re} = 1.4 \times 10^5$

The global flow parameters such as mean drag coefficient and Strouhal number provided some insight into how well the models perform. A further assessment of model performance can be achieved by comparison with other experimental studies. Figure 5-10 depicts the predicted mean stream-wise velocities along the wake centreline by the two different turbulence models. There is fairly good overall agreement between the numerical predictions and the experimental measurement, whilst it is also surprising to see that the URANS model got much better results in predicting the mean stream-wise velocities. The length of the time-averaged recirculation bubble predicted by the LES model was found a little bigger that the value that reported by Cantwell and Coles (1983).
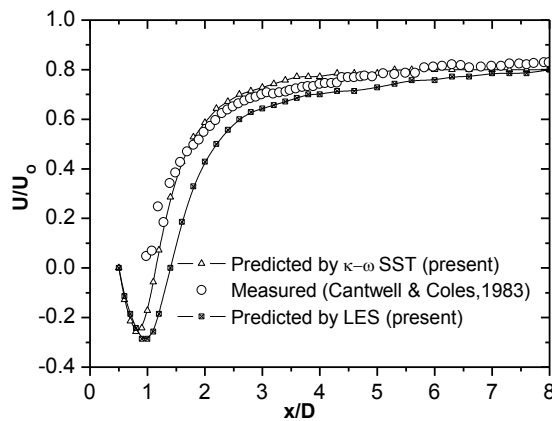
Figure 5-10 Comparison of mean stream-wise velocity along the centreline aft of the cylinder

However, according to the study of Franke and Frank (2002), the accumulation of the averaging time in LES has a notable influence on the accuracy of statistical quantities, such as the recirculation bubble length. For instance, it was found that with the increase of averaging cycles, the recirculation length also increases. In the current study, 50 averaging cycles are used to obtain the mean stream-wise velocity, mean pressure coefficient and recirculation length.

Kim et al. (2005) also did a similar study about flow past a cylinder at Re of 1.4×10^5 by using LES. It seems that in his study the predicted mean stream-wise velocities by LES have quite good agreement with experiment values, although the calculated recirculation length is also slightly over-estimated. It should be noted that in his simulation 6.8 million cells are used while in the current study only 2.1 million cells are used. The grid resolution in the cylinder wake may need to be improved for the current LES to get more accurate predictions of the flow field in the wake. The streamlines of the time-averaged flow obtained from LES and URANS are plotted in Figure 5-11.
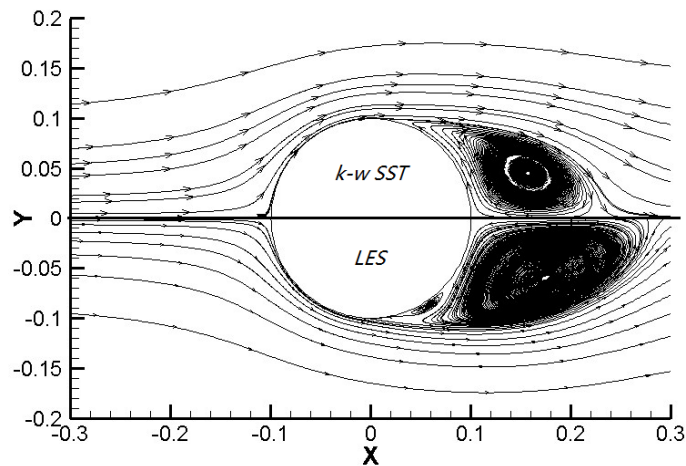
Figure 5-11 Streamline of the time-averaged flow by different turbulence models ($\mathrm{Re} = 1.4 \times 10^5$)

Overall, it can be seen from modelling flow past a cylinder at Re of 1.4×10^5 that the LES model could get more accurate results of global flow parameters when compared to URANS model. The only disadvantage of the LES model is the computational cost, which is also compared between the two turbulence models.

Both of the simulations are completed on the Engineering Faculty's HPC (High Performance Computing) using 12 cores. The dimensionless time step size $\overline{\Delta t}$ is 0.007 for LES and 0.07 for URANS model. For 120s flow time, the run time of simulation for LES is 84 hours and for URANS is 34 hours, as shown in Table 5-9.

Table 5-9 Computational cost of LES and URANS models

Turbulence model	Mesh case	Flow time	Run time (hrs)
LES	3D-C2	120s	84
URANS (SST $k - \omega$)	3D-C2	120s	34

It should be noted that for the URANS model coarser mesh (especially along the span-wise direction) can be used, and hence the run time of simulation would become even less. However, considering the good performance of LES, the computational cost of LES would be totally acceptable, especially with the fast growth of computing capacity.

3. Impact of grid resolution along the span-wise direction

As mentioned before, the mesh independence is important for the simulation results. The 2D mesh independence has been checked by comparing the results obtained from one coarse mesh and one finer mesh. For the 3D mesh situations, the impact of grid resolution along the span-wise direction needs to be investigated as well.

First, for the flow past a cylinder at Re number of 8×10^4, the global flow parameters obtained by LES model from three different mesh cases (see Table 5-5) have been summarised in Table 5-10. It can be seen that the case with 48 span-wise cells considerably under-estimates the mean drag coefficient and *RMS* of lift force coefficient, while the 64 span-wise-cell case and the 80 span-wise-cell case have almost the same acceptable results.

Table 5-10 Impact of span-wise cells on numerical results by LES model ($Re = 8 \times 10^4$)

Mesh case	N_Z	y^+	$\overline{C_D}$	C_L'	St
3D-C0	48	0.58	0.94	0.23	0.22
3D-C1	64	0.62	1.21	0.58	0.21
3D-C2	80	0.66	1.20	0.50	0.21

The time histories of force coefficients for the mesh case '3D-C0' and mesh case '3D-C1' under Re number of 8×10^4 are plotted in Figure 5-12. For the mesh case '3D-C0' without enough span-wide cells, the irregular amplitudes of drag and lift force coefficient decrease with the increase of time.
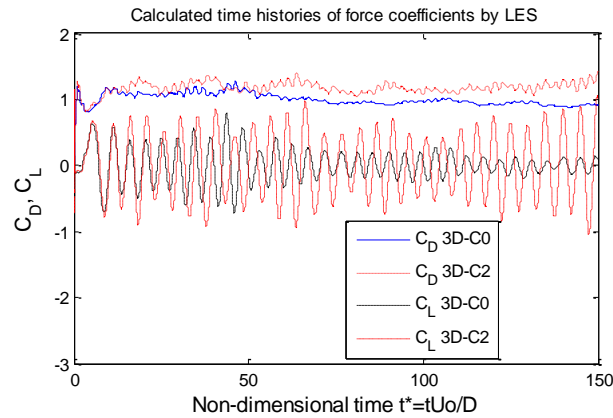
Figure 5-12 Time histories of force coefficients by LES under different mesh cases ($Re = 8 \times 10^4$)

Another flow past a cylinder at Re number of 1.4×10^5 is considered by LES model for mesh case '3D-C1' and '3D-C2'. The calculated global quantities are listed in Table 5-11. For this even higher Re number flow, the 64 span-wise-cell case failed to accurately predict the parameters while the 80 span-wise-cell case has a quite good results.

Table 5-11 Impact of span-wise cells on numerical results by LES model ($Re = 1.4 \times 10^5$)

Mesh case	N_Z	y^+	$\overline{C_D}$	C_L'	St
3D-C1	64	0.96	1.02	0.29	0.22
3D-C2	80	1.00	1.11	0.44	0.22

Young and Ooi (2007) considered the effect of span-wise cells for flow past a cylinder at Re=3900, in which he found that 16 span-wise cell LES case offers similar poor results as 3D URANS case with the same grid while the 32/48 span-wise cell LES case got a fairly good results, as shown in Figure 5-13. To be noted, in his study the domain size along span-wise direction is also πD.

Case	$\overline{C_D}$	$\overline{C_{p_b}}$	St	$C_{L_{rms}}$
Experiment [3], [12], [13]	0.98 ± 0.05	0.90 ±0.005	0.215 ±0.005	0.03 − 0.08
2D URANS	1.59	1.96	0.235	1.17
3D URANS	1.32	1.42	0.223	0.701
LES $n_z = 4$	1.55	1.86	0.217	1.08
LES $n_z = 16$	1.25	1.36	0.196	0.549
LES $n_z = 32$	1.04	0.913	0.212	0.164
LES $n_z = 48$	1.03	0.908	0.212	0.177
[8]	1.04	0.94	0.210	n/a

Table 3: Overall flow parameters obtained over 30 shedding periods.

Figure 5-13 Numerical results for flow past a cylinder at Re=3900 (Young and Ooi, 2007)

The valid span-wise cell numbers for LES model to accurately simulate flow past a cylinder at different Re numbers are summarized in Table 5-12.

Table 5-12 Valid span-wise cell numbers for LES modelling steady flow past a cylinder

Re	Span-wise cell numbers (span-wise domain size πD)				
	16	32	48	64	80
3900	×	√	√	√	√
8×10^4	×	×	×	√	√
1.4×10^5	×	×	×	×	√

Table 5-12 suggests that LES is only effective when sufficient number of cells in the span-wise direction is used to resolve the smaller three-dimensional eddies. The valid number of span-wise cells for LES modelling flow past a cylinder will increase as the Reynolds number increases.

The effect of span-wise grid resolution upon URANS model simulating the flow past a cylinder is also investigated, as is listed in Table 5-13. In contrast to the cases using

the LES model, the number of span-wise cells has no effect upon the simulation results obtained by 3D URANS model.

Table 5-13 Impact of span-wise cells on numerical results by SST $k-\omega$ model ($\mathrm{Re} = 8 \times 10^4$)

Mesh case	N_Z	$\overline{C_D}$	C'_L	St
3D-C0-1	32	0.91	0.62	0.24
3D-C1	64	0.94	0.64	0.25

Three-dimensional effects

As mentioned before, for flow past a cylinder at Re>200, the two-dimensional features of the vortex shedding in the range 40<Re<200 becomes distinctly three-dimensional. The three-dimensional effects of vortex shedding need to be considered by simulations in 3D computational domain. Through the studies of the effect of span-wise grid resolution, the conclusion may be reached that the 3D URANS model ($k-\omega$ SST) can not capture the three-dimensional structures which strongly affect the near-wake of the flow. Compared to the 2D URANS simulation, the 3D URANS could offer comparatively better results for flow past a cylinder at some Re numbers, as shown in Table 5-14, however, at high Reynolds numbers the 2D and 3D URANS models almost have the similar results, all of which under-estimate the mean drag coefficient.

Table 5-14 Predicted global flow parameters by 2D and 3D SST $k-\omega$ models

Reynolds number	Model	$\overline{C_D}$	C'_L	St
2×10^4	2D URANS	1.48	1.13	0.24
	3D URANS	1.25	0.82	0.22
8×10^4	2D URANS	0.90	0.59	0.25
	3D URANS	0.94	0.64	0.25
1.4×10^5	2D URANS	0.85	0.61	0.26
	3D URANS	0.77	0.48	0.24

The iso-surface of vorticity magnitude obtained by LES, 2D and 3D URANS models are illustrated in Figure 5-14, Figure 5-15 and Figure 5-16. It can be seen the LES model reveals the three-dimensionality of the flow while the flow-field of the 3D URANS model is essentially two-dimensional and like the 2D URANS model.
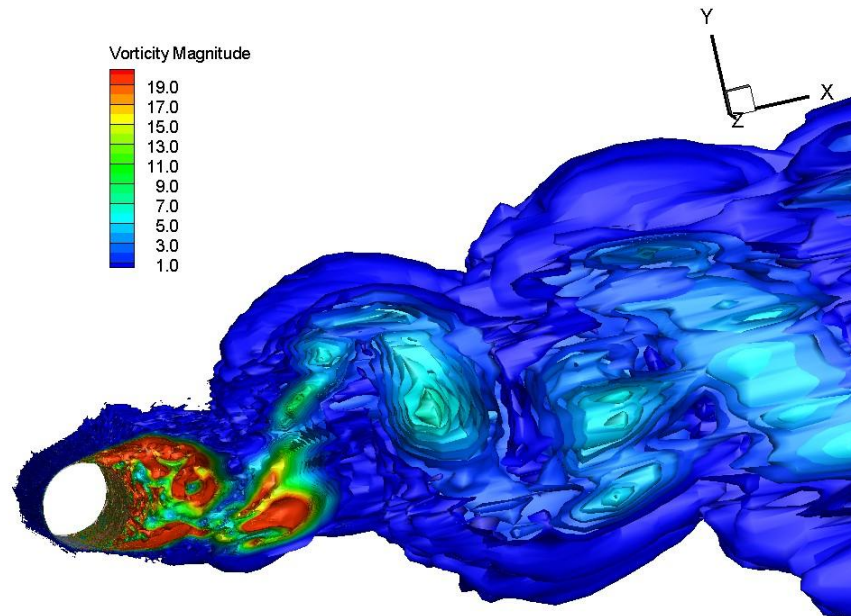
Figure 5-14 Iso-surface of vorticity magnitude by LES model ($\text{Re}=1.4\times10^5$)
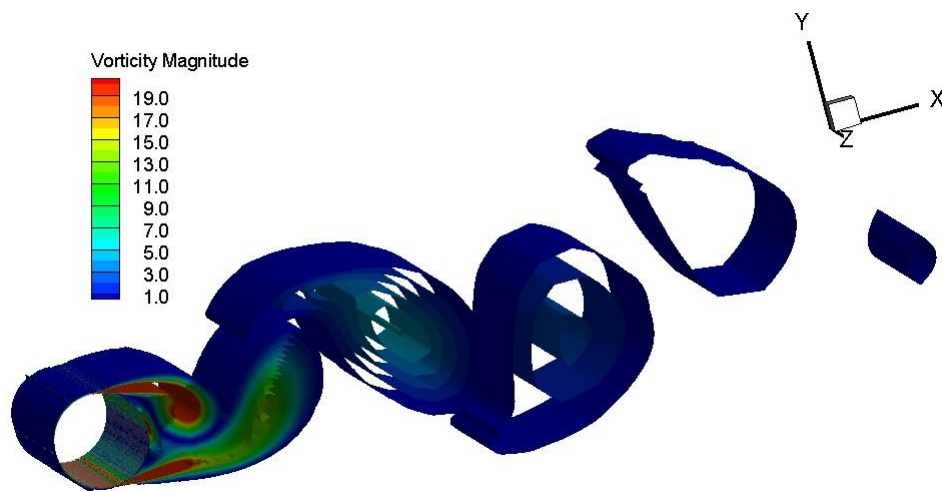
Figure 5-15 Iso-surface of vorticity magnitude by 3D URANS model ($\text{Re}=1.4\times10^5$)
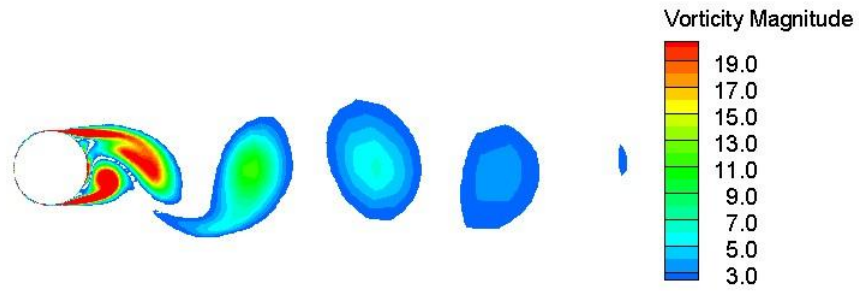
Figure 5-16 Iso-surface of vorticity magnitude by 2D-URANS model ($\mathrm{Re} = 1.4 \times 10^5$)

The iso-surface of Z vorticity obtained by LES and 3D URANS models are illustrated in Figure 5-17 and Figure 5-18, from which the direction of the vorcitity can also be seen.
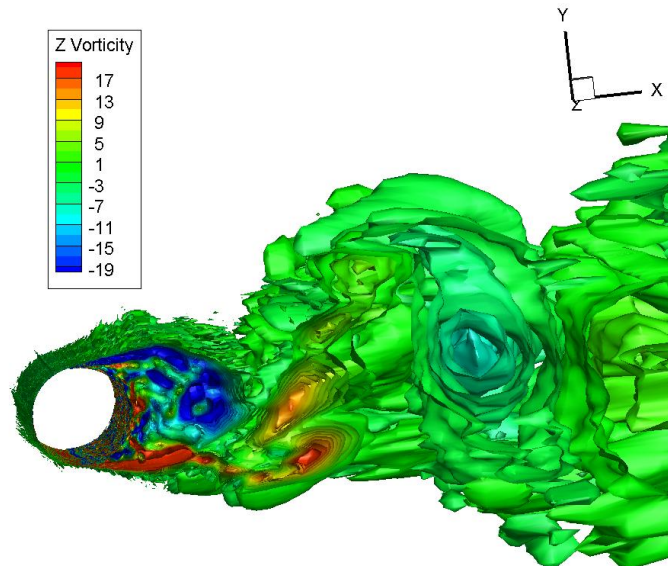
Figure 5-17 Iso-surface of Z vorticity by LES model ($\mathrm{Re} = 1.4 \times 10^5$)
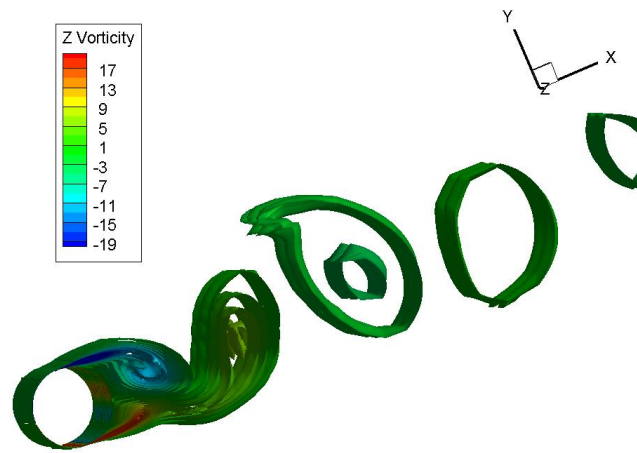
Figure 5-18 Iso-surface of Z vorticity by 3D URANS model ($\mathrm{Re} = 1.4 \times 10^5$)

5.3 CFD model validation2- an oscillating cylinder in still water

An oscillating cylinder in a quiescent fluid, or the converse situation of oscillating flow past a stationary cylinder, is an effective representation of wave–cylinder interaction in the area of ocean engineering where the computation of the fluid forces on an offshore structure is one of the primary tasks. The wave-cylinder-interaction problem has been widely studied by experiments. Among many investigators, Sarpkaya (1976, 1977, 1985, and 1986) did comprehensive experimental studies about the oscillating flow past a stationary cylinder by using a U-shaped tunnel and these experimental results have been well documented.

A brief discussion has been made about the flow regimes of cylinder under oscillatory flows while the forces experienced by the cylinder are also discussed (See Appendix A), which aims to provide the comparative reference for numerical simulations. In this chapter, details of the CFD modelling of an oscillating cylinder in water are depicted, and then the results and discussions are presented.

5.3.1   Numerical representation of the cylinder movement

In order to simulate the effect of cylinder oscillations, a major problem to handle is the treatment of the moving interface between the oscillating cylinder and the fluid. Basically two approaches can be used to tackle cylinder oscillation and simulate the effect of cylinder movement in the flow, regarding to the coordinate system.

In inertial (stationary) reference frame, dynamic mesh can be used to model flows where the shape of the domain is changing with time due to motion of the body. Part or whole of the mesh domain will deform or move with the moving body. Different techniques of dynamic mesh, such as Spring-based Smoothing, Dynamic Layering, Local Re-meshing or the Arbitrary Lagrangian and Eulerian (ALE) method can be used to handle the moving cylinder, which can be seen from work of different people (Nomura, 1993, Wei et al., 1995, Huang and Larsen, 2010). Normally, this method is

computationally expensive and time consuming as it requires lots of mesh points to be transformed to their new positions. However, the advantage of this method is that it can consider motions with several degrees of freedom.

The other approach is to treat the moving boundary in a non-inertial Eulerian frame which is fixed relative to the oscillating cylinder. So, relative to this non-inertial Eulerian grid system, the cylinder with surrounding mesh is stationary. The 'Non-inertial Frame' method has been widely used to simulate the oscillating cylinder (Chilukuri, 1987, Blackburn and Henderson, 1999, Nehari et al., 2004, Rashid et al., 2011).

The 'Non-inertial Frame' method can be achieved by a non-inertial coordinate transformation from the stationary Eulerian frame to a non-inertial Eulerian frame system. The incompressible N-S equations need to be modified with an additional source term to incorporate the moving reference frame of the cylinder, because generally the N-S equations used by CFD software are only applicable in an inertial reference frame. Assume an oscillating cylinder in the X direction with an oscillation frequency ω and an amplitude A and the displacement is given as

$$x_c(t) = -A\cos(\omega t) \qquad \text{Eq. 5-3}$$

Hence the oscillating velocity of cylinder is as follow:

$$u_c(t) = A\omega\sin(\omega t) \qquad \text{Eq. 5-4}$$

The non-inertial coordinate transformation in the X-direction enables the treatment of the time dependent deforming interface as a stationary non-deforming new interface. The constraining of the cylinder motion is only in the X-direction and in other two directions (Y and Z) no relative velocity change is needed. Due to the transformation, the parameters in the X-direction are transformed as:

$$\bar{u} = u - u_c(t) = u - A\omega\sin(\omega t) \qquad \text{Eq. 5-5}$$

$$\bar{P} = P \qquad \text{Eq. 5-6}$$

where, $\bar{u}$ and $\bar{P}$ are velocity and pressure in the moving non-inertial frame.

The momentum equation in X-direction can now be transformed to the new non-inertial coordinate system where the cylinder appears as stationary

$$\frac{D\bar{u}}{Dt} = \frac{-\nabla\bar{P}}{\rho} + \upsilon\nabla^2\bar{u} - \frac{\partial u_c(t)}{\partial t} \qquad \text{Eq. 5-7}$$

In the above equation Eq. 5-7, the term $-\partial u_c(t)/\partial t$ is the extra source term resulting from the coordinate transformation.

In the present study, a similar approach to the 'Non-inertial Frame' method is adopted to model the oscillating cylinder. This is achieved by defining 'Mesh Motion' for the Cell Zone, which can be equivalently transferred to 'Frame Motion'. By this the whole mesh domain including the cylinder is defined as 'rigid body', and a cylinder (mesh) motion, specified by a user defined function, is given on the 'rigid body', where no re-mesh or mesh-deforming is needed.

5.3.2   Other numerical aspects of modelling

Spatial discretization and time stepping

The computational domain is similar to the one used for steady flow past a cylinder. The only difference is the length upstream, which is $25D$ here. So the domain sizes are $50D$ along the X-direction, $20D$ along the Y-direction and πD along the Z-direction, as shown in Figure 5-19.
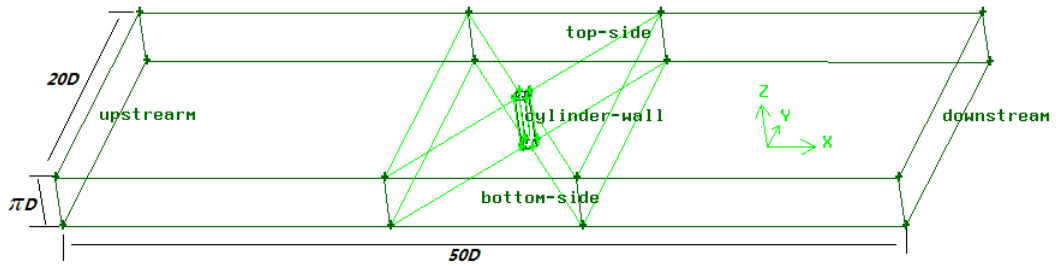
Figure 5-19 Computational domain for an oscillating cylinder in water

The mesh strategy for an oscillating cylinder is similar with that for steady flow past a cylinder. Hexahedra mesh is used in the near-wall region, where a radial distance of $0.5 \times 10^{-4} D$ of wall-adjacent cells from the cylinder surface is selected. This aims to directly resolve the near-wall region by keeping desirable values of y^+ less than 1 for all the Reynolds number concerned. The successive ratio (growth ratio) along the radial direction of cylinder surface is properly selected to guarantee more than 10 cells in the laminar region. In the near wall region, the mesh along the circumferential direction has 160 wall-adjacent cells that can properly incorporate the cylinder curvature. Out of the near-wall region, unstructured mesh is used.

The selection of time-step size for an oscillating cylinder also refers to that for a fixed cylinder under steady flow. Dimensionless time-step size $\overline{\Delta t} = \Delta t U_m / D$ is used to decide the time-step size Δt in the solver. The size of dimensionless time-step will depend on the Reynolds number and the turbulence model, as discussed before.

Boundary conditions

For the oscillating cylinder in still water, the boundary conditions are summarised in Table 5-15. At the 'Up-stream' location, the 'Velocity inlet' boundary condition with absolute velocities equal to zero ($U_x = U_y = U_z = 0$) is used for still water. At the 'Down-stream' location, boundary condition 'Pressure Outlet' is assumed, which often gives better rate of convergence when 'back-flow' occurs, although an 'Outflow' boundary condition is another option for 'Down-Stream' location.

If the 'Non-inertial Frame' method is used to handle the oscillating cylinder, the relative velocities at the 'Up-stream' location can be defined for the 'Velocity Inlet' boundary condition.

Table 5-15 Boundary conditions for the oscillating cylinder in still water

Boundary locations	Boundary conditions
Up-stream	Velocity Inlet
Down-stream	Pressure Outlet
Lateral sides (Y-axis)	Symmetry
Top/bottom sides (Z-axis)	Periodic
Cylinder	No-slip wall

Other numerical aspects include numerical methods adopted in different turbulence models. Basically, for the modelling of oscillating cylinder in still water, the numerical methods adopted by $k-\omega$ SST model and LES model are similar to those listed in Table 5-3 for modelling steady flow past a cylinder. The difference is mainly about the calculation of the gradients of the scalar. Considering the hybrid mesh used in modelling the oscillating cylinder, the 'Green-Gauss Node-Based' method is adopted because this averaging scheme is known to be more accurate than the default cell-based scheme for unstructured meshes, most notably for triangular and tetrahedral meshes.

Although the URANS model has poor performance in predicting the global parameters of steady flow past a smooth circular cylinder, the URANS model is still considered here, together with LES model. This is because the harmonic motion of a long circular cylinder seems to suppress three-dimensionality and make flows more two-dimensional than their fixed-cylinder counterparts, at least in the near-wake region (Blackburn and Henderson, 1999, Blevins, 2006). So the URANS model could get satisfactory results with lower computation cost.

5.3.3 Results and discussions

Numerical simulations are conducted for several cases with KC number in range of $8\sim30$ and Re number in range of $1\times10^4 \sim 1.5\times10^5$. Single-pair regime ($7 < KC < 15$), double-pair regime ($15 < KC < 24$) and three-pair regime ($24 < KC < 32$) are included in these cases. Comparisons are completed for in-line hydrodynamic coefficients obtained by different fitting methods, such as Least-square method and Fourier-averaged method. Numerical results of in-line force coefficients from different turbulence models are also compared.

1. Numerical results by the URAN ($k - \omega$ SST) model

The in-line force coefficients are obtained by the fitting of Morrison equation with calculated in-line forces. Several different fitting methods can be used and detailed descriptions can be seen in the Appendix C. The calculated drag coefficient C_D and added-mass coefficient C_a are presented as a function of KC and β ($\beta = \mathrm{Re}/KC$), which is in order to compare with well-documented experimental results from Sarpkaya (1976). To be kept in mind, the drag coefficients C_D obtained by Sarpkaya could be slightly over-predicted, as mentioned in Appendix B.

Table 5-16 Comparisons of calculated and experimental in-line force coefficients

Fourier-averaged	Case1	Case2	Case3	Case4	Case5	Case6
	$KC = 10.3$ $\beta \approx 3123$	$KC = 20.6$ $\beta \approx 3123$	$KC = 29.8$ $\beta \approx 3123$	$KC = 10.3$ $\beta \approx 5260$	$KC = 20.6$ $\beta \approx 5260$	$KC = 29.8$ $\beta \approx 5260$
Calculated C_D	0.90	0.78	0.65	0.65	0.53	0.52
Experimental C_D [1]	1.40	0.86	0.68	0.96	0.70	0.62
Calculated C_a	0.78	0.44	0.54	0.83	0.79	0.82
Experimental C_a [1]	0.36	0.52	0.61	0.75	0.76	0.80

Notes: [1] values of experimental coefficients here are obtained visually from the curves drawn by Sarpkaya (1976), so small discrepancies could exist;

In Table 5-16 the calculated in-line force coefficients of different cases by URAN ($k - \omega$ SST) model are compared with the experimental results from Sarpkaya. These in-line force coefficients are fitted by the least-square method.

It can be seen from Table 5-16 that:

1) The trend of drag coefficients varying with KC is in agreement between the experiments and numerical calculations. For instance , for a given β, the values of C_D decrease with the increase of these three KC numbers;

2) Generally, the calculated drag coefficients obtained from the $k - \omega$ SST model are in agreement with the experimental values except Case 1 and Case 4 with $KC = 10.3$, of which the calculated C_D are about 30-40% smaller than the experimental values;

3) The discrepancies between calculated and experimental C_a are comparatively small except Case1. Overall agreement of C_a between numerical simulations and experiments is better than that of C_D.

In Figure 5-20, the calculated in-line force and fitted force are illustrated. The fitted total force is in fair agreement with CFD calculated force.
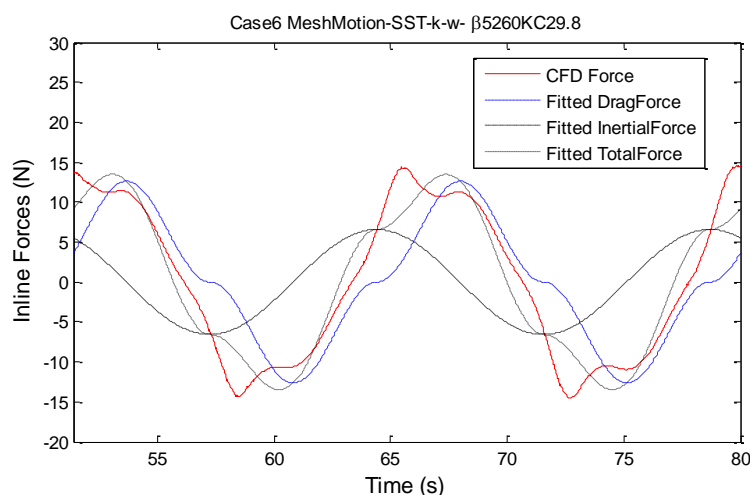
Figure 5-20 Calculated in-inline force and fitted force for Case 6 ($KC = 29.8 \beta \approx 5260$)

The corresponding transverse force coefficient for this Case6 with $KC = 29.8$ and $\beta \approx 5260$ is shown in Figure 5-21. The KC number considered here belongs to the three-pair regime, and the normalized fundamental lift frequency N_L should be 4. However, from the Figure 5-21 it can be seen that the calculated lift force has N_L of around 5.
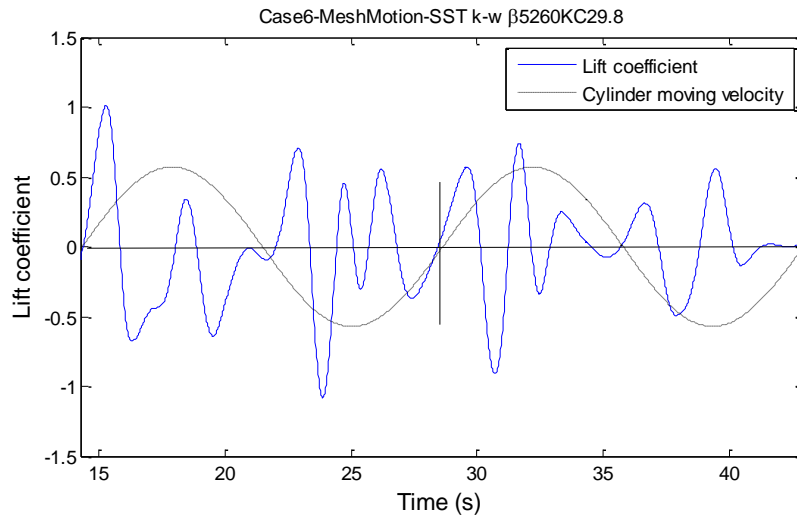
Figure 5-21 Calculated transverse force coefficient for Case 6 ($KC = 29.8 \beta \approx 5260$)

For the given $\beta \approx 5260$, the lift force coefficients for other two cases with KC equal to 10.3 and 20.6 respectively are shown in Figure 5-22 and Figure 5-23.
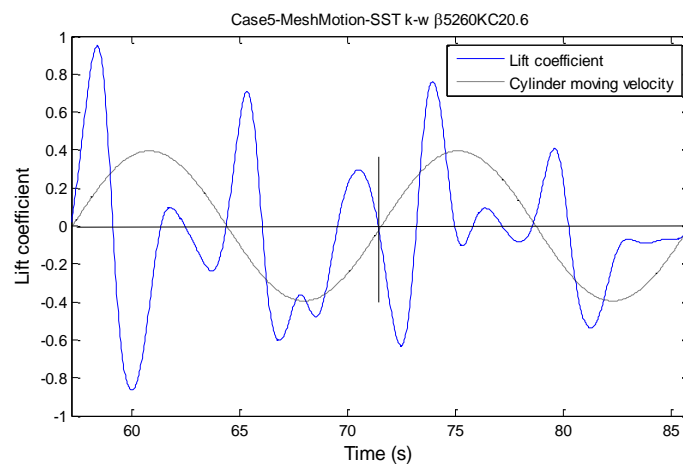
Figure 5-22 Calculated transverse force coefficient for Case 5 ($KC = 20.6 \beta \approx 5260$)
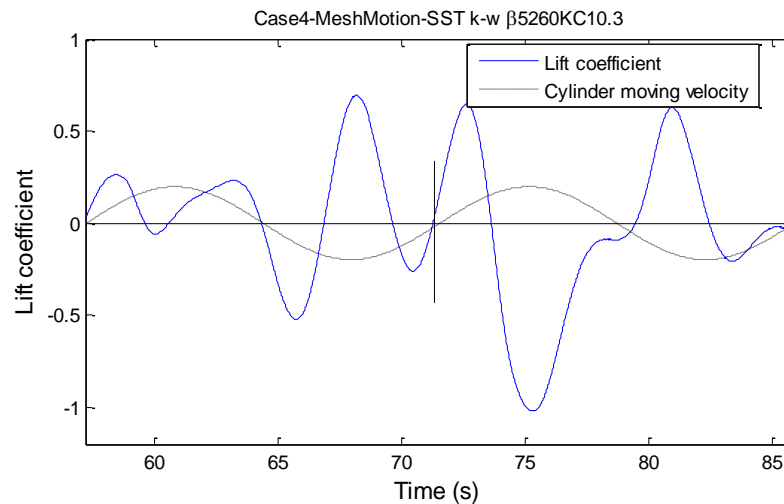
Figure 5-23 Calculated transverse force coefficient for Case 4 ($KC = 10.3\, \beta \approx 5260$)

According to related experiments, for $KC = 20.6$, the flow is in double-pair regime and value of N_L is 3, while for KC number of 10.3 flow regime is single-pair regime with $N_L = 2$. For both KC numbers, the predicted normalized fundamental lift frequencies also do not match the experimental values. For an oscillating cylinder, especially for a cylinder in the lower KC regimes, the lift frequency is not totally related to the 'vortex-shedding frequency' due to the presence of flow reversals. This is unlike the situation of flow past a fixed cylinder, where the lift frequency is decided by the 'frequency of vortex-shedding'. Hydrodynamic forces on an oscillating cylinder still could be affected by the vortex shedding, which significantly affects the hydrodynamic forces on a fixed cylinder under steady flow.

According to the study of Nehari et al. (2004), for an oscillating cylinder in quiescent water, the transverse force on the ocillating cylinder seemed be significantly influenced by the three-dimensional vorticity effects while longitudinal and axial components of the force experienced by the cylinder seemed to be weakly affected. This finding is verified by the numerical results here. The in-line hydrodynamic force coefficients predicted by the URAN model simulations generally agree with the data from experiments (except Case 1 and Case 4). Considering the magnitude of the lift

force $C_{L\max}$, the calculated values are slightly bigger than the corresponding experimental values from Sarpkaya (see Figure A-8).

2. Discussions

1) Goodness-of-fit of the Morison equation

It was found that Morison representation could be not very satisfactory with respect to the measured variation of the in-line force for certain flows. In order to assess the applicability of the Morison equation, a goodness-of-fit parameter δ_F was introduced (Summer and Fredsøe, 1997):

$$\delta_F = \frac{\int_0^{T_t} (F_m - F_p)^2 \, dt}{\int_0^{T_t} F_m^2 \, dt} \qquad \text{Eq. 5-8}$$

where, F_m is measured force; F_p is predicted force by Morison equation; T_t is the duration of data sampling.
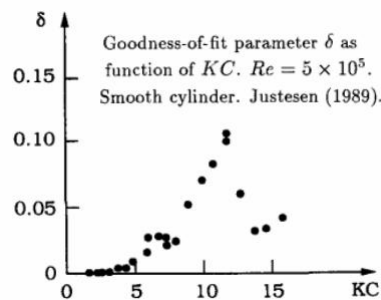
Figure 5-24 Goodness-of-fit parameter as function of *KC* (Summer and Fredsøe, 1997)

Figure 5-24 shows a typical variation of δ_F with respect to *KC* for a smooth cylinder at $\text{Re} = 5 \times 10^5$. Parameter δ_F reaches a maximum value around 0.12 when *KC* increases from 0 to approximately 12. Then, δ_F decreases again with further increase of *KC*.

From Figure 5-20 it can be seen that for $KC = 29.8$, fitted total force and CFD calculated force fairly agree with each. Now, considering another two cases both with β equal to 5260, the comparison between fitted force and CFD calculated force is illustrated respectively in Figure 5-25 and Figure 5-26.
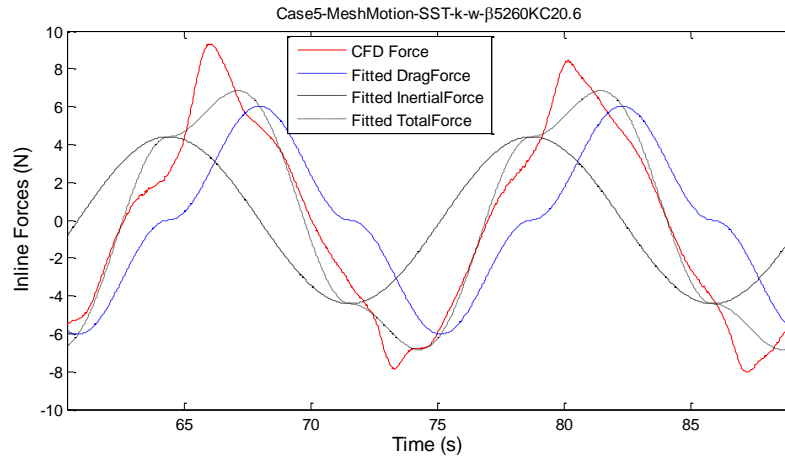
Figure 5-25 Calculated in-inline force and fitted force for Case 5 ($KC = 20.6 \beta \approx 5260$)
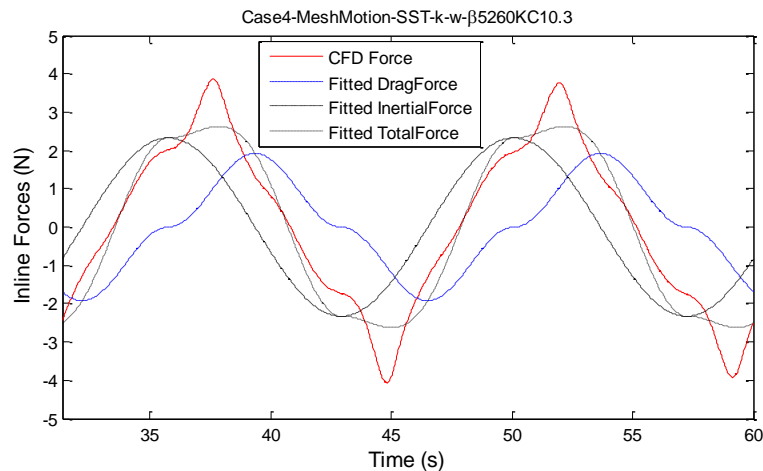
Figure 5-26 Calculated in-inline force and fitted force for Case 4 ($KC = 10.3 \beta \approx 5260$)

As is seen, the match between fitted total force and CFD calculated force for Case 4 and Case 5 is also reasonable. The goodness-of-fit parameter δ_F is calculated for these three cases and listed in Table 5-17.

Table 5-17 Goodness-of-fit parameters for different *KC* cases with $\beta \approx 5260$

Case	Case4	Case5	Case6
δ_F	0.066	0.059	0.091

2) Effect of fitting methods

The results mentioned above are fitted by the least-square method. The Fourier-series approach is only limited to single harmonic motion. The weighted least-square method will try to make the peak values of the fitted curve match the peak of the original curve. However, if the peak of the original curve is not a real reflection of the problem, then this method will introduce errors. Listed in Table 5-18 are the results of Case 4 and Case 6 obtained by these different methods.

As seen from Table 5-18, similar results are obtained by the Fourier-averaged and least-square method. However, the fitted results by the other two methods are generally not good. The Morison-averaged method got smaller drag coefficients and added-mass coefficients. Although for Case 4, by the Weighted-least-square method drag coefficient is in better agreement with experimental value, the added mass coefficient is over-predicted.

Table 5-18 Fitted force coefficients by different fitting methods

Fitting methods	Case 4 $\left(KC = 10.3 \beta \approx 5260 \right)$		Case 6 $\left(KC = 29.8 \beta \approx 5260 \right)$	
	C_D	C_a	C_D	C_a
Fourier-averaged	0.69	0.83	0.55	0.81
Least square	0.65	0.83	0.52	0.82
Morison-averaged	0.44	0.67	0.45	0.77
Weighted least square	0.83	0.94	0.46	1.25
Exp. (Sarpkaya,1976)	0.96	0.75	0.62	0.80

To assess the performance of different fitting methods, the goodness-of-fit parameter δ_F is calculated for different cases under different fitting methods, as summarised in Table 5-19. It can be seen from Table 5-19 that for all three cases, the goodness-of-fit parameters δ_F are small for the Fourier-averaged method as well as for least-square method, which means that the CFD calculated in-line force can be represented by Morison-predicted in-line forces. However, the Morison-predicted in-line forces (coefficients) are poorly predicted by the Morison-averaged method and the weighted-least-square method, since the parameters δ_F of these cases are much bigger.

Table 5-19 Goodness-of-fit parameters for different *KC* cases

Fitting methods	goodness-of-fit parameter δ_F		
	Case 4 $KC = 10.3$ $\beta \approx 5260$	Case 5 $KC = 20.6$ $\beta \approx 5260$	Case 6 $KC = 29.8$ $\beta \approx 5260$
Fourier-averaged	0.067	0.059	0.080
Morison-averaged	0.123	0.094	0.102
Weighted least-square	0.101	0.115	0.169

3) Effect of computational domain

Effect of the X-direction domain size is studied first and it is found that current domain size along the X-direction is big enough. The 'blockage-ratio' problem is checked by enlarging the computational domain along the Y-direction. Compared to the former $20D$ width, the new mesh case has a width of $50D$ along the Y-direction, as shown in Figure 5-27. The blockage ratio D/W for the numerical simulations will change from 0.05 to 0.02.
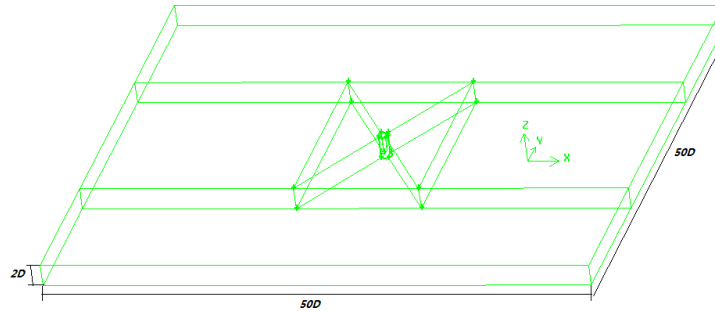
Figure 5-27 Enlarged computational domain for an oscillating cylinder in water

It is to be mentioned here, the cross-section of the test section is $3\text{ft} \times 3\text{ft}$ in Sarpkaya's U-tube experiments (1976), and several circular cylinders with diameters ranging from 2 inches to 6.5 inches were used. So the blockage-ratio in his experiments is in the range of 0.056~0.18.

The comparison of results for Case 6 under different blockage ratios is listed in Table 5-20. It can be seen that the original domain with blockage ratio equal to 0.05 is small enough to eliminate effect of blockage ratio. The comparison of fitted in-line force with CFD force for Case 6 under small blockage ratio is shown in Figure 5-28.

Table 5-20 Effect of blockage ratio of computational domain

Blockage ratio (Domain case)	Case 6 ($KC = 29.8 \beta \approx 5260$)	
	Calculated C_D	Calculated C_a
0.05	0.52	0.82
0.02	0.51	0.86
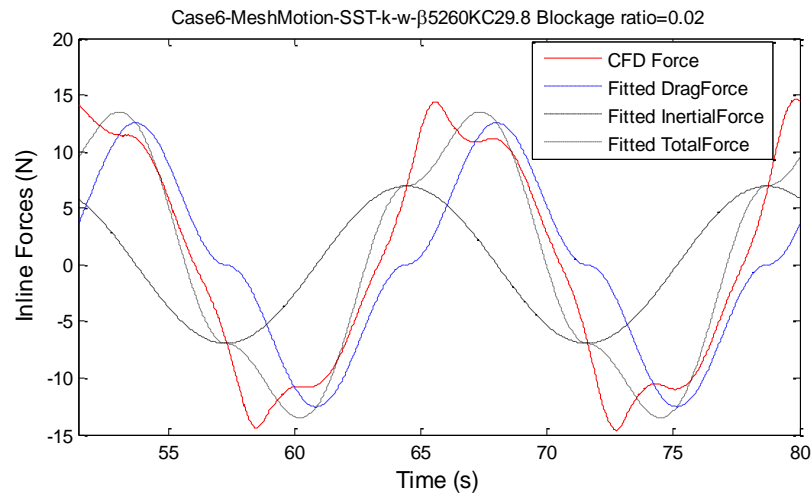
Figure 5-28 Fitted in-inline force and CFD calculated force for Case 6

4) Effect of turbulence models

For steady flow past a cylinder, the comparison between LES turbulence model and URANS ($k-\omega\ SST$) turbulence model has been made. It was found that URANS model failed to capture the three-dimensionality of the wake eddy, and hence normally could not predict the forces with desirable accuracy. As mentioned before, for an oscillating cylinder in water, the three-dimensionality of wake is suppressed, which makes flows more two-dimensional when compared to a fixed cylinder under steady flow. So the in-line force coefficients of an oscillating cylinder in still water are generally predicted by URAN model with acceptable accuracy.

Using the 'Mesh motion' method to model the oscillating cylinder, the performance of the LES model is also studied. However, it is surprising to see that the in-line force coefficients are poorly predicted by the LES model for an oscillating cylinder in still water. The fitted forces and CFD force obtained by LES model are listed in Figure 5-29. The goodness-of-fit parameter δ_F is 0.13, which means the Morison-predicted in-line forces (coefficients) are poorly estimated.
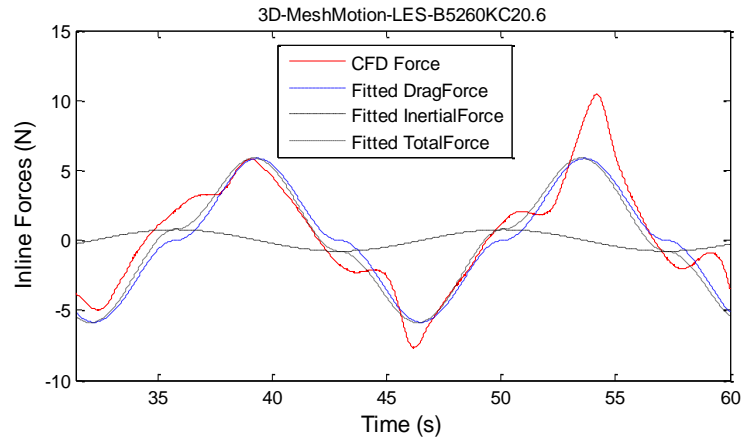
Figure 5-29 Fitted in-inline force and CFD calculated force for Case 5 by LES

Table 5-21 Results obtained by different turbulence models using 'Mesh motion'

Turbulence model	Case 5 ($KC = 20.6 \beta \approx 5260$)	
	Calculated C_D	**Calculated** C_a
LES turbulence model	1.99	0.28
URANS ($SST\ k-\omega$) model	0.53	0.79
Experiments (Sarpkaya,1976)	0.70	0.76

In Table 5-21, the calculated force coefficients of Case 5 obtained by different turbulence models are listed. It can be seen that the LES model obtains even worse results, with significantly over-estimated drag coefficient and a slightly under-predicted added-mass coefficient.

Before doubting the performance of the LES model for modelling unsteady flow past a cylinder, the treatment approach for modelling unsteady flow past a cylinder is first studied. An effort is made to repeat the work of other people who studied unsteady flow past a cylinder by different approaches using the LES model. In the present numerical model, only the approach to model the unsteady flow is changed, while other numerical aspects, such as spatial discretization and numerical methods, are kept the same as the numerical model using 'Mesh Motion' method to model the moving cylinder.

Lu et al. (1997) simulated an oscillating flow past a fixed cylinder by using LES. Sinusoidally oscillating flow was defined at the velocity inlet. No-slip and no-penetration boundary conditions were defined on the wall of the cylinder. Now, this method is also considered here for the case ($KC \approx 10, \beta \approx 1099$) in order to compare with Lu's Case ($KC = 10, \beta \approx 1035$). The UDF 'DEFINE_PROFILE' is used to define the oscillatory flow velocity ($u_x = 0.042\cos(0.092t)$) at the velocity inlet. From Table 5-22 it can be seen that the present simulation could get almost the same results as Lu's work for the given KC and β numbers. The fitted forces and CFD force obtained by LES model are listed in Figure 5-30 with the goodness-of-fit parameter δ_F equal to 0.17.

Table 5-22 Calculated results of oscillatory flow past a fixed cylinder by LES

Case	'Oscillatory flow' method	
	Calculated C_D	Calculated C_M
Present work ($KC \approx 10, \beta \approx 1099$)	2.32	0.73
Lu et al. (1997) ($KC = 10.0, \beta \approx 1035$)	≈ 2.3	≈ 0.7
Exp. by Sarpkaya (1976)	≈ 2.0	≈ 0.7
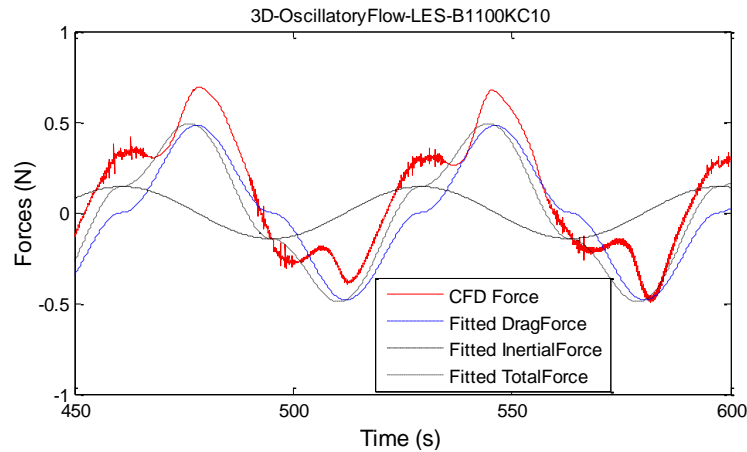
Figure 5-30 Fitted in-inline force and CFD force by LES for oscillatory flow past a cylinder

Using a non-inertial coordinate transformation ('Frame Motion' in FLUENT), the moving cylinder can be treated as 'stationary' in the non-inertial frame. This method has been used to model an oscillating cylinder in still water using LES by Rashid et al. (2011). However, in FLUENT, 'Frame Motion' can be equally transformed to

'Mesh Motion' by selecting 'Copy to Mesh Motion' option, so the results obtained by these two methods should be the same.

The CFD calculated in-line forces obtained by different treatment approaches are shown in Figure 5-31. It shows that the amplitudes of forces obtained by the LES model by different treat approaches are quite similar, while the $k-\omega\ SST$ model got an in-line force with quite smaller amplitude.
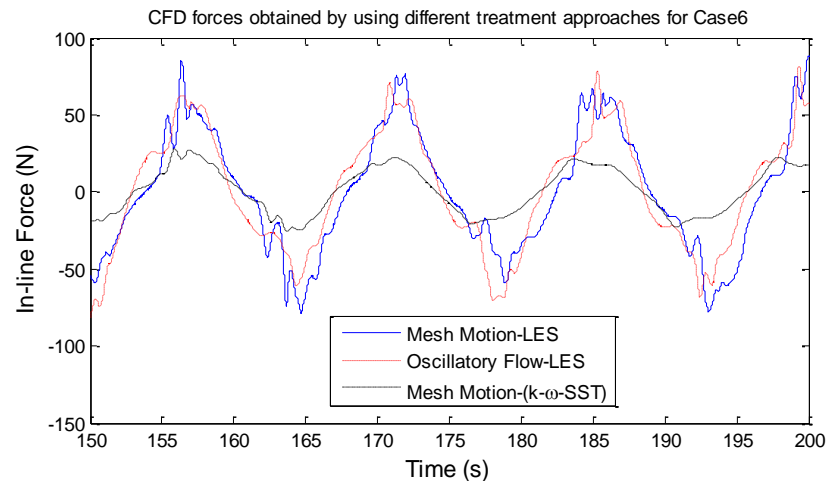
Figure 5-31 CFD in-inline forces obtained by using different treatment approaches

Using the LES model, the fitted in-line hydrodynamic coefficients for Case 6 obtained by different treatment approaches for modelling oscillating cylinder are listed in Table 5-23. It can be seen that force coefficients predicted by 'Mesh Motion' method and by 'Oscillatory flow' method are almost the same, which all significantly over-estimate the drag coefficient while under-predicting the added mass coefficient.

Table 5-23 Comparisons of treatment approaches for oscillating cylinder by LES model

Treatment approach	Case 6 ($KC=29.8\beta\approx5260$)	
	Calculated C_D	Calculated C_a
'Mesh Motion'	1.70	0.12
'Oscillatory flow'	1.63	0.13

In Figure 5-32 are fitted forces and CFD force obtained by LES. It is known that the over-predicted peak in-line CFD forces by LES caused the over-estimated fitted drag force and hence the over-predicted drag coefficient.
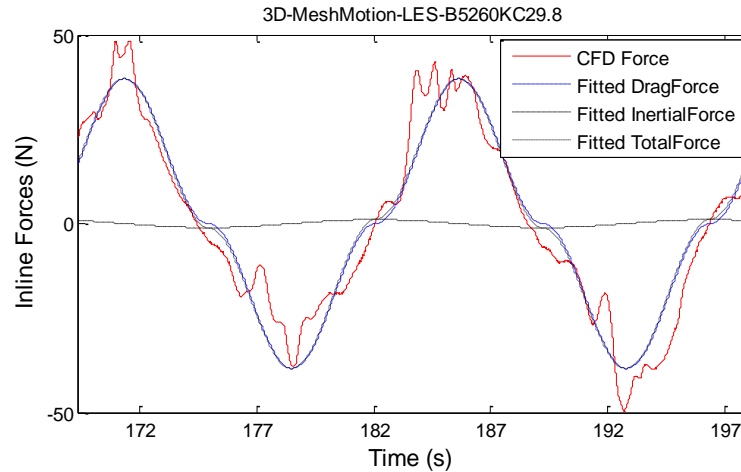
Figure 5-32 Fitted in-inline force and CFD force by LES for Case 6

The vortex shedding could have a dominant effect on the forces experienced by an oscillating cylinder, including the in-line force and transverse lift force. The lift coefficient of Case 6 predicted by LES is illustrated in Figure 5-33. The maximum lift coefficient is also dramatically over-estimated by the LES model. It seems that in oscillatory flow, the present LES model tends to generate enlarged vortex-shedding, which will cause over-predicted forces in both in-line and transverse directions.
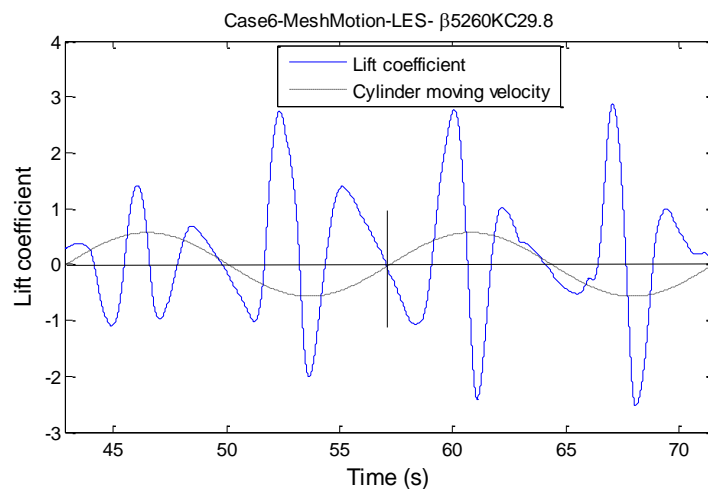
Figure 5-33 CFD calculated lift force coefficient by LES for Case 6

5.4 Summary

In this chapter, numerical simulations have been conducted for steady/unsteady flow past a smooth circular cylinder. As model validations, the main purpose is to select a proper turbulence model that can capture the global flow parameters (especially C_D) of flow past a bluff body. Besides, other numerical aspects, such as the effect of grid resolution, time-step size and near-wall treatment, are also investigated. Simulation results have been compared between different cases, together with available experimental data.

For steady flow past a cylinder, overall, the LES model has a quite good performance. However, it is more difficult to predict the forces on an oscillating cylinder when compared to those of a fixed one. Using 'Mesh motion' method to model a moving cylinder, several cases with KC numbers in the range of 10~30 have been considered. Obtained by the URAN model ($k-\omega\ SST$), the calculated added-mass coefficients are in fair agreement with experimental values while some of the predicted drag coefficients are under-estimated for cases with lower Reynolds number. Unexpectedly, the present LES model appears to have failed to accurately predict the global parameters of oscillating cylinders in still water under given β and KC numbers. The potential possible reason could be due to the enlarged vortex-shedding simulated by the present LES model. Another factor could be due to the fact that, compared to the fixed cylinder under steady flow, the oscillating cylinder will suppress the three-dimensionality of vortex and make flows more two-dimensional in the near-wake region. That could be the reason why the URAN model ($k-\omega\ SST$) can get quite satisfactory results for the oscillatory cylinder in still water.

6. Numerical calculation of drag coefficients of mooring line chain

6.1 Overview

It is known that the mooring line damping/line tension is quite sensitive to the variation of drag coefficient around the touch down zone according to the investigation in Chapter 4, which emphasized the importance of selection of drag coefficient for chain. The influential factors of drag coefficient of chain have been discussed before. Among these factors, however, only the effect of Re and KC number will be considered in the CFD simulation.

In this chapter, the drag coefficient of a smooth stud-less chain under the effect of Reynolds number and KC number is studied by CFD method. Before the numerical calculation, the range of Re number and KC number along the mooring line chain under different motions is investigated first.

6.2 Range of Re and KC number of the chain under different motions

The ranges of Re and KC number under different motions are mainly considered for the chain around touch down zone, where the mooring line damping is very sensitive to the variation of drag coefficient (see Figure 4-5 and Figure 4-7). The Re number and KC number are calculated according to the maximum normal velocity:

$$\text{Re} = \frac{U_M D}{\upsilon} \ , \ KC = \frac{U_M T}{D} = 2\pi \frac{\eta_0}{D} \qquad \textbf{Eq. 6-1}$$

where, U_M is the maximum normal velocity of oscillation motion; η_0 is the normal displacement and D is the nominal diameter of the stud-less chain.

Due to geometric nonlinearities inherent in the catenary equations, the normal displacement η_0 is not symmetric about the mid position. So the KC number is calculated according to the maximum normal displacement on one side.

A single mooring line shown in Figure 3-27 is selected to study the ranges of Re and KC number under different motions. For the slow drift motion, amplitude equal to 10% water depth is considered with four different periods. When it comes to WF motions, the slow drift motion will not be considered. Instead, the WF motions will be exerted on the top of line under 3 different catenary shapes, as shown in Figure 6-1. The horizontal distance of the top ends is $+/-$ 40m away from the mean position.
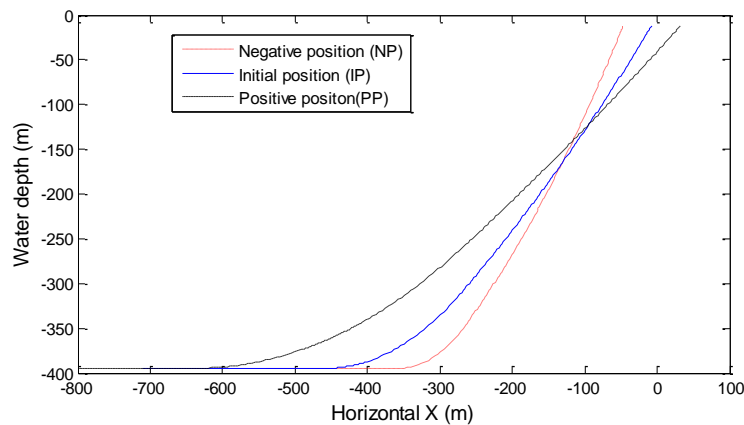
Figure 6-1 Three different catenary shapes of mooring line

The Re and *KC* numbers along the line under WF motions will be calculated for these three positions, which are mainly used to consider the effect of the shape change of mooring due to the slow drift motion while the velocity effect of slow drift motion will be ignored. The maximum Re number along the line will be under-estimated when compared to the case with LF motion and superimposed WF motion.

The maximum Re and *KC* numbers along the R3S chain under the slow drift motions are shown in Figure 6-2. It can be seen that *KC* number is very big under these LF motions, which means only Re number effect needs to be considered for drag coefficients of chain under such LF motions.
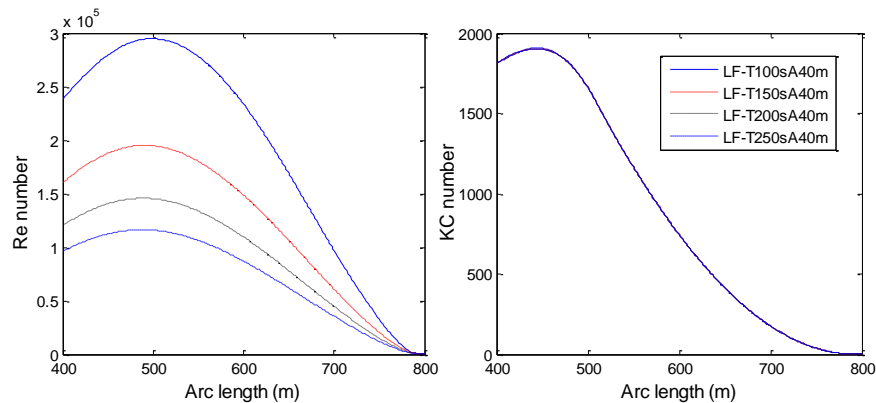
Figure 6-2 Range of Re **and** *KC* **number along the R3S chain under slow drift motion**

The maximum Re and *KC* number along the R3S chain under the different surge WF motion at three different positions are shown in Figure 6-3 and Figure 6-4.
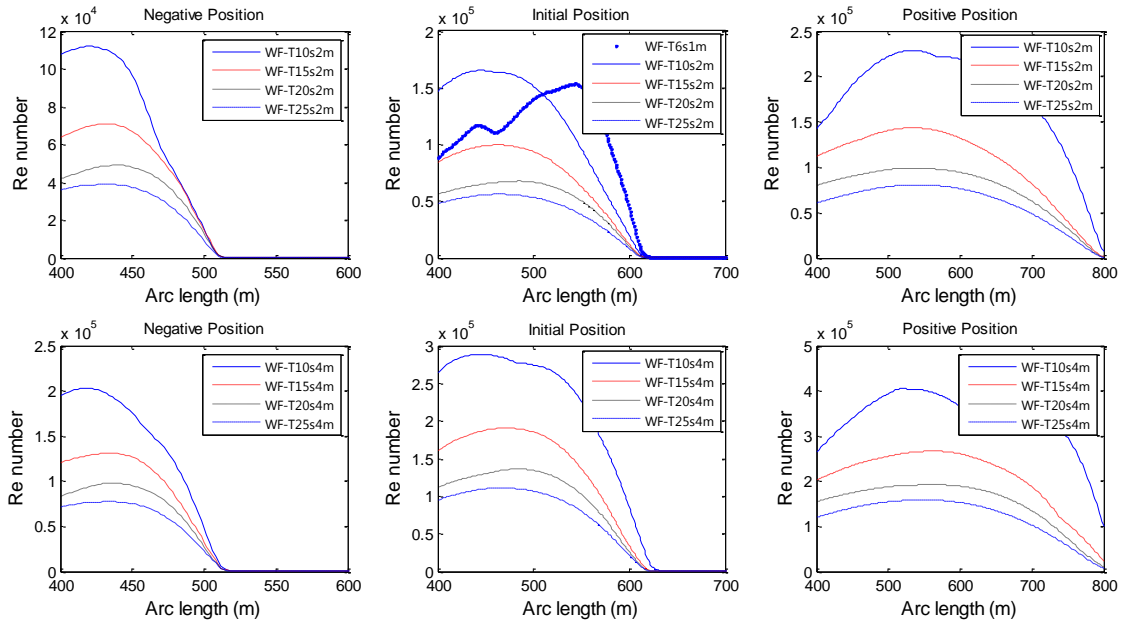
Figure 6-3 Range of Re number along the R3S chain under surge WF motions
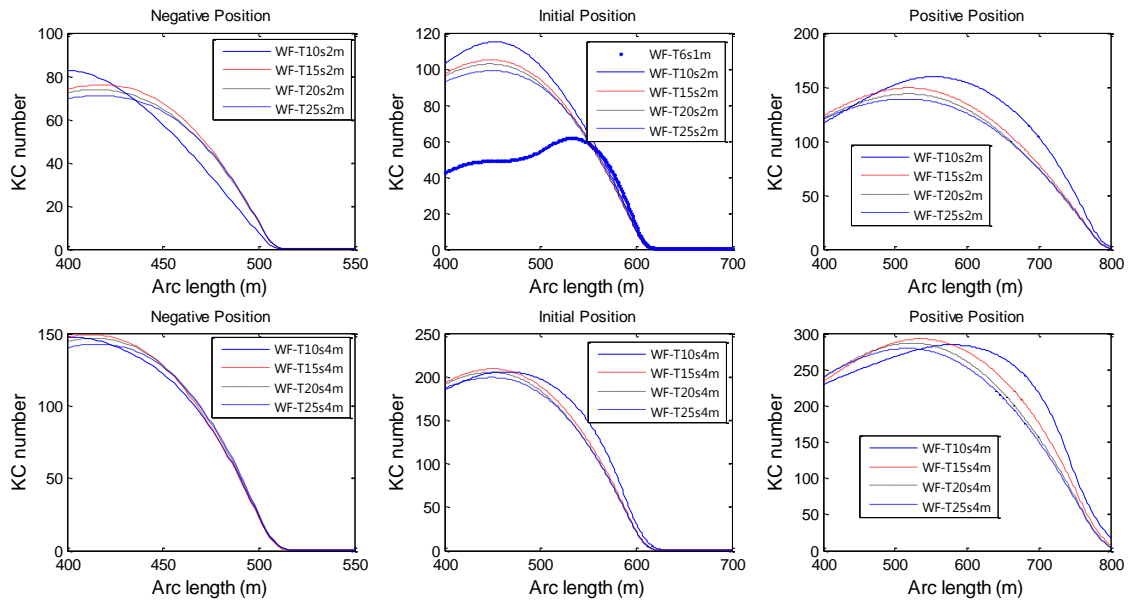
Figure 6-4 Range of KC number along the R3S chain under surge WF motions

The maximum Re and KC number along the R3S chain under the different heave WF motion at three different positions are shown in Figure 6-5 and Figure 6-6.
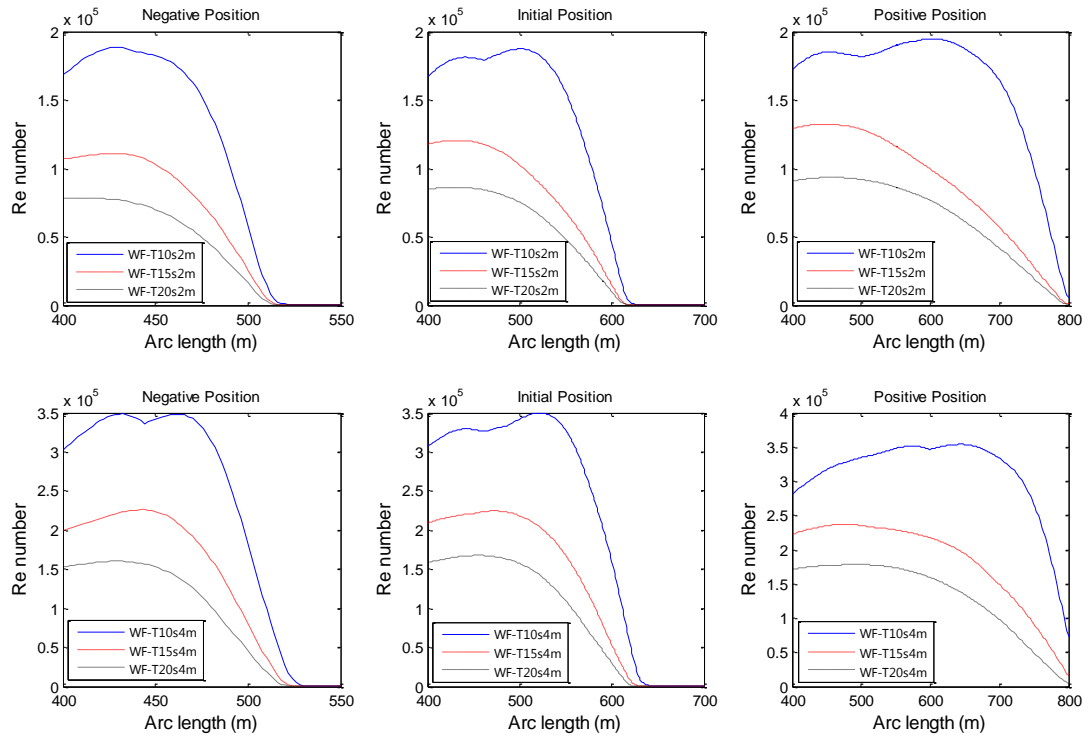
Figure 6-5 Range of Re number along the R3S chain under heave WF motions
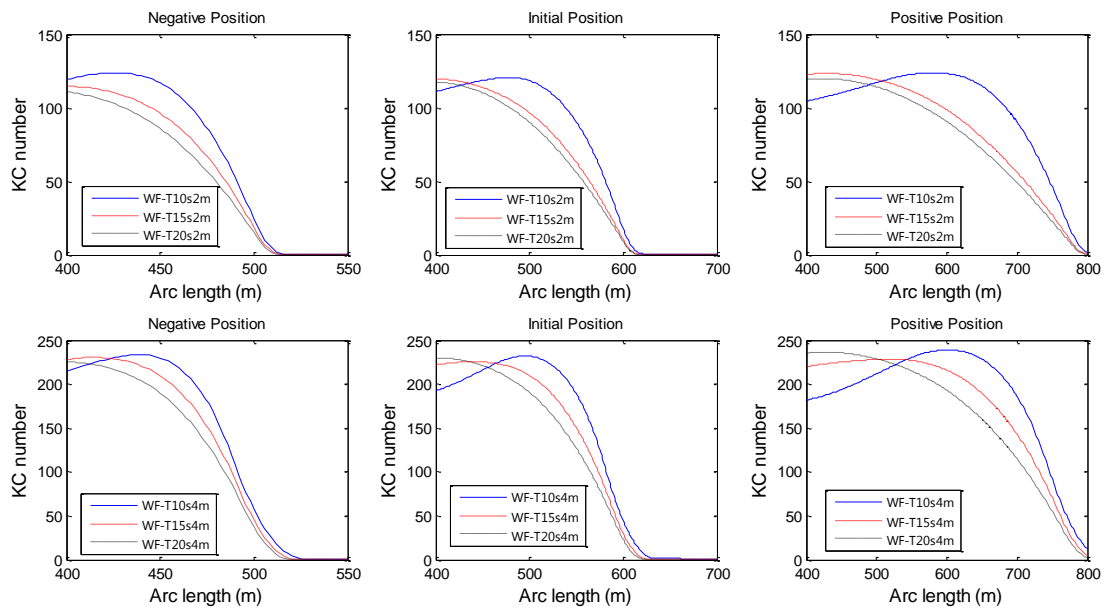
Figure 6-6 Range of KC number along the R3S chain under heave WF motions

It can be seen that under the given surge/heave WF motions, the KC number along the R3S chain at arc length from 400m to 600m is in the range of around 10 to 300,

while Re number is approximately in the range of $10^4 \sim 10^6$. During the following CFD simulation, the values of Re and KC numbers considered are in these range.

6.3 CFD simulation of steady flow past a smooth stud-less chain

From the CFD model validations in the Chapter5, it can be seen that the Reynolds-number-dependent drag coefficient of a circular cylinder under steady flow is well predicted by LES turbulence models while considerable discrepancies exist between the experimental values and numerical results obtained from URANS models for most of the Reynolds numbers at sub-critical regime. Other global flow parameters, such as RMS of lift and Strouhal numbers are also well predicted by the LES model. Therefore, steady flow past a smooth chain is mainly simulated by LES model to decide the drag coefficients under different Re numbers.

6.3.1 Computational domain and boundary conditions

The geometrical model of a pair of stud-less chain links is illustrated in Figure 6-7.
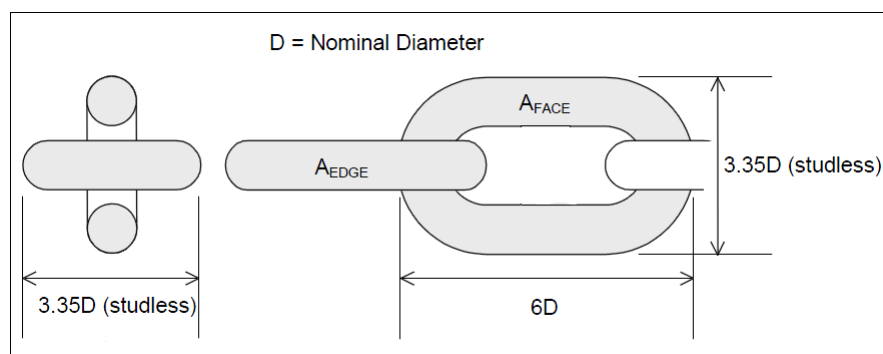
Figure 6-7 Geometrical model of a stud-less chain

The values in the figure are given in term of the nominal bar diameter (D) of the chain normally as standard parts. However, for more detailed properties of chain, one should refer to the catalogue data available from the chain suppliers.

The computational domain of the chain is illustrated in Figure 6-8. Considering the periodicity of the chain geometry, a complete link and two half-links are selected as the simulation object, as shown in Figure 6-8. Correspondingly, the boundary condition of top and bottom surfaces of the domain is defined as 'periodic' boundary condition. The surface of this chain segment is defined as no-slip wall. The inlet at the upstream of the chain segment is defined as 'velocity inlet' and the outlet at the downstream of the chain segment is defined as 'outflow' boundary condition. The turbulent quantities in the 'velocity inlet' are defined as turbulence intensity of 1% and turbulent viscosity ratio of 1. The steady flow around the chain segment is along the X-axis, and hence the velocities at 'velocity inlet' are defined as $U_x = constant$, $U_y = 0$ and $U_z = 0$. The boundary conditions of lateral sides of the domain are defined as 'symmetry'. Actually, the definition of the boundary conditions for the chain segment is the same as those used for CFD modelling of the 3D cylinder.
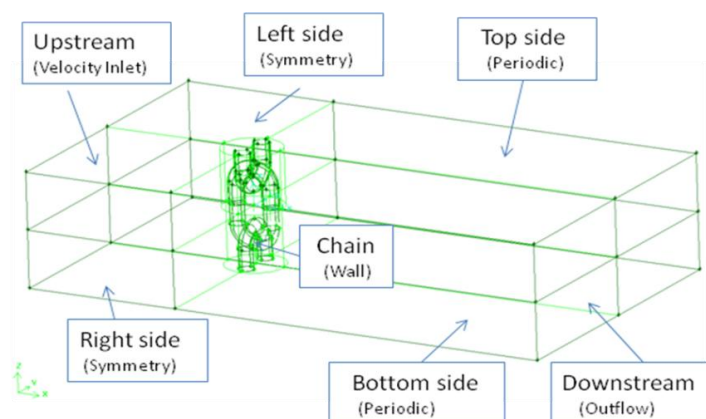
Figure 6-8 Illustration of computational domain and boundary conditions of stud-less chain

The size of computational domain is summarized in Table 6-1. The domain size has been verified by comparing the results of current domain with those from the domain enlarged along X- and Y-axis.

Table 6-1 Size of computational domain for the stud-less chain segment

Computational domain	Domain size
Upstream (X-axis)	10.0D
Downstream (X-axis)	25.0D
Lateral side (Y-axis)	20.0D
Span-wise direction (Z-axis)	8.0D

6.3.2 Computational mesh – spatial discretization

Hybrid meshes are used to discretize the space of the computational domain due to the complexity of the chain geometry, as shown in Figure 6-9.
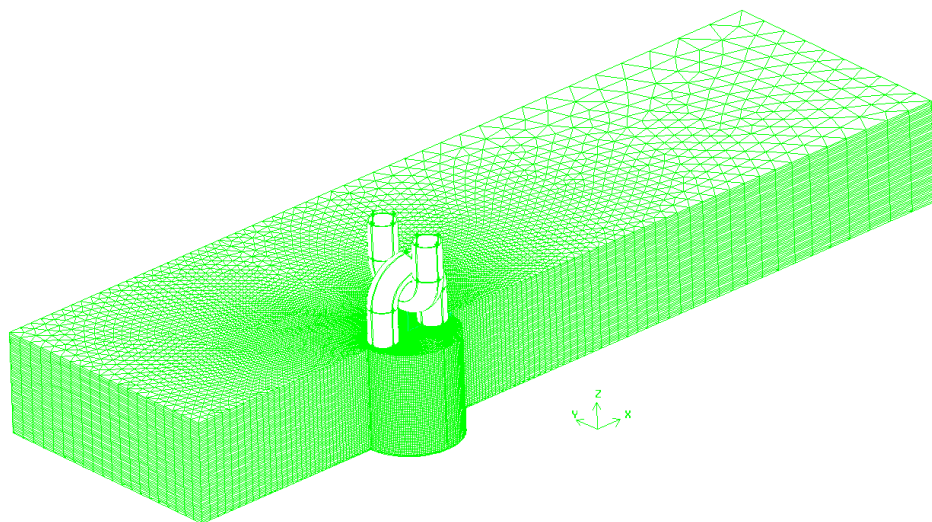
Figure 6-9 Computational mesh for the chain segment (mesh partly displayed)

Around the chain segment, a cylindrical domain is divided from the whole domain as shown in Figure 6-9. By turning the cylindrical domain around the z-axis, different flow angles between the upstream flow along the x-axis and chain segment can be considered. The mesh inside the cylindrical domain is shown in Figure 6-10. Three different flow angles, namely 0, 45 and 90 degree are considered. In Figure 6-10, the flow direction with 0 degree is illustrated.
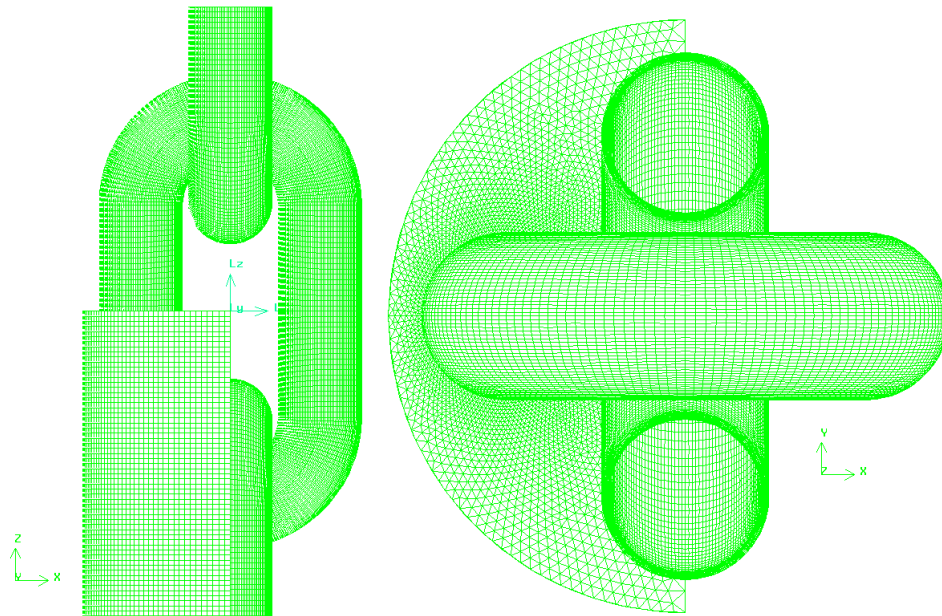
Figure 6-10 Local mesh in the cylindrical domain (0 degree flow direction)

In order to better solve the turbulent boundary layer near the surface of the chain segment, structured mesh with hexahedral cells is used in the inner layer of the wall. This is achieved by separating the connected point of two links with a gap of around 10% D. This sheltered gap is quite small compared to the span-wise length of chain segment and hence its effect could be ignored. The structured mesh around the wall surface of half chain segment is illustrated in Figure 6-11.

The near-wall region is solved directly by the 'Near-wall modelling' method that preferable has a y^+ value less than unit, which is achieved by setting the distance from the wall surface small enough at the wall adjacent cells. A close-up view of the mesh near the chain surface can be seen from Figure 6-12.
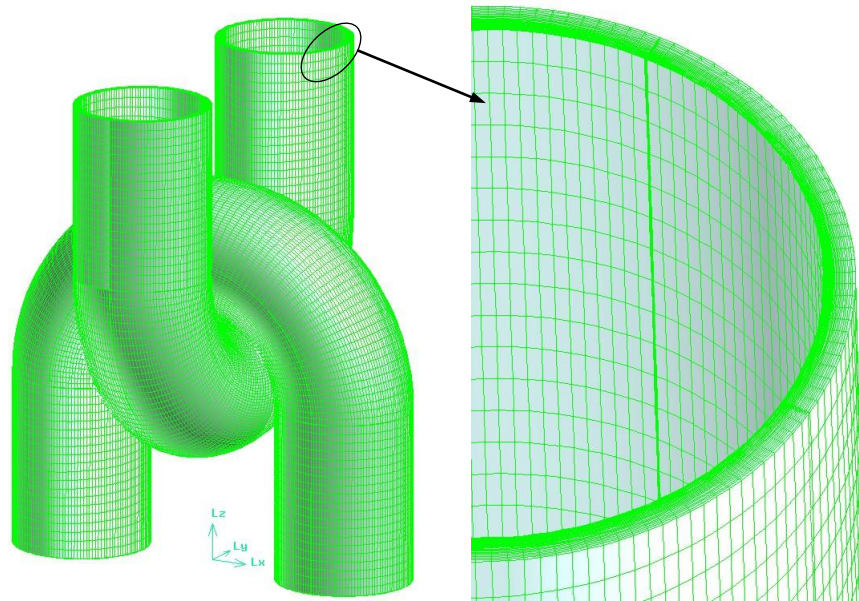
Figure 6-11 Structured mesh around the wall surface of the half-segment-chain
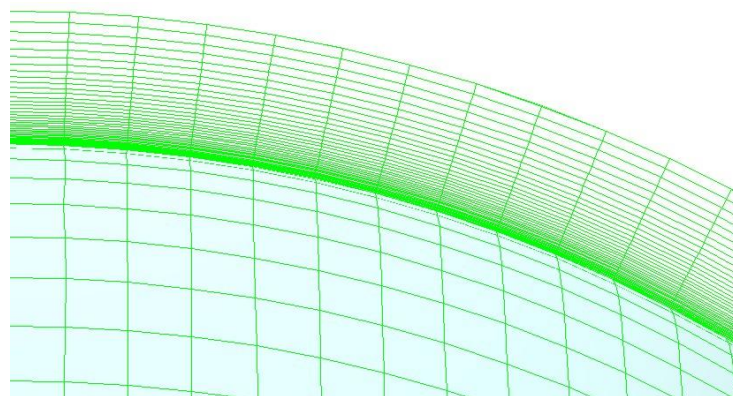
Figure 6-12 Close view of the mesh near the surface of chain segment

The total number of cells is around 6.49 million for the mesh case 1 with first cell height δ of $2 \times 10^{-4} D$, and is around 7.73 million for the mesh case 2 with δ of $5 \times 10^{-5} D$. The cell number along the span-wise direction of chain segment is 120 and a moderate growth ratio (1.08) is used for most of the cells.

6.3.3 Other details of computation

An implicit fractional step method is adopted here to advance the time and the selection of time step size is also referred to the LES simulations of flow past a cylinder. The numerical solution methods are summarized in Table 6-2.

Table 6-2 Setting of solution methods for LES modelling flow past a chain segment

Solution parameters	Method choice
Pressure-velocity coupling	Fractional Step (FSM, NITA)
Pressure	Standard
Momentum equations	Bounded Central Differencing
Gradient	Green-Gauss Node Based
Transient Formulation	1st-order Implicit
SGS model	Smagorinsky-Lilly $C_s = 0.1$

Most of the settings above are the same as LES modelling steady flow past a cylinder. The only difference is for the 'gradient' option, where the 'Green-Gauss Node Based' method is selected because it is known to be more accurate than the default cell-based scheme for unstructured meshes.

6.3.4 Results and discussions

First, in order to illustrate the results, the Reynolds number for steady flow past a fixed chain segment is defined as below:

$$\mathrm{Re} = \frac{U_\infty D}{\upsilon} \qquad \textbf{Eq. 6-2}$$

where, U_∞ is the far field steady flow velocity; D is nominal bar diameter of chain; υ is fluid kinematic viscosity.

The drag coefficient C_D and lift coefficient C_L of the stud-less chain are defined as follows:

$$C_D = \frac{F_D}{\frac{1}{2}\rho L D U_\infty^2} \ , \ C_L = \frac{F_L}{\frac{1}{2}\rho L D U_\infty^2} \qquad \textbf{Eq. 6-3}$$

where, F_D is the drag force on the chain segment; F_L is the lift force on the chain segment; L is length of the chain segment ($L = 8D$); ρ is fluid density.

The drag force per unit length F_D^1 applied to chain can be written as

$$F_D^1 = \frac{1}{2}\rho \cdot C_D \cdot D \cdot U_\infty |U_\infty| \qquad \textbf{Eq. 6-4}$$

From the definition of the force coefficients, it can be seen that the drag coefficient of the stud-less chain is referred to the nominal diameter of chain, which is same as in DNV rules (Such as DNV-OS-E301 and DNV-RP-C205).

1. Numerical results by LES model

1) Calculated force coefficients of the stud-less chain

Impact of flow direction

As mentioned before, three different flow directions have been considered for steady flow past a chain segment, as shown in Figure 6-13.
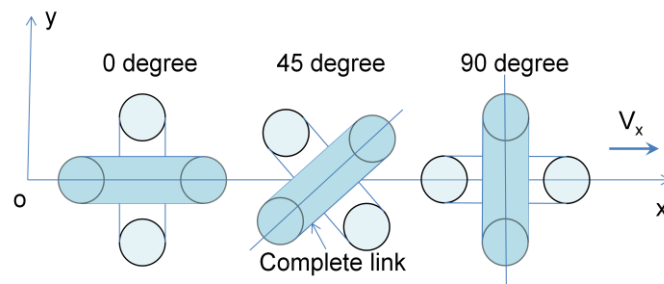
Figure 6-13 Direction definition of flow past a chain segment

To study the effect of the flow direction, steady flow past a chain segment at Reynolds number of 6×10^4 is considered for these three situations. The calculated drag coefficients for different cases are summarized in Table 6-3.

Table 6-3 Impact of flow direction upon drag coefficient of a stud-less chain ($\mathrm{Re}=6\times10^4$)

Case	Predicted C_D
0 degree flow	2.42
45 degree flow	2.36
90 degree flow	2.41

It can be seen from Table 6-3 that the predicted values of C_D are quite similar for these three cases, which is especially true for the 0-degree-flow case and 90-degree-

flow case. This is quite reasonable due to the geometrical characteristics of chain. In summary, the effect of flow direction (at least for these three directions) upon the drag coefficient of the stud-less chain can be ignored.
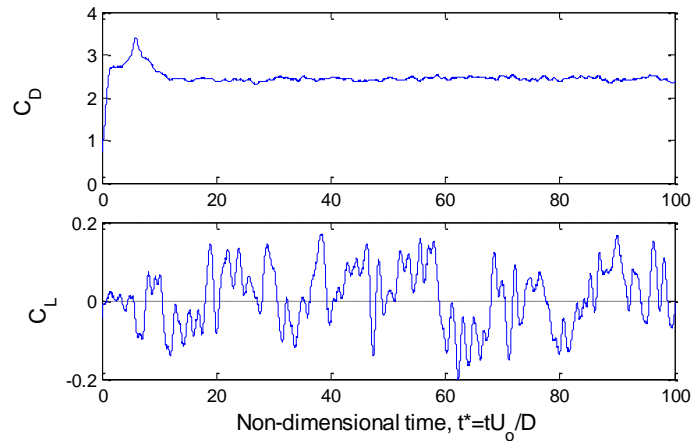
Figure 6-14 Time histories of predicted force coefficients of chain by LES ($\mathrm{Re} = 6 \times 10^4$, **0° flow)**

In Figure 6-14 the time histories of force coefficients of chain are plotted for 0-degree flow at Re of 6×10^4. Using a power spectrum analysis of the lift coefficient history, it can be seen that no obvious single frequency of vortex shedding can be identified, as shown in Figure 6-15. This is totally different from the steady flow past a smooth cylinder at this Reynolds number which has dominate vortex shedding frequency and corresponding Strouhal number.
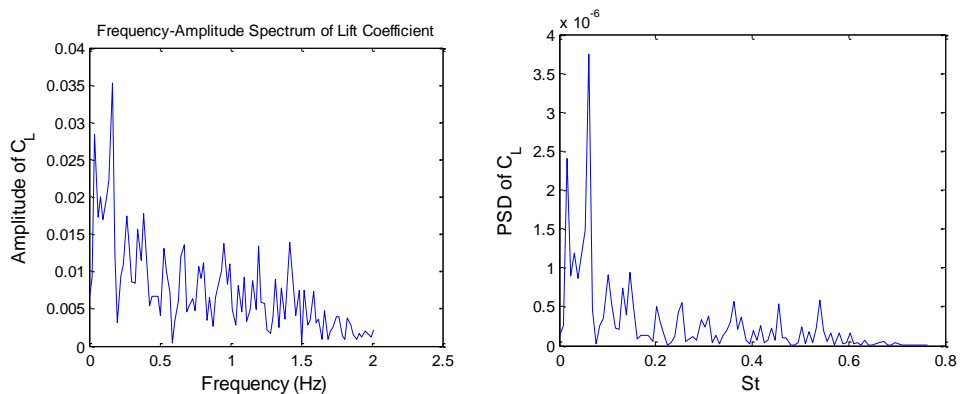
Figure 6-15 Statistical properties of lift coefficient of the chain segment ($\mathrm{Re} = 6 \times 10^4$, **0° flow)**

Reynolds number effect

Due to the negligible effect of flow direction, here, taking the steady flow with flow direction of 0 degree for instance, the impact of Reynolds number upon the drag coefficient of the stud-less chain is considered. The calculated drag coefficient as function of Re is illustrated in Figure 6-16, together with the recommended values from DNV-RP-C205.
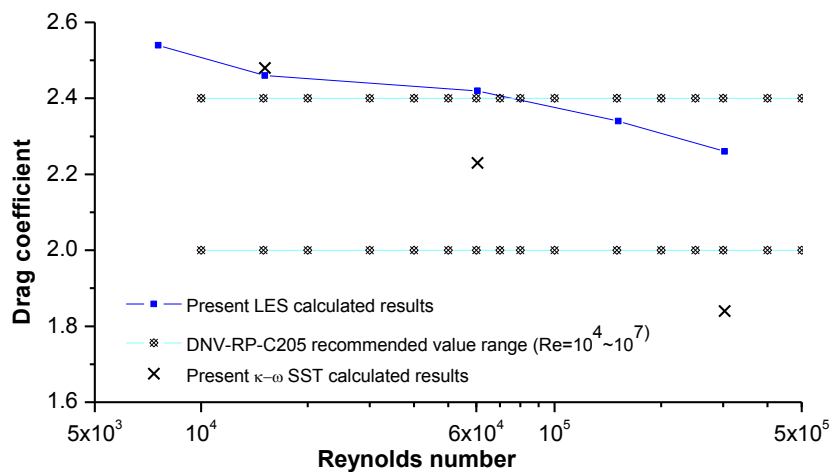
Figure 6-16 Predicted drag coefficient of stud-less chain as function of Reynolds number

From Figure 6-16 it can be seen that with the increase of Reynolds number, the predicted drag coefficient decreases. The range of the numerical predicted C_D is also in quite good agreement with the DNV recommended range ($C_D : 2.4 \sim 2.0$ for $\mathrm{Re}: 10^4 \sim 10^7$) . For the numerical predicted C_D values, the highest Reynolds number considered here is 3×10^5 due to the fact more expensive computational cost is required for even higher Reynolds number.

2) Contours of x-velocity

Contours of x-velocity are plotted for different flows past the chain-segment to give more vivid understanding of the flow characteristics. In order to plot the x-velocity contour at different planes along the span-wise direction, several surfaces have been defined, as shown in Figure 6-17.
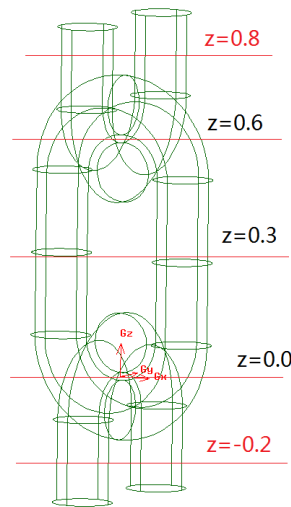
Figure 6-17 Different X-Y planes defined along the span-wise direction of the stud-less chain

Flows past a chain segment at Re of 1.5×10^4 and 6×10^4 with 0-degree direction are considered, together with 45-degree flow at Re of 6×10^4, as illustrated in Figure 6-18, Figure 6-19 and Figure 6-20. From these instantaneous x-velocity contours (especially at the locations z=-0.2/0.8), it can be seen that the reason why lift force of the chain segment is quite small is due to the flow interaction.

Contours of X Velocity (m/s) (Time=1.0000e+02)

ANSYS FLUENT 13.0 (3d, dp, pbns,

Contours of X Velocity (m/s) (Time=1.0000e+02)

ANSYS FLUENT 13.0 (3d, dp, pbns, l

Contours of X Velocity (m/s) (Time=1.0000e+02)

ANSYS FLUENT 13.0 (3d, dp, pbns
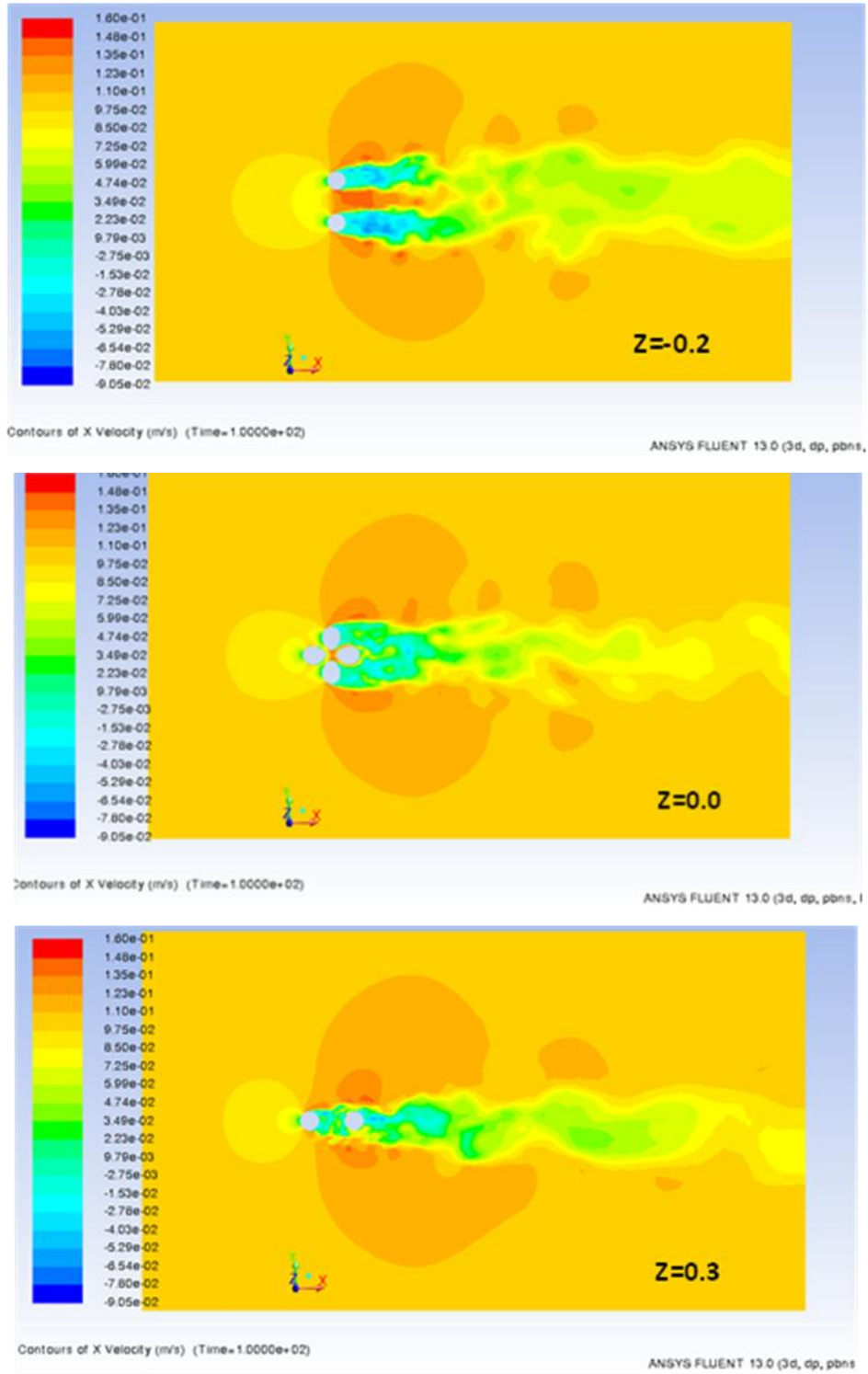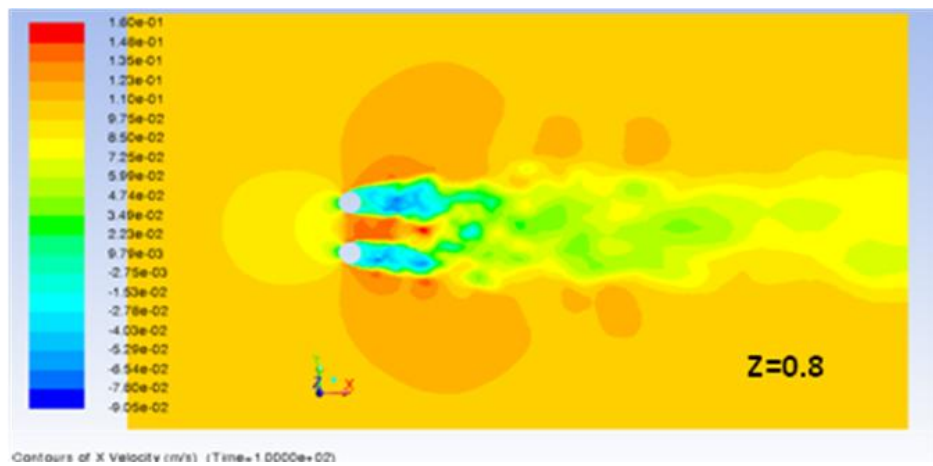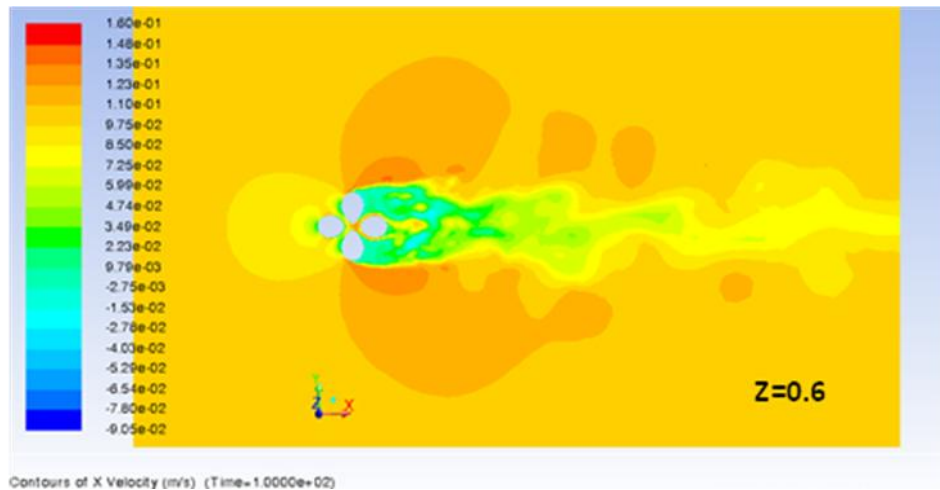
Figure 6-18 Instantaneous x-velocity contour for 0-degree flow at $\mathrm{Re} = 1.5 \times 10^4$
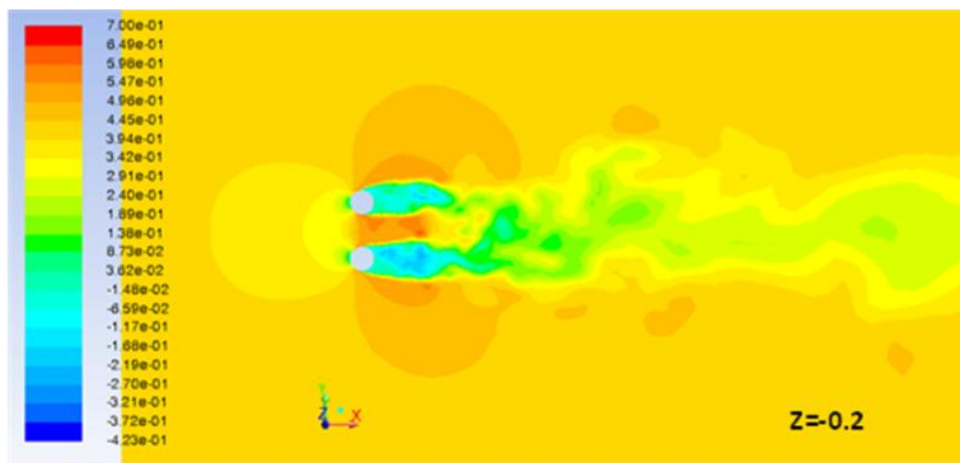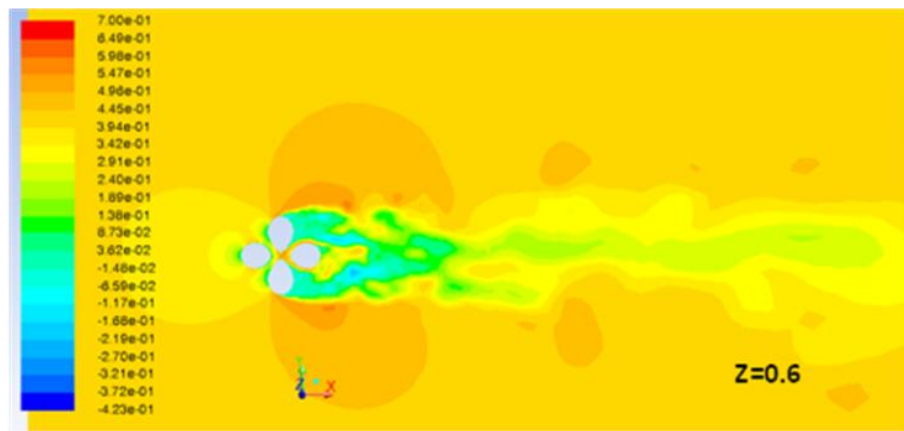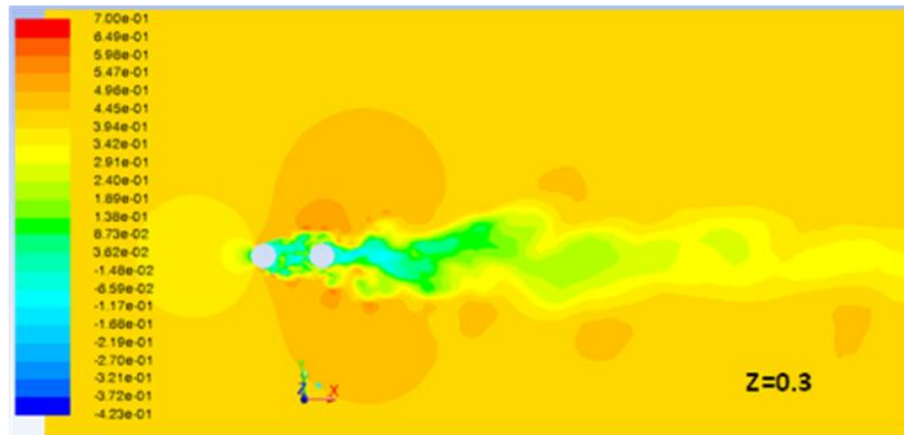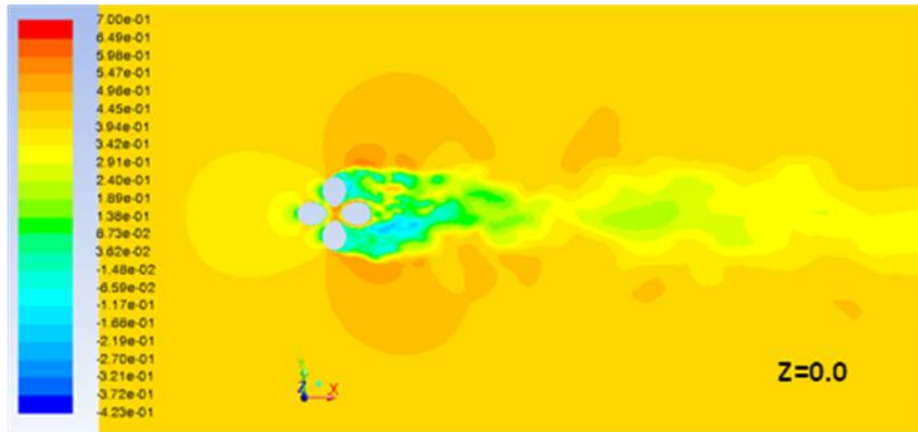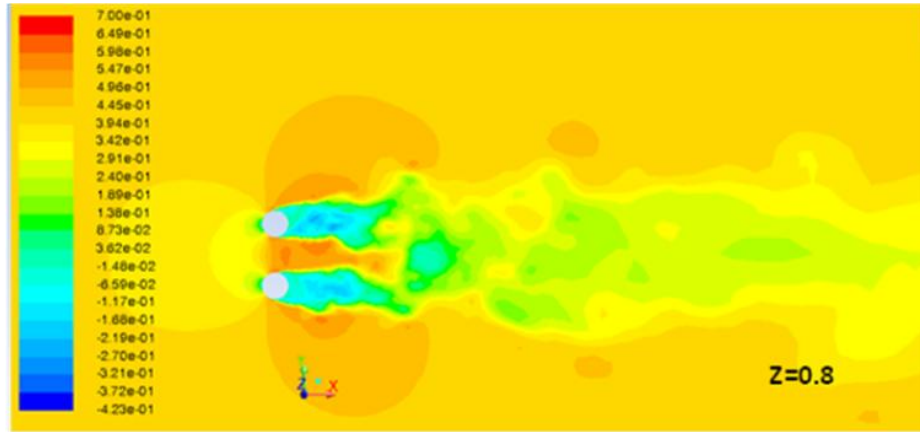
Figure 6-19 Instantaneous x-velocity contour for 0-degree flow at $\mathrm{Re} = 6 \times 10^4$
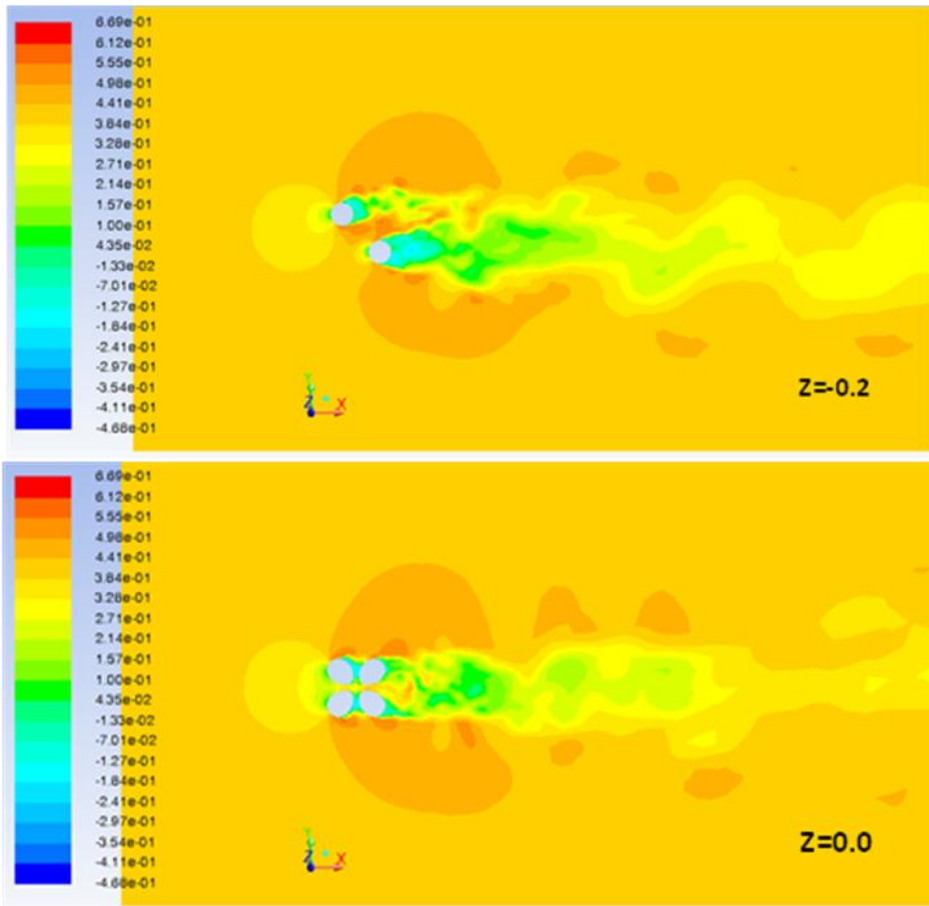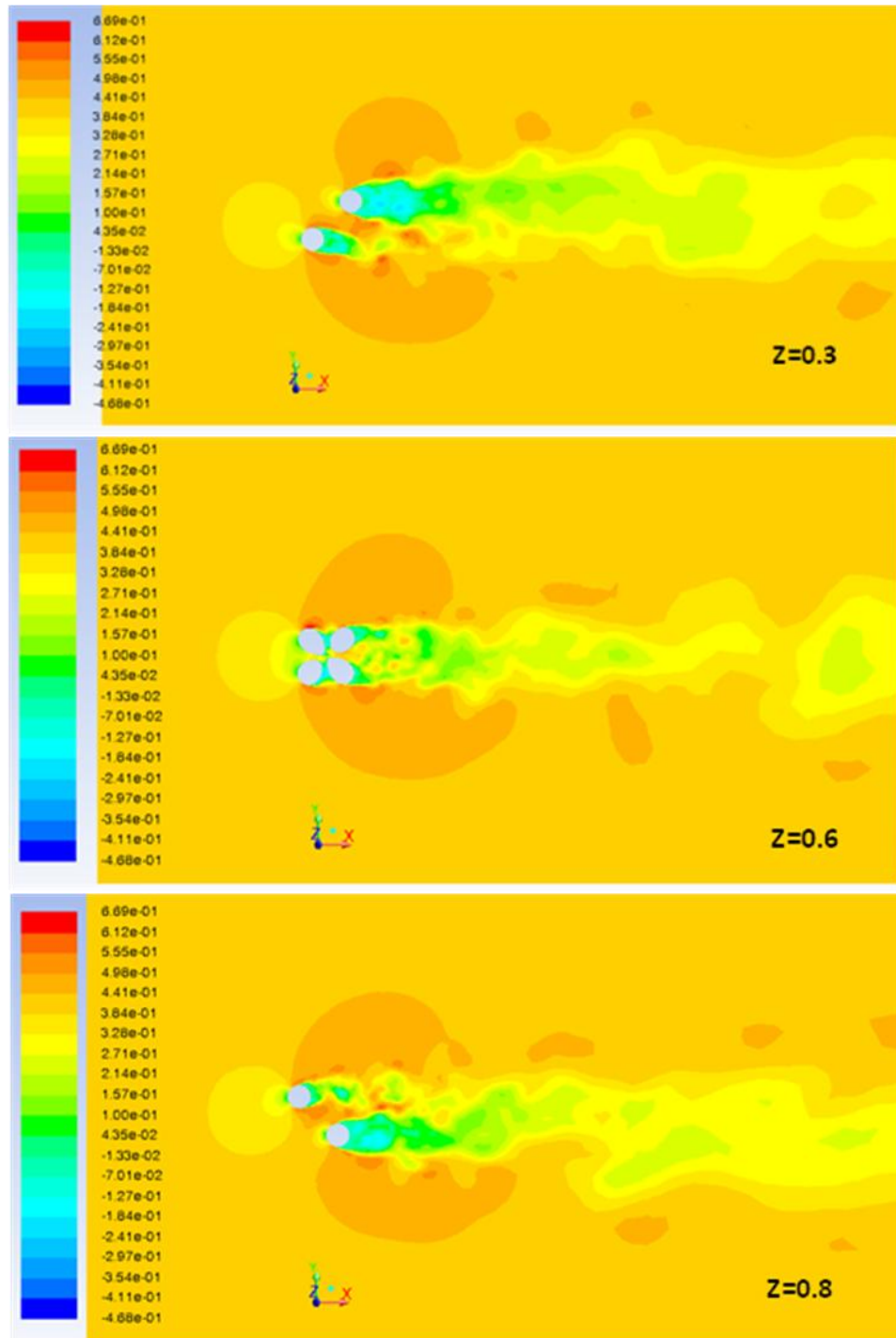
Figure 6-20 Instantaneous x-velocity contour for 45-degree flow at $\mathrm{Re} = 6 \times 10^4$

2. Discussions

1) Effect of computational domain and boundary conditions

If only considering the geometrical characteristics of chain, two half-links could be selected for the simulation, due to its geometrical symmetry as shown in Figure 6-21.
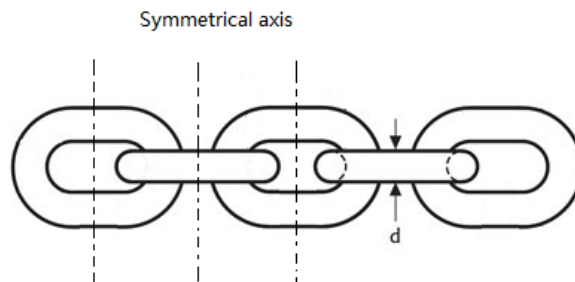
Figure 6-21 Geometrical symmetry of stud-less chain

The corresponding domain and boundary conditions can be defined as shown in Figure 6-22. One obvious difference of this numerical model from the one shown in Figure 6-8 is that the number of cells can be half reduced if under same mesh strategy. The other difference is that 'symmetry' boundary conditions instead of 'periodic' are applied on the top and bottom surfaces, because the physical geometry does not have a periodically repeating nature.
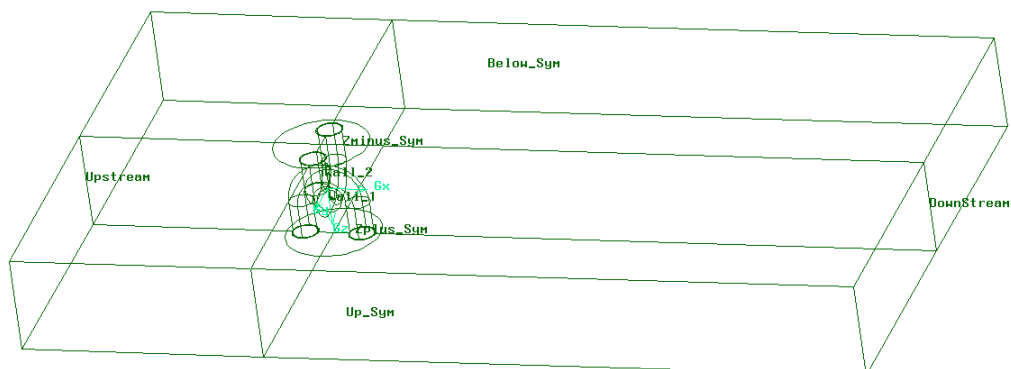
Figure 6-22 Alternative computational domain of the stud-less chain

However, 'Symmetry' boundary conditions are used not only when the physical geometry of interest has mirror symmetry but also when the expected pattern of the flow/thermal solution does. In order to verify this model, steady flow with 0-degree direction past the chain at Re of 6×10^4 is considered, of which calculated drag coefficient is compared with the value obtained from the model shown in Figure 6-8.

Table 6-4 Calculated C_D from two different models by LES model ($\mathrm{Re} = 6 \times 10^4$)

Model case	Number of cells	Predicted C_D
Two half-links (symmetry)	3.24 Million	2.57
One link plus two half-links (period)	6.49 Million	2.42

It can be seen from Table 6-4 that the first model seems to slightly over-predict the drag coefficient of the chain, which could be due to the selection of the 'Symmetry' boundary condition. However, when considering the saving of computational cost, this model is acceptable.

2) Effect of grid resolution

For the near-wall region, the 'Near-wall modelling' method adopted here requires a desirable y^+ of value less than unit. Two mesh cases with different first cell heights ($\delta_1 = 2 \times 10^{-4} D, \delta_2 = 0.5 \times 10^{-4} D$) have been considered in order to study the effect of y^+ upon the calculated drag coefficient. The simulation results listed in Table 6-5 are for steady flows past a chain segment with 0-degree direction at different Reynolds numbers.

Table 6-5 Impact of y^+ upon the calculated C_D of stud-less chain

Reynolds number	Mesh case/Cell number/δ	y^+	Predicted C_D
6×10^4	case1/6.49Million/δ_1	1.22	2.42
	case2/7.73 Million /δ_2	0.36	2.43
1.5×10^5	case1/6.49 Million /δ_1	2.43	2.20
	case2/7.73 Million /δ_2	0.65	2.34

As listed in Table 6-5, calculated C_D values for cases with Re number of 6×10^4 are almost the same when values of y^+ of two cases are 1.22 and 0.36 respectively. However, at Re of 1.5×10^5 results of two cases show some discrepancies, which could be due to the comparatively big y^+ of mesh case1.

Besides, the impact of grid resolution along the span-wise direction could be non-negligible, especially for the high Reynolds number. From the experience of LES modelling steady flow past a smooth cylinder, it is known that without enough grids along the span-wise direction, the predicted drag coefficient by LES is a little smaller than the experimental value for high Reynolds number. That could explain why the LES predicted drag coefficient of chain seems to decrease quickly with the increase of the high Reynolds number, as shown in Figure 6-16. Normally, it would be expected that the Reynolds number effect on the drag coefficient of chain would be less important when compared to that of the smooth circular cylinder.

3) Effect of turbulence model

The performance of the LES and URANS models has been assessed by comparison of simulation results of steady flow past a cylinder. It is found that URANS would over-estimate the drag coefficient of a cylinder for small Reynolds number and under-estimate the drag coefficient for high Reynolds number.

Taking 0-degree flow past a chain segment at several different Re numbers, the simulation results obtained from LES and URANS are compared, as shown in Figure 6-16 and Table 6-6.

Table 6-6 Predicted C_D for stud-less chain by different turbulence models

Re number	Predicted C_D	
	LES model	$k-\omega\ SST$ model
1.5×10^4	2.46	2.48
6×10^4	2.42	2.23
3×10^5	2.26	1.84

As indicated in Table 6-6, the $k-\omega\ SST$ model noticeably under-estimates the drag coefficient of stud-less chain at high Reynolds number.

6.4 CFD simulation of a smooth chain oscillating in water

The effect of Re number on drag coefficients of a smooth stud-less chain has been studied by considering different steady flows past a fixed smooth stud-less chain segment. It can be seen that, with the increase of Re, the drag coefficient of the smooth stud-less chain decreases. However, the effect of Re on the drag coefficient

of the smooth chain is not as important as that for a smooth circular cylinder. The effect of KC on the drag coefficients of the chain is considered here by simulating a smooth chain segment oscillating in water. In order to emphasise the KC number effect, the Re number will be fixed during one set of oscillating motions while the KC number varies. This is achieved by simultaneously changing the amplitude A and the period T of the oscillating motion to keep the same velocity amplitude ($U_M = A \cdot 2\pi / T$).

6.4.1 Computational model and methods

CFD simulations of a smooth circular cylinder oscillating in still water have been done to verify the numerical models. For modelling the chain segment oscillating in water, computational model and methods will refer to those for oscillating cylinder in water. The harmonic motion of the stud-less chain segment is represented by the movement of whole cell zone (defined by Mesh Motion) in the numerical model. The URANS ($k - \omega\ SST$) turbulence model is mainly selected to calculate the in-line force of the oscillating stud-less chain due to its desirable performance in modelling the oscillating cylinder in still water. However, the effect of this turbulence model will be studied by comparison of results obtained from the URANS and LES models.

Considering the big KC number concerned for the oscillating chain, the computational domain along the X- and Y-direction has been enlarged to $120D$ and $60D$ respectively, while the domain size along span-wise direction keeps the same as that for the chain under steady flow. A quarter of the computational domain together with the chain segment is shown in Figure 6-23.
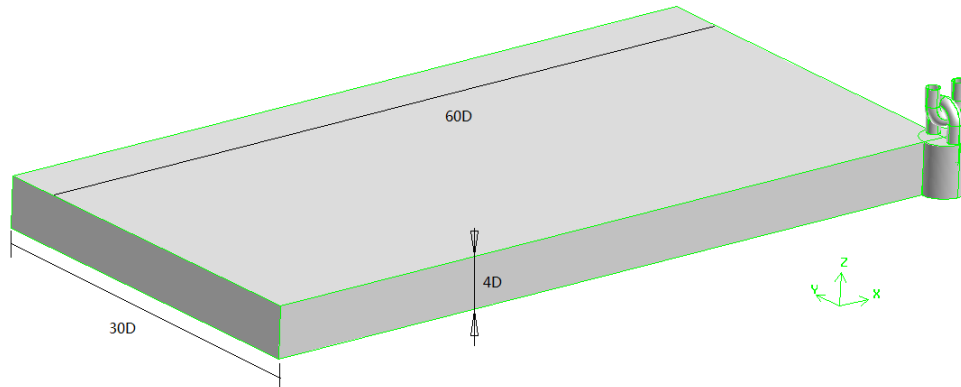
Figure 6-23 Quarter computational domain of the stud-less chain under oscillation motion

Hybrid meshes are also used to discretize the space of the computational domain due to the complexity of the chain geometry. A structured mesh with hexahedral cells is used in the inner layer of the wall in order to better solve the turbulent boundary layer near the surface of the chain segment. The distance from the wall surface at the wall adjacent cells is set as $5\times10^{-5}D$, in order to guarantee a desirable y^+ value less than unity for all the Re number considered. The near-wall region is then solved directly by 'Near-wall modelling' method. The mesh inside the cylindrical zone is similar to that of the chain segment under steady flow. The total mesh number is around 9.65 million.

Table 6-7 Boundary conditions for the oscillating chain segment in still water

Boundary locations	Boundary conditions
Up-stream	Velocity Inlet
Down-stream	Pressure Outlet
Lateral sides (Y-axis)	Symmetry
Top/bottom sides (Z-axis)	Periodic
Stud-less chain	No-slip wall

The boundary conditions are summarised in Table 6-7 for the oscillating stud-less chain segment in still water, which are similar as those for oscillating cylinder in still water.

Other numerical aspects include time-stepping size and numerical methods adopted in the turbulence models. The size of time-stepping will mainly depend on the Re number. However, the effect of the KC number, which is related to the oscillation period T, is also included. For oscillating motions with same Re number, the motion with bigger KC number (bigger period T), a slightly bigger time-step is used to accelerate the simulation. The numerical methods adopted by LES model are similar as those in Table 6-2. For URANS turbulence model, the numerical methods are summarised in Table 6-8.

Table 6-8 Numerical methods for URANS modelling an oscillating chain segment

Solution parameters	Method choice
Pressure-velocity coupling	SIMPLE
Pressure	Standard
Momentum equations	2nd-order Upstream
Gradient	Green-Gauss Node Based
Transient Formulation	1st-order Implicit

6.4.2 Numerical results and discussions

For the stud-less chain oscillating in water along X-direction, the chain segment with 0-degree-flow direction (see Figure 6-13) is considered. Several series of different oscillation motions are considered. For each series of oscillation motions with same

Re numbers, the numerical results of in-line force coefficients are compared to mainly investigate the effect of KC number on drag coefficients of stud-less chain.

Before plotting the results, the definitions of force coefficients are illustrated first. For the transverse lift force coefficient, the definition for oscillating stud-less chain is similar as that for the fixed stud-less chain segment under steady flow

$$C_{L\max} = \frac{F_{L\max}}{\frac{1}{2}\rho LDU_M^2} \qquad \textbf{Eq. 6-5}$$

For the in-line force coefficients, the drag coefficient and added mass coefficient is determined by the formula:

$$F_x = \tfrac{1}{2} C_D \cdot \rho LDU |U| + C_m \cdot \rho \cdot \Delta V \cdot \dot{U} \qquad \textbf{Eq. 6-6}$$

where, F_x is the inline force along the X-axis; L is the length of the chain segment ($8D$); ΔV is the displaced volume corresponding to the chain segment.

From the definition of drag coefficient and added mass coefficient, it can be seen that the drag coefficient of stud-less chain under oscillation is also referred to the nominal diameter whist the added mass coefficient is based on the actual volume.

1. Numerical results by the URANS model

By the fitting of Morrison equation (Eq. 6-6) with calculated in-line forces obtained from the URANS ($k-\omega$ SST) model and with the in-line force coefficients obtained through 'least-square' fitting method, the time series of fitted forces and

CFD force are shown in Figure 6-24 and Figure 6-25 for oscillating chains with different Re and KC numbers.
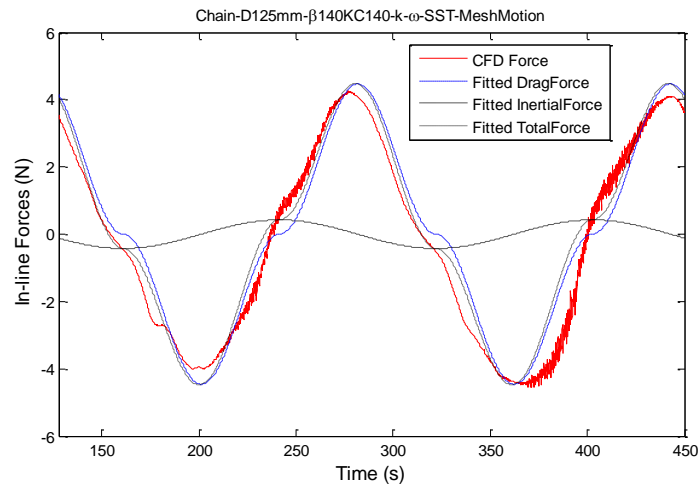
Figure 6-24 CFD force and fitted forces for oscillating chain with $KC140\beta140$
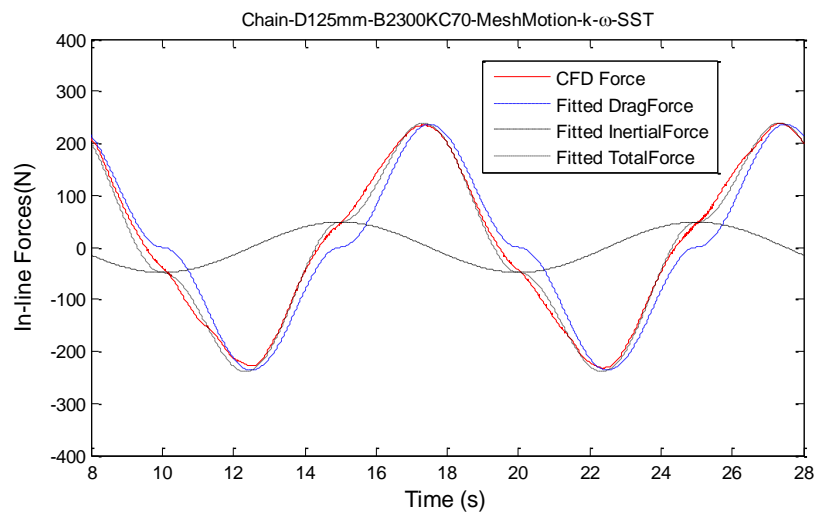
Figure 6-25 CFD force and fitted forces for oscillating chain with $KC70\beta2300$

For the oscillating chain in still water, the in-line force coefficients are plotted as a function of KC number and Re number (see Figure 6-26, Figure 6-27), although alternatively the in-line force coefficients could be plotted as a function of KC and β ($\beta = \mathrm{Re}/KC$).
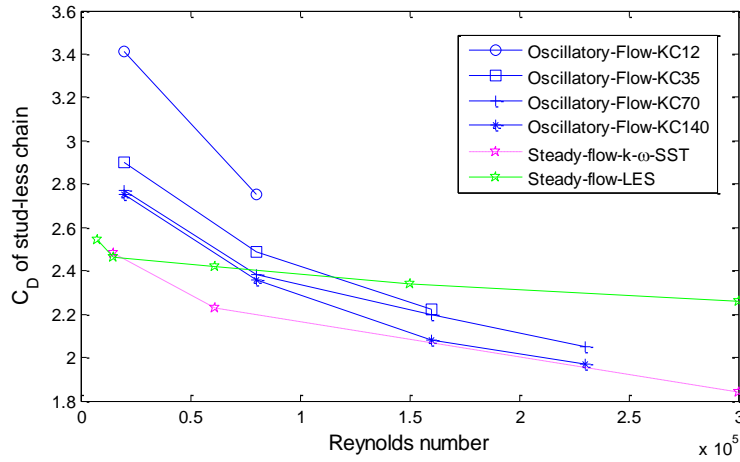
Figure 6-26 Drag coefficients of stud-less chain under different Re **and** KC **numbers**
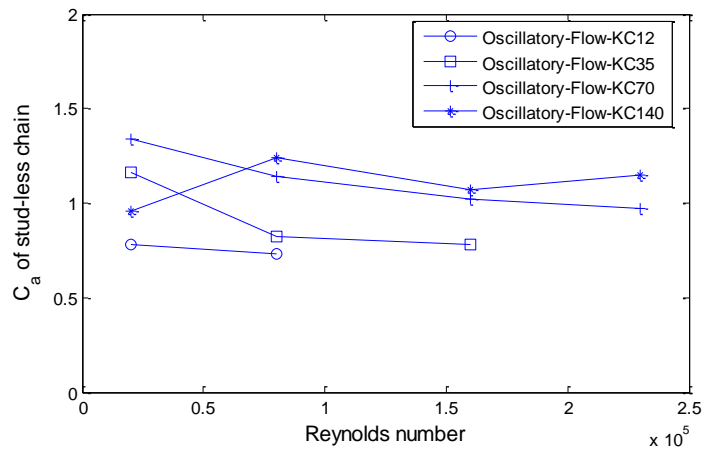
Figure 6-27 Added-mass coefficients of stud-less chain under different Re **and** KC **numbers**

The fitted added-mass coefficients of stud-less chain exhibits a small range of scatter around 1.0 for all the oscillatory flows, which are better than the results obtained by Young (2005) (see Figure 2-6), which showed big scatter. For fitted drag coefficients, from Figure 6-26 it can be seen that:

1) For flows with lower Re, effect of KC on C_D of stud-less chain is very important.

Under smaller KC number, the C_D of stud-less chain is much greater than the

C_D value of stud-less chain under steady flow with same Reynolds number. With increase of KC number, the C_D of stud-less chain will decrease and would tend to the C_D value under steady flow;

2) When the Reynolds number increases to a higher value, it seems that the effect of KC on C_D value becomes less important, while the high Re value will dominate the C_D value;

3) For oscillatory flows with a certain fixed KC number, the C_D of stud-less chain will decrease with increase of Re, which is similar with that for steady flow.

As mentioned before, limited experiments of chain under unsteady flows have been completed. These experiments were conducted for oscillating chain under low Reynolds numbers and their results seem to be a less reliable benchmark. In Figure 2-2, C_D values of a stud-link chain under oscillation tests are included. It can be seen that under given Re $(\sim 10^4)$ and KC $(163 \sim 306)$, C_D values of the stud-link chain are quite close to those under towing tests with similar Re. It indicates that the effect of KC will become less significant when KC is big enough, which is in agreement with the present numerical results of a stud-less chain.

2. Further discussion-effect of turbulence model

Despite the unsatisfying performance of the LES model for oscillating cylinder in still water, an attempt is still made to check the results obtained by LES for the oscillating chain in still water. The results comparisons between the LES and $k - \omega$ SST models are listed in Table 6-9 for two different oscillations.

Table 6-9 Comparisons of numerical results obtained by different turbulence models

Turbulence models	Oscillating chain $\beta140KC140$			Oscillating chain $\beta2300KC35$		
	C_D	C_a	δ_F	C_D	C_a	δ_F
LES	2.69	2.31	0.013	3.23	1.07	0.023
$k-\omega\ SST$	2.75	0.96	0.048	2.49	0.82	0.015

For the oscillating chain with $KC140\beta140$, the C_D value obtained by LES model is close to that obtained through $k-\omega\ SST$ model, while the added-mass coefficient of the oscillating chain obtained by LES model is over-predicted. To investigate the cause of discrepancies, time series of CFD in-line forces calculated by different turbulence models and their corresponding fitted inertial forces are shown in Figure 6-28.
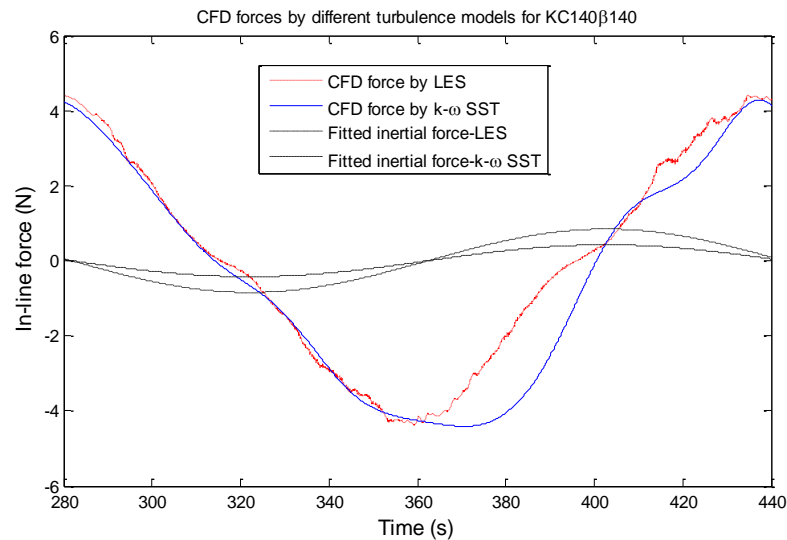
Figure 6-28 Time histories of in-line forces and fitted inertial forces

The CFD force obtained by $k-\omega\ SST$ model is filtered to remove the high-frequency undesirable vibrations as seen in Figure 6-24. It can be observed that the CFD in-line forces predicted by LES and URAN models have similar peak values

while slight differences exist in their shape. For this oscillation with high KC equal to 140, drag force is much bigger than inertial force, which can also be seen from Figure 6-24. So a small difference between the CFD in-line forces could cause big discrepancies between the fitted add-mass coefficients.

For the oscillating chain with $KC35\beta2300$, both in-line force coefficients of the oscillating chain obtained by LES model are bigger than those obtained by the $k-\omega$ SST model. The time histories of CFD in-line forces calculated by these two turbulence model, together with fitted forces for the $k-\omega$ SST model, are plotted in Figure 6-29. The peak value of the CFD in-line force calculated by LES is bigger than that predicted from the $k-\omega$ SST model, which leads to a bigger fitted drag coefficient. Under this given KC, the inertial force is comparable with the drag force, and hence the error of fitted added-mass coefficient is reduced.
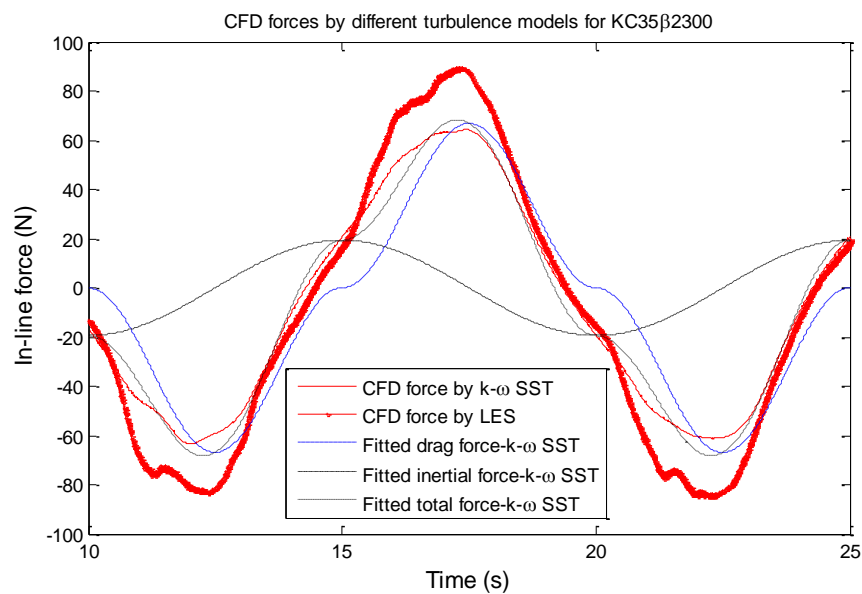
Figure 6-29 Time histories of in-line forces obtained by different turbulence models

Overall, it can be seen that results obtained by LES for the oscillating chain are not very satisfactory, although its performance seems to be better than that for the oscillating cylinder.

6.5 Concluding summary

In this chapter, drag coefficients of a stud-less chain under a range of KC and Re numbers are predicted by CFD methods. For steady flow past the stud-less chain the LES model is mainly used. It is found that the effect of Re number (in the range of $10^4 \sim 10^6$) on C_D of the stud-less chain is less important, although with an increase of Re number the drag coefficient decreases.

The URANS model ($k - \omega\ SST$) is mainly used for modelling oscillating stud-less chain in still water. The effect of KC number on C_D of the stud-less chain is significant for flows with low Re numbers while the effect of KC seems to be less noticeable for unsteady flows with high Re numbers.

Overall, with respect to the problem of concern in this thesis, the $k - \omega\ SST$ model is more desirable for engineering applications due to its low computational cost and acceptable accuracy.

7. Damping effect on FPSO motions of moorings with C_D variation

7.1 Overview

FPSOs are often attached to the moorings through a swivelling turret and weather vane into the direction of the environmental forces. FPSO's horizontal motions have smaller natural frequencies than those of significant wave energy, and thus are more likely to be excited by second-order difference-frequency wave forces. For such platforms, LF surge motions are the most significant horizontal motions. During part of the slow-drift cycle when the mooring is most taut, wave-frequency motions will contribute and cause the maximum tension in the taut lines. While these ship-like platforms have very little inherent surge damping, damping of moorings/risers can play a significant role in limiting surge resonant response and consequently reducing the probability of mooring failure.

In this chapter, the system damping of a moored FPSO system in the surge direction is first considered. Except damping of moorings, which has already been discussed, other damping contributions to the slow-drift motion are discussed in order to mainly know the comparative importance of each component. Unlike in a separated analysis where each component of system damping has to be estimated as input to the calculation, in the coupled analysis the damping effect of moorings is considered by the direct calculation of the mooring forces that lead to damping. Responses of the moored FPSO system under collinear environmental conditions are calculated here using coupled analysis, however the responses of the FPSO could be more severe in non-collinear environmental conditions (Ward et al., 2001). In the coupled analysis,

the effect of mooring line damping on the motion responses of the moored FPSO is investigated by considering the C_D variation.

7.2 System damping of a moored FPSO system

A ship-shaped FPSO moored in deep water can experience resonant low frequency (LF) motions in the horizontal plane due to action from the slowly changing second-order wave forces. The resonant response of the FPSO is limited only by the relevant damping mechanisms. While for wave-frequency response, most of the damping is provided by the radiation of free surface waves, the wave radiation damping is normally negligible for most of practical slow drift motions. The damping of slow-drift motions of a moored system, except the damping of moorings mentioned before, mainly consist of the following components:

1) Wave drift damping;

2) Damping of viscous resistance of floating structure;

3) Wind damping;

4) Damping from the riser/mooring seabed interaction;

5) Damping of risers.

Damping from the riser/mooring seabed interaction results from the line friction on the seabed, hence it will depend on the nature of the bottom soil. Limited work has been performed on this kind of damping. However, it seems that in most situations, this damping is very small when compared to the damping of moorings/risers due to hydrodynamic forces (Qiao and Ou, 2010).

Wind damping is due to the drag force of wind acting on the upper structures, which is normally calculated by using OCIMF (Oil Companies International Marine Forum) data for typical VLCCs. The damping of hull viscous resistance results from the viscous force, which is approximately proportional to the square of the motion velocity. The viscous resistance force in surge direction can be calculated according to the ITTC'57 method or by using OCIMF data, which will be discussed later.

The magnitude of wave drift damping is related to the second order wave force and proportional to the square of wave height (Wichers, 1982). According to the study of Tahar and Kim (2003), for slowly varying horizontal plane responses, wave drift damping in surge is much smaller than viscous damping from hull, mooring, and risers, even under 100-year hurricane with large wave (significant wave height $H_s = 12.2m$).

Damping contributions (linear damping B) as function of significant wave height H_s for an FPSO have been studied by Molin (1993), as shown in Figure 7-1.
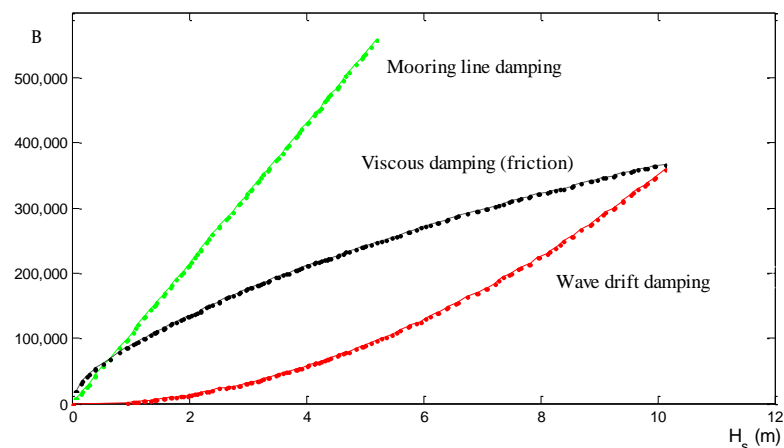
Figure 7-1 Comparison of slow-drift damping components (reproduce from Molin, 1993)

It can be seen from Figure 7-1 that although proportional to the wave height squared, the wave drift damping in surge is smaller than the viscous damping from hull/moorings. In the coupled dynamic analysis of a turret-moored FPSO (Kim et al., 2005), it was also found that the wave drift damping is small and thus was not included in their analysis. Therefore, only the damping of hull viscous resistance and damping of moorings/risers are considered in the ensuing discussion.

7.2.1 Damping of hull viscous resistance

The prediction of hull viscous damping will depend on the estimation of hull viscous forces, which are normally calculated by empirical formulas. Accurate estimation of hull viscous damping is one of the difficult factors in the numerical simulation of a turret-moored FPSO (Tahar and Kim, 2003). The viscous part in normal direction contributes significantly to the hull dynamic responses, especially in currents. The coupling terms due to the combined modes of motions in still water and in current are not easy to handle as well. The damping of hull viscous resistance is important to the sway and roll motions of the vessel, however, given the problem concerned, only the hull viscous damping in surge will be considered.

1. Viscous resistance

The viscous resistance of the hull consists of two parts, namely skin friction and form drag. The first term is the tangential-to-surface component of viscous resistance due to surface roughness, while the second term is the viscous part in normal-to-surface direction caused by the unbalanced pressure distribution. The complex nature of the problem results in the viscous force normally being calculated by empirical formulas.

1) ITTC'57 method

The viscous resistance of ship can be calculated by the following formula:

$$R_v = \frac{1}{2} \cdot C_v \cdot \rho \cdot S_W \cdot U^2 \qquad \textbf{Eq. 7-1}$$

where, C_v is the viscous resistance coefficient; ρ is the water density; S_W is wetted surface of hull; U is ship relative velocity.

C_v contains two parts, i.e. $C_v = C_F + C_N$, where, C_F is the tangential component of viscous resistance coefficient and C_N is the normal component of viscous resistance coefficient. C_F is due to skin friction parallel to ship's hull and can be calculated according to the Correlation Line of ITTC' 57:

$$C_F = \frac{0.075}{\left(Log\,\mathrm{Re} - 2\right)^2} \qquad \textbf{Eq. 7-2}$$

where, $\mathrm{Re} = UL/\upsilon$ ($\upsilon = 1.35\mathrm{E}\text{-}6\,m^2/s$); L is length of ship.

C_N is caused by unbalanced pressure distribution along the hull form of ship and can be calculated by the product of C_F with form factor K_F, namely $C_N = K_F \cdot C_F$. So,

$$R_v = \frac{1}{2} \cdot (1 + K_F) \cdot C_F \cdot \rho \cdot S_W \cdot U^2 \qquad \textbf{Eq. 7-3}$$

2) OCIMF method

The OCIMF has performed extensive towing test for VLCCs, and experimental data were compiled into the current load coefficient. Here, according to the relative velocity, the longitudinal current force coefficient (see Figure 7-2) is used to calculate the viscous resistance of the FPSO in comparison with that from ITTC'57 method

$$F_{Xc} = \frac{1}{2} C_{Xc} \rho U_c{}^2 L_{BP} T_D \qquad \text{Eq. 7-4}$$

where, F_{Xc} is surge current force on vessel; C_{Xc} is longitudinal current force coefficient; U_c is average current velocity.

It should be noted that the towed test program mainly concerned L/B ratios between 6.3 and 6.5 to consider the majority of existing VLCCs. For a VLCC with L/B of 5.0 an increase in the longitudinal coefficients of maximum 25% to 30% is to be expected for the smaller current angles.

FIGURE 16   COMPARISON OF "OLD OCIMF" AND "NEW OCIMF"
LONGITUDINAL CURRENT FORCE COEFFICIENTS
FOR WATER DEPTH TO DRAFT RATIO OF 3.0 – LOADED TANKER
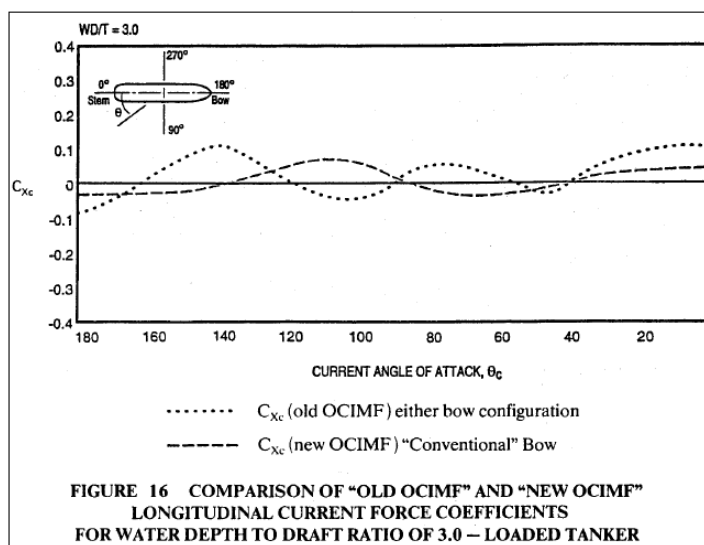
Figure 7-2 Longitudinal current force coefficients of OCIMF

3) Comparison between two different methods

The wetted surface area can be approximately calculated by Denny-Mumford formula, namely:

$$S_W = L_{BP}(1.7T_D + B \cdot C_B)$$
  Eq. 7-5

Take $C_B = 0.82$, $B = 52m$, $T_D = 12m$, $K_F = 0.21$, then

$$R_v = \frac{1}{2} \cdot 6.35 \cdot C_F \cdot \rho \cdot U^2 \cdot L_{BP} \cdot T_D$$
  Eq. 7-6

In the range of $0.3 - 2m/s$ of flow velocity, C_F value varies slightly $(1.7 \times 10^{-3} - 2.2 \times 10^{-3})$. C_{Xc} is around 0.04 according to the Figure 7-2, then

$$R_v \approx \frac{1}{2} \cdot [0.011 \sim 0.014] \cdot \rho \cdot U^2 \cdot L_{BP} \cdot T_D$$
  Eq. 7-7

$$F_{Xc} = \frac{1}{2} \cdot 0.04 \cdot \rho_c \cdot U_c^2 \cdot L_{BP} \cdot T_D$$
  Eq. 7-8

From above, it can be seen that in the velocity range of $0.3 - 2m/s$ the viscous resistance of the FPSO calculated by OCIMF formulae is around 3.0 times bigger than that obtained by the ITTC'57 method. The potential cause of this discrepancy could be due to the over-estimated longitudinal coefficients in OCIMF, which were obtained through Froude scaling without any corrections for Reynolds number. Reynolds number of the model tests was not similar to the prototype: the lowest

Reynolds number in the model tests was 0.9×10^5 compared to 5×10^7 for the prototype.

The OCIMF method is much more useful in predicting the transverse force and yaw moment of moored tankers for routine design calculations. It is argued that for the OCIMF method the small longitudinal forces were not measured with sufficient accuracy and thus the ITTC-1957 frictional resistance formula should be used to predict the longitudinal force (Mercier and Huijs, 2005).

2. Damping of hull viscous resistance and effect of steady current

The damping of viscous resistance in surge is calculated through the energy dissipation E_{vx} in one period of slow drift motion

$$E_{vx} = \int_{x_0}^{x_\tau} R_v \cdot dx = \int_t^{t+T} R_v \cdot U \cdot dt \qquad \text{Eq. 7-9}$$

Similarly, equivalent linear damping c_{vx} and damping ratio ζ_{vx} are given by

$$c_{vx} = \frac{E_{vx}T}{2\pi^2 X_o^2} = \frac{E_{vx}}{\pi \omega X_o^2} \; ; \; \zeta_{vx} = \frac{c_{vx}}{c_c} \qquad \text{Eq. 7-10}$$

The current force acting on the FPSO is also calculated by the 'ITTC-57' method. Different current velocities and different amplitudes of LF motion with the same period ($T = 149.6s$) are considered. The effect of current and amplitude of the slow drift motion on the damping from hull viscous resistance are studied, as showed in Figure 7-3.
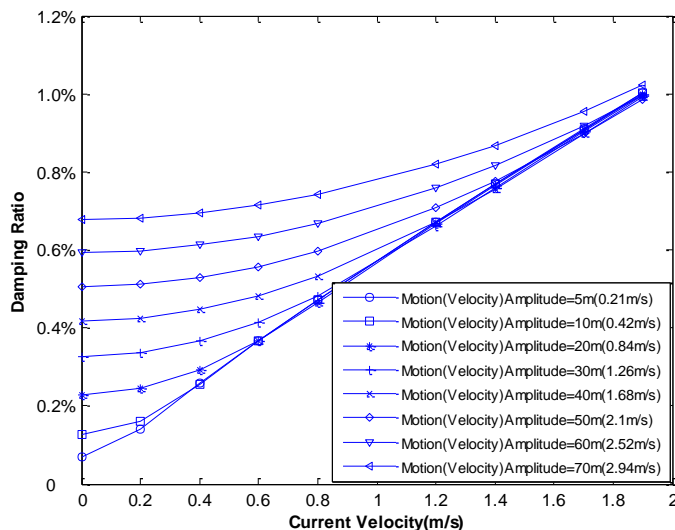
Figure 7-3 Effect of current on damping of hull viscous resistance under different motions

From Figure 7-3 it can be seen that:

1) The damping of hull viscous resistance in surge is very small when compared to the damping of moorings (compared with Figure 3-25);

2) Increase of current velocity will increase the damping of hull viscous resistance for the same drift motion of the FPSO;

3) For the same current velocity, the minimum damping ratio will occur when the motion velocity amplitude is similar to the current velocity.

7.2.2 Damping of risers

The contribution of risers to the dynamic response of a moored FPSO is not only the current loads on the risers, which could dominate the displacement of the FPSO especially under Gulf of Mexico loop current conditions, but also the damping effect due to the considerable drag force caused by large diameter risers.

In the moored FPSO system 24 risers are included. Their layout is illustrated in Figure 3-7. Riser properties and configuration parameters are listed in Table 7-1.

Table 7-1 Riser properties and configuration parameters

Parameter	Value
Outer diameter (m)	0.373
Inter diameter (m)	0.250
Mass of internal fluid (kg/m)	14.75
Mass (in air) empty (kg/m)	254.04
Total mass (kg/m)	268.79
Bending Stiffness ($N \cdot m^2$)	6.482E4
Torsion Stiffness ($N \cdot m^2 / rad$)	1.7E7
Axial Stiffness (N)	1.11E9
Total length of riser (m)	629

The buoyancy section of the riser is $175\,m$ long and has diameter of $0.945\,m$. The mass of the buoyancy section (in air) with internal fluid is $490.65\,kg/m$. A single riser configuration is illustrated in Figure 7-4.
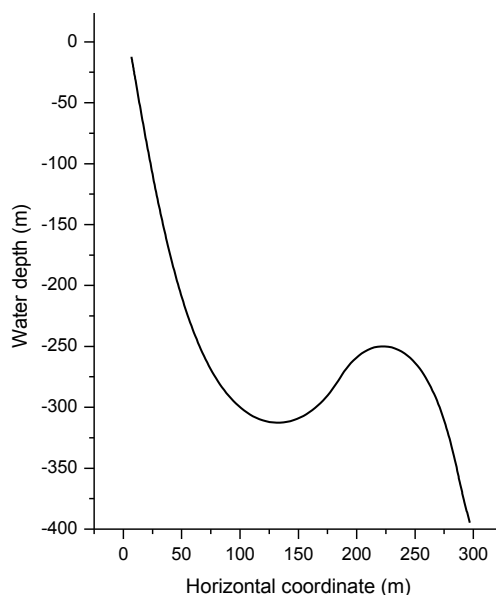
Figure 7-4 Illustration of single riser configuration

The damping of risers can be calculated by the same 'Indicator diagram' method. C_d = 1.1 for risers is assumed with respect to their nominal diameter. The energy dissipated in one cycle of slow drift motion can be obtained from the 'Indicator diagram' as illustrated in Figure 7-5. Similarly, equivalent linear damping c_r can be approximately given by $c_r = E/(\pi \omega X_o^2)$.
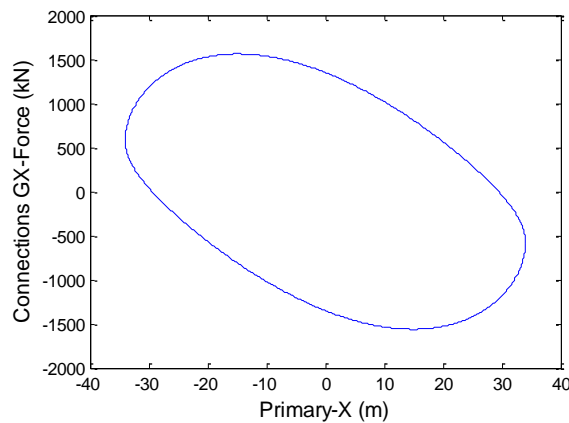
Figure 7-5 Energy dissipation of risers calculated by 'Indicator diagram' method

In Table 7-2, damping of risers are calculated for two cases, one case with LF motion only and the other case with superimposed surge WF motions, in order to consider the effect of superimposed WF motion on the damping of risers.

Table 7-2 Effect of superimposed WF motions on damping of risers

Case	c_r ($N \cdot s/m$)	Damping Ratio
Surge LF only ($A = 34m, T = 149.6s$)	9.15E+05	14.26%
Superimposed surge WF motion ($A = 4m, T = 15s$)	1.18E+06	18.38%

It can be seen from Table 7-2 that

1) Under the same LF motion, the damping ratio from risers is (41.6%) bigger than that from moorings;

2) With superposed surge WF motion, the damping from the risers increases when compared to that under LF motion only; however, the increase of damping from the risers due to the effect of superposed WF motion is much smaller than that of moorings. Potential reason could be due to the shape of the steep wave risers, which makes the normal motion of risers not so sensitive to the relative small WF motions.

The effect of steady current on damping of risers is studied by considering the risers under the LF motion only ($A = 34m, T = 149.6s$). The current velocity profile is the same as shown Figure 3-23 and the surface current velocity is taken as $1.0m/s$. It is found that the damping from the risers increased by 31.6% due to the existence of steady current, which has a slightly more important influence upon the LF damping from risers than from the moorings. This could be because, compared to moorings, risers have bigger effective drag diameter and are more sensitive to the drag effect of the current.

7.2.3 Comparisons of viscous resistance damping and damping of moorings and risers

System damping of the moored FPSO system in surge has been assessed. From the summarization in Table 7-3, it can be seen that, in the surge direction, the hull viscous resistance damping is much smaller when compared with the damping of moorings/risers.

Table 7-3 Components of system damping under different motions

Case	Damping Ratio of		
	hull viscous	risers	moorings
Surge LF only ($A = 34m, T = 149.6s$)	0.36%	14.26%	10.07%
Superimposed surge WF motion ($A = 4m, T = 15s$)	-	18.38%	18.78%

For the given moored FPSO system, when only considering the LF motion, the damping from the risers is slightly bigger than damping of moorings. However, the effect of superimposed WF motion on damping from the risers is moderate when compared to the effect on damping of moorings. Under superimposed WF motions, the damping of moorings could increase dramatically (see Figure 7-6). As a result, the contribution of mooring line damping to the total system damping could be comparative to that of risers or even be dominant.
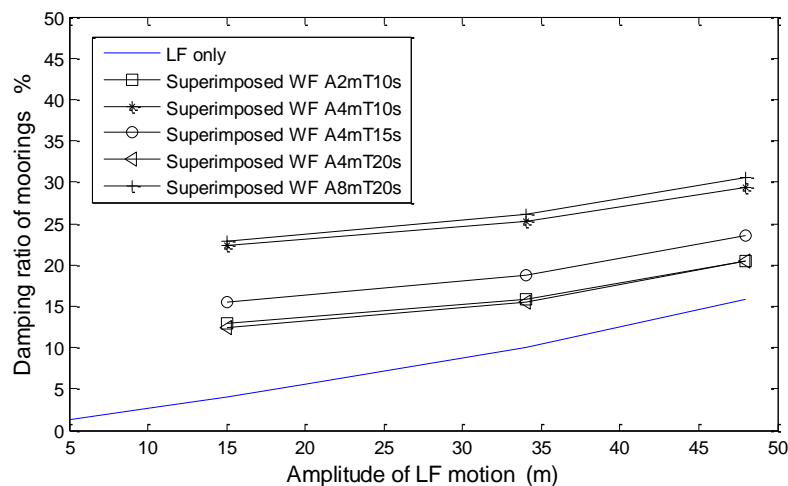
Figure 7-6 Effect of superimposed surge WF motions on mooring line damping

Actually, the mooring line damping is very complicated and can not be modelled as simple linear damping. From the previous discussion it can be seen that the magnitude of mooring line damping will depend on the top oscillation motions,

including LF and especially WF motions, which have a dominant impact on damping of moorings. Besides, it is also affected by the mean tension in the line (line layout), ocean current, as well as the water depth and the mooring line configuration. In the time-domain coupled analysis, the linearization of mooring line damping is not necessary, because the damping effect of moorings will be included directly by considering the drag coefficients and hence the drag loads acting on them.

7.3 Coupled analysis of the moored FPSO system

7.3.1 Numerical model

Slender structures, such as mooring lines and risers are modelled here by a 'Lumped-mass and spring model'. The load model for these slender structures accounts for buoyancy, weight, internal fluid flow, seabed contact and hydrodynamic loads. Seabed contact is simulated by spring and friction models while the hydrodynamic loads are calculated by the Morison load model.

The large floater (FPSO) is represented by a six-degree-freedom (6-DOF) rigid body, which is actually introduced as a 'nodal component' in the model. The load model for the rigid body includes wind, current and wave forces. The wind and current forces are based on a set of direction-dependent coefficients for each of six degrees of freedom. The current force coefficients are determined by OCIMF data in the OrcaFlex program. The viscous hull damping for the horizontal slow drift motions is included automatically by the calculation of drag force/moment on the hull. It should be mentioned that the calculation of current force with desirable accuracy is still a tough task, which can be seen from the work of Schellin (2003). The results of predicted maximum load in the mooring hawsers and the horizontal motions of the

tankers were characterized by large spread among different research participants for a SMP tanker in a steady current (Schellin, 2003).

The wave loads on the rigid body are based on frequency-dependent coefficients obtained by hydrodynamic potential theory. Based on the three-dimensional panel method and Green's theorem with a free surface Green function, a second-order diffraction/radiation program called WAMIT is used. The calculations of 1st order wave motions have been mentioned before. An FPSO's horizontal motions have smaller natural frequencies than those of significant wave energy, and thus are more likely excited by second-order difference-frequency wave forces. Therefore, the inclusion of the second-order slowly varying wave forces in FPSO motion analysis is very important.

By using a diffraction-radiation analysis and the Newman approximation, the 2nd order difference-frequency wave load can be calculated and represented by mean quadratic transfer function (QTF), as shown in Figure 7-7. (The alternative of calculating the slow drift force obtained from integration of the second-order pressure will require a finer discretization on the body surface and very long run times). A convergence test is made by comparing results from the numerical model with those from Ha's study (2011) for the Schiehallion FPSO, as shown in Figure 7-7 (right). The discrepancies at shorter periods could be due to the coarser panel discretization.

However, the convergence of the difference-frequency QTFs is known to be much faster than the sum-frequency QTFs. The off-diagonal value $Q(\omega_1, \omega_2)$ in the full QTF matrix is equal to an average of the corresponding diagonal values $Q(\omega_1, \omega_1)$ and $Q(\omega_2, \omega_2)$ according to the Newman approximation. When the full QTF matrix is

known, one can compute the low-frequency force spectrum $S_F(\Delta\omega)$, where

$\Delta\omega = \omega_1 - \omega_2$ is the difference frequency.
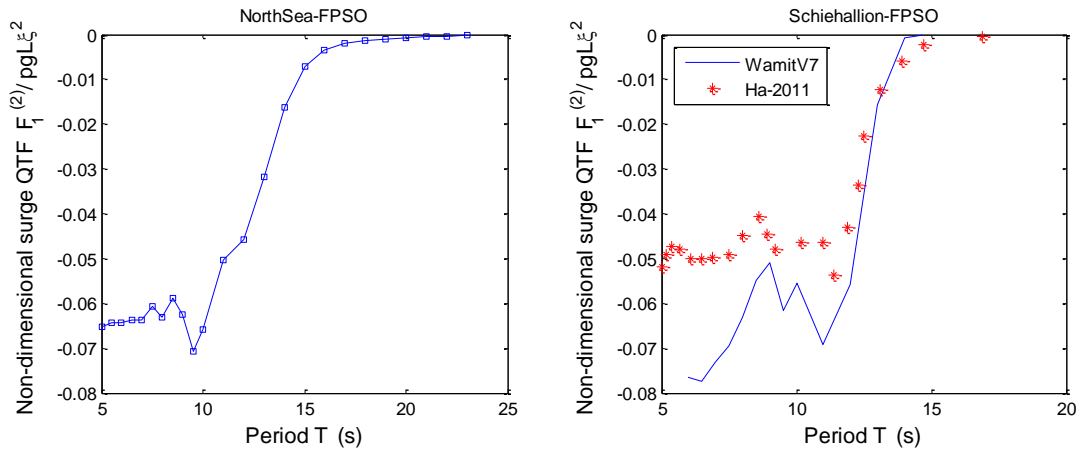
Figure 7-7 Non-dimensional mean surge QTF of the FPSO vessels

7.3.2 Consideration of C_D variation of mooring line

For steady flow, it is known that the effect of Re in the range of $10^4 - 10^7$ upon C_D of the chain is not as important as that on a smooth cylinder, which can be seen both from the former numerical calculation and from the DNV recommended values. For harmonic oscillatory flow, the effect of KC on C_D of the chain, known from the numerical calculations, also depends on the Re number concerned. For the flows with small Re, the effect of KC on C_D is significant. With an increase of KC number, the value of C_D of the stud-less chain decrease, which shows the value of C_D will gradually get close to that under steady flow with same Re. However, for the

flows with high Re number, it seems the effect of KC upon C_D is not important while the effect of Re is dominant.

To study the damping effect of mooring line on the motions of a moored FPSO system, the normal practice in the coupled analysis is to simply change the constant value of C_D by a factor of 2 (Wichers and Devlin, 2001, Luo and Baudic, 2003). The variation of C_D due to effect of Re and especially KC has not been included in the coupled analysis, which is due to several factors.

First, limited data about the relationship of C_D with Re and KC is available for chains. Second, for the vessel in random waves, the effect of random flows due to random WF motions upon C_D values of the chain is unclear. Third, in time-domain coupled analysis it is hard to consider the effect of KC, which is a parameter related to the time period. By contrast, the effect of Re upon C_D of chain, which seems to be negligible, can easily be included in the coupled analysis.

To consider the C_D variations in the coupled analysis, it is necessary to handle the problems mainly due to the last two factors. In the present study, an attempt is made based on a statistical view and the assumption of 'energy dissipation' equality.

It has been shown that the superimposed WF motions have a dominant effect on mooring line damping and without considering the C_D variations, the effect of random WF motions on mooring line damping can be represented by an equivalent harmonic WF motion. The C_D selection of chain under the random WF motions, if

possible, should be represented by the value of C_D under the equivalent harmonic WF motion. Consequently, the proper C_D of chain in the coupled analysis can reflect the damping effect of moorings, which could have considerable impact on the LF motions. This could be practical because the random WF motions of the vessel are not affected by the coupling effect of slender structures and one can predict the vessel's random WF motions under given environments before coupled analysis. Another reason is that effect of superimposed WF motions is dominant upon the mooring line damping.

The effect of random flows upon the C_D of a smooth circular cylinder has been studied (Longoria et al., 1991). Although in the inertia-drag regime, the random flow C_D values of the cylinder are significantly different from the sinusoidal flow values, it can be seen that the discrepancies between the random flow values and the sinusoidal flow values are small outside the inertia-drag regime.

Therefore, it is assumed that the random flow C_D values of the chain can be represented by the sinusoidal flow values. The C_D selection for the chain in the coupled analysis will depend on the Re and KC numbers related to the equivalent harmonic WF motion, which is represent of the corresponding random WF motions under given environments (as demonstrated in section 3.3.2).

7.3.3 Weather conditions and cases considered

A parallel wave-current environment is considered here while the wind environment is not included. Although wind will affect the mean offset and slow drift motion of

the FPSO, the reason why wind effect is not considered here in the coupled analysis is twofold. First, the main objective of the coupled analysis is to study the damping effect of moorings on the LF motions of the moored FPSO system. The wind has no impact on the damping of moorings. Second, the calculation of wind force and the contribution of wind damping to the system damping are separate research area, which is not included in the present study. The parameters of wave and current corresponding to a typical 100-year hurricane mentioned before are summarized in Table 7-4.

Table 7-4 Environmental conditions for coupled analysis

Description	Parameters		
	Waves		Current
Hurricane	H_s/T_p: 12.2m/14s Wave spectrum type: JONSWAP ($\gamma = 2.5$) Wave direction: 180degree		surface velocity 1.0m/s (profile see Figure 3-23) Direction:180degree

As is known from former study, the damping of risers could have considerable contribution to the system damping. If the damping of risers is dominant in the system damping, the LF motions of the moored FPSO system will be not sensitive to the C_D variations of moorings. In order to study the damping effect of moorings on the motions of moored FPSO vessel, some cases without risers in the coupled model are also considered. These cases are also in accordance with the experimental tests where the risers are normally not included in the coupled model test.

Table 7-5 Cases considered in the coupled analysis

	Vessel/moorings/risers	Vessel/moorings
100-year Hurricane	Case1	Case2

For each case mentioned in Table 7-5, the C_D variations of moorings with a factor of 2 are first considered in the coupled analysis. Then for the case which is most sensitive to the C_D variation with respect to the primary surge motion, the C_D selection with Re and KC number taken into account is made for the chain in the coupled analysis and its effect on the LF surge motion of the FPSO is assessed. So there are three cases of C_D variations considered for the moorings. The hydrodynamic coefficients for moorings of each case and risers with respect to the drag diameters are summarized in Table 7-6.

Table 7-6 Hydrodynamic coefficients for risers and moorings

$C_D\_$**Case**	**Item**	**Normal** C_D	**Normal** C_a
Case$\_C_{D1}$	Chain	1.1	1.0
	Wire	1.2	1.0
Case$\_C_{D2}$	Chain	2.2	1.0
	Wire	2.4	1.0
$C_D\_$CFD	Chain	Decided by Re & KC	1.0
	wire	1.2	1.0
-	Risers	1.1	1.0

7.4 Results and discussions

For each case under given environment, in order to reflect the statistical properties of waves, all computations are performed in the same wave train with a duration of three-hours full scale. Regarding the comparison of results, the focus is mainly on the surge motion of the moored FPSO. However, line tensions of the tautest line under some cases are also investigated.

7.4.1 Damping effect of moorings by doubling C_D values of moorings

1. Coupled analysis of Vessel/moorings/risers

In this coupled model, 20 mooring lines and 24 steep-wave risers, together with the FPSO are included. The damping effect of moorings on the surge motion of the moored FPSO system under 100-year-hurricane waves is studied by changing the C_D values of moorings by a factor of 2. The spectrum of surge motion of the vessel under 100-year hurricane and time history of Case-C_{D1} are illustrated in Figure 7-8. It can be seen that the LF surge motion is dominant in the surge motion. The increase of mooring line damping due to the doubling of C_D will mainly reduce the LF surge motions around the resonant situation.
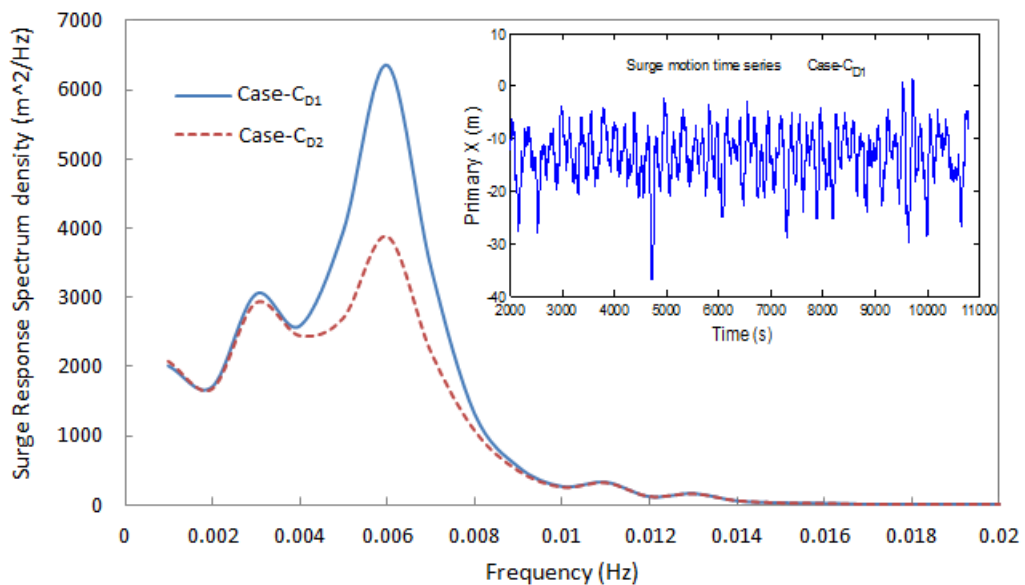
Figure 7-8 Spectral density of surge motion of the FPSO under 100-year hurricane

The statistical results of surge motion under two different C_D_Cases are listed in Table 7-7. It can be seen from Table 7-7 that the mean surge offset increases while

the standard deviation of surge decreases due to the doubling of C_D values of moorings. The results show that the maximum surge motion of vessel slightly decreases due to the combination of increased damping and increased current loads on moorings.

Table 7-7 Statistics results of FPSO's surge motion under 100-year hurricane waves

Case1 (100-year Hurricane)	Primary X (m)		Discrepancy by
	Case_C_{D1}	Case_C_{D2}	
Mean (m)	-13.36	-14.50	8.53%
Standard Deviation	5.27	4.73	-10.25%
Max (m)	-37.19	-35.91	-3.44%
Mean up-crossing period T_z (s)	84.40	76.72	-
m_0	27.79	22.34	-

The statistical results of mooring loads of the Case 1 are also listed in Table 7-8. Line3 and Line13 are the tautest and slackest lines in the plane of the surge direction. The results show that the standard deviation and maximum value of line force at top increase considerably due to the doubling of C_D values of moorings.

Table 7-8 Statistics results of line forces under 100-year hurricane waves

Case1 (Hurricane)	Force in Line3 (kN)			Force in Line13 (kN)		
	Case_C_{D1}	Case_C_{D2}	Discr.	Case_C_{D1}	Case_C_{D2}	Discr.
Mean	1820.68	1866.62	2.52%	1200.15	1164.26	-2.99%
St. Dev.	202.27	243.65	20.46%	167.25	231.35	38.33%
Max	3440.42	3988.27	15.92%	1993.54	2326.68	16.71%

For both C_D cases, the maximum line force of Line3 occurs at around 4711s, which is slightly earlier than the moment (4734.8s) that the vessel reaches the maximum surge motion. This is in agreement with former discussion that under superimposed

wave WF motions the maximum tension will occur around the moment that the line reaches the maximum offset.

In Figure 7-9 the spectral densities of line forces under different moorings C_D are illustrated. Through the spectral analysis it can be seen that with the doubling C_D of moorings, the line force related to the slow drift motion decreases due to the increase of mooring line damping while the line force related to the WF motions increases due to the increase of dynamic drag force.

Also, as shown in Figure 7-9, for the taut-side-line the force is dominated by the slowly varying component while the slack-side-mooring has appreciable WF component. Therefore, the WF dynamic effects, relative to the LF forces, are more important on the slack side.
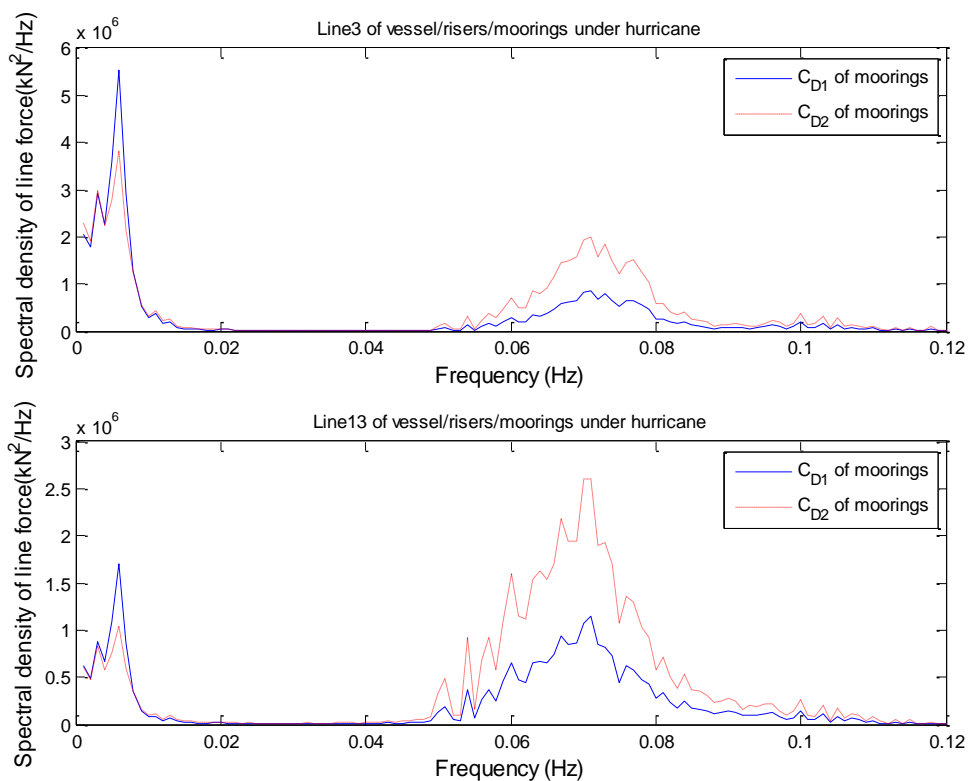
Figure 7-9 Spectral densities of line top forces (Line3, taut; Line13, slack)

Overall, in current case doubling C_D of moorings will have considerable effect on line tension, especially line dynamic tension, while its effect on global surge motion of the vessel is relative small.

It should be noted that Wichers and Devlin (2001) also studied the coupling effect on the global motions and the mooring forces by systematically changing the C_D values of moorings and risers. For the moored FPSO system in 914m water depth and under 100-year hurricane condition, it was found that the sensitivity of C_D (=1 or 2) on the global motions and mooring forces is relatively small, which is a little different from the conclusion of current study.

After checking the data of Wichers and Devlin (2001), it is found that the C_D variation is only made for the steel wire segment, which is the main component of the mooring line (total length is 2088m, wire segment is 1127.8m). As known from the former sensitivity study of C_D variation, the C_D variation on the wire segment, which is in the middle of chain-wire-chain mooring, has little effect on the damping and line tension of moorings. That is the potential reason why Wichers and Devlin (2001) reached the conclusion that doubling of C_D values would result in only slightly different results of mooring forces and global motions in their study.

2. Coupled analysis of Vessel/moorings

As is known, the damping of risers can have a considerable contribution to the system damping depending on the numbers and configurations of risers. The damping contribution of risers will reduce the effect of C_D variations of moorings on

the motion of the FPSO system. Here, the risers are not included in the coupled model in order to have a better understanding of the effect of C_D variations of moorings.

The surge spectrum of the FPSO with moorings only under 100-year hurricane waves is shown in Figure 7-10 for two different C_D_Cases. It can be seen that without damping of risers the spectral density of slow drift surge motion increase dramatically (compared with Figure 7-8), while doubling the C_D values of moorings (C_{D1} vs. C_{D2}) will significantly reduce the peak of the spectral density.
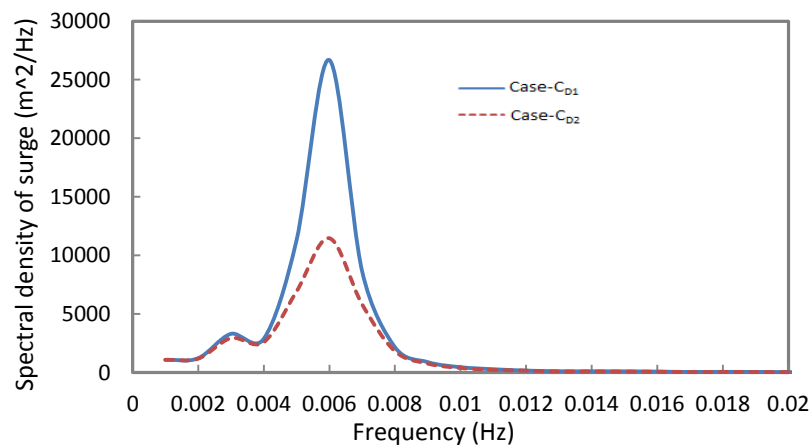
Figure 7-10 Surge spectral density of the FPSO/moorings under 100-year hurricane

The statistical results of the surge motion of the FPSO under hurricane conditions, with moorings only, are compared between the two C_D cases, as illustrated in Table 7-9. It can be seen that standard deviation of surge motion decreases considerably due to the increase of mooring line damping from doubling the C_D of the moorings, which also causes a larger mean offset due to the increase of current drag. However,

little difference exists between the maximum surge motions of the two C_D_Cases, which occur almost at the same time.

Table 7-9 Statistics results of FPSO's surge under hurricane with only moorings

Case2 (Hurricane)	Case_C_{D1}		Case_C_{D2}		Discrepancy by
	Time (s)	Primary X (m)	Time (s)	Primary X (m)	
Mean	-	-9.87	-	-11.08	12.26%
St. Dev.	-	7.36	-	5.86	-20.38%
Max	4735.1	-36.66	4734.9	-35.65	-2.76%
Mean T_z (s)	-	119.32	-	94.63	-
m_0	-	54.10	-	34.38	-

From Figure 7-11 it can be seen that the maximum surge motion is mainly caused by the peak wave drift force. It should be noted that the slow drift force spectrum is flat in the low-frequency range of interest and hence it is hopeless to try to detune the mooring line system from an eventual frequency where the excitation would be higher (Aranha and Fernandes, 1995).
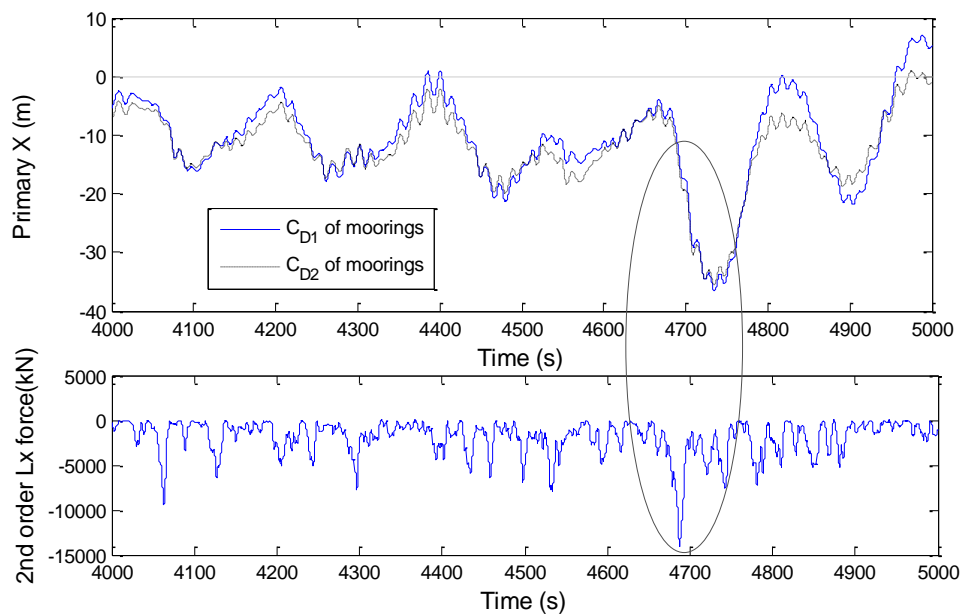
Figure 7-11 Surge motion and 2nd order wave drift force in surge direction

The corresponding line forces of two lines in the plane of surge motion are investigated and their statistical results are listed in Table 7-10. Also, doubling the C_D values of moorings will have a significant effect on line tensions.

Table 7-10 Statistics of line forces under hurricane with vessel/moorings

Case2 (Hurricane)	Force in Line3 (kN)			Force in Line13 (kN)		
	Case_C_{D1}	Case_C_{D2}	Discr.	Case_C_{D1}	Case_C_{D2}	Discr.
Mean	1737.78	1780.63	2.47%	1265.01	1222.54	-3.36%
St. Dev.	236.97	252.84	6.70%	202.61	256.30	26.50%
Max	3298.19	3939.78	19.45%	2234.43	2537.87	13.58%

The spectra of corresponding line forces are illustrated in Figure 7-12. Compared with the case of vessel/risers/moorings, it can be observed in the case of vessel/moorings that the slowly varying components are generally greater than the wave-frequency components. This is caused by the more dominant LF surge motion due to the absence of damping of risers.
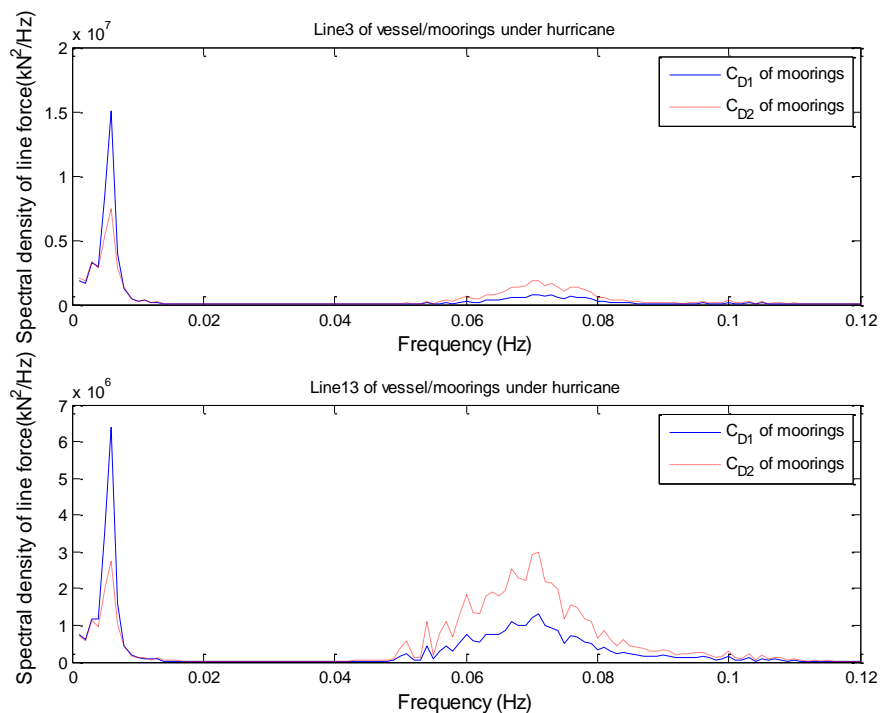
Figure 7-12 Spectral densities of line forces under hurricane with moorings only

The effect of risers in the coupled analysis can be emphasised by comparing results between cases with/without risers. Taking moorings with C_D values of Case_C_{D1}, the surge motions and line forces of Line3 under the cases with/without risers are compared and listed in Table 7-11.

Table 7-11 Effect of 24 risers on global surge motion and line forces

Hurricane	Vessel primary X (m)			Force in Line3 (kN)		
	With risers	Without risers	Discr.	With risers	Without risers	Discr.
Mean	-13.36	-9.87	-26.12%	1820.68	1737.78	-4.55%
St. Dev.	5.27	7.36	39.66%	202.27	236.97	17.16%
Max	-37.19	-36.66	-1.43%	3440.42	3298.19	-4.13%

It is shown in Table 7-11 that, with risers included in the coupled analysis, the mean offset will increase due to the current drag force while the standard deviation of surge motion will reduce, as a result of the contribution of damping from the risers.

7.4.2 Effect of moorings with C_D variations due to Re and KC numbers

The consideration of C_D variations due to Re and KC numbers in the coupled analysis has been mentioned in chapter 7.3.2. Under hurricane condition, the heave WF motions at turret of the FPSO are much bigger than the surge WF motions partly due to pitch effect. The heave WF motions would have dominant effect on the mooring line damping, so the corresponding equivalent harmonic heave WF motion will be used to decide the Re and KC numbers, and consequently the selection of C_D.

Under the typical 100-year hurricane waves, the random heave WF motions and the corresponding equivalent harmonic heave WF motion are mentioned in Table 3-8. The amplitude and period of the equivalent harmonic heave WF motion are $3.2\,m$ and $14.7\,s$ respectively. From Figure 6-5 and Figure 6-6 one can approximately estimate that under given harmonic heave WF motion, the KC number is in the range of 50~200 and the Re number is in the range of $1 \times 10^5 \sim 2 \times 10^5$ for the part of R3S chain, which is very sensitive to the C_D variation with respect to mooring line damping.

From the numerical results of C_D of the oscillating chain (see Figure 6-26), it is known that under such Re and KC numbers, normal C_D of the stud-less chain is around 2.0 for the nominal diameter or is about 0.95 with respect to the drag diameter. Compared to C_D of the stud-less chain in Case_C_{D1}, the C_D value of Case C_D_CFD is about 13.6% smaller. The FPSO's surge motion and line tension obtained by vessel/moorings coupled analysis under such C_D are compared with the results of vessel/moorings under Case_C_{D1} (see Table 7-12 and Table 7-13).

Table 7-12 Statistics of FPSO's surge under hurricane under different C_D cases

Case2 (Hurricane)	Case_C_{D1}		C_D_CFD		Discrepancy by
	Time (s)	Primary X (m)	Time (s)	Primary X (m)	
Mean	-	-9.87	-	-9.81	-0.61%
St. Dev.	-	7.36	-	7.57	2.85%
Max	4735.1	-36.66	4735.1	-36.83	0.46%
Mean T_z (s)	-	119.32	-	116.12	-
m_0	-	54.10	-	57.25	-

Table 7-13 Statistics of line forces under hurricane under different C_D cases

Case2 (Hurricane)	Force in Line3 (kN)			Force in Line13 (kN)		
	Case_C_{D1}	C_D_CFD	Discr.	Case_C_{D1}	C_D_CFD	Discr.
Mean	1737.78	1737.47	-0.02%	1265.01	1267.82	0.22%
St. Dev.	236.97	237.64	0.28%	202.61	195.84	-3.34%
Max	3298.19	3215.83	-2.50%	2234.43	2222.72	-0.52%

It can be seen from Table 7-12 and Table 7-13 that statistical results of surge motion, as well as line forces, between these two C_D cases have only little difference, which indicates that the effect of C_D variation due to the given Re and KC numbers can be ignored. The C_D value recommended by DNV rules for steady flow can be used in the coupled analysis under the given Re and KC numbers if one only needs to consider effect of Re and KC numbers on C_D of mooring chains.

However, it is known that C_D values are affected by many other factors. In reality the surface roughness and especially the marine growth, whose effect can be considered by C_D variations, could remarkably increase the C_D values of moorings. The effect of C_D variations on global motions of FPSO and line forces needs to be investigated by coupled analysis.

7.5 Concluding summary

In this chapter, different components of system damping in the surge direction are first studied for a turret moored FPSO system, which aims to show their potential effect on global response of the moored system and also to emphasize the damping contribution of moorings and risers. Then, by coupled analysis, the damping effect of

moorings upon the surge motion of an FPSO is investigated by considering the C_D variations of moorings. Meanwhile, the effect of C_D variations of moorings upon line forces, especially the dynamic line tension, is also stressed.

From the comparison of results obtained by coupled analysis for the moored FPSO system under typical 100-year hurricane condition, it is observed that:

1) The standard deviation of surge motion of FPSO will be noticeably reduced due to increase of damping effect of moorings caused by doubling C_D values of moorings. The damping of moorings mainly effects LF surge motions whose frequencies are near the natural frequency of the moored system, which can be seen from the spectra comparisons of surge motions under different C_D cases;

2) Line forces related to LF motion decreases notably while the line force related to WF motions increase appreciably under the doubling C_D of moorings. This is due to combination of the increase of mooring line damping and dynamic drag forces. The maximum line force, which changes as a result of decreased LF component and increased WF component, are increased here due to the doubling C_D values. It is also noticed that the WF component of the line force is relatively more important in the slack line than in the taut line condition.

8. Discussion, conclusion and recommended future work

This chapter will first discuss selected methods to tackle the problems and challenges encountered during the research. Then it will describe the contributions of this study and summarize the main conclusions learnt from the study. Finally, further research work is recommended.

8.1 Discussion

8.1.1 Work review

Mooring line integrity is very important for the floating structures in deep-water. As water depth increases the interaction/coupling between the slender structures and the large volume floater will have significant effect on the floater's LF motions and mean offset, which in turn affect the estimation of dynamic loads in the moorings. Especially for the surge motion of low-damped FPSOs, damping effect from slender structures such as risers and moorings can be very significant.

Mooring line damping has been widely studied due to its importance and complexity. However, its magnitude will depend on many factors, such as floater motions, environmental conditions, line configurations and water depth. Different researchers get different conclusions under their parameter studies.

In order to establish the base-case for this study, a turret-moored FPSO system operating in 400m water depth with 20 moorings and 24 risers was selected. Under given sea conditions, realistic WF motions of the FPSO, which have significant

effect on mooring line damping, were determined from displacement RAOs and the given wave spectrum. The damping of moorings was assessed under these WF motions, together with other factors, such as LF motions, mean offset and current. The equivalent linear damping of moorings can be used as input in an uncoupled analysis. Although, in coupled analysis, the damping effect of moorings will be included by considering the drag force on the moorings, the preliminary assessment of damping of moorings will clarify its contribution to the system damping and hence its effect on the global response.

The effect of random WF motions on mooring line damping was also included, because former studies only considered the effect of harmonic WF motions. Assuming the C_D of moorings as constant values, the mooring line damping under superimposed random WF motions was calculated for each period of LF motions and averaged over the cycles of LF motions. From a statistical analysis, it was found the effect of random WF motions on mooring line damping can be represented by an equivalent harmonic WF motion.

As is well known, damping of moorings is mainly caused by the drag force, which is related to the selection of drag coefficient. However, in previous studies about damping of moorings, a typically constant value of C_D was assumed, while the variation of C_D due to Re, KC numbers and other factors was ignored. The neglect of C_D variation would not only cause the discrepancies of mooring line damping between numerical results and experimental results, but also affect the prediction of line tensions.

Before the attempt to decide the C_D variation of moorings, it is desirable to know which parts of a mooring line are more important with respect to the contribution to mooring line damping. By a sensitivity study of mooring line damping to C_D variation, it was found that at the top and around touch-down zone, where chain is normally used for a chain-wire-chain line, the line has a dominant contribution to mooring line damping. With regard to sensitivity study of line tension to C_D variation, a similar conclusion can be made: the dynamic tension mainly results from chain segment at top and around touch-down area.

Actually, due to the fact that damping and line dynamic tension of mooring are mainly caused by drag forces, one would know that drag forces of line at top and touch-down zone are of significant importance. Recalling that drag force is related to effective drag diameter, drag coefficient and relative moving velocity, special attention needs to be paid to not only drag coefficient but also the drag diameter, which could be dramatically changed by marine growth. However, the change of drag diameter can be reflected by the variation of drag coefficient.

The limited available data of C_D values and the importance of C_D selection of chains are two of the main reasons to initiate the research. The C_D determination of stud-less chain under different flows was conducted by the CFD method rather than experimental methods, which is now practical due to the limitation of experiments and recent advancement in CFD. In order to guarantee the reliability of the numerical results, it is essential to complete the validation of numerical CFD models, which is achieved by modelling a smooth circular cylinder under different flows. The reasons to select a smooth circular cylinder for the numerical validation are twofold. First, lots of available experimental results about flows past a cylinder make it a good

benchmark for the numerical validation. Second, the shape similarity between the circular cylinder and chain should make the flow characteristics around them have some similarities.

In the numerical validation, effects of near-wall modelling, turbulence models, mesh independence, time-step sizing, and other numerical aspects were considered. For the fixed cylinder under steady flow in the sub-critical regime, the effect of three-dimensional vortex in the wake makes the LES model more desirable for obtaining satisfactory results, especially for higher Reynolds numbers.

However, for the oscillating cylinder in still water, flows in the wake are more two-dimensional than their fixed-cylinder counterparts, which could be due to the suppression of three-dimensionality caused by the harmonic motion of a long circular cylinder. The main difficulty in the numerical modelling seems to be the capture of shedding vortices and its interaction with moving structure. Small phase discrepancies between the calculated force and moving velocity of cylinder could cause considerable error in the fitted force coefficients. In comparison with experiments, the URAN model ($k - \omega \ SST$) normally can obtain good in-line force coefficients, while the LES model surprisingly failed by over-predicting the drag coefficient. By comparing the time histories of calculated in-line forces obtained through the LES and URAN models (Figure 5-31), it can be seen that the peak of in-line force calculated by the LES model is over-predicted. Similarly, the maximum lift force coefficient predicted by the LES model is also over-estimated. It seems the effect of vortex shedding has been exaggerated by the LES model.

The C_D values of a stud-less chain segment under different flows were calculated by the CFD method after the numerical model validation. The range of Re and *KC*

numbers is decided by considering the FPSO's potential WF motions and LF motions. The numerical results indicate that the effect of Reynolds number, in the given range, on C_D values of the stud-less chain is less important, which is in agreement with the recommendation of DNV practices. For the oscillating chain in still water, the effect of KC number on C_D values is significant for flows with smaller Re numbers, while for flows at higher Re number the KC effect on C_D seems to be negligible.

Coupled analysis was conducted to investigate the damping effect of moorings on surge motion of the PFSO system and line tensions by considering C_D variations of moorings. A typical 100-year hurricane is selected as the environmental condition. Under this realistic situation with high Re and big KC, it seems that small C_D variations, due to the impact of Re and KC numbers, have little effect on line tensions and surge motion of the FPSO. However, a change in C_D values of moorings by a factor of 2, which could reflect the effect of surface roughness and marine growth in reality, will have a significant effect both on the LF surge motion of the FPSO and especially on WF line dynamic tensions.

8.1.2 Own contributions

The research mainly focuses on mooring line damping due to hydrodynamic drag force. Due to the complexity of mooring line damping, the research objective is limited to a turret moored FPSO with 20 catenary moorings operating at 400m water depth. The main work is to determine the C_D values of chain under different flows.

This study supplements several aspects of the knowledge of drag coefficients and damping of moorings, some of which are outlined below:

1) Due to the fact that only the effect of superimposed harmonic WF motion on mooring line damping is included in former studies, the effect of random WF motions on mooring line damping is originally investigated from a statistical viewpoint;

2) Through sensitivity study, the most important part of a catenary mooring line is identified with respect to mooring line damping and dynamic tension. For this kind of chain-wire-chain mooring, special attention needs to be paid to the chain segments around the touch-down zone and near the water surface ;

3) Drag coefficients of a stud-less chain under different flows are initially estimated by the CFD method, due to the limitation of experiments. The validations of numerical models by simulating flows around a smooth circular cylinder deepen the understanding of different turbulence models and other numerical aspects;

4) The systematic study of mooring line damping under realistic environments and vessel motions provides a valuable reference for designers to improve the global performance analysis of deepwater FPSO system by uncoupled analysis;

5) An attempt to consider the C_D variations of moorings in the coupled analysis has been made. The comparative importance of the C_D effect on surge motion and line tension is clarified for the FPSO system under a given hurricane. Compared to the effect of changing C_D on the surge LF motion of the FPSO, the impact of changing C_D on the line dynamic tension seems to be more significant and hence needs more attention.

8.2 Conclusion

The main conclusions drawn from the present study are:

1) The damping of slender structures, such as moorings and risers, has a dominant contribution to system damping of the moored FPSO in surge direction. Given the comparable numbers of risers and moorings in the present study, the damping contribution of risers to the system damping is close to that of moorings;

2) The magnitude of mooring line damping is affected by many factors, among which the superimposed WF motion has the most significant influence on damping of catenary moorings;

3) The effect of random WF motions on mooring line damping can be represented by an equivalent harmonic WF motion from a statistical perspective if the C_D variations under these different flow motions are ignored;

4) With respect to mooring line damping and dynamic tension, the most important parts along a catenary mooring line are at top and especially around the touch-down zone, both of which normally consist of chain for a chain-wire-chain mooring line. Because both mooring line damping and dynamic tension mainly result from the hydrodynamic drag force, this finding indicates that it is very important to accurately estimate the drag forces of the chain segment around the touch-down zone. Consequently, special attention needs to be paid to effective drag diameter and selection of C_D values, which could be changed due to surface roughness, marine growth and flow regimes;

5) Recent advancement of computing capacity and the CFD method make it practical to determine hydrodynamic coefficients of bluff bodies. From the validation of numerical models, it is seen that LES model can get more satisfactory results for steady flow past a fixed cylinder, where three-dimensional vortex is important.

However, for oscillating cylinder in still water, where the harmonic motion of a cylinder suppresses three-dimensional vortex and makes flow more two-dimensional, the URAN model ($k - \omega\ SST$) can get good results while the performance of LES is not satisfactory. Overall, the $k - \omega\ SST$ turbulence model is more desirable for engineering practice considering the low computational cost and acceptable accuracy.

6) According to the numerical results, Re number in the range of $10^4 \sim 10^6$ has less effect on drag coefficient of the stud-less chain, which is in agreement with DNV recommendation (DNV-RP-C205). For an oscillating chain in still water, the effect of KC number on C_D is important for flow with lower Re number while for oscillating chain with higher Re number the effect of KC number on C_D seems to be negligible; Besides, regarding the effect of turbulence models on numerical results, it seems that for chain the numerical results obtained by the LES and URAN models have a smaller difference than those for a circular cylinder;

7) As mentioned above, for mooring chains under flows with high Re and big KC numbers, which are normally the case in reality, C_D variations of the stud-less chain due to effect of Re and KC numbers is quite small and the recommended C_D value by DNV can be adopted. However, special attention needs to be paid to other factors, such as surface roughness and marine growth, which could be equivalently considered by the increase of C_D value. In the coupled analysis a change of C_D of moorings by a factor of 2 will considerably affect the LF motions and significantly increase the WF dynamic tensions;

8) It is known from numerical results that under low- Re -number oscillatory flows, the effect of KC number on C_D values is important. This indicates that in model tests, where the Re number is usually low, people need to be aware of variations of C_D values caused by the KC number effect.

8.3 Recommended future work

The present study has contributed to the insight into drag coefficients, damping of moorings and their effect on the global performance of the turret moored FPSO system. During the research, other issues and areas are also identified and deserve further investigation:

1) Effect of surface roughness on C_D values of mooring chains needs to be considered. In reality, surface roughness is very common and could have considerable impact on the C_D values. So it is necessary to investigate this effect in future work. The effect of surface roughness can be considered in the $k - \omega \, SST$ model by defining the roughness height as part of the wall boundary conditions rather than modelling it geometrically (Hellsten and Laine, 1997).

2) CFD simulations are only conducted for single harmonic oscillations in the present work. In reality, combined high frequency and low frequency oscillations are more common and thus the numerical simulations of bi-harmonic oscillations will have more practical significance. However, the numerical simulations of bi-harmonic oscillations require increased mesh refinement and consequently reduced time steps, which will cause further computational demands. The

expensive computational cost is the main reason that CFD simulations of bi-harmonic oscillations are not included in the present study.

3) Reliable results of C_D values under different flows are required to be obtained from enhanced experiments, which then can be used as benchmarks for validation of numerical methods;

4) In the present study, only flows with direction normal to the axis of bluff bodies are considered. For flows past bluff bodies with a big oblique angle, the validity of the cross-flow principle needs to be investigated;

5) The enhancement of the database of mooring line damping for different water depths is desirable. The approximate estimation of mooring line damping by systematical study can be used as a reference by designers to improve the accuracy of uncoupled analysis, which is popular in preliminary design due to its high efficiency. Although coupled analysis can normally get more accurate results, it is often only adopted in final design due to its high computing cost;

6) Model tests for the coupled system of vessel/moorings/risers in deepwater still need to improve to serve as benchmark for numerical models. Effort is needed to eliminate the limitations of model tests, such as the effect of truncation of mooring system and ultra-small scale.

References

AN, H., CHENG, L. & ZHAO, M. 2011. Direct numerical simulation of oscillatory flow around a circular cylinder at low Keulegan-Carpenter number. *Journal of Fluid Mechanics,* 666**,** 77-103.

API-RP2RD 1998. Design of risers for Floating Production Systems (FPSs) and Tension-Leg Platforms (TLPs). American Petroleum Institute.

API-RP2SK 2005. Design and analysis of stationkeeping systems for floating structures. American Petroleum Institute.

ARANHA, J. A. P. & FERNANDES, A. C. 1995. On the second order slow drift force spectrum. *Applied Ocean Research,* 17**,** 311-313.

BABA, N. & MIYATA, H. 1987. Higher-order accurate difference solutions of vortex generation from a circular-cylinder in an oscillatory flow. *Journal of Computational Physics,* 69**,** 362-396.

BAUDUIN, C. & NACIRI, M. 2000. Contribution on quasi-static mooring line damping. *Journal of Offshore Mechanics and Arctic Engineering-Transactions of the Asme,* 122**,** 125-133.

BEAUDAN, P. & MOIN, P. 1994. *Numerical experiments on the flow past a circularcylinder at sub-critical Reynolds number*, Department of Mechanical Engineering, Stanford University.

BELL, B. 2003. Turbulent flow cases. Fluent Inc.

BLACKBURN, H. M. & HENDERSON, R. D. 1999. A study of two-dimensional flow past an oscillating cylinder. *Journal of Fluid Mechanics,* 385**,** 255-286.

BLEVINS, R. D. 2006. *Flow-induced Vibration*, Krieger Publishing Company.

BOUSSINESQ, T. V. 1877. *Essai sur la théorie des eaux courantes*, Mémoires présentés par divers savantsà l'Académie des Sciences.

BREUER, M. 1998a. Large eddy simulation of the subcritical flow past a circular cylinder: Numerical and modeling aspects. *International Journal for Numerical Methods in Fluids,* 28**,** 1281-1302.

BREUER, M. 1998b. Numerical and modeling influences on large eddy simulations for the flow past a circular cylinder. *International Journal of Heat and Fluid Flow,* 19**,** 512-521.

BREUER, M. 2000. A challenging test case for large eddy simulation: high Reynolds number circular cylinder flow. *International Journal of Heat and Fluid Flow,* 21**,** 648-654.

BROWN, D. T. & MAVRAKOS, S. 1999. Comparative study on mooring line dynamic loading. *Marine Structures,* 12**,** 131-151.

CANTWELL, B. & COLES, D. 1983. An experimental study of entrainment and transport in the turbulent near wake of a circular cylinder. *Journal of Fluid Mechanics,* 136**,** 321-374.

CATALANO, P., WANG, M., IACCARINO, G. & MOIN, P. 2003. Numerical simulation of the flow around a circular cylinder at high Reynolds numbers. *International Journal of Heat and Fluid Flow,* 24**,** 463-469.

CHAKRABARTI, P., CHANDWANI, R. & LARSEN, I. Analyzing the effect of integrating riser/mooring line design. Proceedings of Offshore Mechanics and Arctic Engineering (OMAE), 1996.

CHILUKURI, R. 1987. Incompressible laminar flow past a transversely vibrating cylinder. *Journal of Fluids Engineering-Transactions of the Asme,* 109**,** 166-171.

DNV-OS-E301 2010. Position Mooring. DNV Offshore Standard.

DNV-RP-C205 2010. Environmental Conditions and Environmental Loads. DNV Recommended Practice.

DNV-RP-F205 2010. Global Performance Analysis of Deepwater Floating Structures. DNV Recommended Practice.

DUTSCH, H., DURST, F., BECKER, S. & LIENHART, H. 1998. Low-Reynolds-number flow around an oscillating circular cylinder at low Keulegan-Carpenter numbers. *Journal of Fluid Mechanics,* 360**,** 249-271.

FALTINSEN, O. M. 1990. *Sea loads on ships and offshore structures*, Cambridge University Press.

FLUENT12.1 2010. Ansys Fluent Theory Guide. Fluent Inc.

FPS2000 1992. Mooring and Positioning. Marintek.

FRANKE, J. & FRANK, W. 2002. Large eddy simulation of the flow past a circular cylinder at Re(D)=3900. *Journal of Wind Engineering and Industrial Aerodynamics,* 90**,** 1191-1206.

FRANKE, R., RODI, W. & SCHONUNG, B. Analysis of experimental vortex shedding data with respect to turbulence modeling. Proceedings of the 7th turbulent shear flow symposium, 1989 Stanford, USA.

GARRETT, D. L., CHAPPELL, J. F. & GORDON, R. B. 2002. Global performance of floating production systems. *Offshore Technology Conference.* Houston, Texas.

GARRISON, C. J. 1990. Drag and inertia forces on circular cylinders in harmonic flow. *Journal of Waterway Port Coastal and Ocean Engineering-Asce,* 116**,** 169-190.

GERLACH, C. R. & DODGE, F. T. An engineering approach to tube flow induced vibrations. Proc. Conf. on Flow-induced Vibrations in Reactor System Components, 1970 Argonne National Laboratory. 205-225.

GUILMINEAU, E. & QUEUTEY, P. 2002. A numerical simulation of vortex shedding from an oscillating circular cylinder. *Journal of Fluids and Structures,* 16**,** 773-794.

HA, T. 2011. *Frequency and time domain motion and mooring analyses for a FPSO operating in deep water.* PhD, NEWCASTLE UNIVERSITY.

HALLAM, M. G., HEAF, N. J. & WOOTTON, L. R. 1977. Dynamics of marine structures. CIRIA Underwater Engineering Group,Atkins Research and Development.

HELLSTEN, A. & LAINE, S. 1997. Extension of the k-omega-SST turbulence model for flows over rough surfaces. *22nd Atmospheric Flight Mechanics Conference.*

HEURTIER, J. M., LE BUHAN, P., FONTAINE, E., LE CUNFF, C., BIOLLEY, F. & BERHAULT, C. 2001. Coupled dynamic response of moored FPSO with risers. *In:* CHUNG, J. S., SAYED, M., SAEKI, H. & SETOGUCHI, T. (eds.) *Proceedings of the Eleventh.*

HSE 2003. Analysis of accident statistics for floating monohull and fixed installations.

HUANG, Z. Y. & LARSEN, C. M. 2010. Large eddy simulation on interaction between in-line and cross-flow oscillation of a circular cylinder. *China Ocean Engineering,* 24**,** 663-676.

HUSE, E. 1986. Influence of mooring line damping upon rig motions. *Offshore Technology Conference.* Houston, Texas.

HUSE, E. 1991. New development in prediction of mooring line damping. *Offshore Technology Conference.* Houston, Texas.

HUSE, E. & MATSUMOTO, K. 1988. Practical estimation of mooring line damping. *Offshore Technology Conference.* Houston, Texas.

HUSE, E. & MATSUMOTO, K. 1989. Mooring line damping due to first- and second-order vessel motion. *Offshore Technology Conference.* Houston, Texas.

IMA/EMA 2013. Floating Production Systems: assessment of the outlook for FPSOs, Semis, TLPs, Spars, FLNGs, FSRUs and FSOs.

JOHANNING, L., SMITH, G. H. & WOLFRAM, J. 2007. Measurements of static and dynamic mooring line damping and their importance for floating WEC devices. *Ocean Engineering,* 34**,** 1918-1934.

JOURNÉE, J. M. J. & MASSIE, W. W. 2001. *Offshore Hydromechanics*, Delft University of Technology.

KIM, M. H., KOO, B., MERCIER, R. M. & WARD, E. G. 2005. Vessel/mooring/riser coupled dynamic analysis of a turret-moored FPSO compared with OTRC experiment. *Ocean Engineering,* 32**,** 1780-1802.

KIM, M. H., WARD, E. G. & HARING, R. 2001. Comparison of numerical models for the capability of hull/mooring/riser coupled dynamic analysis for spars and TLPs in deep and ultra-deep waters. *In:* CHUNG, J. S., PREVOSTO, M. & MIZUTANI, N. (eds.) *Proceedings of the Eleventh.*

KIM, S. E. & MOHAN, L. S. 2005. Prediction of unsteady loading on a circular cylinder in high Reynolds number flows using large eddy simulation. *Proceedings of the 24th International Conference on Offshore Mechanics and Arctic Engineering, Vol 3***,** 775-783.

KIM, Y. B. & KIM, M. H. 2002. Hull/mooring/riser coupled dynamic analysis of a tanker-based turret-moored FPSO in deep water. *12th International Offshore and Polar Engineering Conference (ISOPE-2002).* Kyushu, Japan.

KIYA, M., SUZUKI, Y., ARIE, M. & HAGINO, M. 1982. A contribution to the free-stream turbulence effect on the flow past a circular-cylinder. *Journal of Fluid Mechanics,* 115**,** 151-164.

KOLMOGOROV, A. N. 1942. Equations of turbulent motion in an incompressible fluid. *zv. Akad. Nauk SSSR, Seria fizicheska,* 6**,** 56-58.

KRAVCHENKO, A. G. & MOIN, P. 2000. Numerical studies of flow over a circular cylinder at Re-D=3900. *Physics of Fluids,* 12**,** 403-417.

LAYA, E. J. 1980. *Effect of structural motion on the hydrodynamic forcing of offshore steel structures.* Msc, the Massachusetts Institute of Technology.

LAYA, E. J., CONNOR, J. J. & SUNDER, S. S. 1984. Hydrodynamic forces on flexible offshore structures. *ASCE Journal of Engineering Mechanics,* 110**,** 433–448.

LIU, Y. & BERGDAHL, L. 1998. Improvement on Huse's model for estimating mooring cable induced damping. *Proceeding of 17th Offshore Mechanics and Arctic Engineering.*

LONGORIA, R. G., MIKSAD, R. W. & BEAMAN, J. J. 1991. An experimental investigation of forces induced on cylinders by random oscillatory flow. *J. Offshore Mech. Arct. Eng.,* 113(4)**,** 275-285.

LOW, Y. M. & LANGLEY, R. S. 2006. Time and frequency domain coupled analysis of deepwater floating production systems. *Applied Ocean Research,* 28**,** 371-385.

LOW, Y. M. & LANGLEY, R. S. 2008. A hybrid time/frequency domain approach for efficient coupled analysis of vessel/mooring/riser dynamics. *Ocean Engineering,* 35**,** 433-446.

LU, X. Y., DALTON, C. & ZHANG, J. F. 1997. Application of large eddy simulation to an oscillating flow past a circular cylinder. *Journal of Fluids Engineering-Transactions of the Asme,* 119**,** 519-525.

LU, X. Y. & LING, G. C. 2003. Three-dimensional instability of an oscillating viscous flow past a circular cylinder. *Applied Mathematics and Mechanics-English Edition,* 24**,** 791-800.

LUO, Y. & BAUDIC, S. 2003. Predicting FPSO responses using model tests and numerical analysis. 13th International Offshore and Polar Engineering Conference (ISOPE-2003), 2003 Honolulu, Hi. 167-174.

LYONS, G. J., BROWN, D. T. & LIN, H. M. 1997. Drag coefficients for mooring line hydrodynamic damping. *Proceedings of the Seventh International Offshore and Polar Engineering Conference.* Honolulu, USA.

MA, K. T., DUGGAL, A., SMEDLEY, P., HOSTIS, D. L., SA, T. & SHU, H. B. 2013. A historical review on integrity issues of permanent mooring systems. *Offshore Technology Conference.* Houston, Texas.

MA, W., LEE, M. Y., ZOU, J. & HUANG, E. W. 2000. Deepwater nonlinear coupled analysis tool. *Offshore Technology Conference.* Houston, Texas.

MENTER, F. R. & RUMSEY, C. L. 1994. *Assessment of two-equation turbulence models for transonic flows*, AIAA Paper 94–2343.

MERCIER, R. S. & HUIJS, F. A. 2005. Steady current forces on tanker-based FPSOs. *WIT Transactions on The Built Environment,* 84**,** 36-45.

MITTAL, R. & MOIN, P. 1997. Suitability of upwind-biased finite difference schemes for Large-Eddy simulation of turbulent flows. *Aiaa Journal,* 35**,** 1415-1417.

MMS 2005. Leasing oil and natural gas resources. U.S. MINERALS MANAGEMENT SERVICE.

MMS 2009. Deepwater Gulf of Mexico 2009: Interim Report of 2008 Highlights. U.S. MINERALS MANAGEMENT SERVICE.

MOE, G. & VERLEY, R. L. P. 1978. An Investigation into the Hydrodynamic Damping of Cylinders Oscillated in Steady Currents of Various Velocities. *Report of the River and Harbor Laboratory.* Norwegian Institute of Technology.

MOE, G. & VERLEY, R. L. P. 1980. Hydrodynamic damping of offshore structures in waves and currents. *Offshore Technology Conference.* Houston, Texas.

MOLIN, B. 1993. Second-order hydrodynamics applied to moored structures. 19th Wegemt School, Nantes.

NAKAMURA, M., KOTERAYAMA, W. & KYOZUKA, Y. 1991. Slow drift damping due to drag forces acting on mooring lines. *Ocean Engineering,* 18**,** 283-296.

NEHARI, D., ARMENIO, V. & BALLIO, F. 2004. Three-dimensional analysis of the unidirectional oscillatory flow around a circular cylinder at low Keulegan-Carpenter and beta numbers. *Journal of Fluid Mechanics,* 520**,** 157-186.

NOBLEDENTON 2005. FPS Mooring Integrity JIP Report, A4163. Aberdeen.

NOMURA, T. 1993. A numerical study on vortex-excited oscillations of bluff cylinders. *Journal of Wind Engineering and Industrial Aerodynamics,* 50**,** 75-84.

ONG, M. C., UTNES, T., HOLMEDAL, L. E., MYRHAUG, D. & PETTERSEN, B. 2009. Numerical simulation of flow around a smooth circular cylinder at very high Reynolds numbers. *Marine Structures,* 22**,** 142-153.

ORMBERG, H. & LARSEN, K. 1998. Coupled analysis of floater motion and mooring dynamics for a turret-moored ship. *Applied Ocean Research,* 20**,** 55-67.

OTTER, A. 1990. Damping forces on a cylinder oscillating in a viscous-fluid. *Applied Ocean Research,* 12**,** 153-155.

PAN, Z. Y., CUI, W. C. & MIAO, Q. M. 2007. Numerical simulation of vortex-induced vibration of a circular cylinder at low mass-damping using RANS code. *Journal of Fluids and Structures,* 23**,** 23-37.

PAPAZOGLOU, V. J., MAVRAKOS, S. A. & TRIANTAFYLLOU, M. S. 1990. Nonlinear cable response and model testing in water. *Journal of Sound and Vibration,* 140**,** 103-115.

PATEL, Y. 2010. *Numerical investigation of flow past a circular cylinder and in a staggered tube bundle using various turbulence models.* MCS, LAPPEENRANTA UNIVERSITY OF TECHNOLOGY.

PAULLING, J. R. & WEBSTER, W. C. 1986. A consistent, large-amplitude analysis of the coupled response of a TLP and tendon system. *Proceedings of the fifth international offshore mechanics and arctic engineering.*

PRANDTL, L. 1925. Bericht über Untersuchungen zur ausgebildeten Turbulenz. *Journal of Applied Mathematics and Mechanics,* 5**,** 136–139.

PRANDTL, L. 1945. Über die Rolle der Zähigkeit im Mechanismus der ausgebildete Turbulenz: The Role of Viscosity in the Mechanism of Developed Turbulence. *GOAR 3712, DLR Archive.*

QIAO, D. S. & OU, J. P. 2010. Time domain simulation of the mooring induced damping in low frequency excitation. *Computer Application and System Modeling, 2010 International Conference.* Taiyuan.

RASHID, F., VARTDAL, M. & GRUE, J. 2011. Oscillating cylinder in viscous fluid: calculation of flow patterns and forces. *Journal of Engineering Mathematics,* 70**,** 281-295.

RAYLEIGH, L. 1876. On the resistance of fluids. *Philosophical Magazine,* 5(2)**,** 430–441.

REYNOLDS, O. 1895. On the dynamical theory of incompressible fluids and the determination of the criterion. *Philosophical Transactions of the Royal Society of London,* 186**,** 123-164.

RODI, W. 1997. Comparison of LES and RANS calculations of the flow around bluff bodies. *Journal of Wind Engineering and Industrial Aerodynamics,* 71**,** 55-75.

ROTTA, J. 1951. Statistische Theorie nichthomogener Turbulenz. *Zeitschrift Fur Physik,* 129**,** 547-572.

SAGHAFIAN, M., STANSBY, P. K., SAIDI, M. S. & APSLEY, D. D. 2003. Simulation of turbulent flows around a circular cylinder using nonlinear eddy-viscosity modelling: steady and oscillatory ambient flows. *Journal of Fluids and Structures,* 17**,** 1213-1236.

SARPKAYA, T. 1976. Vortex shedding and resistance in harmonic flow about smooth and rough cylinders at high Reynolds numbers. *Technical Report No. NPS-59SL76021.* Monterey, California: Naval Postgraduate School.

SARPKAYA, T. 1986. Force on a circular-cylinder in viscous oscillatory flow at low Keulegan-Carpenter numbers. *Journal of Fluid Mechanics,* 165**,** 61-71.

SARPKAYA, T. & STORM, M. 1985. In-line force on a cylinder translating in oscillatory flow. *Applied Ocean Research,* 7**,** 188-196.

SCHELLIN, T. E. 2003. Mooring load of a ship single-point moored in a steady current. *Marine Structures,* 16**,** 135-148.

SCHEWE, G. 1983. On the force fluctuations acting on a circular-cylinder in cross-flow from subcritical up to transcritical Reynolds-numbers *Journal of Fluid Mechanics,* 133**,** 265-285.

SHIMAMURA, Y. 2002. FPSO/FSO: State of the art. *Journal of Marine Science and Technology,* 7**,** 59-70.

SUMMER, B. M. & FREDSØE, J. 1997. *Hydrodynamics around Cylindrical Structures*, World Scientific.

SURRY, D. 1972. Some effects of intense turbulence on the aerodynamics of a circular cylinder at subcritical Reynolds number. *Journal of Fluid Mechanics,* 52**,** 543-563.

TAHAR, A. & KIM, M. H. 2003. Hull/mooring/riser coupled dynamic analysis and sensitivity study of a tanker-based FPSO. *Applied Ocean Research,* 25**,** 367-382.

TUTAR, M. & HOLDO, A. E. 2001. Computational modelling of flow around a circular cylinder in sub-critical flow regime with various turbulence models. *International Journal for Numerical Methods in Fluids,* 35**,** 763-784.

VAN DEN BOOM , H. J. J. 1985. Dynamic behaviour of mooring lines. *Behaviour of Offshore Structures.* Amsterdam.

WARD, E. G., IRANI, M. B. & JOHNSON, R. P. 2001. Responses of a tanker-based FPSO to Hurricanes. *Offshore Technology Conference.* Houston, Texas.

WEBSTER, W. C. 1995. Mooring-induced damping. *Ocean Engineering,* 22**,** 571-591.

WEI, R., SEKINE, A. & SHIMURA, M. 1995. Numerical-analysis of 2D vortex-induced oscillations of a circular-cylinder. *International Journal for Numerical Methods in Fluids,* 21**,** 993-1005.

WICHERS, J. E. W. 1988. *A Simulation Model for a Single Point Moored Tanker.* PhD, Delft University of Technology.

WICHERS, J. E. W. & DEVLIN, P. V. 2001. Effect of coupling of mooring lines and risers on the design values for a turret moored FPSO in deep water of the Gulf of Mexico. 11th International Offshore and Polar Engineering Conference (ISOPE-2001), 2001 Stavanger, Norway. 480-487.

YANG, W. S. 2007. *Hydrodynamic analysis of mooring lines based on optical tracking experiments.* PhD, Texas A&M University.

YOUNG, M. E. & OOI, A. 2004. Turbulence models and boudary conditions for bluff body flow. *15th Australasian Fluid Mechanics Conference.* Sydney.

YOUNG, M. E. & OOI, A. 2007. Comparative assessment of LES and URANS for flow over a cylinder at a Reynolds number of 3900. *16th Australasian Fluid Mechanics Conference.* Crown Plaza, Gold Coast, Australia.

ZDRAVKOVICH, M. M. 1997. *Flow around circular cylinders*, Oxford Univ. Press.

ZHAO, X. Y. 2010. Cross-Flow around and Stability of Multiple Circular Cylinders. *Naval Architecture and Marine Engineering,* PhD.

Appendix A Flows around a smooth circular cylinder

The flow past a smooth cylinder has been widely experimentally studied, partly due to the wide applications of cylindrical structures in offshore industry and partly due to the abundant flow regimes. Experiments about steady viscous flow past circular cylinders were first conducted by different researchers (Thom 1933; Taneda 1956; Grove et al. 1964). It should be mentioned that the Reynolds number is quite small (30-300) in those early studies.

A cylinder sinusoidally oscillating in a rest fluid or sinusoidal oscillatory flow around a cylinder attracts more interests of researches and hence has being widely studied (Keulegan and Carpenter, 1958; Sarpkaya, 1976, 1986; Williamson, 1985; Bearman et al., 1985; Obasaju et al., 1988; Anaturk, 1991). Considering the common phenomena of wave-current interaction, tests about a cylinder in the co-existing flow field (uniform flow plus the sinusoidal oscillatory flow) were performed (Moe and Verley, 1980; Kato et al., 1983; Sarpkaya and Storm, 1985). Except these three flow fields (uniform flow, sinusoidal oscillating flow; uniform plus oscillatory flow), the cylinder in random oscillatory flows was also experimentally studied (Longoria, 1989; Longoria et al, 1991). The experiments mentioned above are all about cylinders vertical to the flow direction. Tests of inclined cylinders in oscillatory flows were also conducted by some researchers (Sarpkaya et al., 1982; Sundar et al., 1998).

Here, the main focus of the review is on uniform and sinusoidal oscillating flows past a smooth circular cylinder vertical to the flow direction. To begin with, the flow regimes and flow characteristics, such as vortex shedding and forces, are reviewed for steady flow past a cylinder.

A.1 Steady flow past a smooth circular cylinder

Flow regimes of a smooth circular cylinder under steady flow

The flow around a smooth circular cylinder changes tremendously with the increase of the Reynolds number, which is defined as

$$Re = \frac{UD}{\upsilon}$$
Eq. A-1

Reynolds number is a dimensionless number that gives a measurement of the ratio of inertial force to viscous force. The various flow regimes under different Re numbers are illustrated in Figure A-1.
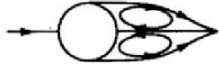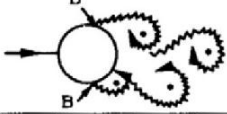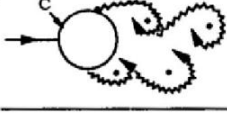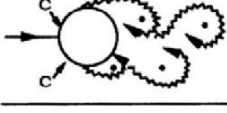
a)		No separation. Creeping flow	Re < 5
b)		A fixed pair of symmetric vortices	5 < Re < 40
c)		Laminar vortex street	40 < Re < 200
d)		Transition to turbulence in the wake	200 < Re < 300
e)		Wake completely turbulent. A:Laminar boundary layer separation	$300 < Re < 3 \times 10^5$ Subcritical
f)		A:Laminar boundary layer separation B:Turbulent boundary layer separation;but boundary layer laminar	$3 \times 10^5 < Re < 3.5 \times 10^5$ Critical (Lower transition)
g)		B: Turbulent boundary layer separation;the boundary layer partly laminar partly turbulent	$3.5 \times 10^5 < Re < 1.5 \times 10^6$ Supercritical
h)		C: Boundary layer completely turbulent at one side	$1.5 \times 10^6 < Re < 4 \times 10^6$ Upper transition
i)		C: Boundary layer completely turbulent at two sides	$4 \times 10^6 < Re$ Transcritical

Figure A-1 Flow regimes of a smooth cylinder in steady current (Summer and FredsØe, 1997)

From Figure A-1 it can be seen that there are mainly two different flow regions for each flow regime, namely the boundary layer and the wake. The boundary layer normally has a very small thickness δ when compared with cylinder diameter D while the wake extends over a distance which is comparable with the cylinder diameter (Summer and FredsØe, 1997). The definition sketch about the boundary layer and the wake is shown in Figure A-2.
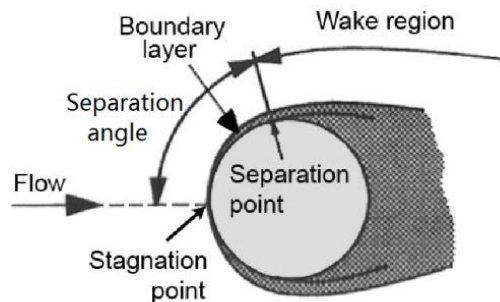
Figure A-2 Definition sketch (modified from Summer and FredsØe, 1997)

A detailed description of each regime in Figure A-1 can be seen from the book written by Summer and FredsØe (1997). Here, several main regimes are mentioned according to the different flow types, namely the laminar and turbulent flows in the wake and the boundary layer.

For $Re < 200$, the flow around a smooth cylinder in the wake and the boundary layer is laminar. The vortex shedding is essentially two-dimensional without varying in the span-wise direction, which means a 2D numerical simulation is desirable for this kind of laminar flow past an infinite cylinder. The wake becomes partly turbulent at $200 < Re < 300$, where the two-dimensional features of the vortex shedding in the range $40 < Re < 200$ becomes distinctly three-dimensional.

The three-dimensional vortex shedding continues at Reynolds numbers greater than 300 with completely turbulent wake and following three ranges could be described: the sub-critical flow regime where $300 < Re < 3 \times 10^5$, the critical flow regime where $3 \times 10^5 < Re < 3.5 \times 10^5$ and supercritical flow regime where $3.5 \times 10^5 < Re < 1.5 \times 10^6$.

The boundary layer over the cylinder surface remains laminar in sub-critical range while followed by a completely turbulent wake. The so-called critical flow regime

shows a turbulent boundary layer separation at one side of the cylinder and laminar one at the other side, but the boundary layer is still laminar. In the supercritical flow regime the boundary layer separation becomes turbulent at both sides of the cylinder and the boundary layer is partly laminar and partly turbulent (Summer and FredsØe, 1997).

Forces on a cylinder in steady current

As has been discussed, the feature of vortex shedding is common to all the flow regimes except for very small Reynolds numbers ($Re \leq 40$). The pressure distribution around the cylinder undergoes a periodic change as a consequence of vortex-shedding process. As a result, a periodic variation occurs in the force components of the cylinder, which include in-line force (drag) and transverse force (lift).

Drag and drag coefficient

The total in-line force (drag) consists of two parts: friction drag and form drag. The contribution of the friction drag to the total drag force is less than 2-3% for the range of Re numbers normally encountered in practice (Achenbac, 1968). The majority of the total in-line force, the form drag, results from the negative pressure at the rear side of the cylinder due to separation.

The drag force can be divided into the so-called mean drag and oscillating drag originated from the vortex shedding. The magnitude of the oscillating part is not a constant set of value and can be characterized by their statistical properties such as the root-mean-square (RMS) value.

$$F'_D = F_D - \overline{F}_D \qquad \text{Eq. A-2}$$

The (mean) drag coefficient commonly used in engineering practice is defined as follows:

$$\overline{C}_D = \frac{\overline{F}_D}{\frac{1}{2}\rho D U^2} \qquad \text{Eq. A-3}$$

The drag coefficients values for a smooth circular cylinder under steady flow can be seen from Figure A-3 as a function of Reynolds numbers.

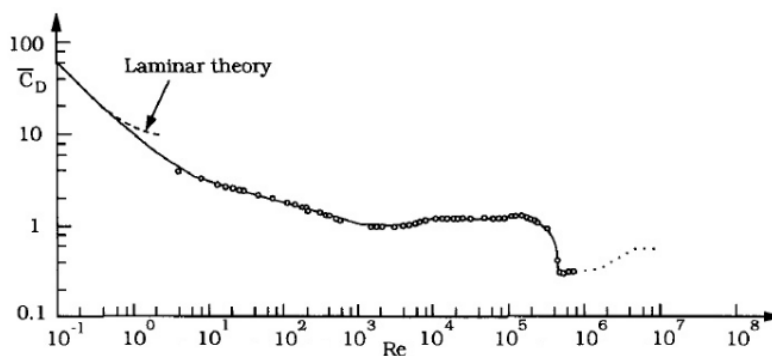**Figure A-3 Drag coefficient vs. Re for a smooth cylinder in steady flow (Schlichting, 1979)**

Lift and lift coefficient

The lift force on the cylinder is perpendicular to the oncoming flow direction. The lift force oscillates at the vortex-shedding frequency (f_v), while the drag force oscillates at a frequency which is twice the vortex-shedding frequency.

The lift coefficient is defined as follows:

$$C'_L = \frac{F'_L}{\frac{1}{2}\rho D U^2} \qquad \text{Eq. A-4}$$

Like the oscillating part of drag force, the amplitude of lift (coefficient) is also measured by its statistical properties. The RMS values of lift force of flow past a fixed cylinder are shown in Figure A-4.
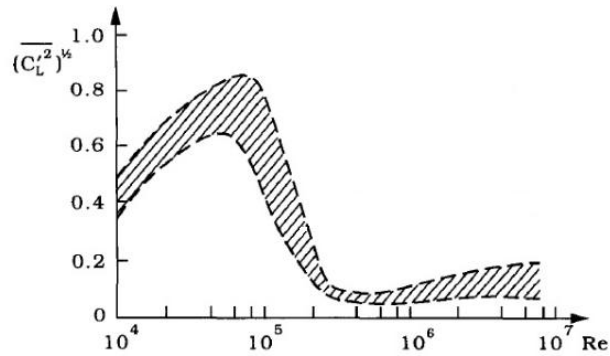
Figure A-4 RMS values of lift coefficient of a fixed cylinder (Hallam et al., 1977)

The vortex shedding frequency, also as the frequency of oscillating lift force can be related to Strouhal number (St) defined in Eq. A-5.

$$St = \frac{f_v \cdot D}{U} \qquad \text{Eq. A-5}$$

The values of Strouhal number for a smooth circular cylinder under steady flow are illustrated as function of Re in Figure A-5. It can be seen from Figure A-5 that for the sub-critical flow regime the Strouhal number is almost constant with value nearly equal to 0.20.
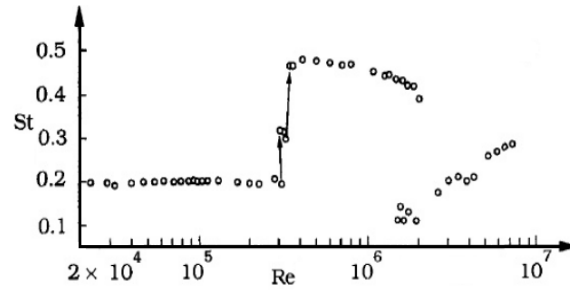
Figure A-5 Strouhal number as function of Re for a smooth circular cylinder (Scheme, 1983)

A.2 Unsteady flow around a smooth circular cylinder

Different from a circular cylinder in steady flow, the hydrodynamic quantities describing the cylinder exposed to an oscillatory flow depend not only on the Reynolds number but also on the Keulegan-Carpenter (KC) number, which is defined in Eq. A-6.

$$KC = \frac{U_m T}{D}$$

Eq. A-6

For sinusoidal motion, the KC number will be identical to

$$KC = \frac{2\pi A_m}{D}$$

Eq. A-7

As a dimensionless quantity describing the relative importance of the drag forces over inertia forces for bluff objects in oscillatory flows or similarly for oscillating objects in a rest fluid, the physical meaning of the KC number can probably be well explained by reference to Eq. A-7. On the right-hand side of the equation, the numerator is proportional to the stroke of the motion, namely $2A_m$, while the

denominator, the cylinder diameter D, represents the width of the cylinder. Therefore, small KC numbers mean separation behind the cylinder may not even occur because that the motion of water particles is small relative to the total width of the cylinder. On the other hand, large KC numbers mean that the water particles travel quite large distances compared to the total width of the cylinder, resulting in separation and probably vortex shedding (Summer and Fredsøe, 1997). The flow regimes of cylinder under oscillatory flows will depend on the KC number as well as Reynolds number. Consequently, the forces experienced by the cylinder in oscillatory flows will also be related to KC number and Re number.

Flow regimes of cylinder under oscillatory flows

According to the studies of Williamson (1985) and Sarpkaya (1986), for cylinder in oscillatory flows at $\mathrm{Re} = 10^3$, where Re is defined as $\mathrm{Re} = {DU_m}/{\upsilon}$, flow regimes as a function of KC number can be classified into several groups. For $KC < 1.1$, laminar flow is around the cylinder and no separation occurs. As KC number increases, separation happens with different types of vortices, and then the so-called vortex-shedding regimes appear when $KC > 7$. The vortex shedding occurs during the course of each half period of the oscillatory motion in the vortex-shedding regimes, which have been further grouped according to the ranges of KC number. For instance, in the single-pair regime ($7 < KC < 15$), one vortex is shed in each half cycle and hence one pair of vortices convects away from the cylinder in each cycle (see Figure A-6); in the double-pair regime ($15 < KC < 24$), two vortices are shed in each half cycle, and as a result two trails of vortex pairs convect away from the cylinder in opposite directions and from opposite sides of the cylinder (Williamson 1985). The number of vortex pairs will be increased by one each time when the KC regime is changed to a higher one, which means the number of vortex pairs

convecting away from the cylinder will be three in the case when $24 < KC < 32$ for each cycle of motion and four in the case when $32 < KC < 40$ and so on. This result is a direct consequence of the familiar Strouhal law in oscillatory flows (Summer and Fredsøe, 1997).

The vortex-shedding frequency, which is equal to the lift-force frequency of cylinder under steady flows, is not identical to the lift-force frequency of cylinder in oscillatory flows due to the presence of flow reversals. As illustrated in Figure A-6, the positive peak (mark B) in the lift force is induced just after the flow reversal by the return of the most recently shed vortex (vortex N) towards the cylinder, while the negative peaks (mark A and C) in the lift force are associated with the growth and shedding of vortices (Summer and Fredsøe, 1997).
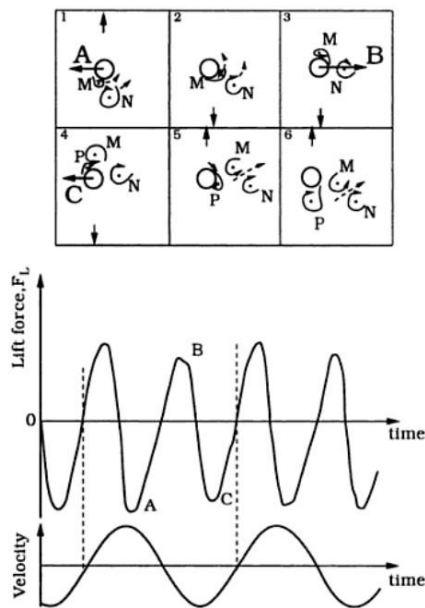

Figure A-6 Lift-force time series (KC =11) obtained with flow visualization (Williamson, 1985)

The fundamental lift frequency f_L can be normalized by the oscillatory-flow frequency f_w, namely:

$$N_L = \frac{f_L}{f_w}$$ **Eq. A-8**

N_L is the normalized fundamental lift frequency, which means the number of oscillations in the lift force per flow cycle. It has been indicated that N_L increases with the increase of KC number by Williamson's work (1985), as listed in Table A-1.

Table A-1 Normalized fundamental lift frequencies observed by Williamson (1985)

KC regime	KC range	Reynolds number	N_L
Single pair	$7 < KC < 15$	$1.8 - 3.8 \times 10^3$	2
Double pair	$15 < KC < 24$	$3.8 - 6.1 \times 10^3$	3
Three pairs	$24 < KC < 32$	$6.1 - 8.2 \times 10^3$	4
Four pairs	$32 < KC < 40$	$8.2 - 10 \times 10^3$	5

It should be noted that the flow regimes mentioned above may also change as Reynolds number is changed. The effect of Reynolds number upon flow regimes of cylinder under oscillatory flows can be seen from Figure A-7. As Reynolds number approaches to the value of 10^5 the curves begin to bend down, which means the normalized lift frequency N_L increases with the increase of Re in this region.
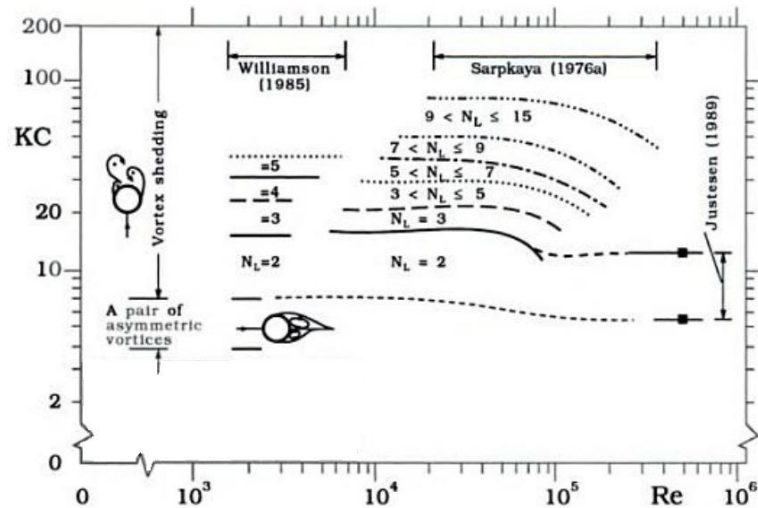
Figure A-7 Vortex-shedding regimes in oscillatory flows (Summer and Fredsøe, 1997)

Forces on a cylinder in oscillatory flows

Similar to steady flow, a cylinder under oscillatory flow may experience two kinds of forces: the in-line force and transverse lift force. The lift-force frequency of a cylinder under oscillatory flow, which is directly related to the vortex motions around the cylinder, has already been discussed above. Another important quantity to depict the time-varying lift force is the magnitude of the lift force, which can be assessed by two methods. One method is to consider the maximum value while the other is to use the root-mean-square value of the lift force to represent the magnitude of the lift force. These may be written as follows in terms of the force coefficients:

$$F_{L\max} = \tfrac{1}{2}\rho C_{L\max} D U_m^2 \qquad\qquad \textbf{Eq. A-9}$$

$$F_{Lrms} = \tfrac{1}{2}\rho C_{Lrms} D U_m^2 \qquad\qquad \textbf{Eq. A-10}$$

If the time-varying lift force can be approximately taken as a sinusoidal form, then the relationship between the two coefficients can be formulized as follow:

$$C_{L\max} = \sqrt{2}C_{Lrms} \qquad\qquad \textbf{Eq. A-11}$$
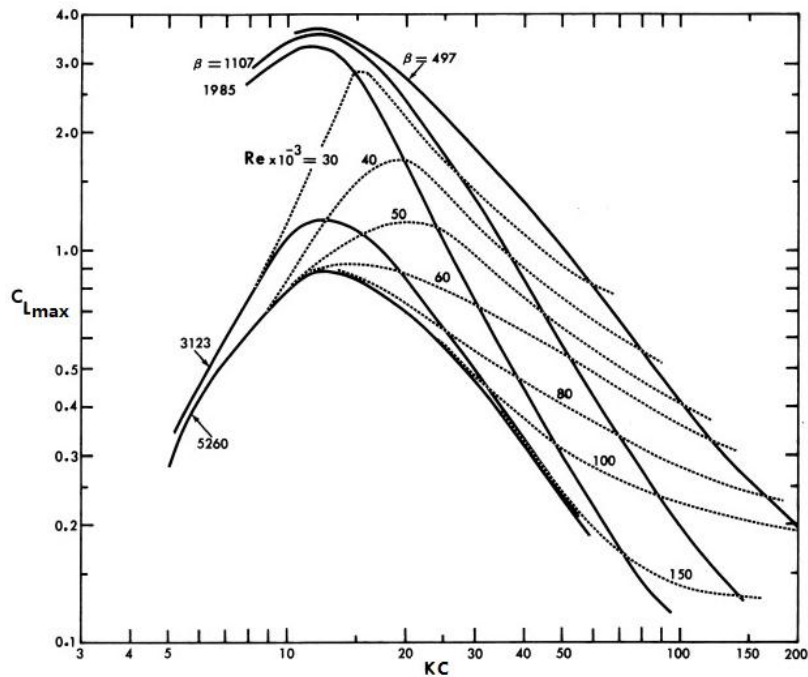
Figure A-8 Maximum lift coefficient as a function of *KC* and Re (Sarpkaya and Isaacson, 1981)

The maximum lift coefficient as a function of *KC* and Re is illustrated in Figure A-8. It can be seen that the value of $C_{L\max}$ will normally decrease as the Re number increases for a given *KC* number.

More attention will be paid to the in-line force. In contrast to the steady flow, the in-line force for cylinder under oscillatory flow consists of not only drag force, but also inertia force. This in-line force is usually calculated by the semi-empirical Morison equation, which can be written as:

$$F = \tfrac{1}{2}\rho C_D D U |U| + C_M \rho A \dot{U} \qquad\qquad \textbf{Eq. A-12}$$

It can be seen that the inertia force consists of two parts:

$$F_I = C_a \rho A \dot{U} + \rho A \dot{U} \qquad\qquad \textbf{Eq. A-13}$$

The first item called 'added-mass force' is caused by the acceleration of the fluid in the immediate surroundings of the cylinder, and the second item termed 'Froude-Krylov force' is induced by the accelerated motion of the oscillatory flow itself. So, to be noted here, there is main difference between an oscillating cylinder in quiescent water and a fixed cylinder under oscillatory flow about the inertial force. For the former case, the only contribution to inertia force is added-mass force, while for the latter case the inertia force is composed of Froude-Krylov force and added-mass force.

The measurements of C_D and C_M are still significantly based on the experiments. In Figure A-9, effect of KC number upon the C_D is illustrated. In Figure A-10, effect of Re number upon the hydrodynamic coefficients is illustrated. It can be apparently seen that for a given KC number, C_D of cylinder under oscillatory flow decrease first with increasing Re number, and then begins to increase with increase of Re, and finally reaches a plateau where it remains approximately constant. This shows the same manner as cylinder in steady flows. However, for cylinder under oscillatory flows the drop in C_D with Re occurs a little earlier while not as abruptly as in steady flows. The general trend of inertia coefficient C_M is opposite to that observed for C_D, as shown in Figure A-10.
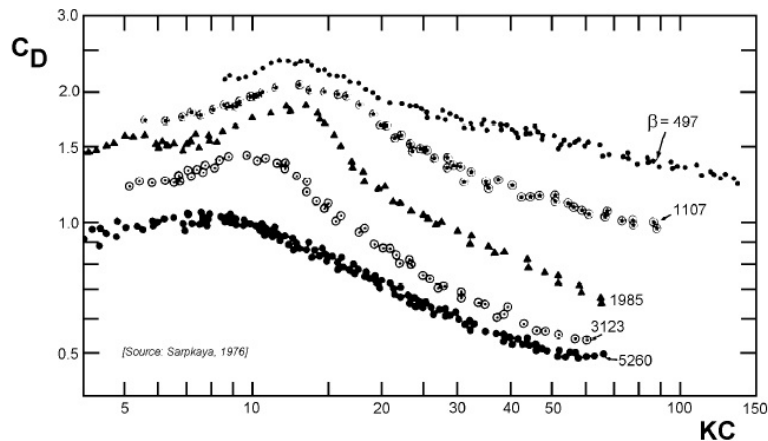
Figure A-9 Typical Laboratory Measurement Results from U-tube by Sarpkaya (1976)
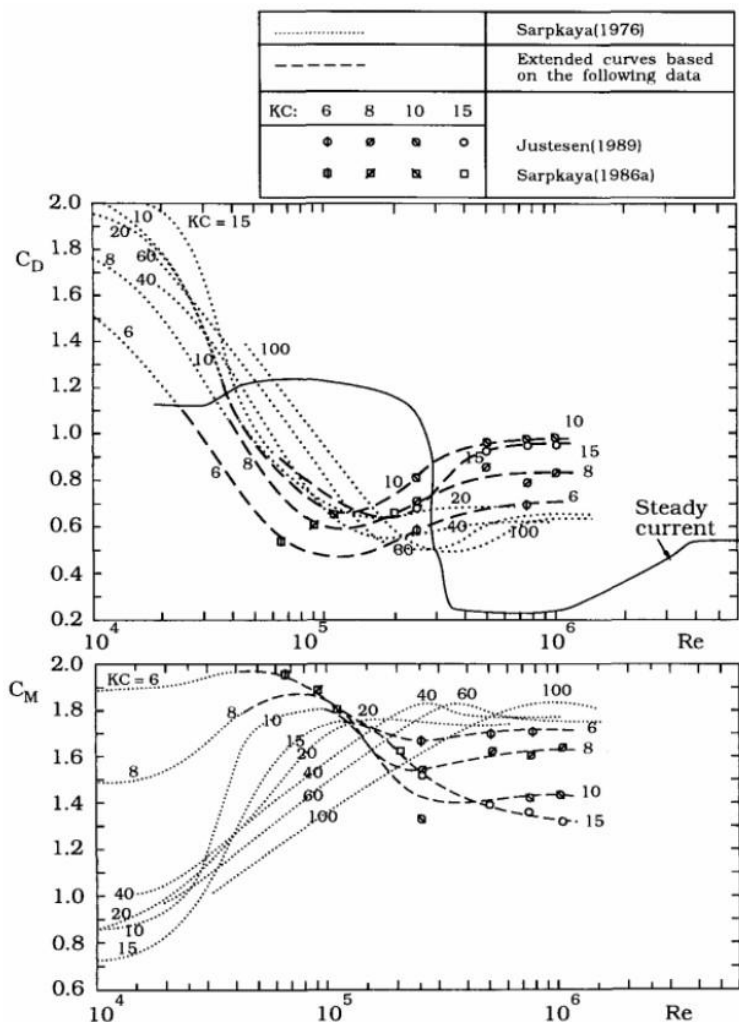
Figure A-10 Force coefficients for a cylinder in oscillatory flows (Summer and Fredsøe, 1997)

The effect of KC number upon C_D and C_M has also been studied for a given Reynolds number of 1.7×10^4, as illustrated in Figure A-11. The C_D reaches the maximum value with KC around 13 and will not change extensively with increasing KC. Regarding the inertia coefficient C_M, it shows opposite trend against that of C_D. Where C_D has high value, C_M experiences low value smaller than unit, which means the added-mass coefficient ($C_a = C_M - 1$) will have a negative value. This is due to the interaction between the vortex shedding and the hydrodynamic process generating the added mass (Summer and Fredsøe, 1997). The negative values of C_a can be also observed for other Reynolds numbers from Figure A-10, which also shows the variation of C_D and C_M with KC for other Re numbers could be different from that for Re of 1.7×10^4.
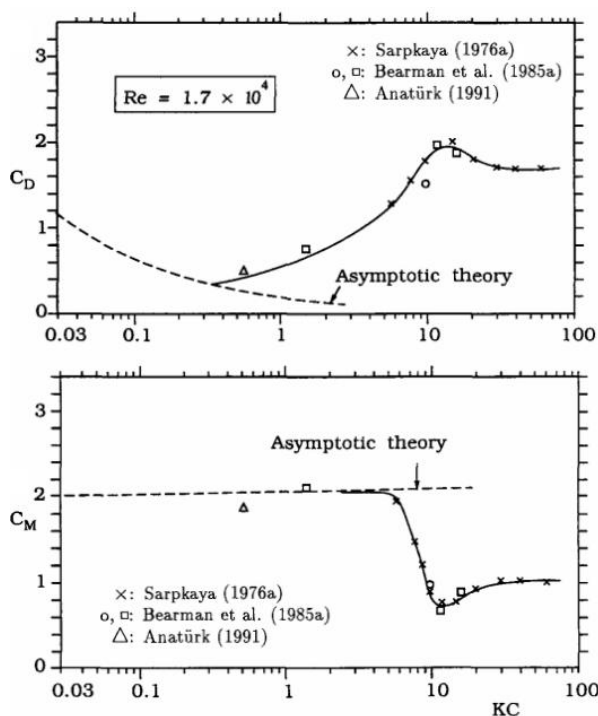
Figure A-11 Effect of KC number on in-line force coefficients for a given Re number (reproduced from Summer and Fredsøe, 1997)

Oscillating flow past a stationary cylinder has been discussed above. The converse situation of an oscillating cylinder in a quiescent fluid is another effective representation of wave–cylinder interaction in the area of ocean engineering where the computation of the fluid forces on an offshore structure is one of the primary tasks. In Appendix B, discussions have been made about the relationship between the fluid mechanics of a fixed cylinder under oscillatory flow and an oscillating cylinder in a still fluid.

Appendix B Relationship between fixed and oscillating cylinders

Before the numerical simulation of an oscillating cylinder in water, it is necessary to discuss the relationship between the fluid mechanics of a fixed cylinder under oscillatory flow and an oscillating cylinder in a still fluid. In order to understand the behaviour of wave loads on slender structures, most of the experiments are conducted based on these two simple flow situations. It is important to know how to interpret results of such experiments. Because the numerical simulations are about an oscillating cylinder in water, in order to compare the numerical results with experimental values from U-tube experiments which are well documented, it is quite desirable, wherever if available, to make the comparison between experimental results from U-tube experiments and tests of oscillating cylinder in still water.

Theoretical relationship

It has been shown by Garrison (1980) that an oscillating cylinder in still water is kinematically identical to a fixed cylinder under oscillatory flow. The only difference between these two cases is about the inertia force, as mentioned before. Therefore, results from both types of experiments should be equally applicable to the situation of wave force acting on the cylinder. The theoretical relationship of these two cases can be seen from the following deduction.

The forces on the cylinder can be obtained by the integral of the pressure P around the cylinder surface, which can be expressed as

$$P = P_\infty + P^*$$ <div align="right">**Eq. B-1**</div>

where, P_∞ is the pressure in the oscillatory external flow with the absence of the cylinder ($P_\infty = 0$ for cylinder in still water); P^* is the pressure due to the disturbance caused by the cylinder.

For the case of a fixed cylinder under oscillation flow, assume the fluid-velocity vector as v and the instantaneous velocity of oscillation flow along the x-direction as $-iU$, the Navier-Stokes equation for the fixed cylinder under oscillation flow can be written as

$$\frac{Dv}{Dt} = \frac{-\nabla P}{\rho} + \upsilon \nabla^2 v = \frac{-\nabla(P_\infty + P^*)}{\rho} + \upsilon \nabla^2 v$$ <div align="right">**Eq. B-2**</div>

At the far-away distance from the cylinder the viscous and convective acceleration terms vanish in Eq. B-2, then the Navier-Stokes equation at infinite distance can be expressed as

$$-i\frac{\partial U}{\partial t} = \frac{-1}{\rho}\frac{\partial P_\infty}{\partial x}$$ <div align="right">**Eq. B-3**</div>

Using Eq. B-3 to remove the P_∞ item in Eq. B-2, then the Navier-Stokes equation for the fixed cylinder under oscillation flow will be transformed as follow, together with other equations for the complete boundary-value problem for the fixed cylinder under oscillatory flow

$$i\frac{\partial U}{\partial t} + \frac{Dv}{Dt} = \frac{-\nabla P^*}{\rho} + \upsilon\nabla^2 v \qquad \textbf{Eq. B-4}$$

$$\nabla \cdot v = 0 \qquad \textbf{Eq. B-5}$$

$$v = -iU\,(at\ \infty) \qquad \textbf{Eq. B-6}$$

$$v = 0\,(on\ r = a\,(a = radius\ of\ cylinder)) \qquad \textbf{Eq. B-7}$$

As mentioned earlier, Eq. B-4 is Navier-Stokes equation. Eq. B-5 is the continuity equation, Eq. B-6 is the far-away kinematic boundary condition and Eq. B-7 is the kinematic boundary condition on the cylinder surface.

Then, for the case of an oscillating cylinder in still water, the use of moving coordinates attached to the cylinder is convenient. Assuming the instantaneous velocity of the oscillating cylinder as iU, the total derivative of the fluid-velocity vector v may be written in terms of moving coordinates attached to the cylinder as $Dv/Dt = Dv'/Dt + i\partial U/\partial t$, where v' denotes the fluid-velocity vector measured in moving coordinates. The ∇ operator is the same in either the moving- or fixed-coordinate system. Considering the pressure P equal to P^* for oscillating cylinder in still water ($P_\infty = 0$ for cylinder in still water), the complete boundary-value problem for oscillating cylinder in still water can be written in moving coordinates as

$$i\frac{\partial U}{\partial t} + \frac{Dv'}{Dt} = \frac{-\nabla P^*}{\rho} + \upsilon\nabla^2 v' \qquad \textbf{Eq. B-8}$$

$$\nabla \cdot v' = 0 \qquad\qquad \textbf{Eq. B-9}$$

$$v' = -iU\,(at\ \ \infty) \qquad\qquad \textbf{Eq. B-10}$$

$$v' = 0(on\ \ r = a) \qquad\qquad \textbf{Eq. B-11}$$

It can be seen that the boundary-value problem for the fixed cylinder under oscillation flow (Eq. B-4~Eq. B-7) is identical to that for the oscillating cylinder in still water (Eq. B-8~Eq. B-11). So the solutions to the boundary-value problems must be identical and therefore the pressure P^* is the same.

The only difference between oscillating the water and oscillating the cylinder is that in the case of oscillating the water the total pressure includes the extra term P_∞, which is required to accelerate the flow with magnitude of $\partial U / \partial t$ and gives rise to an inertia force of $\rho(\pi d^2 / 4)\partial U / \partial t$ per unit length when integrated around the cylinder. This inertia force of $\rho(\pi d^2 / 4)\partial U / \partial t$ generates the 1.0 part in the inertia coefficient written as $C_M = 1 + C_a$ for an oscillatory flow past a fixed cylinder.

The in-line integral of P^* gives rise to the remainder of the force, which consists of drag force and added-mass force. So, in terms of the force coefficients, the drag coefficient C_D (or the added-mass coefficient C_a) of the oscillating cylinder in still water will be the same as that of the fixed cylinder under oscillatory flow.

It is important to show the demonstration that the case of an oscillating cylinder in still water is kinematically identical to the case of a fixed cylinder under oscillatory

flow. It means as much can be learned about the wave-force problem through study of an oscillating cylinder in still water or a fixed cylinder under oscillatory flow.

Comparisons of U-Tube experiments with tests of an oscillating cylinder in still water

As discussed before, an oscillating cylinder in still water is kinematically identical to a fixed cylinder under oscillatory flow. So, theoretically, the values of coefficient C_D (or C_a) obtained from these two experimental methods should be the same. However, experimentally, uncertainties and discrepancies of the results could be caused by the difficulties encountered in these two situations, which are of significant difference. As a representative of oscillating-flow tests, U-tube experiments have been popularly used by Sarpkaya. In his experiments, a new term called frequency parameter $\beta = D^2 / \upsilon T$ is defined, where D is diameter of cylinder, and T is oscillation period. Experiments were carried out with non-forced oscillations with a natural period T, which depends on the size of U-Tubes. The amplitude of oscillation will decrease slowly per cycle, for example, over a period of 4 complete cycles of oscillation at any mean amplitude, the amplitude, velocity, and the acceleration of the fluid would only change about 1%. Then one test which could last a period of about an hour would show the evolution of the in-line and transverse forces for all possible values of KC for a given β (Sarpkaya, 1976).

The disadvantages and advantages of each method have been discussed by several people (Sarpkaya, 1976; Garrison, 1990), which are summarized below.

1) Advantages and disadvantages of oscillating the cylinder include:

a) The advantages are are that one can independently vary the Reynolds number and the amplitude. Also, one determines the fluid induced forces and hence C_D and C_a instead of C_D and $1+C_a$ since no pressure gradient exists in the fluid at rest;

b) Potential disadvantages mainly consist of several aspects. First, about the driving mechanism, vibration and supporting components can cause additional disturbances and time-dependent forces which are not easy to eliminate. Second, the inertial force due to the mass of the oscillating cylinder has to be subtracted from the total force by carrying out the experiments once in air and once in water. However, a small error in the phase angle can lead to large errors in the coefficients especially in the region where drag and inertia force are comparable. Third, this method devotes merely to the determination of the in-line force without due regard to the transverse force. Last but not the least, the effect of waves and free surface disturbances in the test created by the oscillating cylinder can be difficult to assess.

2) Disadvantages and advantages of oscillating the flow around a cylinder include:

a) If the oscillating fluid involves a free surface, one has to deal with the fact that the free surface is inherently unstable;

b) The U-tube tunnel could cause wake-blockage problem, which means the tube walls limit the influx of momentum into the wake so that diffusion of the wake-velocity profile is hindered. Therefore, the wake is more pronounced than it would be in unbounded flow;

c) Another problem with the U-tube experiments is that the input flow may become polluted by boundary-layer effects and turbulence (Rashid et al., 2011);

d) One of the advantages of U-tube experiments is that the oscillations can be so smooth that there is no need for filters between the transducer outputs and the recording system. Another advantage is that the in-line force and transverse force can be measured simultaneously.

It can be seen the selection of one method over the other needs to carefully consider all the difficulties as well as benefits. Now, in order to further investigate the performance of these two situations, some results from U-tube experiments (oscillating-flow tests) are compared with those from oscillating-cylinder tests, which can be seen from Figure B-1 to Figure B-5.
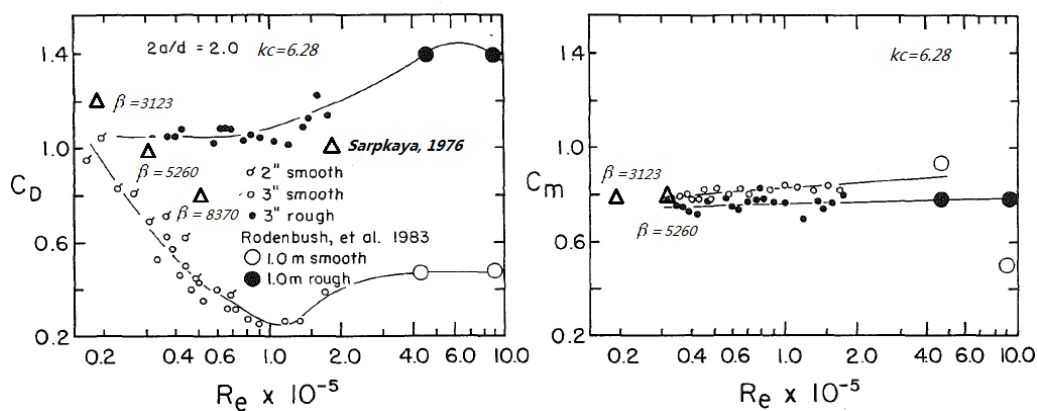

Figure B-1 Drag and added mass coefficients for a cylinder in relative unsteady flow *KC*=6.28 (reproduced from Garrison, 1990; the data from Sarpkaya (1976) is for a smooth cylinder)

Figure B-2 Drag and added mass coefficients for a cylinder in relative unsteady flow _KC_=9.4 (reproduced from Garrison, 1990; the data from Sarpkaya (1976) is for a smooth cylinder)

Figure B-3 Drag and added mass coefficients for a cylinder in relative unsteady flow _KC_=15.7 (reproduced from Garrison, 1990; the data from Sarpkaya (1976) is for a smooth cylinder)
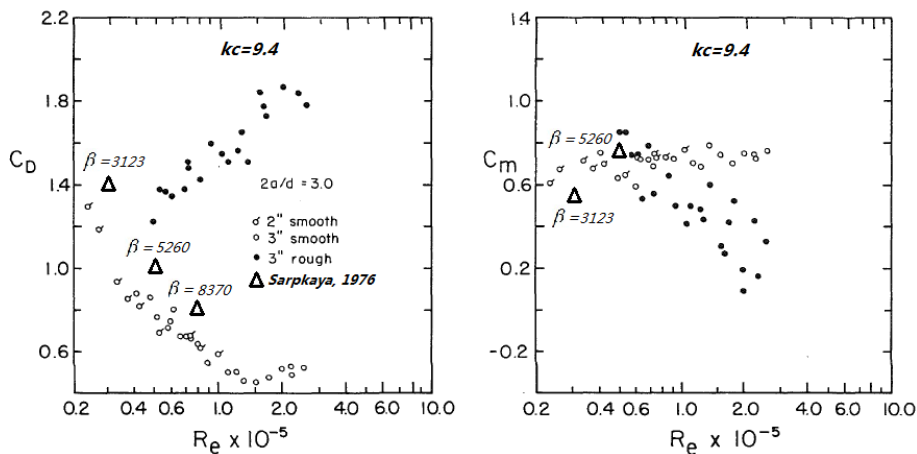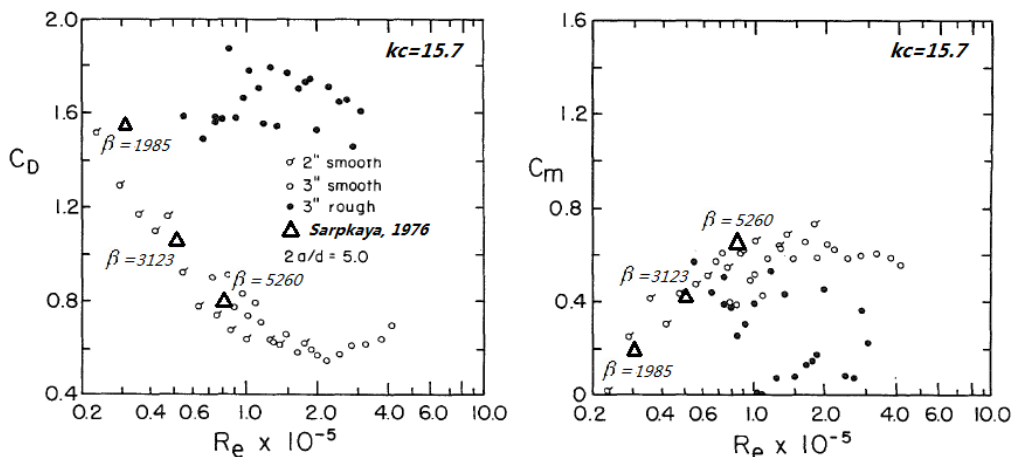
As seen from Figure B-1 and Figure B-2, for comparatively small _KC_ numbers ($KC = 6.3/9.4$) drag coefficients predicted by U-tube experiments are greater than those from oscillating-cylinder tests. With the increase of _KC_ and Re numbers, the predicted drag coefficients by two situations have fairly good agreement with each other, although it seems those from U-tube experiments are still slightly greater (see

255

Figure B-3, Figure B-4 and Figure B-5). However, the added-mass coefficients measured by two situations are generally in good agreement.
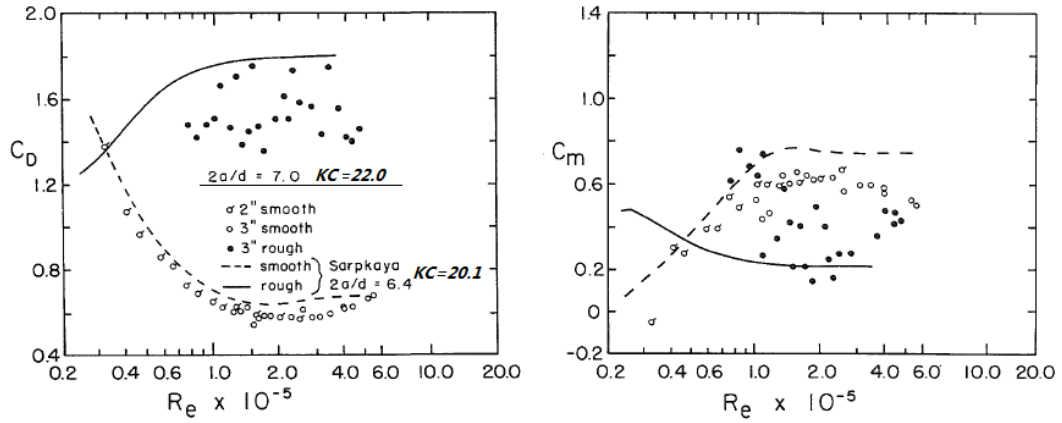

Figure B-4 Drag and added mass coefficients for a cylinder in unsteady oscillatory flow (reproduced from Garrison, 1990)
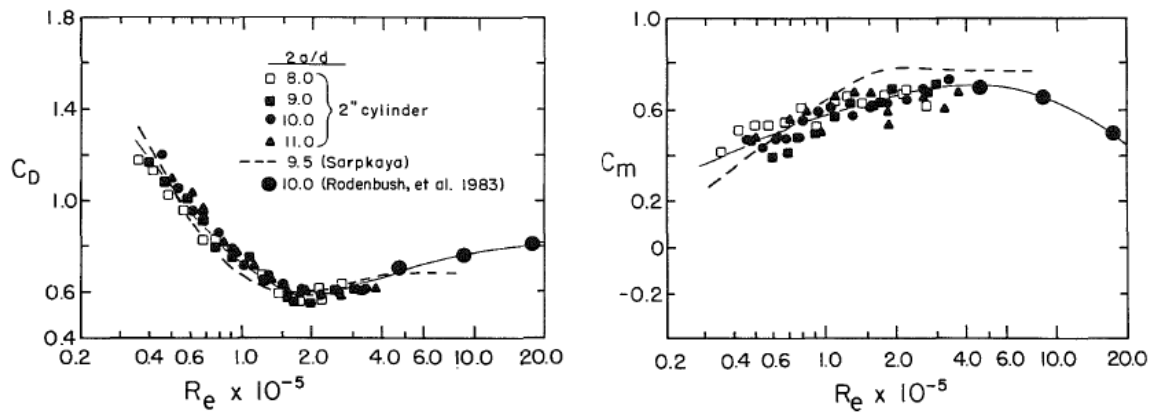

Figure B-5 Drag and added mass coefficients for a cylinder in unsteady oscillatory flow (Garrison, 1990)

Appendix C Fitting methods

The hydrodynamic coefficients of slender structures are determined based on Morison's equation, in which drag force and inertia forces are linearly added together. For a circular cylinder with diameter D, the in-line force acting on the unit-length cylinder can be calculated by

$$F(t) = \frac{1}{2} C_D \rho D U |U| + \frac{1}{4} C_M \rho \pi D^2 \dot{U} \qquad \textbf{Eq. C-1}$$

where, the in-line force F, velocity U, and acceleration $\dot{U}$, are measured quantities.

The coefficients C_D and C_M are the only unknowns, which are usually assumed to be time-invariant over a cycle for oscillatory flows. There are several different methods to compute C_D and C_M, which will be investigated below. The oscillatory velocity here is assumed as

$$U = U_m \sin(\omega t) \qquad \textbf{Eq. C-2}$$

where, U_m is the amplitude of velocity; $\theta = \omega t = 2\pi t / T$ is the phase angle.

C.1 Fourier-average approach

The method was introduced by Keulegan and Carpenter (1958), and can be used only for simple harmonic motions. Together with Eq. C-1 and Eq. C-2, one can get that

$$\frac{F(t)}{\rho U_m^2 D} = \frac{1}{2} C_D \sin\theta |\sin\theta| + \frac{\pi\omega}{4U_m} C_M D \cos\theta \qquad \textbf{Eq. C-3}$$

According to the Fourier analysis, one can obtain

$$\frac{F(t)}{\rho U_m^2 D} = \frac{A_0}{2} + \sum_{n=1}^{\infty}(A_n \sin n\theta + B_n \cos n\theta) \qquad \textbf{Eq. C-4}$$

where,

$$A_n = \frac{1}{\pi}\int_0^{2\pi}\frac{F(t)}{\rho U_m^2 D}\sin n\theta \cdot d\theta \qquad \textbf{Eq. C-5}$$

$$B_n = \frac{1}{\pi}\int_0^{2\pi}\frac{F(t)}{\rho U_m^2 D}\cos n\theta \cdot d\theta \qquad \textbf{Eq. C-6}$$

Bearing in mind that F is periodic, namely $F(\theta) = -F(\theta+\pi)$, so all even terms are zero. Thus by neglecting higher-order terms, Eq. C-4 can be written as

$$\frac{F(t)}{\rho U_m^2 D} = A_1 \sin\theta + B_1 \cos\theta \qquad \textbf{Eq. C-7}$$

Similarly, by the rule of Fourier, item $\sin\theta|\sin\theta|$ can be written as

$$\sin\theta|\sin\theta| = \frac{8}{3\pi}\sin\theta + \frac{8}{15\pi}\sin 3\theta + \frac{8}{105\pi}\sin 5\theta + ... \qquad \textbf{Eq. C-8}$$

By only keeping the linear item in Eq. C-8, then Eq. C-3 can be written as

$$\frac{F(t)}{\rho U_m^2 D} = \frac{4}{3\pi} C_D \sin\theta + \frac{\pi\omega}{4U_m} C_M D \cos\theta \qquad \textbf{Eq. C-9}$$

Considering Eq. C-7 and Eq. C-9 together, one could get that

$$C_D = \frac{3\pi}{4} A_1 = \frac{3}{4} \int_0^{2\pi} \frac{F(t)}{\rho U_m^2 D} \sin\theta \cdot d\theta$$
$$= \frac{3\omega}{4\rho U_m^2 D} \int_{t_1}^{t_1+T} F(t)\sin\omega t \cdot dt \qquad \textbf{Eq. C-10}$$

$$C_M = \frac{4U_m}{\pi\omega D} B_1 = \frac{4}{\pi^2 \omega D^2 \rho U_m} \int_0^{2\pi} F(t)\cos\theta \cdot d\theta$$
$$= \frac{4}{\pi^2 D^2 \rho U_m} \int_{t_1}^{t_1+T} F(t)\cos\omega t \cdot dt \qquad \textbf{Eq. C-11}$$

C.2 Least-squares method

The least-squares method can be applied to the non-sinusoidal-motion situation, and therefore is probably the most versatile method. Considering Morison's equation in Eq. C-1, the most desirable values of C_D and C_M would give a minimum error term on the right, namely

$$\min \Delta_e^2 = \sum_{n=1}^N [F - (\frac{1}{2} C_D \rho D U |U| + \frac{1}{4} C_M \rho\pi D^2 \dot{U})]^2 \qquad \textbf{Eq. C-12}$$

where, N means the number of sampling points.

Differentiating with respect C_D and C_M gives

$$\frac{\partial (\min \Delta_e^{\,2})}{\partial (C_D)} = 0 \; ; \; \frac{\partial (\min \Delta_e^{\,2})}{\partial (C_M)} = 0 \qquad \textbf{Eq. C-13}$$

Then,

$$\sum_{n=1}^{N} [F - (\frac{1}{2} C_D \rho D U |U| + \frac{1}{4} C_M \rho \pi D^2 \dot{U})] * (-1/2 * \rho D U |U|) = 0 \qquad \textbf{Eq. C-14}$$

$$\sum_{n=1}^{N} [F - (\frac{1}{2} C_D \rho D U |U| + \frac{1}{4} C_M \rho \pi D^2 \dot{U})] * (\frac{1}{4} \rho \pi D^2 \dot{U}) = 0 \qquad \textbf{Eq. C-15}$$

Together Eq. C-14 with   Eq. C-15 , one can get the C_D and C_M . Now assume that cross-section area of cylinder $A_s = \pi D^2 / 4$, and assume k_1 , k_2 , k_3 , k_4 and k_5 as follows:

$$k_1 = \sum_{n=1}^{N} 1/2 * F \rho D U |U| \qquad \textbf{Eq. C-16}$$

$$k_2 = \sum_{n=1}^{N} 1/2 * \rho^2 D A_s U |U| \dot{U} \qquad \textbf{Eq. C-17}$$

$$k_3 = \sum_{n=1}^{N} (1/2 * \rho D U |U|)^2 \qquad \textbf{Eq. C-18}$$

$$k_4 = \sum_{n=1}^{N} F \rho A_s \dot{U} \qquad \text{Eq. C-19}$$

$$k_5 = \sum_{n=1}^{N} (\rho A_s \dot{U})^2 \qquad \text{Eq. C-20}$$

Then,

$$C_D = \frac{k_1 k_5 - k_2 k_4}{k_3 k_5 - k_2 k_2} ; \ C_M = \frac{k_3 k_4 - k_1 k_2}{k_3 k_5 - k_2 k_2} \qquad \text{Eq. C-21}$$

C.3 Weighted least-squares method

Sometimes, for offshore design purposes, it is more important that the Morison equation predict the force peaks accurately than to be as precise at moments when the force is nearly zero. The weighted least-squares method is to improve the fitting near the peak forces by applying a weight factor. The processing of C_D and C_M of this method is quite similar with the least-squares method. The only difference is the weights F^2 are applied on the right side of Eq. C-12 as follows

$$\min \Delta_e^2 = \sum_{n=1}^{N} F^2 [F - (\frac{1}{2} C_D \rho D U |U| + \frac{1}{4} C_M \rho \pi D^2 \dot{U})]^2 \quad \text{Eq. C-22}$$

Using similar deduction, and assume the following parameters:

$$k^w{}_1 = \sum_{n=1}^{N} 1/2 * F^3 \rho DU|U| \qquad \text{Eq. C-23}$$

$$k^w{}_3 = \sum_{n=1}^{N} F^2 (1/2 * \rho DU|U|)^2 \qquad \text{Eq. C-24}$$

$$k^w{}_4 = \sum_{n=1}^{N} F^3 \rho A_s \dot{U} \qquad \text{Eq. C-25}$$

$$k^w{}_5 = \sum_{n=1}^{N} F^2 (\rho A_s \dot{U})^2 \qquad \text{Eq. C-26}$$

Then one could get

$$C_D = \frac{k^w{}_1 k^w{}_5 - k^w{}_2 k^w{}_4}{k^w{}_3 k^w{}_5 - k^w{}_2 k^w{}_2} ; \; C_M = \frac{k^w{}_3 k^w{}_4 - k^w{}_1 k^w{}_2}{k^w{}_3 k^w{}_5 - k^w{}_2 k^w{}_2} \qquad \text{Eq. C-27}$$

C.4 Morrison method

Morison method was suggested by Morison to determine the two unknown coefficients. His method is quite straightforward that can be done by hand processing. As illustrated in Figure C-1, when velocity is zero, then acceleration is maximum, and hence measured force is equal to the inertial force at that instant. The added mass

coefficient can be calculated according to the formula shown in the figure. Similar procedure can be used to calculate the drag coefficient.

Morison method is simple but could lack accuracy, because a significant phase error can be caused by a small error in the velocity record. Besides, the coefficients are determined by using only two instants in the time record while the rest is thrown away, although potential error resource of the latter can be reduced by averaging the coefficients over a large number of measurements.
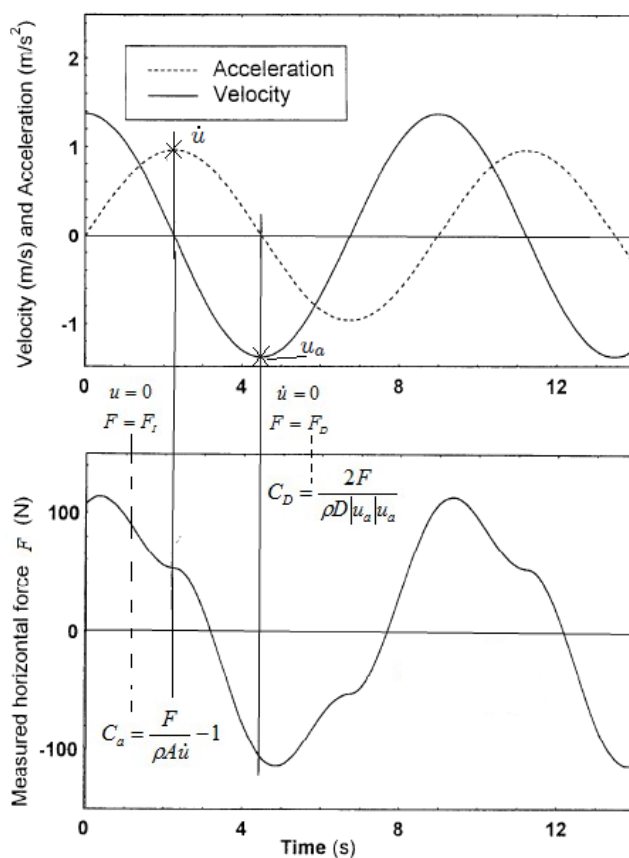

Figure C-1 Morison method for force coefficients (reproduced from Journée and Massie, 2001)

Reference of appendix

ACHENBAC, E. 1968. Distribution of local pressure and skin friction around a circular cylinder in cross-flow up to Re=5X10^6. *Journal of Fluid Mechanics*, 34, 625-639.

ANATURK, A. R. 1991. An experimental investigation to measure hydrodynamic-forces at small amplitudes and high-frequencies. *Applied Ocean Research*, 13, 200-208.

BEARMAN, P. W., DOWNIE, M. J., GRAHAM, J. M. R. & OBASAJU, E. D. 1985. Forces on cylinders in viscous oscillatory flow at low Keulegan-Carpenter numbers. *Journal of Fluid Mechanics*, 154, 337-356.

GARRISON, C. J. 1980. A review of drag and inertia forces on circular cylinders. *Offshore Technology Conference*. Houston, Texas.

GARRISON, C. J. 1990. Drag and inertia forces on circular cylinders in harmonic flow. *Journal of Waterway Port Coastal and Ocean Engineering-Asce*, 116, 169-190.

GROVE, A. S., SHAIR, F. H., PETERSEN, E. E. & ACRIVOS, A. 1964. An experimental investigation of the steady separated flow past a circular cylinder. *Journal of Fluid Mechanics*, 19, 60-80.

HALLAM, M. G., HEAF, N. J. & WOOTTON, L. R. 1977. Dynamics of marine structures. CIRIA Underwater Engineering Group, Atkins Research and Development.

JOURNÉE, J. M. J. & MASSIE, W. W. 2001. *Offshore Hydromechanics*, Delft University of Technology.

KATO, M., ABE, T., TAMIYA, M. & KUMAKIRI, T. 1983. Drag forces on oscillating cylinders in a uniform flow. *Offshore Technology Conference*. Houston, Texas.

KEULEGAN, G. H. & CARPENTER, L. H. 1958. Forces on cylinders and plates in an oscillating fluid. *Journal of Research of the National Bureau of Standards*, 60, 423–440.

LONGORIA, R. G. 1989. *An experimental investigation of hydrodynamic forces on circular cylinders in sinusoidal and random oscillating flow*. PhD, The University of Texas at Austin, Austin.

LONGORIA, R. G., MIKSAD, R. W. & BEAMAN, J. J. 1991. An experimental investigation of forces induced on cylinders by random oscillatory flow. *J. Offshore Mech. Arct. Eng.*, 113(4), 275-285.

MOE, G. & VERLEY, R. L. P. 1980. Hydrodynamic damping of offshore structures in waves and currents. *Offshore Technology Conference*. Houston, Texas.

OBASAJU, E. D., BEARMAN, P. W. & GRAHAM, J. M. R. 1988. A study of forces, circulation and vortex patterns around a circular-cylinder in oscillating flow. *Journal of Fluid Mechanics*, 196, 467-494.

RASHID, F., VARTDAL, M. & GRUE, J. 2011. Oscillating cylinder in viscous fluid: calculation of flow patterns and forces. *Journal of Engineering Mathematics*, 70, 281-295.

SARPKAYA, T. 1976. Vortex shedding and resistance in harmonic flow about smooth and rough cylinders at high Reynolds numbers. *Technical Report No. NPS-59SL76021*. Monterey, California: Naval Postgraduate School.

SARPKAYA, T. 1986. Force on a circular-cylinder in viscous oscillatory flow at low Keulegan-Carpenter numbers. *Journal of Fluid Mechanics*, 165, 61-71.

SARPKAYA, T. & ISAACSON, M. 1981. *Mechanics of Wave Forces on Offshore Structures*, Van Nostrand Reinhold Co.

SARPKAYA, T., RAINES, T. S. & TRYTTEN, D. O. 1982. Wave forces on inclined smooth and rough circular cylinders. *Offshore Technology Conference*. Houston,Texas.

SARPKAYA, T. & STORM, M. 1985. In-line force on a cylinder translating in oscillatory flow. *Applied Ocean Research*, 7, 188-196.

SCHEWE, G. 1983. On the force fluctuations acting on a circular-cylinder in cross-flow from subcritical up to transcritical Reynolds-numbers. *Journal of Fluid Mechanics*, 133, 265-285.

SCHLICHTING, H. 1979. *Boundary Layer Theory*, McGraw-Hill.

SUMMER, B. M. & FREDSØE, J. 1997. *Hydrodynamics around Cylindrical Structures*, World Scientific.

SUNDAR, V., VENGATESAN, V., ANANDKUMAR, G. & SCHLENKHOFF, A. 1998. Hydrodynamic coefficients for inclined cylinders. *Ocean Engineering*, 25, 277-294.

TANEDA, S. 1956. Experimental investigation of the wakes behind cylinders and plates at low Reynolds numbers. *Journal of the Physical Society of Japan*, 11, 302-307.

THOM, A. 1933. The flow past circular cylinders at low speeds. *Proceedings of the Royal Society of London Series a-Containing Papers of a Mathematical and Physical Character*, 141, 651-669.

WILLIAMSON, C. H. K. 1985. Sinusoidal flow relative to circular-cylinders. *Journal of Fluid Mechanics*, 155, 141-174.